Universitat Politècnica de València
Departamento de Máquinas y Motores Térmicos

Study on Advanced Spray-guided Gasoline Direct Injection Systems

Doctoral Thesis
by:
Mr. Daniel Vaquerizo Sánchez
Thesis supervisor:
Prof. Raul Payri Marín

Valencia, February 2018

DOCTORAL THESIS

STUDY ON ADVANCED SPRAY-GUIDED GASOLINE DIRECT INJECTION SYSTEMS

By:

Daniel Vaquerizo Sánchez

Submitted to:

Departamento de Máquinas y Motores Térmicos
Universitat Politècnica de València

In fulfillment of the requirements for the degree of

DOCTOR OF PHILOSOPHY

Valencia, February 2018

DOCTORAL THESIS

STUDY ON ADVANCED SPRAY-GUIDED GASOLINE DIRECT INJECTION SYSTEMS

By:	*M*r. Daniel Vaquerizo Sánchez
Supervisor:	*D*r. Raul Payri Marín

Doctoral Examination Board:

Chairman:	*D*r. Jesús Benajes Calvo
Secretary:	*D*r. Octavio Armas Vergel
Member:	*D*r. Jérôme Hélie

Review Committee:

✓	*D*r. Jérôme Hélie
✓	*D*r. Panos Sphicas
✓	*D*ra. María del Carmen Mata

Valencia, February 2018

Abstract

Fuel injection systems have been one of the main focal points of engine research, particularly in Diesel engines, where the internal geometry, needle lift and flow behavior are known to affect the external spray an in turn completely determine the combustion process inside engines. Because of environmental regulation and the potential development of the more inefficient Otto engines, a lot of research efforts are currently focused into gasoline direct injection systems. GDi engines have the potential to greatly increase fuel economy and comply with pollutant and greenhouse gases emissions limits, although many challenges still remain. The current thesis studies in detail a modern type of GDi nozzle that was specifically developed for the international research group known as the Engine Combustion Network (ECN). With the objective of employing state-of-the-art techniques, this hardware has been used in a wide range of experimental facilities in order to characterize the internal flow and several geometrical and constructive aspects like needle lift; and assess how it relates to the effects seen external spray.

For the internal flow characterization, the goal was to determine the nozzle geometry and needle displacement, to characterize the rate of injection and rate of momentum, and evaluate the near-nozzle flow. Some methodologies applied here have never been applied to a GDi injector before, and many have only been applied rarely. For the internal geometry, needle lift and near-nozzle flow, several advanced x-rays techniques were used at Argonne National Laboratory. For the rate of injection and rate of momentum measurements, the techniques available in CMT-Motores Térmicos have been adapted from Diesel spray research and brought to multi-hole GDi injectors. Given the novelty of the techniques used, the particular methodologies and setups are discussed in detail. Despite the high turbulence of the flow, it was seen that the injector behaves consistently injection to injection, even when studying variation in individual holes. This is attributed to the repetitive behavior of the needle that was observed in the experiments. It was also observed that the stabilized flow has a high frequency variability that could not be explained by random movement of the needle, but rather by the particular design of the nozzle. The geometrical analysis done to eight, nominally equal nozzles, allowed a unique view into the construction of the nozzle and provided insights about the variability of key dimensions. The rate of injection measurements allowed to study the hydraulic response of the injector to the main

variables like rail pressure, discharge pressure, fuel temperature and command signal duration. These measurements were combined with the rate of momentum measurements to study the low value of the discharge coefficient, that ultimately was attributed to the low needle lift and low L/D ratio of the orifices. On the other hand, the study of the external spray yielded the identification of very important phenomena specific to this particular hardware, the spray collapse. The extensive experimental campaigns featuring shadowgraph (Schlieren) and Diffused Back Illumination (DBI) visualization techniques allowed identifying and describing the macroscopic characteristics of the spray and the conditions under which the collapse occurs. The spray collapse engenders from a combination of the internal flow that creates plume interaction, and ambient conditions that promote air entrainment and evaporation. At moderate density and temperature levels the collapse develops, completely modifying the expected trends in the behavior of the plumes.

Resumen

Los sistemas de inyección directa han sido uno de los principales puntos focales de la investigación en motores, particularmente en sistemas Diésel, donde la geometría interna, movimiento de aguja y comportamiento del flujo afectan el spray externo y por tanto determinan completamente el proceso de combustión dentro del motor. Debido a regulaciones medioambientales y al potencial de los (más ineficientes) motores "Otto", grandes esfuerzos se están aportando en investigación sobre sistemas de inyección directa de gasolina. Los motores GDi tienen el potencial de incrementar sustancialmente la economía de combustible y cumplir con las regulaciones de gases contaminantes y de efecto invernadero, aunque aún existen muchos desafíos por delante. Esta tesis estudia en detalle una moderna tobera GDi que fue específicamente diseñada para el grupo de investigación conocido como Engine Combustion Network (ECN). Con metodologías punteras, este inyector ha sido usado en un amplio abanico de instalaciones experimentales para caracterizar el flujo interno y varias características clave de geometría y funcionamiento, y aplicarlo para evaluar cómo se relaciona con los efectos observados del comportamiento del chorro externo.

Para la caracterización interna del flujo, el objetivo ha sido determinar la geometría de la tobera y el desplazamiento de aguja, caracterizar la tasa de inyección y el flujo de cantidad de movimiento, y evaluar el flujo cercano. Algunas metodologías nunca antes habían sido empleadas en inyectores GDi, y muchas otras lo han sido solo eventualmente. Para la geometría interna, el levantamiento de aguja y el flujo cercano, varias técnicas avanzadas con rayos-x fueron aplicadas en las instalaciones de Argonne National Laboratory. Para la tasa de inyección y flujo de cantidad de movimiento, las técnicas disponibles en el departamento han sido adaptadas desde Diésel y aplicadas en inyectores GDi multiorificio. Dado lo novedoso de las técnicas aplicadas, las particularidades de las metodologías han sido discutidas en detalle en el documento. Aún con la elevada turbulencia del flujo interno, el inyector se comporta de forma consistente inyección a inyección, incluso cuando el estudio se centra en la variabilidad orificio a orificio. Esto ha sido atribuido al comportamiento repetitivo de la aguja, evaluado en los experimentos. También fue observado que el flujo estabilizado tiene una variación de alta frecuencia que no pude ser explicado por el movimiento de la aguja, sino por el

particular diseño de las toberas. El análisis de geometría interna realizado a ocho toberas nominalmente iguales resultó en la obtención de un punto vista único en la construcción de toberas y la variabilidad de dimensiones clave. Las medidas de tasa de inyección permitieron estudiar la respuesta hidráulica del inyector a varias variables como la presión de inyección, presión de descarga, temperatura de combustible y la duración de la señal de comando. Estas medidas fueron combinadas con medidas de flujo de cantidad de movimiento para estudiar el bajo valor del coeficiente de descarga, el cual fue atribuido al bajo levantamiento de aguja y coeficiente L/D de los orificios. Por otro lado, el estudio del spray externo resultó en la identificación de un importante fenómeno específico a este particular hardware, el colapso del spray. Las extensivas campañas experimentales, utilizando Schlieren e iluminación trasera difusa (DBI) permitieron identificar y describir las características macroscópicas del spray y las condiciones bajo las que el colapso ocurre. El colapso del spray se forma por una combinación de interacción de las diferentes plumas (causado por el flujo interno) y determinadas condiciones ambiente que promueven evaporación y entrada de aire. Fue determinado que a niveles de densidad y temperatura moderados se desarrolla el colapso, modificando completamente el comportamiento esperado del spray.

Resum

Els sistemes d'injecció directa han sigut un dels principals punts focals de la investigació en motors, particularment en sistemes dièsel, en què la geometria interna, el moviment de l'agulla i el comportament del flux afecten l'esprai extern i per tant determinen completament el procés de combustió dins del motor. Degut a regulacions mediambientals i al potencial dels (més ineficients) motors "Otto", grans esforços s'estan aportant en investigació sobre sistemes d'injecció directa de gasolina. Els motors GDi tenen el potencial d'incrementar substancialment l'economia del combustible i complir les regulacions de gasos contaminants i d'efecte hivernacle, encara que existeixen molts desafiaments per davant. Esta tesi estudia en detall una moderna tovera GDi que va ser especialment dissenyada per al grup d'investigació conegut com a ECN. Amb l'objectiu de desenvolupar metodologies punteres, este injector ha sigut usat en un ampli ventall d'instal·lacions experimentals per tal de caracteritzar el flux intern i diverses característiques clau de la seua geometria i funcionament, per tal d'avaluar com es relacionen amb els efectes observats del comportament de l'esprai extern. Per a la caracterització interna del flux, l'objectiu ha sigut determinar la geometria de la tovera i el desplaçament de l'agulla, caracteritzar la taxa d'injecció i el flux de quantitat de moviment, i avaluar el flux proper. Algunes metodologies no s'havien empleat abans en injectors GDi, i moltes altres ho han sigut únicament de manera eventual. Per a la geometria interna, l'alçament de l'agulla i el flux proper, s'han aplicat diverses tècniques avançades amb raigs-x a les instal·lacions d'Argonne National Laboratory. Per a la taxa d'injecció i el flux de quantitat de moviment, les tècniques disponibles al departament han sigut adaptades des de Dièsel i aplicades a injectors GDi multi-orifici. Considerant la novetat de les tècniques aplicades, les particularitats de les metodologies es discuteixen en detall al document. A pesar de l'elevada turbulència del flux intern, l'injector es comporta de manera consistent injecció a injecció, inclús quan l'estudi se centra en la variabilitat orifici a orifici. Aquest fet s'ha atribuït al comportament repetitiu de l'agulla, avaluat als experiments. També es va observar que el flux estabilitzat té una variació d'altra freqüència que no pot ser explicat pel moviment de l'agulla, sinó pel particular disseny de les toveres. L'anàlisi de la geometria interna realitzat a vuit toveres nominalment iguals va permetre obtenir un punt de vista únic en la construcció de toveres i la variabilitat de dimensions clau. Les mesures de

taxa d'injecció van permetre estudiar la resposta hidràulica de l'injector a diverses variables com la pressió d'injecció, la pressió de descàrrega, la temperatura del combustible i la duració de la senyal de comandament. Estes mesures van ser combinades amb mesures de flux de quantitat de moviment per tal d'estudiar el baix valor del coeficient de descàrrega, el qual va ser atribuït al baix alçament de l'agulla i al coeficient L/D dels orificis. D'altra banda, l'estudi de l'esprai extern va permetre identificar un important fenomen específic d'aquest hardware particular: el col · lapse de l'esprai. Les extensives campanyes experimentals, utilitzant Schlieren i il · luminació darrera difusa (DBI) van permetre identificar i descriure les característiques macroscòpiques de l'esprai i les condicions sota les quals el col · lapse té lloc. El col · lapse de l'esprai es forma per una combinació d'interacció de les diverses plomes (causat pel flux intern) i determinades condicions ambient que promouen evaporació i entrada d'aire. Es va determinar a quins nivells de densitat i temperatura moderats es desenvolupa el col · lapse, modificant completament el comportament esperat de l'esprai.

A mi familia

Agradecimientos

Quiero aprovechar esta oportunidad para agradecer a todas aquellas personas que han contribuido de alguna manera en la realización de este trabajo. Durante estos cuatro años han sido muchas personas las que me han marcado, me han enseñado, y me han hecho mejorar como ingeniero y como persona.

En primer lugar me gustaría agradecer a mi director de tesis Raúl Payri, por su inestimable ayuda y consejo durante mi trabajo en CMT. Raúl no solo ha sido un gran mentor, siempre orientando en la dirección correcta, también es un excelente manager para todo el grupo de inyección, tratando en todo momento de conseguir lo mejor para el equipo y sus miembros.

Asimismo, debo agradecer al Instituto CMT-Motores Térmicos, y en particular a Francisco Payri, José María Desantes y Jesús Benajes la oportunidad de permitirme formar parte de este prestigioso grupo de investigación. Sus recursos tecnológicos, económicos y humanos han posibilitado la realización de esta Tésis Doctoral.

Me gustaría dar un especial agradecimiento a Christopher Powell por darme la oportunidad de realizar la estancia de investigación en Argonne National Laboratory y tratarme como un miembro más del equipo. Asímismo, agradecer al equipo de Fuel Spray: Katarzyna Matusik, Daniel Duke, Alan Kastergren y Nicholas Sovis por su ayuda y compañerismo durante la estancia.

Mi mas sincera gratitud a los miembros del equipo de Inyección de CMT. Mención especial a Jaime Gimeno, Gabriela Bracho y Juan Pablo Viera por su infinita paciencia resolviendo mis preguntas y ofreciendo su ayuda y tiempo cuando lo he necesitado; y tambien, a Abian, María y Dácil por su ayuda en la revisión del documento final. Asímismo, gracias al resto de profesores y doctorandos por su compañerismo y amistad durante todo este tiempo: Marcos, Pedro, Javi, Joaquín, Alberto, Sebastian, Mary, Jesús, Abian, Marco, Vincenzo, Armando, Santiago, Mario, María. Gracias también a los técnicos encargados de las instalaciónes experimentales, en especial a Omar y Borja; y por último José Enrique.

Fuera del equipo también he de agradecer a muchos miembros de

CMT, en especial a Dani, Ricardo, Diego, y Jordi (miembro proxy) por tantos buenos momentos tanto en la pista de fútbol como fuera. Además me gustaría extender mi agradecimiento al resto de profesores, técnicos, informáticos, secretarios y secretarias y personal de servicios que hacen que todo funcione cada día.

Por supuesto, no puedo olvidar a toda la gente que fuera del trabajo me ha aportado tanto. Gracias a todos los amigos de Toledo, que a pesar que la distancia hace mas complejos los encuentros, siempre han estado ahí para pasar buenos momentos y cuando lo he necesitado.

Gracias a Nicole, por este año tan especial. Cerca o lejos, por ayudarme siempre y por motivarme a ser una mejor persona cada día.

Por último, gracias a mi familia, que siempre me ha apoyado y que me da confianza cada día para probar cualquier camino. Gracias a mi Madre por su valentía para superar los malos momentos, por su soporte y por su apoyo incondicional. Gracias a mi hermano por haber sido una roca donde apoyarme y por haberme ayudado en todo desde que era un mocoso. Gracias a mi Padre, que aunque ya no esté, me enseñó lo que significa el esfuerzo y sacrificio, y por que su memoria siempre me ha servido como brújula para continuar adelante.

A todos vosotros, gracias.

Funding acknowledgments

Daniel Vaquerizo is partially supported through contract FPI-S2-2015-1069 of “Programa de Apoyo para la Investigación y Desarrollo (PAID)” of Universitat Politècnica de València.

The research during the stay was performed at the 32-ID and 7–BM beamlines of the APS at Argonne National Laboratory. Use of the APS is supported by the U.S. Department of Energy (DOE) under Contract No. DE–AC02–06CH11357. Argonne’s x–ray research of Advanced Combustion is funded by the DOE Office of Energy Efficiency and Renewable Energy Vehicle Technologies Office under the direction of Gurpreet Singh and Leo Breton.

Contents

Contents **i**

List of Figures **v**

List of Tables **xii**

Nomenclature **xiii**

1 Introduction **1**
1.1 General context 1
1.2 Objectives 4
1.3 Outline 6

2 Background **9**
2.1 Introduction 9
2.2 Definition of SI and CI engines 11
2.3 Fuel delivery in ICE 13
2.3.1 Diesel Engines 13
2.3.2 Gasoline Engines 16
2.4 Gasoline direct injection 20
2.4.1 Introduction 20
2.4.2 Stratified-charge mode 23
2.4.3 Potential technologies of GDi 27
2.5 Fuel injectors in GDi engines 28
2.5.1 Types of modern GDi injectors 28
2.5.2 Multi-hole solenoid-actuated GDi injectors 32
References 44

3 Experimental and analytical methodologies 57
3.1 Introduction 57
3.2 Injection system 58
3.2.1 GDi Injector 58
3.2.2 Standard conditions 59
3.2.3 Engine Control Unit 61
3.2.4 High-pressure fuel delivery system 62
3.3 Rate of Injection 63
3.3.1 Background 63
3.3.2 Set-up and methodology 65
3.4 Rate of Momentum 68
3.4.1 Background 68
3.4.2 Set-up and measurement methodology 70
3.5 X-ray measurements 75
3.5.1 Background 75
3.5.2 X-ray imaging. Needle displacement 77
3.5.3 Internal nozzle geometry. X-ray tomography . . . 79
3.5.4 Near-field x-ray radiography 84
3.5.5 Near-nozzle x-ray tomographic radiography 87
3.6 External Spray Visualization 88
3.6.1 Introduction 88
3.6.2 Single-Pass Schlieren technique 90
3.6.3 Diffused Back Illumination 91
3.6.4 Spray data processing methodology 92
References 98

4 Internal and near-nozzle flow 105
4.1 Introduction 105
4.2 Spray G Nozzle Geometry 106
4.3 Needle displacement 111
4.4 Rate of injection 117
4.4.1 Effect of injection pressure and ambient pressure . 120
4.4.2 Effect of Temperature 122
4.4.3 Injection duration study 123
4.4.4 Multiple injections 126
4.5 Rate of momentum 134
4.5.1 Evaluation of the frontal and lateral methodologies 134
4.5.2 Hydraulic coefficients 138

4.6 Near-nozzle x-ray radiography and spray tomography . . 141
  4.6.1 X-ray radiography. Projected mass 141
  4.6.2 X-ray tomographic radiography. Plume Isolation . 147
4.7 Conclusions 154
References 158

5 External spray 165
5.1 Introduction 165
5.2 ECN Spray G visualization experiments. 166
  5.2.1 Vapor phase visualization. 167
  5.2.2 Liquid phase visualization 170
  5.2.3 Comparison of liquid and vapor visualization with computational results. 178
5.3 Spray Collapse 186
  5.3.1 Background 186
  5.3.2 Test Matrix 187
  5.3.3 Effects of gas density variations 187
  5.3.4 Effect of gas temperature variations 194
  5.3.5 Effect of injection pressure variation 199
  5.3.6 Further analysis of density and temperature variations 202
5.4 Conclusions 204
References 207

6 Summary and future works 211
6.1 Summary 211
6.2 Future works 216

Bibliography 219

List of Figures

2.1 Drawing of a cut-section of an engine block and cylinder in a indirect injection Diesel engine 14
2.2 Drawing of a cut-section of an engine block and cylinder in a direct injection Diesel engine 15
2.3 Port fuel injection schematic 19
2.4 Schematic representation of a common GDi engine 22
2.5 Schematic representation of the homogeneous mode (left) and stratified mode (right) 24
2.6 Representation of the three strategies to achieve stratification: wall guided (left), air guided (center) and spray guided (right) 25
2.7 Schematic of a GDi piezo injector 30
2.8 Comparison of the spray formed by a piezoelectric GDi injector using and a solenoid multi-hole injector 31
2.9 Parts of a solenoid-actuated multi-hole GDi injector 32
2.10 Close-up picture of the nozzle of the ECN Spray G injector. 33
2.11 Slice of an x-ray tomographic reconstruction featuring two orifices, their counterbores, as well as the sac and needle ball of a multi-hole GDi injector (ECN Spray G). 35
2.12 Iso-surface of the internal geometry of one of the Spray G nozzles, reveling the internal geometry and the surface finish 38
2.13 Injection and discharge pressure conditions relationship with cavitating and non-cavitating flow for Diesel injectors and two GDi multi-hole injectors with drill angles of 45° (N45) and 50° (N50) 39

2.14 Representation of an injection under flashing conditions compared to the conventional case in a pressure-enthalpy diagram 40

3.1 Picture of the Delphi Spray G injector AV67-026 with inlet fuel feed (cast rail) mounted. 59
3.2 Sketch showing the main characteristics of the ECN GDi injector. The sketch represents a cut-plane of the nozzle showing the cross-section of two orifices, needle, needle seat and sac. All dimensions in µm. 60
3.3 Definition of primary and secondary orientation defined for visualization for the ECN GDi injector. 62
3.4 Engine Control Unit and driving signals produced for three different energizing times. 63
3.5 Diagram of the circuit used to pressurize and deliver the fuel to the GDi injector. 64
3.6 Diagram illustrating the parts of the instrument used to determine the mass flow rate. 64
3.7 Representation of a cut-section of the injector holder used for mass flow rate measurements. 66
3.8 Injector, injector holder and IAV rate meter used in the experimental set-up. 66
3.9 Sketch featuring the experimental set-up used for rate of injection measurements. 67
3.10 Representation of realistic flow at the exit of a nozzle and the simplified description of the fluid through the effective area and effective velocity coefficients. 69
3.11 Render of the rate of momentum test rig showing the piezoelectric sensor through the optical access. 71
3.12 Schematic of a spray impacting the sensor for the rate of momentum measurements. Adapted from [43]. 72
3.13 Render of the rate of momentum rig with the sensor, GDi injector, and injector holder in the lateral configuration . . . 73
3.14 Render of the rate of momentum rig with the sensor, GDi injector, and injector holder in the frontal configuration. . . 74
3.15 Six frames from the moment of injection recorded with a high speed camera through the optical access of the rate of momentum test rig. 75
3.16 Aerial photograph of the Advanced Photon Source 76

3.17 Diagram of the set-up for needle lift measurements 77
3.18 Two images from the Spray G needle lift experiments, a) with needle complete closed and b) with needle fully opened. . . . 79
3.19 Cross-correlation algorithm demonstration 80
3.20 Diagram of the experimental set-up used for the x-ray tomography 81
3.21 One of the 1800 images taken for tomographic reconstruction for one of the Spray G injectors (AV67-018). 81
3.22 Slice at the longitudinal plane (left) and transverse plane (right) of the reconstructed geometry. 82
3.23 Slice of hole in its longitudinal plane (left) and on its transverse plane (right). 83
3.24 Extracted profiles of all the orifices for one of the injectors tested. 83
3.25 Key dimensions investigated for the Spray G nozzles geometry. 84
3.26 Diagram of the experimental set-up used in 7-BM beamline for the x-ray radiography measurements. 85
3.27 X-ray radiography maps at two time instants showing the mass per unit area for the AV67-012 ECN injector. 86
3.28 Simplified representation of the experimental set-up for the spray tomography measurements. 88
3.29 Schematic representation of the optical arrangement. 89
3.30 Example of the image processing for an Schlieren image. . . 94
3.31 DBI Images at different temperature and density conditions with the detected contours overlapped to show the angle determination methodology. 95
3.32 Schlieren Images at different temperature and density conditions with the detected contours overlapped to show the angle determination methodology for vapor phase. 96

4.1 Measured dimensions of Spray G from x-ray nozzle tomography 106
4.2 Detail of inlet corner radius in ten rotation positions (rotating along the hole axis) for a hole of one of the Spray G injector. The red circle underlays the feature of interest and how the radius varies (decreases) as θ increases, from a higher radius to almost a straight angle. 109
4.3 Inlet radius for all holes of one of the injectors versus hole rotation (θ). 109

4.4 Discharge coefficients for nozzles with different L/D 110
4.5 Montage of needle lift visualization images for one of the conditions 113
4.6 Driving current from the ECU on the top. Needle lift and horizontal "wobble" motion for the modified Spray G conditions on the bottom. 114
4.7 The three different intensity outputs available in the ECU (top) and the needle lift produced by each (bottom). High is the standard output. 115
4.8 Needle lift for a command duration swipe. The durations tested varied from 160 µs to 350 µs. 116
4.9 Needle lift for the Spray G multiple injection condition (Spray G-M1). The needle lift reached in the post-injection is not what it would correspond for a single injection of that duration. 118
4.10 Rate of injection versus time for standard Spray G conditions 119
4.11 Rate of injection measured in the second experimental campaign for Spray G AV67-026 compared with ROI measured by GM of injectors AV67-016 and AV67-028. 120
4.12 Measured mass flow for an injection pressure swipe maintaining the rest of parameters at standard Spray G conditions. . 121
4.13 Measured mass flow for a discharge pressure swipe maintaining the rest of parameters at standard Spray G conditions. . 122
4.14 Mass flow rate divided by the square root of the pressure drop. All lines should merge into one if this factor completely explained the effect of injection pressure and ambient pressure on injection rate. 123
4.15 Effect of temperature on steady state ROI (a) and on the rate of injection signal (b) 124
4.16 Rate of injection (top) and needle lift (bottom) for a range of short ET pulses. 125
4.17 Injection rate comparison at two rail pressures for 5 different energizing times. 126
4.18 Mass flow rate for multiple injection commands signals. . . . 127
4.19 Needle lift comparison for a split and a single injection. . . . 128
4.20 Injection rate for split injection strategies with a variation of the duration of the dwell time from 400 µs to 1000 µs. 129

4.21 Pressure signals measured at the rail for the conditions presented in 4.20. 130
4.22 Energizing signal in Amperes sent to the injector from the driver (ECU) for several conditions. 131
4.23 Screen capture of the needle feature. 132
4.24 Rate of injection for three of the conditions in Fig 4.20 on the left axis, needle lift extracted with the manual procedure on the right axis in red. 134
4.25 Momentum flux versus time using the frontal configuration for three distances between the sensor and the nozzle tip. . . 135
4.26 Stabilized rate of momentum at different ambient pressures versus the distance from the nozzle tip to the sensor. 136
4.27 Stabilized momentum flux comparison between the lateral and frontal configurations for three different back pressure (BP) levels. 137
4.28 relationship of the velocity coefficient with the square root of the pressure drop 138
4.29 Effective velocity of the flow coming out of the orifices versus the square root of the pressure drop. 139
4.30 Evolution of the effective diameter of the nozzle with the square root of the pressure drop. 139
4.31 Discharge coefficient (Cd) of the Spray G nozzle evolution with the square root of the pressure drop. 140
4.32 Montage of injection process for one of the tests of spray radiography. The images are created by plotting together all of the measured positions (one per shot) and interpolating the grid. Therefore, one image contains a large number of injections. 142
4.33 Double integration of x-ray radiography data in the domain versus time. The slope of the fit represents the stabilized rate of injection 143
4.34 Transeve Integrated Mass (TIM) for all the axial positions experimented in the x-ray radiography of the SprayG-028. At steady state, an increase in the TIM is related to a deceleration of the flow. 145
4.35 Normalized velocity decay profiles for Spray G compared to ECN Spray A diesel injectors 146

4.36 Montage of the reconstructed x-rays radiography slices at 2 mm from the nozzle tip for all the Spray G nozzles measured. 148
4.37 Transverse integraged mass at 2 mm from the nozzle tip for all the Spray G injectors tested. 149
4.38 Transverse integrated mass at the 2mm axial position from the nozzle tip for 4 out of the 8 nozzles measured. 151
4.39 Relative standard deviation σ for the geometrical dimensions measured. 152
4.40 Scatter plots of response versus the most significant predictors (lowest p-value) 154

5.1 Maximum axial vapor penetration calculated using 3 different thresholding values for the vapor visualization data at Spray G conditions. 168
5.2 Radial profiles at 15 mm axial position from nozzle tip. Movies from University of Melbourne and CMT-Motores Térmicos. Each column of pixels is taken from the 15 mm axial position in the original images and concatenated to generate this kind of visualization. 169
5.3 Radial width versus time for the Schlieren visualization (vapor) at Spray G standard conditions. Comparison between data gathered at CMT and University of Melbourne using three thresholds for binarization in the processing algorithm. 170
5.4 Radial profile comparison of the Mie Scattering visualization between CMT and University of Melbourne. 172
5.5 Comparison of the optical thickness values in 4 images obtained using a DBI technique from Sandia (left) and CMT (right.) 174
5.6 Comparison of the liquid penetration using the images from SNL and CMT at Spray G (top) and Spray G9 conditions (bottom) using 4 different thresholds. 176
5.7 Radial width comparison between CMT and SNL liquid contours 177
5.8 Definition of plume direction and plume cone angle. 180
5.9 Vapor axial penetration comparison between RANS simulations from Polimi and experimental data from CMT (red). . 181
5.10 Vapor and liquid axial penetration from RANS simulations from Polimi compared to the experimental results (red). . . 182

5.11 LES simulation results for liquid axial penetration calculated using 4 different methodologies versus the experimental results (red). 184
5.12 Axial penetration comparison between liquid and vapor for the data obtained by KWA group. 185
5.13 Density variations for 500 K (top) and 700 K (bottom) for 20 MPa injection pressure and 1200 μs of energizing time for vapor and liquid penetration. 189
5.14 Liquid spray comparison between lower density conditions (left) and higher density conditions (right) using raw images and the detected contours. 191
5.15 Liquid spray angle for different density values for 500 K (top) and 700 K (bottom) for 20 MPa injection pressure and 1200 μs of energizing time. 193
5.16 Density variations at non-vaporizing conditions (400 K) for liquid spray angle. 194
5.17 Spray width at 4 different axial distances from the nozzle tip. 195
5.18 Temperature variations for 3 kg/m^3 density (top) and 9 kg/m^3 (bottom) and 20 MPa injection pressure for liquid and vapor penetration. 196
5.19 Vapor spray comparisons between low temperature case (left) and high temperature case (right) at 9 kg/m^3 of chamber density using raw images and the detected contours overlapped. 197
5.20 Temperature variations for 3 kg/m^3 density (top) and 9 kg/m^3 (bottom) and 20 MPa injection pressure for liquid spray angle. 199
5.21 Injection pressure variations between a lower (top) and higher (bottom) level of chamber density at 700 K of chamber temperature for liquid and vapor penetration. 200
5.22 Liquid and vapor spray contours comparison between a lower (left) and a higher (right) density level at 700 K of chamber temperature and 20 MPa injection pressure. 201
5.23 Minimum liquid spray angle calculated in the range of 900 to 1300 μs at 20 MPa injection pressure versus density (top) and temperature (bottom). The minimum spray angle has been chosen as a qualitative parameter to represent the degree of spray collapse. 203

6.1 Render of the new vessel for GDi sprays visualization experiments 217

List of Tables

3.1 List of the main and back-up Spray G injectors, the paired drivers, and the institutions in which they are located. . . . 58
3.2 Injector specifications 60
3.3 *Spray G conditions.* 61
3.4 Differences between the boundary conditions for x-rays measurements and nominal Spray G. 87
3.5 Summary of settings for the two cameras. 90

4.1 Hole dimensions measured by x-ray nozzle tomography and norminal dimensions from the manufacturer. 108
4.2 comparison of the steady state roi for the SprayG-026 and the integrated mass of the SprayG-028 144
4.3 Axial positions for the x-ray radiography experiments for SprayG-028 144
4.4 Coefficients and standard errors for the multiple regression model 153

5.1 Set-up parameters of the models used by the CFD data contributors 179
5.2 Summary of conditions tested in the experimental campaign. 188

Nomenclature

Acronyms

A1	Drill Angle.
ANL	Argonne National Laboratory.
APS	Advanced Photon Source.
BM	Bending Magnet.
CAD	Crank Angle Degree.
CFD	Computational Fluid Dynamics.
CIDI	Compression-Ignition Direct Injection.
CI	Compression-Ignition.
D1	Orifice upstream diameter.
D2	Orifice downstream diameter.
D3	Counterbore upstream diameter.
D4	Counterbore upstream diameter.
DI	Direct Injection.
DT	Dwell Time.
ECU	Electronic Control Unit.
ELSA	Eulerian-Lagrangian Spray Atomization.
ET	Energizing Time.
GDI	Gasoline Direct Injection.
HRM	Homogeneous Relaxation Model.
IDI	Indirect Injection.
ID	Insertion Device.
IRDCI	Injection Rate Discharge Curve Indicator.
L1	Orifice length.

L2	Counterbore length.
LDV	Laser Doppler Velocimetry.
LES	Large-Eddy Simulation.
LL	Liquid Length.
MPFI	Multi-point Fuel Injection.
PDA	Phase Doppler Anemometry.
PDPA	Phase Doppler Particle Analyzer.
PFI	Port Fuel Injection.
PID	Proportional-Integral-Derivative.
PIM	Planar Integrated Mass.
R1	Inlet radius.
R2	Outlet radius.
ROC	Radius of Curvature.
ROI	Rate of Injection.
ROM	Rate of Momentum.
RSD	Relative Standard Deviation.
SEM	Scanning Electron Microscope.
SMD	Sauter Mean Diameter.
SNL	Sandia National Laboratories.
SOE	Start of Energizing.
SOI	Start of Injection.
TIM	Tranverse Integrated Mass.
UHC	Unburned Hydrocarbon.
VCO	Valve Covered Orifice.

Greek

Δp	Pressure difference.
η	Dynamic viscosity.
μ	Mean value.
ν	Kinematic viscosity.
ρ	Density (general).
σ	Standard deviation.

Latin

$\ddot{y}$	Second derivative of fitting polynomial.
$\dot{M}$	Momentum flux.
$\dot{m}$	Mass flow rate.
$\dot{M}_{th}$	Theoretical momentum flux.

$\dot{m}_{th}$	Theoretical mass flow rate.
$\dot{y}$	First derivative of fitting polynomial.
μ_f	Absoption coefficient of the fuel.
A	Cross-sectional area.
a_f	Fuel (liquid) speed of sound.
A_t	Tube cross-sectional area.
A_{eff}	Effective flow area.
C_a	Area coefficient.
C_d	Discharge coefficient.
C_M	Momentum coefficient.
c_p	Specific heat capacity at constant pressure.
C_v	Velocity coefficient.
c_v	Specific heat capacity at constant volume.
CN	Cavitation number.
D	Diameter.
D_i	Orifice inlet diameter.
D_o	Orifice outlet diameter.
D_{eff}	Effective diameter.
F	Force.
g	Gravitational acceleration.
I	Transmission of monochromatic beam after test zone.
I_0	Transmission of monochromatic beam before test zone.
$k - factor$	Orifice conicity factor.
K_{crit}	Critical cavitation number.
L	Characteristic length.
m	Mass.
M_l	Mass in the line of sight of the x-ray beam.
n	Unit vector normal to an orifice cross-section.
n_e	Engine speed (rpm).
p	Pressure (general).
p_{inj}	Injection pressure.
p_b	Discharge pressure.
p_v	Vapor pressure.
Re	Reynolds number.
Re_{th}	Theoretical Reynolds number.
S	Spray penetration.
T	Temperature (general).
t_d	Delay among SOE and SOI.

T_f	Fuel (liquid) temperature.
T_i	Fuel temperature at the injector inlet.
t_{aSOE}	Time after Start of Energizing.
t_{aSOI}	Time after Start of Injection.
t_{inj}	Injection time.
U	Flow velocity.
u_{eff}	Effective flow velocity.
u_{th}	Theoretical flow velocity (according to the Bernoulli equation).
V	Voltage.
v	Specific volume.
V_i	Volume (general).
Y_f	Fuel (liquid) concentration.

Chapter 1

Introduction

1.1 General context

Since the invention of the Internal Combustion Engine and the first patented automobile in 1885, the auto market has been growing steadily to become one of the biggest industries today. Combustion engines transform the chemical energy in fuels to mechanical power by the controlled release of a combustion reaction. The success of the ICE as the primary source to power transportation systems is mainly owned to the high energy density of fossil fuels, high power-to-weight ratio, and cost effectiveness.

The widespread use of the engines and the emissions caused by the combustion reaction of fuels led to heavy regulation both in harmful pollutants like nitrate oxides (NOx) or soot particles, and in greenhouse gases like CO_2. Europe, the US and Asia are all increasing pollutant regulations in order to maintain the societal needs of clean air and mitigate the development of climate change. The ever-tightening emissions limits are currently forcing the automotive industry to keep improving the fuel economy and lowering emissions, which has become significantly more difficult and expensive over the last few years.

New technologies alternative to the ICE are gaining momentum given the higher cost and efforts required to meet the stringent regulations. Electrification is one of the most promising as it does not cause emissions directly and it facilitates the use of renewable energy sources. In the middle ground between completely electric cars and combustion engines are the hybrid concepts which try to bring the best parts of both worlds. However, most market projections show the internal combustion engine as the predominant power source for transportation for the near future. Also, even if the electric cars do not directly emit pollutants and greenhouse gases, their extensive use can be worse for climate change and atmospheric pollution depending on the technology used for power generation. Until the grid is significantly shifted to low greenhouse gases sources, the well-to-wheels analyses of electric vehicles might not be better than those using internal combustion engines.

In Europe, Diesel engines have been the predominant type of systems used in light-duty engines. The main reason has been the superior fuel economy of Diesel over gasoline engines, which resulted more attractive to customers given the higher cost of fuel in Europe compared to the US. In recent years, with the increasing regulation of NOx and soot particles, gasoline engines are gaining attention in Europe. The manufacturers are attracted to gasoline engines given their more simple design and aftertreatment systems, which can be reflected in the final price of cars. In addition, with the current trend of downsizing and turbocharging, gasoline engines are steadily improving fuel economy. Moreover, gasoline engines are the natural choice for hybrid cars, which represent one of the main strategies for auto manufacturers to meet the emissions regulations in the mid future.

Gasoline direct injection (GDi) was first implemented in several cars in the 1960s but it was ultimately dropped because of the limitations, cost and inflexibility of the systems. In 1996 Mitsubishi reintroduced them, taking advantage of the stratification mode to reduce the volumetric losses caused by the throttle-valve, necessary in gasoline engines. In the following years, significant research and development efforts were applied to provide newer generations of GDi systems. The main advantage of GDi systems over port fuel injection (PFI) is that the fuel is directly introduced in the cylinder, which eliminates the wall wetting of the intake port and valves that occurred before. The evaporation process that takes place in the cylinder also cools the air, which is beneficial for knocking resistance and therefore for the compression ratio of the engine. GDi engines also allow the use of other technologies like turbocharging and downsizing that are considerably harder to implement otherwise. They also permit the use of the stratified mode and advanced combustion strategies like Gasoline Compression Ignition that aim to reduce the inherent limitations that the gasoline engines have since the first Otto engine. As the enviromental regulations continue to restrict the fuel consumption in passenger cars, GDi engines are expected to continue the growth in market share and overtake PFI systems.

GDi engines still face many challenges in terms of fuel consumption and production of pollutants, and significant research efforts are being carried out by automakers and universities to realize their potential. Diesel fuel injectors have been the focus of research because of the major implications that the fuel delivery characteristics have on the combustion process and ultimately the fuel consumption and production of emissions. However, in PFI gasoline engines, the injectors were not as critical. It was only in recent years, with the development of GDi systems, that the fuel injection process became critical, promoting the research on gasoline injectors. In these engines, the fuel injector is of capital importance, as it is the responsible to provide the appropriate amount of fuel in such conditions to promote atomization, evaporation, and mixing at the appropriate location inside the cylinder. The injectors have to respond to the opening and closing commands very fast, and do so consistently while avoiding the formation of deposits and wall impingement.

The Engine Combustion Network (ECN) is a group formed by industry and academia institutions that agree and work on several combustion problems, oriented in obtaining high quality experimental datasets by using established and well-documented methodologies. The focus on the methodologies is to allow comparison between different research institutions and to provide trustworthy data sets for CFD model development. The ECN was primarly devoted to Diesel sprays until 2012, when the “Spray G” topics were created in order to study gasoline sprays for the new spray-guided injectors. The group established a multi-hole nozzle valve as the standard hardware for the Spray G topics and proposed several standard conditions to be studied. With the hardware and the conditions, several groups started working and identifying the particular aspect to study and development areas. Given the open access hardware and research results of the group, it was chosen as the framework for this research work and the base for all the experimental results presented in this doctoral thesis.

Even though only the Spray G hardware was used for the experimental work, the results and the conclusions presented are a representation of the general behavior expected in typical multi-hole spray-guided GDi injectors, and the methodologies developed for measuring and analysis can be applied to new generations of GDi injectors.

This thesis has been realized at the research institute CMT-Motores Térmicos, within the Universitat Politècnica de València (Spain). The department was founded more than 30 years ago and has worked on all thermodynamic aspects of Diesel engines, from air management to fuel injection and combustion, aftertreatment, noise, computational simulations, etc. During all those years, with more than 150 theses completed, more than 500 publications in journals and almost one thousand publications in congresses; the institute has acquired a prestigious position in the research of Diesel engines and it is recognized worldwide. Given the increasing interest in GDi engines, the department started an effort to expand their knowledge to GDi engines. The current thesis is a part of this effort and the first one inside the department focused on GDi injection systems.

1.2 Objectives

There are two main objectives in this thesis. Because of the novelty of this work in the department, the first objective is to reach the state of the art in gasoline direct injection systems, and transfer the accumulated knowledge and know-how from Diesel injection to contribute with new methodologies and techniques rarely applied before to GDi systems. This objective can be divided in several sub-objectives

- Compilation of technical literature on Gasoline direct injection from the early state to the modern studies to acquire a global vision of the topic.
- Reach the technical know-how to use and control the new hardware.
- Identify the key areas to study and the transferable methodologies from Diesel to GDi systems.
- Design of the equipment and study of new methodologies to perform the required experiments to obtain the desired data.

- Obtain high-quality datasets through the proposed experimentation and validate the results using similar datasets from other ECN institutions.
- Coordinate the ECN Spray G experimental efforts for access to data and knowledge of the state of the art of technical experimentation from contributing institutions.
- Develop the necessary post-processing and analysis tools through the adaptation of existing software tools and the design of new ones.

The second main objective is to contribute to the understanding of the relationship of the hydraulic behavior of the injector (internal flow) and the effects on the injected spray. This was achieved by the use of extensive experimental campaigns in multiple state-of-the-art equipment and by applying the new methodologies developed and the ones adapted from Diesel research. The objective can be sub-divided as follows:

- Exhaustive experimental testing using the methodologies and techniques developed.
- Determination and study of the internal geometry of the Spray G nozzles, needle movement and its influence on the rate of injection.
- Extensive study of the rate of injection and rate of momentum with all the governing variables to establish a baseline for understanding the internal flow of multi-hole GDi injectors.
- Study of the near-nozzle flow with focus on validation with other experimental data and study of the variability and the conection of the flow with the internal geometry.
- Evaluation of the external spray characteristics of the spray produced by the new hardware by adapting and applying the visualization methodologies available in the department.
- Analyze and understand the results to identify the controlling parameters and relationships that govern the internal and external flow of GDi systems.
- Disseminate the results and methodologies through publications in journals and presentations to the ECN group to contribute to the understanding of the internal and external flow of GDi nozzles.

As previously stated, the main objectives could be summarized as to first reach the state of the art and then contribute with the know-how obtained through the experience in the Diesel field. Therefore, most of the experimental work obtained was extracted using existing laboratory equipment. However, most of the equipment had to be modified in some manner to adapt to the different geometry and particularities of the GDi systems. From the high pressure pump to the rate of injection, rate of momentum, high pressure and temperature installations; everything required new parts and a redefinition of the methodologies, which has been included in the document. New post-processing methodologies have also been developed that account for the particular results that were obtained from the many experimental facilities. All the new designs and tools developed in the framework of this project were done taking into account the long-term vision of the research into GDi engines and many particular details can also be encountered throughout the document.

1.3 Outline

The document is separated into 6 chapters. After the general context and objectives, the second chapter introduces the work in more detail. First by briefly discussing the progression of the automotive industry and then introducing general concepts of Diesel and Gasoline engines. The chapter goes from the more general concepts to the particular aspects of GDi nozzles, with each section getting closer to the actual topic of the thesis. This chapter also provides most of the bibliography used for this work, discussing the most important work related to the present topic as a foundation for the document.

The third chapter establishes the methodology and presents the installations and equipment used to obtain the experimental data. The chapter starts presenting the Spray G injector and standard conditions to then describe the rate of injection and rate of momentum vessels and setups. The x-rays installations and methodologies used to determine the internal geometry, needle lift and near-nozzle flow are described after, detailing the particular post-processing techniques used for the experiments performed in the research visit to Argonne National Laboratory. The last part focuses on the external spray visualization techniques, explaining the optical arrangements and detailing the image processing algorithms used and the treatment done to the data to obtain the final results presented here. Each of the sections motivates the use of the particular technique and briefly discuss relevant work obtained using the same or similar methodologies.

The fourth chapter presents the results obtained for the geometry, internal flow and near-nozzle flow are presented and discussed. The sections are distributed from the inside of the nozzle (geometry) to the outside (near-nozzle flow) passing through the behavior of the internal components and flow (needle lift, rate of injection, and rate of momentum). The conditions tested are detailed and motivated in each of the sections. Even though the sections are clearly separated by the experimental tools, there are instances of results from several experimental facilities discussed in one section. This has been done in order to present the interactions of effects between some measurements and provide a more global picture by combining several results.

The fifth chapter focuses on the results of the external spray. It starts discussing the visualization experiments from several institutions with focus on uncertainties that might appear with the different methodologies. Later, and even though Computational Fluid Dynamics (CFD) simulations are out of the scope of this work, modeling efforts contributed by several institutions to the ECN group are discussed and compared to the experimental visualization results. This was done because of the importance of evaluating the possible biases that can affect the comparison between experimental and simulation data, and because it is important to properly define both types of approaches in order for the comparisons to make sense. After the discussion, the visualization experiments explained in chapter three are presented. Here, the extensive experimental conditions tested for liquid and vapor contour determination allowed to detect and study the spray collapse phenonema, particular to this type of GDi hardware. The spray collapse is described by studing the vapor penetration, liquid penetration, spray width, angle and contours under several density and temperature parametric variations; identifying the possible causes and the effects of such phenomena.

The sixth and last chapter provides a summary and overview of all the work presented, underlying the most important conclusions of the previous chapters. Lastly, several pathways are identified and proposed to continue advancing the current work and develop future projects.

Chapter 2

Background: Gasoline fuel injection.

2.1 Introduction

The internal combustion engine (ICE) is regarded as one of the most important inventions of the last century, and it has had a very significant impact on society. The ICE revolutionized mobility and transportation, and it was the foundation of many technological advancements. The favorable weight-to-power ratio, simple and robust operation and high efficiency opened many industrial and commercial routes and boosted the growth of society.

The ICE goes back very far in time. It was in 1876 when Nikolaus Otto patented the first practical four-stroke engine with a compression ratio of 2.5 and a brake efficiency of 14%. The concept of four stroke was first patented by A. de Rochas, however Otto is recognized as the first person to build and commercialize a working flame ignition engine [1]. In 1872, Otto founded Otto and Cie, and hired Cottlieb Daimler and Wilhelm Mayback, who later started the first automobile company, the Daimler Motor Company in 1890. Daimler was one of the fathers of the auto industry. They developed a four-stroke high-speed gasoline engine and built, in 1886, the first four-wheeled automobile. On the other hand, Rudolph Diesel developed the first engine using direct injection of liquid fuel into the cylinder. Diesel obtained his bachelor from Munich Polytechnic and worked closely with one of his professors Carl Von Linde. He started focusing on replicating the Carnot cycle, however he never realized it in practice and adopted a different strategy with constant pressure combustion. Diesel colaborated with MAN in the compression ignition engine, in their first iteration the fuel was delivered using air injection and was able to reach an efficiency of 27% at full load, which was significantly superior to SI engines at that time [2]. In 1885 Carl Benz patented the first automobile, his patent marks a milestone in the development of motorized transportation. In the years that followed, the industry grew with the arrival of companies such as Peugeot, Citroën, Renaul, Fiat, Ford, Rolls-Royce, Austin, etc. By this time, each automobile was an individual product of handcrafted labor. It was in 1913 with the introduction of the assembly line by Henry Ford which sparkled the automobile revolution. With the mass production of model T, the car changed from luxury item to being affordable by the working class.

After the first Diesel design by Rudolph and MAN, Sir Harry Ricardo patented a prechamber that increased the fuel-air mixing rate and allowing Diesel engines to be used at high speed (2000 rpm). The Diesel engines that used the prechamber were called indirect injection engines, and they were used extensively until the direct injection (DI) systems took over. Many technological advancements were introduced in the 19th century, such as supercharging, the production line, electronic injectors, fuel pumps, etc. One of the most significant milestones of these advancements is the patent of the first common rail by Denso in 1995.In 1997, Alfa Romeo released to the market the first Diesel passenger car that used the common rail system, which completely overtook the market and made indirect injection in Diesel engines obsolete.

From the Otto and Diesel engines and the early cars, the industry has been evolving and growing, being a driving force of technological development. Today, the emphasis is on passenger safety, clean operation, driveability, robustness, etc. Even as new concepts are introduced with the hybridization or electrification, the main aspects that made the internal combustion engine attractive one and a half centuries ago still holds true today. It has unmatched power-to-weight ratio and energy density. However, as new technology is implemented and environmental issues are addressed, the research on ICE needs to keep pushing forward to drive the development of cleaner and better engines.

2.2 Definition of SI and CI engines

There are two main internal combustion engine operation concepts that are based on different thermodynamics cycles. The two major cycles used in internal combustion engines are the Otto and Diesel cycles, named after the men who successfully used them first in their engine concepts.

Engines that use the Diesel cycle are compression ignition (CI) engines, where the fuel and air mixture is auto-ignited in the cylinder due to the high temperature and pressure conditions. The simplified four-stroke cycle can be summarized as follows:

1. Induction stroke. Cylinder moves downward and draws air through the intake valve.
2. Compression stroke. Valves close and cylinder moves back up, compressing the air and raising its temperature above the autoignition point of the fuel. Fuel is injected at the end of the compression stroke.
3. Expansion stroke. The fuel evaporates, mixes, and combustion starts. The combustion occurs in the surrounding area of the injected fuel and lasts until no more fuel is introduced into the chamber. The energy released by the combustion increases the pressure and temperature, and the piston goes down.
4. Exhaust stroke. The combustion products are scavenged out of the cylinder through the exhaust valve.

To control the start of the ignition, only air is introduced in the induction stroke. When the piston is close to top dead center, liquid fuel is injected into the chamber which starts evaporating and mixing with air. At this point, the ignition starts and a diffusion flame is formed surrounding the jet that lasts as long as fresh fuel is delivered inside the combustion chamber. In CI engines, the global mixture between fuel and air is heterogeneous, and the combustion only occurs in zones where there is the air-fuel mixture is sufficiently rich (i.e in the surrounding of the jet). The combustion is therefore not located at a well-defined place, rather it depends on the evolution of the fuel jet and the movement of the air in the combustion chamber. For this reason, the combustion of these engines highly depends on the injection process and by the physical phenomena developing such as atomization, evaporation, and mixing.

The Otto cycle is known as a constant volume combustion and is used in spark ignition (SI) engines. The simplified four-stroke Otto cycle can be described as follows:

1. Induction stroke. In this phase the cylinder moves downward, drawing a mixture of fuel and air into the cylinder through the open valves.
2. Compression stroke. The valves close and the cylinder moves upward, compressing the fuel and air mixture which causes a rise in temperature. A spark plug ignites the mixture when the cylinder is close to top dead center (TDP).
3. Power stroke. The cylinder moves downward again by the action of the gases expanding due to the release of energy by the combustion.
4. Exhaust stroke. In this last phase, the cylinder moves back up again with the valves open to scavenge the products of the combustion.

In these engines the combustion starts by an external source of energy, the spark from the spark plug. The precise instant is controlled in order to produce the best possible combustion depending on the condition of the engine in terms of load and speed. In this case, the mixture formed for the combustion is a homogeneous charge, normally at stoichiometric air-fuel ratio. However there are many more possible combustion modes that will be addressed later in the chapter. In the more common mode, the homogeneous charge at stoichometric conditions, the quantity of air must be what is needed for the fuel. For this reason, the airflow is controlled by a throttle valve, positioned upstream of the intake valves. When the requirement of fuel diminishes, the throttle closes and the quantity flowing inside the cylinder is reduced, causing a reduction in the cylinder pressure. Since the fuel is metered in proportion to the airflow, the power in an Otto cycle is controlled by the throttle valve. Contrary to the Diesel engines, the mixture in this case is done before the combustion starts, whether by using a carburator, fuel injection outside the cylinder (indirect injection) or fuel injection inside the cylinder (direct injection).

The main differences between the two concepts is therefore how the mixture is formed and the way the combustion start and progresses. Most of the differences in design of these two types of engines are a direct consequence of that [1].

2.3 Fuel delivery in Internal Combustion Engines

2.3.1 Diesel Engines

As it was stated before, for Diesel engines, the combustion occurs because of the temperature and pressure conditions inside the combustion chamber. Therefore, the fuel delivery system must be able to provide the fuel inside the chamber under high-pressure conditions. The injection system in Diesel engines is a critical part of their design, as the combustion is linked to the way the injection occurs [3–5]. Two concepts have been used to deliver the fuel into the chamber, the first was using a prechamber and then transfer the fuel to the combustion chamber in what is known as an indirect injection strategy. The most modern way is directly injecting inside the combustion chamber using a direct injection (DI) approach.

Indirect injection

In indirect injection Diesel engines, the combustion chamber is divided into two parts joined by a conduit (see Fig 2.1); the prechamber, and the combustion chamber, located between the piston head and the cylinder head. During the compression stroke, the air goes from the cylinder to the prechamber. The prechamber is designed in such a way to transfer a turbulent movement to the passing air, which will facilitate the mixing process between air and fuel. In this case, the fuel injection system was not as critical as in the later direct injection systems, as the mixing and atomization are primarily affected by the turbulence and swirl caused by the prechamber. The diameter of the nozzle of the injectors was generally big (1 mm) and the pressures were relatively small (20-30 MPa).

The main drawback of these systems was that they had poor efficiency compared to the direct injection systems. This was due to the high velocity and turbulence of the air and the bigger volume of the cylinder, which produced much higher heat losses. Moreover, these systems also had extra pumping losses because the air had to go through the conduit from the main chamber to the prechamber and back. The superior performance of the direct injection systems resulted in the over-

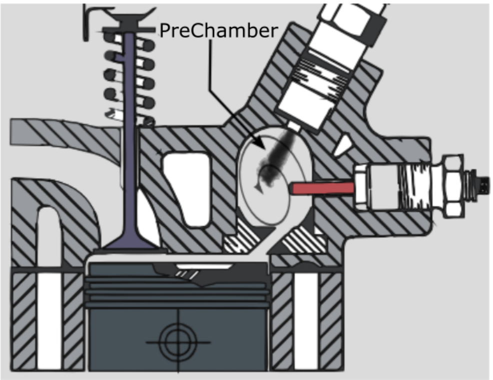

Figure 2.1: Drawing of a cut-section of an engine block and cylinder in a indirect injection Diesel engine. From [3]

taking of the market and the eventual obsolesce of the indirect injection in Diesel engines.

Direct injection

In direct injection Diesel engines, the fuel is directly introduced into the combustion chamber (see Fig 2.2). In this case, the turbulence and the swirl movement of the air are achieved by the shape of the carving in the piston head. In the previously described indirect injection systems, the injection system was not as important because it was the high velocity and turbulence of the air that was responsible for the mixing. Here, however, the velocity of the air is much lower, and the responsibility for creating fuel-air mixture falls on the injector.

In direct injection systems, the fuel atomization is critical which is related to the nozzle diameter. Therefore, small nozzle diameters are used, with several holes to provide the sufficient flow of fuel needed [6]. The injection pressure is also a critical parameter in these systems and has been ever-increasing since the first systems until today, where car manufacturers are introducing systems with more than 200 MPa of maximum pressure, and even systems of 400 MPa are being researched [7].

Due to the importance of the injectors and fuel pressure, there have been many developments over the years to get to the technology that is in use in modern engines. The first systems used a rotatory pump that

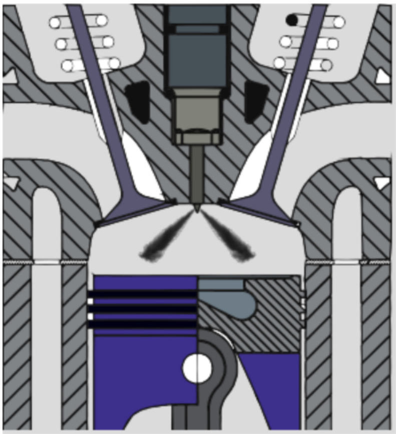

Figure 2.2: Drawing of a cut-section of an engine block and cylinder in a direct injection Diesel engine. From [3]

increased the fuel pressure and directly actuated on the injectors which had a major drawback of limiting control over the fuel pressure over time, which depended on the pump speed and therefore on the engine speed. The next systems were formed by an injection unit composed of an injector and a pump mounted together. In these systems, the duration of the injection was controlled by a solenoid actuator in each injector which could be controlled by Engine Control Unit (ECU). The electronic actuation and controllable fuel pressure provided many advantages over the previous systems. Eventually, the injector-pump was replaced by common rail systems, which were simpler, easier to control and cheaper. The common rail was patented by Denso in 1995 and basically consist on an accumulator connected to a high -pressure pump The accumulator (termed rail) controls the pressure by a solenoid valve that lets fuel return to the fuel deposit. The rail feeds each of the injectors, which in turn controls the injection by a solenoid or piezoelectric valve. In this system, only one high-pressure pump is required, with a low-pressure pump to feed it, which simplified previous designs and was widely adopted by manufacturers [8]. A drawback of this concept was that it pressurizes more fuel than what is needed by the injectors, this was resolved in updated designs by adding a valve upstream of the pump that could control the mass flow to the pump [9].

2.3.2 Gasoline Engines

Fuel and mixture formation requirements

When the power required from engines change, the quantity of fuel that has to be delivered must be adapted. In CI engines, the air-fuel mixture is regulated qualitatively, whereas, in an SI engine working in a normal (homogeneous) mode, the air-fuel mixture is regulated quantitatively, which means that the air and fuel are precisely metered to achieve the optimum air-fuel ratio for the load and speed conditions needed. In order to control the amount of air entering, a throttle valve is used to create pressure head losses that limit the flow of air. This throttle valve decreases the volumetric efficiency and is one of the main reasons to pursue direct injection systems [10], as will be discussed in the next section.

The excess-air factor, or Lambda (λ), indicates the extent to which the amount of air deviates from the exact quantity that the fuel needs for a complete combustion process, as expressed in (2.1).

$$\lambda = \frac{\text{Inducted air mass}}{\text{Stoichiometric air mass}} \tag{2.1}$$

A stoichiometric mixture has $\lambda = 1$, lean mixtures have $\lambda > 1$ and rich mixtures have $\lambda < 1$. The equivalence ratio Φ is also common to describe the air-fuel mixture. It is defined as the actual air-fuel ratio divided by the stoichiometric air-fuel ratio as presented in (2.2) and coincides with the inverse of the excess-air factor.

$$\Phi = \frac{m_a/m_f}{m_a/m_f|_{\text{st}}} = 1/\lambda \tag{2.2}$$

SI engines work with much more restrictive limits of the air-fuel ratio than Diesel engines because the inflammability limits are much narrower. The inflammability limits for normal operation are usually within $0.6 < \Phi < 1.6$, although they depend on several factors like the throttle-valve angle, cylinder pressure and temperature (which depend on engine load and speed), etc [1].

The maximum fuel efficiency for SI engines occurs for slightly poor air-fuel mixtures ($\Phi \leq 1$), whereas the maximum power occurs for slightly rich mixtures ($\Phi \approx 1.15$) [1]. It is clear then how important the fuel and air metering is in these engines, outside those margins, with leaner or richer mixtures, the efficiency and power would rapidly decrease. Moreover, if the three-way catalyst is being used, a stricter equivalence ratio has to be maintained at all engine conditions (very close to 1 for good performance). There are three basic systems to deliver the proper quantity of fuel for mixture formation, although only the injection systems are still in use in modern engines [8].

Carburetors

For gasoline engines, the development of systems to introduce the fuel into the combustion chamber, atomize it and mix it with air has been evolving since the early engines. The carburetor was patented by Karl Benz in 1885 as he developed internal combustion engines and their components. The carburetor is a device that blends air with fuel before the mixture is suctioned inside the cylinders. Early models consisted of the surface type, which exposed the fuel to the incoming airflow to produce the mixture. The carburetor works similarly to a Venturi tube, following Bernoulli's principle. With these systems, the throttle actuates on the carburetor mechanisms, controlling the flow of air that is pushed into the engine. The speed of this flow, and therefore its pressure, determines the amount of fuel drawn into the airstream. The basic carburetor designs were improved over the years and used extensively in passenger cars until gasoline injectors replaced them. They were first introduced in the aircraft industry as it was required to use pressurized fuel. Bosch started the mass production of gasoline injection systems in 1937 for the aeronautical industry, and in 1952 the first vehicles equipped with gasoline direct injection were presented in the market. The carburetor was developed in parallel to the fuel injection systems. In the late 70s, the complexity was very high and the development stagnated. In 1967, Bosch presented the first robust electronic injector termed the D-Jetronic The introduction of electronic injectors in combination with the 3-way catalyst and more severe emissions regulations, would result in the end of the carburetor in the 90s.

Fuel injection systems replaced the carburetor for their superiority in fuel metering and atomization, which has been increasing in importance as environmental regulations became more severe. Gasoline fuel injection systems can also be classified as indirect injection or direct injection (DI) depending on whether the fuel was mixed with air inside or outside the combustion chamber.

Indirect injection

Indirect injection has been used extensively in the past and continues to be used in the present in many gasoline engines. In this case, the fuel is delivered upstream the intake valve by one or several fuel injectors.

The first electronic fuel injector (EFI) was patented by Bendix Corporation in 1957 and called Electrojector [11]. The first EFI systems were much more expensive than the carburetor and had several problems so there were just a few production cars equipped with them [12]. Bosch acquired the patent from Bendix [1] and in 1967 introduced the first electronic injection system controlled by intake pressure, the D-Jetronic, which was superseded by the L-Jetronic and K-Jetronic, which featured mechanical hydraulic control. The K-Jetronic was the first automotive system to incorporate a Lambda closed-loop sensor. In 1979, the L-Jetronic was combined with the new Motronic (engine management) technology and resulted in a program-map control for the ignition. Three years later, the KE-Jetronic was introduced, which included an electronic closed-loop control and a Lambda oxygen sensor. All of these were multi-point injection systems, as they delivered fuel onto the intake valve of each cylinder. However, widespread use of fuel-injection systems was only possible with a lower-cost design. In 1987, the Mono-Jetronic, with only one single electromagnetic fuel injection (single point injection or throttle body injector) enabled fuel-injection technology to be used in mid-size and small cars. The carburetor was then made superfluous because of the superiority of gasoline injection regarding fuel consumption, power output, emissions, etc. The introduction of the three-way catalyst permitted a major decrease in emissions. However, the catalyst needed proper fuel metering and closed-loop control with a Lambda sensor to function properly, which was only possible with fuel injection. Today, only the Motronic engine-management technology coupled with multi-point injection is still used in as indirect injection systems in gasoline engines, as it is the only ale to comply with the demanding emissions and consumption limits [8].

The multi-point fuel systems (MPFI) also called port-fuel injection (PFI) systems deliver the fuel upstream of the intake valve(s) in each of the cylinders as can be seen in Fig 2.3. These systems provide lower exhaust emissions, increased volumetric efficiency, output and torque, lower fuel consumption, better engine response and driveability and less noise [2, 13] than the carburetors.

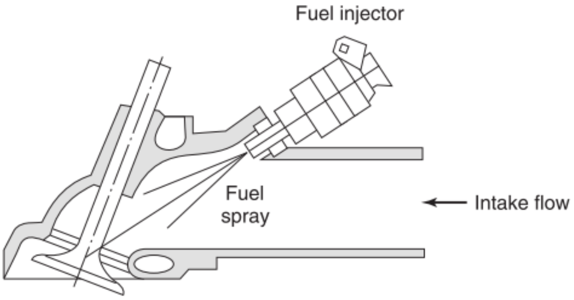

Figure 2.3: Port fuel injection schematic. Adapted from [2]

In PFI, the fuel is sprayed into the port and onto the inlet valve, which cools the valve and starts the vaporization of the fuel. Depending on the load and speed conditions, the amount of fuel required can be enough so that the fuel injector continues to spray even when the intake valve is closed, so fuel can not enter the cylinder until the next intake stroke. Heat from the manifold facilitates fuel vaporization, and then the air fuel mixture is entrained with high velocity into the combustion chamber, where a high level of homogeneity is achieved when the spark plug is triggered [14]. One of the main advantages of PFI over the throttle body injection (TBI) design is that the latter produces much more wall wetting on account of the fact that the air-fuel mixture travels a longer distance before entering the cylinder. MPFI allows decreasing wall wetting problems, resulting in a higher volumetric efficiency and lower emissions levels [14]. Moreover, the inlet manifold in these systems can be designed to have optimum air flow, rather than optimum mixture preparation. On the other hand, MPFI requires detailed actuation and control to overcome the challenges with the short opening time in idle conditions. In addition, the short travel distance can produce a rich air-fuel mixture which can decrease efficiency and torque output [15].

PF injectors work with a fuel pressure of 2-5 bar [2]. A pintle-nozzle fuel injector is normally used, where the upward movement of the pintle opens the valve. At the required timing, the ECU sends a command signal and the pintle is rapidly lifted by a solenoid. The quantity of fuel depends linearly on the duration of the injection since the opening and closing transients are much shorter than the typical duration of the injections. Port fuel injectors must satisfy numerous performance requirements: accurate fuel metering, rapid opening and closing, good atomization, minimal leakage, small pulse-to-pulse variation, wide flow range, resistance to deposits, etc; which makes them complex hardware still being researched and developed [8, 14, 16–18].

2.4 Gasoline direct injection

2.4.1 Introduction

High specific power, good driveability, and low cost made the gasoline engine the dominant system of vehicles. However, the pressure to decrease emissions and fuel consumption requires the development of more efficient gasoline engines. The reduction of average CO_2 emissions in Europe has been achieved mainly by the widespread use of direct injection Diesel engines, which represent more than half the cars sold in Europe. However, the refinery process of oil yields a minimum quantity of both Diesel and Gasoline fuel, which mandates the use of gasoline engines. Moreover, Diesel engines require more complex injection systems and after-treatment devices, which typically make them more expensive. It is therefore important to keep developing and improving the gasoline engines in order to make them more fuel efficient and competitive. In this regard, direct injection gasoline engines have the potential to achieve higher specific power output and better fuel economy on account of their ability to minimize knocking at full-load operation, reduce pumping losses at part load conditions [19], and reduce NO_x and HC emissions. The capacity to minimize knock comes from the cooling effect of the evaporation of the fuel inside the cylinder, which also helps to reduce NO_x generation. DI can also reduce HC emissions generated during cold start by using a split injection strategy and reducing wall- wetting at the intake valve. The reduction in pumping losses comes from the potential use of stratified mode, where the equivalence ratio in the combustion chamber is rich around the spark plug but lean globally. The stratified mode has been thoroughly researched due to the great fuel savings potential, but its use is not widespread because of several important drawbacks. In addition, the GDi technology facilitates other practices and technologies that have great potential for decreasing emissions and improving fuel economy like engine downsizing, increased compression ratio, turbocharging, etc. Also, the advancements in GDi injection systems have permitted the research and development new combustion strategies like GDCI (Gasoline Direct Compression Ignition), HCCI (Homogeneous-Charge Compression Ignition), RCCI (Reactivity Controlled Compression Ignition), Homogeneous-Lean SI, water injection for knocking control, advanced start-stop, etc [13, 19–23].

The first GDi systems started to being developed in the 1930s for aircraft engines. The first automobile with direct injection of gasoline was the Goliath GP700E and the Butbrod Superior 600, introduced in 1952 by Goliath and Gutbrod [2]. Afterward, the well-known Mercedes 300SL was released, the first four-stroke GDi engine in production. At this time, the objective of direct injection was mainly to increase the SI engines performance. During the 1970s, significant development was not achieved in gasoline engines using direct injection systems, and the few projects pursued were canceled on account of the high costs and inflexibility of the systems [19]. In the 1990s, with the introduction of the electronic injectors, better control systems (ECU), and the implementation of the common rail in Diesel engines, the fundamental limitations that prevented the development of GDi were solved. In 1996 Mitsubishi Motors introduced the Galant, the first modern gasoline direct injection engine, featuring a 1.8 L, 4-cylinder block which was presented three years later in Europe as the Mitsubishi Carisma [24]. At the same time, Toyota also introduced DI gasoline engines in Europe and Japan [25]. After, most other European and Japanese manufacturers started introducing GDi engines in gasoline car models, while also maintaining engines with the PFI systems.

The typical constructive elements of a GDi engine can be seen in Fig 2.4. In this case, the injector mounted inside the cylinder, delivers the fuel to the metered air that comes from the electronic throttle-valve and the intake valve. The lambda sensor is used in a closed-loop control with the injector to finely dose the quantity of fuel depending on the oxygen content in the combustion products.

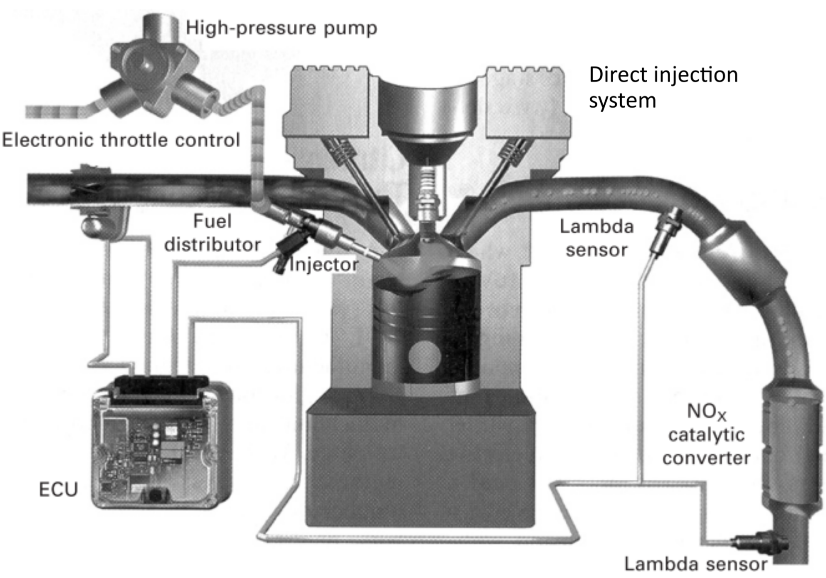

Figure 2.4: Schematic representation of a common GDi engine. Adapted from [19].

The fuel efficiency in real-world driving for these early GDi systems was less than claimed [19]. Because the three-way catalyst can only work with stoichiometric air-fuel mixtures, the GDi systems required the use of a less efficient lean-burn NO_x after-treatment, similar to the ones used in Diesel engines for the stratified lean combustion mode. Also, SI engines using stratified combustion suffered from HC emissions due to overmixing and flame quenching, and soot generation caused by liquid fuel films in the piston surface [26]. As a result, GDi engines after 2001 were primarily designed to operate in the homogeneous charge mode, with the focus of the direct injection on increasing performance [27].

At full load, a GDi system might not have enough time to deliver all the required fuel. To solve this, some manufacturers used a PFI system combined with a GDi system. The combination of direct injection and port fuel injection was used to increase maximum power, and to provide smooth operation with the stoichiometric mixture at part load conditions.

In the early 2000s, the focus for GDi engines was to use in high-end engines and cars for their improved performance, a new trend started with the combination of downsized and turbocharged engines like in the TSI 1.4 that continues today [19, 22]. Downsizing and turbocharging are strategies that can significantly improve the efficiency of gasoline engines as the load can also be controlled by the boost degree instead of using the throttle valve.

Even with the difficulties encountered, there is still much effort and research done on the stratified combustion in GDi engines on account of the high potential for improving fuel economy and emissions [14, 19, 20, 26, 28–31].

2.4.2 Stratified-charge mode

Conventional gasoline engines (working with homogeneous charge) are designed to operate for stoichiometric operation, and the engine load is controlled by the intake throttle valve. These systems present many disadvantages concerning efficiency, in part-load operation. A reduction in throttling loss during the induction cycle can provide considerable potential for reduction in fuel consumption. In the stratified-charge mode, the main idea is to try to overcome this limitation inherent to gasoline engines by limiting or eliminating the use of the throttle valve to control the engine load. At the beginning of the chapter, it was stated that the equivalence ratio in gasoline engines has to be within a narrow window, considering the inflammability limits of gasoline. By using fuel stratification, a rich (ignitable) air-fuel mixture can be supplied surrounding the spark plug, while maintaining a globally lean air-fuel mixture in the combustion chamber. This strategy reduces part-load pumping losses compared to throttled operation, decreases heat losses and NOx generation on account of the lower temperatures reached in the combustion chamber, and increases the thermodynamic efficiency by increasing the ratio of specific heats $\gamma = C_P/C_V$ [26]. These effects can be seen in the relationship between engine efficiency (η) with γ and the compression ratio r_c defined through (2.3).

$$\eta = 1 - \frac{1}{r_c^{\gamma-1}} \tag{2.3}$$

In the homogeneous mode, the fuel is injected during the intake stroke, at around 270-300 crank-angle degrees (CAD) before top dead center (BTDC), while in the stratified-charge mode, the fuel is delivered in the compression stroke, around 60-70 CAD BTDC [14]. A schematic representation of the stratified (wall-guided) versus the homogeneous mode is shown in Fig 2.5. It can be easily appreciated that in the homogeneous mode, the injection is done much earlier and by the time the spark plug ignites, the fuel and air will be well mixed over the combustion chamber. In the stratified mode, the injection is done right before the spark plug ignites, so there might not be enough time for the fuel to mix homogeneously with air. As previously mentioned, this strategy is preferred in part-load regimes, where the valve throttle normally is only halfway open, hence producing severe volumetric losses. At full load, the homogeneous mode is preferred, as in this case, the throttle-valve is wide open [19]

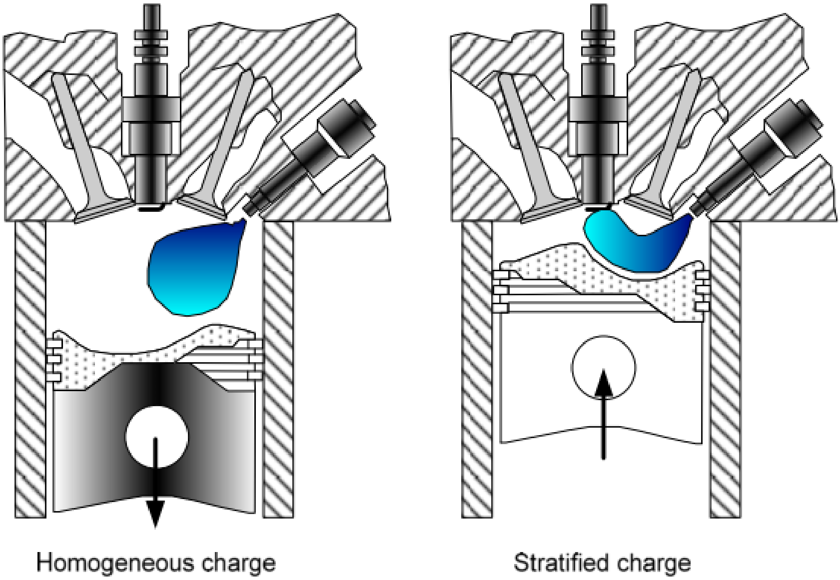

Figure 2.5: Schematic representation of the homogeneous mode (left) and stratified mode (right). From [13].

Achieving the proper mixture around the correct zone around the spark plug in the stratified mode is not an easy task. There are many variables affecting the mixing rate and the convection of the fuel inside the chamber. Three different strategies have been used to produce the stratified cloud in the proper location. The first engines used a wall-guided direct injection system, which took advantage of the shape of the piston to create the stratification [32]. Similar to these, the air-guided direct injection used a combination of the air movement and the shape of the piston head to locate the fuel cloud. The most modern type are the spray-guided direct injection systems (SGDI), where the air-fuel mixture preparation is done mostly by the injector. An example of these systems is presented in Fig 2.6.

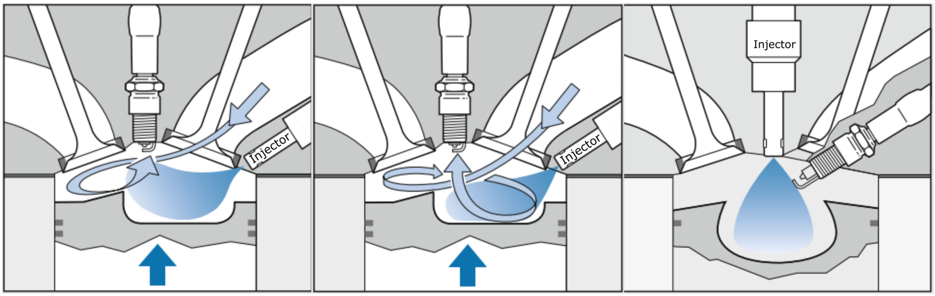

Figure 2.6: Representation of the three strategies to achieve stratification: wall guided (left), air guided (center) and spray guided (right). Adapted from [8].

In wall/air-guided systems the injector is usually mounted between the intake valves. In this case, the mixture is transported by interacting with the piston head (wall guided) or by the airflow coming in from the valves (air-guided). Real stratified-charge combustion is usually a combination of both. At low speed, the fuel barely impacts the cylinder because of the low injected quantities, at higher loads, a certain amount of fuel impacts the piston directly, even in the air-guided process [8]. The early stratified-charge combustion system implanted by VW in the 2000s (FSI) was a combination of the air-guided and wall-guided systems. The piston head had two bowls, one at the side of the injector (between the intake valves) and another at the side of the exhaust. The bowl closer to the nozzle was used to directly project the fuel towards the spark plug, whereas the other bowl was used to create an air motion that would carry the remaining fuel to the spark plug [33]. The wall-guided and air-guided systems are considered in the first generation of stratified GDi engines. These systems rely heavily on the presence of large-scale in-cylinder motion and an unfavorable shape of the piston geometry, both factors contributing to a decrease in performance and thermodynamic efficiency due to heat losses. In addition, they inherently cause wetting in the piston, which results in excessive HC and soot emissions. Lastly, the range of engine speed and or stratified mode was very limited in these early systems.

The second generation of direct injection engines was brought to market in 2006 by BMW and Mercedes, with an extended operational range for the stratified mode [14]. This second generation used the Spray-Guided direct injection systems. In this case, the injector is closely located to the spark-plug and is mainly responsible for preparing and transporting the stratified cloud to the spark plug. The injector is, therefore, a decisive factor here, it must produce a spray pattern that is repeatable for all the possible pressure and flow conditions inside the chamber. The spray-guided systems are considered an upgrade of the air and wall-guided systems and are still researched today for stratified mode and new combustion concepts [28, 32, 34]. As a result of the unique properties required for the SGDI systems, there are particular problems derived. Cocking at the nozzle tip of the injector may occur mainly due to low combustion temperatures, which can be addressed by careful design of the hole and counter-bore [30], although the cocking might also affect the spark-plug. Tolerances of the spray pattern must be small in order to have a robust operation at all engine conditions. One of the important points to consider in SG stratified mode is that the fuel is injected shortly before ignition at TDC. Hence, very little time is available to prepare the mixture, which can result in increased HC emissions (rich zones), misfire (lean zones) and unstable combustion. Stratification can lead to an increase in particulate matter (PM), which started to be regulated in Europe with the introduction of the Euro VI. Homogeneous stratified (HoS) combustion uses a split injection to first prepare a lean, homogeneous charge and then provide a richer cloud around the spark plug with the second injection, this new concept and others are currently being researched, showing potential to solve some shortcomings of the stratified mode [32]. However, even today, after significant research efforts, and technological advancements, the robust operation of a GDi engine working in a stratified mode remains a challenge; and the full potential of GDi engines is still in the future [14, 20, 21, 26, 28, 32].

2.4.3 Potential technologies of GDi

Outside the stratified-charge mode, the GDi systems are also attractive because they facilitate the use of other technologies and combustion strategies. Engine downsizing was developed as an alternative means to dethrottle GDi engines and still maintain the use of the cost-effect and robust three-way catalyst for exhaust emissions control. In DI gasoline engines, downsizing was made possible by synergies between DI and turbocharging. One of the main advantages of DI engines with turbocharging is the increased knock resistance, which, in combination with variable camshaft phasing devices, allows to increase the manifold pressure and operate the engines at significantly higher BMEP levels [19]. The compressor map shifting is made possible by increased scavenging, which is enabled by delaying fuel introduction until after the exhaust valve is closed (only possible in DI systems). This practice leads to benefits in driveability through a reduction in turbo lag which is one of the main issues why the customer give more value to big displacement engines. Moreover, variable valve actuation can be used to partially dethrottle a GDi engine and significantly increase its efficiency [35]

Knocking is one of main concerning factors of gasoline engines as it severely limits the compression ratio (which increases thermal efficiency) and the degree of turbocharging or supercharging. Methods like applying cooled EGR at full-load conditions and excess air show good potential for knock suppression [36]. However, just the use of DI in itself is very beneficial in terms of controlling knocking. Even with the low heat of vaporization of gasoline, the effect is marked. The use of alcohols can provide even more benefits in this regards due to their increased heat of vaporization.

Other combustion strategies like gasoline compression ignition (GCI) or gasoline direct compression ignition (GDCI), which utilizes a GDi injection system and mixture stratification through multiple-late injections to decrease fuel consumption, NO_x and PM emissions shows great potential to address several shortcomings of the stratified-charge combustion discussed before [37, 38]. GCI could spark a new generation of engines that can take advantage of SI and CI concepts. Here, lighter fuels with low cetane number are auto-ignited. The low cetane number leads to longer ignition delays, resulting in more time to improve mixture quality, resulting in less soot and unburnt HC [14].

All the technologies and strategies facilitated by the direct injection of gasoline rely largely on the characteristics of the injector and the produced spray. As the requirements on the injection systems increase, so does the necessary understanding of their behavior. Even PFI injectors are complex systems that satisfy multiple necessities. In GDi, where the time to deliver, mix and atomize the fuel is much shorter, the requirements increase. Not only the amount of fuel provided and the degree of atomization are important parameters, the shape of the spray, direction of the plumes, cone angle, the penetration, etc; become critical in GDi engines. The following section discusses the types of GDi injectors, with the focus on the spray-guided multi-hole injectors as the main topic of this work.

2.5 Fuel injectors in GDi engines

2.5.1 Types of modern GDi injectors

In general, the injector features that were favorable for diesel engines can also be expected to provide improvements for GDi engines [39]. In DI, the fuel injection system becomes critical, as it must be able to provide the fuel under high pressure for late-injection strategies and lower pressure under early-injection strategies robustly and accurately. The homogeneous mode requires well-atomized fuel distributed over the chamber equally, whereas modes like the stratified charge, require the cloud of fuel surrounding the spark plug. The injectors used for DI have considerably less time to provide the fuel for mixing with air, so high-pressure valves are used. The usual range of operation of modern GDi injectors 30 to 200 bar [8, 40, 41] but higher pressures are being studied and introduced. JOHANSSON et al. [31] used a 350 bar fuel injector to decrease particulate emissions and found that the biggest effect of increasing the injection pressure was in the soot formation. HUSTED et al. [42] analyzed the effects of increased injection pressure on fuel consumption. They used a 400 bar multi-hole fuel injector and concluded that the increased pressure would provide a slight fuel consumption benefit, canceling out the increased energy requirements of the fuel pump. Delphi, Bosch, Magneti Marelli, and other injector manufacturers are developing 400 and 500 bar maximum injection pressures for GDi concepts and advertising the benefits of fewer emissions and better fuel economy of the increased injection pressure [30, 39, 43].

The first generation of modern GDi engines were designed with a wall-guided stratification system. The injectors at this point were mostly of swirl-type design which is provided with an inwardly opening pintle and a single-exit orifice, working at an injection pressure level between 50 and 100 bar. This type of injector applied a strong rotational momentum to the fuel in the nozzle which was achieved by a series of tangential holes or slots that fed into a swirl chamber. The liquid would then exit from the orifice forming an hollow-cone spray [10]. One of the main disadvantages of the high-pressure-swirl injector was that the cone angle varied significantly with the ambient conditions of the engine, which made the design and calibration quite difficult. Moreover, these types of systems used a swirl chamber to provide turbulence to the air which led to reduced volumetric efficiency, which motivated the design of the slit-type (or fan-type injector [44]. The second generation of GDi engines introduced the use of the spray-guided systems, which were necessary to improve full-load performance and extend the range of stratified mode. For these systems, the solenoid-actuated multi-hole nozzle injector and piezo-electrically actuated injectors were developed and utilized [19].

Solenoid-actuated GDi injectors use the electromagnetic force generated in a copper coil to directly lift the needle (against the injection pressure), piezoelectric injectors use the dimensional change in certain ceramics after being excited by a current. The dimensional change of a piezoelectric material is very low, so in order to provide a sufficient displacement for opening the needle, the injectors are equipped with a stack of crystals, frequently referred to as piezo stack [45]. A schematic representation of a piezo injector is shown in Fig 2.7. GDi piezo injectors open outwardly (the needle is pushed away from the injector) leaving a radial slit that forms a hollow-cone thin spray. The outward opening of these injectors is beneficial because they are not affected by cocking, which can create deposits in the nozzle tip that would otherwise interfere with the flow (as it is the case for multi-hole injectors). One of the main advantages of piezoelectric actuated injectors is their rapid response, which allows them to provide very small quantities of fuel when needed and makes them more suitable for multiple injection strategies. DAHLANDER et al. [46] measured the rate of injection of solenoid-actuated and a piezoelectric injector for GDi application and demonstrated that the piezoelectric delivered mass more robustly than the multi-hole injector for short energizing times. They also found that the minimum quantity that could be delivered by the multi-hole injector was around 1.8 mg (at 50 bar of injection pressure), while the piezo injector could accurately deliver fuel doses of less than 1 mg. However, these two disadvantages can be addressed in new solenoid-driven GDi injectors. Low doses can be achieved by accurately using the solenoid injectors in the ballistic regime, which requires a combination of precise metering of the injected fuel and an advanced electronic management system that can adjust the driving signals of the injectors in real time [26, 30].

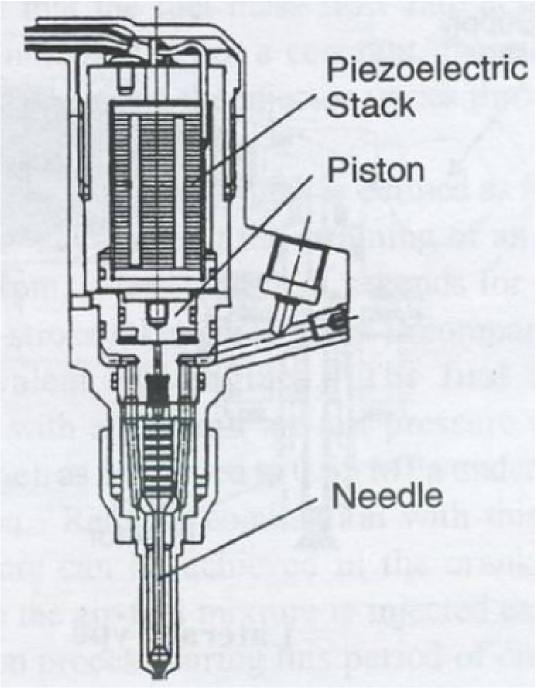

Figure 2.7: Schematic of a GDi piezo injector from [45]

In GDi engines, the spray penetration velocity is a critical parameter that determines the mixing process. High penetration velocities can improve mixing but they also have the potential to create impingement on the piston head or the walls, which can increase unburnt HC and soot formation that lead to particulate emissions. The use of piezo injectors can also serve to decrease penetration and improve fuel mixing as was claimed by Mercedes in their BlueDirect technology [47]. A comparison of the BlueDirect system featuring a piezoelectric-actuated injector and a solenoid multi-hole injector is shown in Fig 2.8.

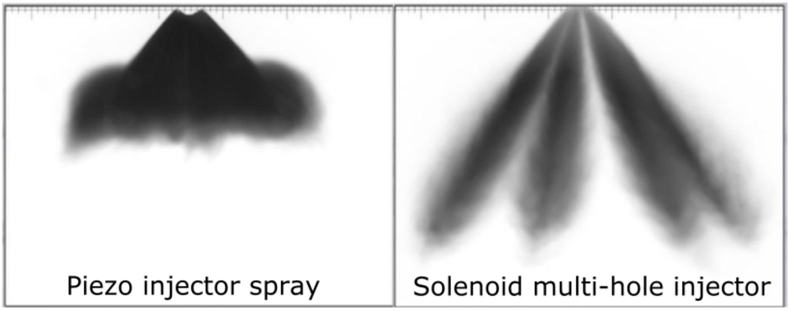

Figure 2.8: Comparison of the spray formed by a piezoelectric GDi injector using and a solenoid multi-hole injector. Adapted from [47].

The combination of the deposit resistance, the fast response, and the preferable penetration make these piezoelectric injectors very attractive to GDi operation both in homogeneous and stratified combustion [32, 47, 48]. Their apparent benefits might not always reproduce in real engine testing. Smith et al. [49] compared the performance of SGSC combustion between an outward-opening piezo and a multi-hole solenoid injector and found that over a Federal Test Procedure (FTP) cycle, the multi-hole system had 15% lower HC and 18% lower CO_2 emissions, which resulted in lower fuel consumption of the engine using the multi-hole injector. Solenoid-actuated injectors have been typically preferred over the piezoelectric actuation because of their lower cost [26]. The other main advantage of the multi-hole injectors is that they allow almost every configuration of holes possible, so the plumes can be optimally located where they are less probable of impacting the walls or the valves depending on the actual geometry of the cylinder, which makes them very versatile [19, 50, 51]. Because of this, GDi engines more commonly use multi-hole injectors, and the amount of research that features these kinds of nozzles is also greater [26].

Due to the more popularity and research efforts for the solenoid-actuated multi-hole GDi injectors, the ECN (introduced in Chapter 1) defined this hardware as the standard for the “Spray G” topic [52].

2.5.2 Multi-hole solenoid-actuated GDi injectors

GDi injectors are an evolution of the older PFI injectors, redesigned to withstand significantly greater pressures [51], with the development still pushing forward today, focused in precise metering, improved atomization, resistance to deposit formation and faster response [30].

The main parts of modern multi-hole injectors can be seen in Fig 2.9. The design in Fig 2.9 is made by Bosch, although it is very similar to the design that other manufacturers like Delphi, Hitachi, Magneti Morelli, and others, use for their solutions. The fuel is fed through the inlet, which is directly connected to the valve seat. The ball at the end of the needle covers the outlet of the orifice unless it is lifted by the electromagnetic force of the coil, which draws energy from the electrical connector. A spring is used to close the valve shortly after the actuation.

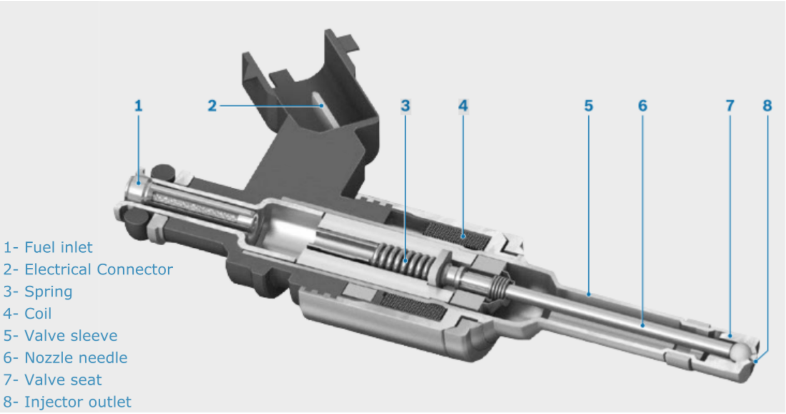

Figure 2.9: Parts of a solenoid-actuated multi-hole GDi injector. Adapted from [8].

The normal range of operation of modern GDi injectors is 30 to 200 bar [8, 40, 41], but higher injection pressures like 350 bar [31], 400 bar [30, 53] are already in the market, and injectors able to operate at 500 bar are being researched [43].

The injector used in the current work is a valve covered orifice (VCO) type, with eight straight holes designed with a stepped geometry (counterbore). A close-up picture of the Spray G multi-hole nozzle (a common multi-hole GDi nozzle), can be seen in Fig 2.10. The orifices are located in a bump with a hemispherical shape that provides the proper angle for the holes. In the picture, the orifices look much closer than in a Diesel injector, mainly due to the big diameter of the counterbores and the small angle between the injector centerline and the axes of the holes (what is termed later in the document as drill angle). In the case studied here, the injector axis is at the center of the holes, but this is not always the case. In fact, is common to have a skew angle between the injector axis and the axis formed by the circumference joining the holes.

Figure 2.10: Close-up picture of the nozzle of the ECN Spray G injector.

As stated before, the possible arrangements of holes in the nozzle are one of the main advantages of the multi-hole injectors as they can be configured to avoid impingement of the valves and optimize mixing. Multi-hole SG injectors can be centrally mounted on the combustion chamber or mounted at one side. If they are installed at the side (usually at the intake port side), the skew angle can also be adjusted to avoid impinging the walls [54]. Rivera et al. [50] studied a variety of possible hole arrangements and spray patterns to optimize mixing while minimizing wall impingement using CFD simulations, as did Yi et al. [51]. Configurations with a small number of holes (single-hole or three-hole) are mostly used for research purposes, as the geometry can simplify certain measurements [55, 56], or make easier and computationally more simple to study isolated effects of nozzle geometry [53]. For real applications, the injectors are usually designed with more holes, which makes the fuel distribution across the chamber easier and is usually the only way to provide enough flow at all conditions. Moon et al. [57] studied the spray formation of several multi-hole GDi injectors with configurations of two and ten holes. One of the conclusions was that the axial and radial flow velocity decrease as the number of holes increase, which produced a decrease in the flow breakup and atomization, with a lower spray deceleration. The needle lift of these injectors is usually very low, of a few tens of micrometers, which makes the opening left by the needle several times smaller than the orifices of the nozzle. The small lift produces a throttling of the fuel upstream of the sac that influences the flow during the complete injection process by introducing turbulence that causes perturbations on the jet flow. The turbulence created by the low lift can be favorable to atomize the fuel, but it can also create a decreased pressure inside the sac for nozzle arrangements with many holes, which causes a decreased flow velocity and break-up. Therefore, there is a trade-off between the number of holes and the needle lift that requires significant effort to optimize because of the complexity of the in-nozzle flow in these injectors.

Fig 2.11 shows a slice of an x-ray tomographic reconstruction (shown in Chapter 4 through two opposing holes. The geometry of the sac, two holes and their counterbores can be appreciated in the image, as well as a part of the needle ball resting in the needle seat. It can be appreciated that the length of the holes is very similar to their diameter (in this case L/D = 1), this is also a common feature in GDi injectors. Reducing the L/D ratio is attractive because it increases velocity, spray angle and reduces the droplet size and break-up length [58]. Befrui et al. [59] performed VOF-LES (Volume of Fluid) simulations in a single-hole geometry and revealed that the characteristics of the flow in GDi nozzles holes are markedly different than in Diesel holes, owing to the short L/D ratio of 1 (versus 6 or 7 in Diesel nozzle). The simulations showed the full detachment of the flow, caused by flow separation at the nozzle entrance and accompanied by the hydraulic flip in nozzles with L/D ratio between 0.8 and 1.5. The hydraulic flip is a phenomenon predominantly associated with cavitation. Here, the cavitation bubbles extend beyond the nozzle domain and merge with the ambient. As a consequence, the ambient air (normally at a higher pressure than the vapor saturation pressure) is drawn upstream the domain, between the nozzle wall and the liquid core. This has significant influences on the flow through inhibition of liquid-wall interaction and enhancement of liquid-air interface instabilities [60]. Shost [61] evaluated the effect of the L/D ratio by comparing the flow of a base geometry with L/D = 1.1 with a geometry featuring a longer holes with L/D = 3 in LES simulations, resulting in a significant increase of the discharge coefficient from about 0.6 for the short nozzle to 0.8 of the long one. Shost et al. [62] also simulated the flow of two nozzles with L/D ratios of 1.1 and 0.5 and found that the plume cone angles were bigger for the shorter holes. Moon et al. [57] studied the effect of the length of the orifices in several multi-hole GDi nozzles and found that shorter holes increased the axial and radial flow velocity and void fraction inside the hole at orifices exit. The higher axial and radial velocities of the flow promoted a faster breakup and stronger turbulence, and an increase in spray deceleration in the spray axis. These results are also consistent with LES simulations studying the effect of nozzle length [59].

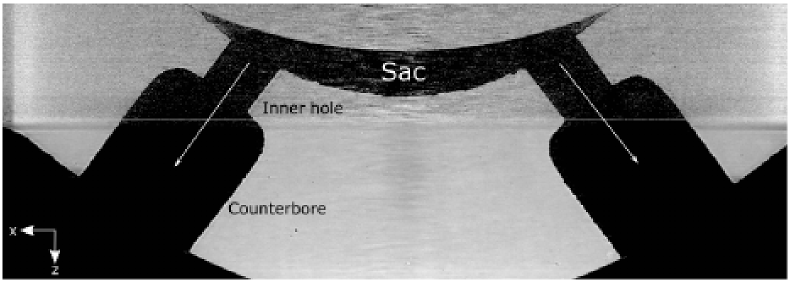

Figure 2.11: Slice of an x-ray tomographic reconstruction featuring two orifices, their counterbores, as well as the sac and needle ball of a multi-hole GDi injector (ECN Spray G).

Multi-hole GDi injectors are usually designed with what is known as a counterbore, which is an enlargement in diameter of the orifices of the nozzle. The counterbore can be appreciated in Fig 2.10 above, looking closely at the orifices. The external diameter, visible in the picture is the counterbore diameter, a smaller orifice can be seen inside these larger holes if looking carefully, these are the holes connected to the sac inside the injector. It can be appreciated more clearly in the x-ray slice in Fig 2.11. The counterbore is a typical feature in multi-hole GDi injectors. Given that short lengths are used in these nozzles, the counterbore is necessary to provide sufficient mechanical strength to withstand the working pressures. Apart from the added thickness for structural integrity, the counterbore is also important to provide isolation for the inner holes exit from the high temperatures of the combustion chamber. One critical design requirement is robustness to buildup of deposits at the nozzle exit since they directly impact spray morphology and hence combustion performance [61]. SHOST [61] studied the influence on the counterbore by performing VOF-LES simulations of a base geometry with a single stepped-hole nozzle and a geometry with a hole of the same length and diameter, but no counterbore. The internal flow of the nozzle without counterbore was very similar to the flow in the base geometry with the plume angles for both cases also the same. However, SHOST reported noticeable spread of vorticity from the jet into the surrounding air within the counterbore, which is attributed to a combination of jet-induced air motion and pressure disturbances. Further VOF-LES simulations and visualization experiments in a three-hole nozzle resulted in a reduction in the plume cone angle attributed to interactions between the spray and counterbore [53]. Counterbore design is also important because it can interact with the spray and be a source of liquid droplets in the nozzle tip, which can produce a major amount of particulate matter [30]. In the case of the Spray G injector used for the current work, a noteworthy characteristic is the small counterbore diameter, which was necessary in order to fit the eight holes of the nozzle. As a result, a significant interaction between the flow and counterbore wall was found in internal flow simulations [63].

The holes in Diesel nozzles can be cylindrical (straight) or conical (tapered). Straight nozzles tend to cavitate due to the flow separation (especially at the edges) and lower the discharge coefficient. However, they can be beneficial to promote atomization and cleanup of deposits in the holes [64]. The orifices of GDi nozzles are usually straight as that can be helpful for spray break-up. SHOST [61] and [59] studied the influence of cylindrical versus tapered holes in GDi nozzles and found that tapering resulted in a drastic increase of the discharge coefficient ($C_d \approx 0.9$ vs $C_d \approx 0.6$ for the straight nozzle). However, the instabilities generated by flow separation diminished greatly, resulting in a marked increase of the jet primary breakup length.

The nozzle geometry is very important to the development of the internal flow and external spray. The injector geometry in multi-hole GDi injectors can be measured in different ways. An optical microscope can serve to take pictures of the counterbores and inner holes, obtaining the external diameters of both. Although, careful positioning is required to measure the actual circumferences and not its projections. Payri et al. [65] used a silicone mold to create a negative of the orifices for a Spray G nozzle that was later measured by a scanning electron microscope (SEM) using a methodology derived from the one introduced by Macian et al. [66]. In multi-hole GDi injectors, where the nozzle can not be separated from the injector, the methodology is harder to implement than in Diesel nozzles. In addition, the particular geometry created a mold that was difficult to homogeneously coat in gold, which is critical to obtain good contrast in the pictures of the SEM. X-rays also provide a way to visualize and measure the internal geometry of injectors. Manin et al. [67] presented results obtained using x-ray tomography from a commercial x-ray source. The results showed good pixel resolution in zones in the counterbore, where the metal is still not thick, but the contrast was much more limited in the inner hole and the nozzle seat, where the x-ray has to go through more metal. Matusik et al. [68] also used x-rays to perform high-resolution tomography of a Spray G nozzle, showing increased contrast, pixel resolution and decreased artifacts in the final geometry owed to the implementation and upgrade of the beamline 7-BM in the Advance Photon Source at Argonne National Laboratory. The resulting geometry is easier to post-process due to the increased contrast between metal and air, with a pixel resolution of 1.17 µm. Even the surface finish could be obtained with this methodology and the high-energy x-rays from the APS as shown in an example in Fig 2.12. The geometry of one of the Spray G nozzles was also measured by Strek et al. [69], who also used the x-rays to obtain the density maps of the near-nozzle flow and compared them with internal flow (Eulerian) simulations. The same methodology for determining the geometry was applied later to eight Spray G nozzles, the geometry data for the set of injectors were used to study the influence of small variability in key geometrical dimensions with the differences observed in the time-resolved projected mass of all the nozzles [70].

Cavitation plays a significant role in GDi nozzles, due to a combination of effects from the geometry of the holes (cylindrical and short), the low needle lift, and very important, the low vapor pressure of the fuels used in GDi nozzles (Gasoline, ethanol, or light mono-component hydrocarbons for research purposes like iso-octane or n-heptane). The potential of cavitation onset and development on a flow can be defined by the cavitation number (CN), as in equation (2.4) [71].

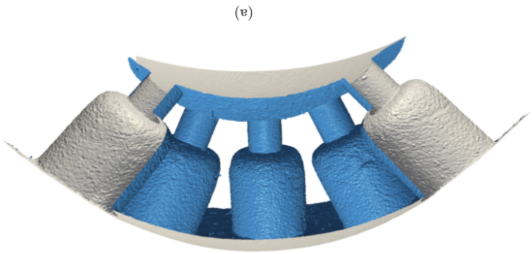

Figure 2.12: Isosuface of the internal geometry of one of the Spray G nozzles, reveling the internal geometry and the surface finish. From Matusik *et al. [68]*

$$\mathrm{CN} = \frac{P_{\mathrm{inj}} - P_b}{P_b - P_v}, \tag{2.4}$$

With $\mathrm{P}_{\mathrm{inj}}$ the injection pressure, P_v the vapor pressure of the fuel, and P_b the pressure at the discharge volume.

The cavitation number represents the ratio of the forces supporting to the ones suppressing cavitation and has been thoroughly studied in Diesel nozzles [47]. Bode et al. [72] shown that the limit between cavitating and non-cavitating flow (critical cavitation number) in real-sized holes of diesel injectors was for a CN of around 5. Later, Arcoumanis et al. [73] identified that the onset of cavitation for diesel injector happened for a cavitation number value of 2. However, for gasoline injectors, Gilles-Birth et al. [74] showed that the critical cavitation number was significantly lower and dependent on the angles of the holes (or drill angle), finding values of 0.81 for a nozzle with 50° drill angle and 0.64 for the one with 45°. A comparison of the critical CN for Diesel injectors (from several authors) and multi-hole GDi injectors is presented in Fig 2.13. As can be seen in the figure, due to the low values of the critical cavitation number for multi-hole DISI injectors, Gilles-Birth et al. [74] argued that cavitation happens in the entire operational domain of these injectors, only changing the type of the phenomena from string cavitation, bubbles, and super-cavitation depending on the particular conditions. A significant result of the study is that the cavitation in these types of nozzles relies heavily on the drill angle, being the onset and development of cavitation more severe for the nozzle with the lowest drill angle.

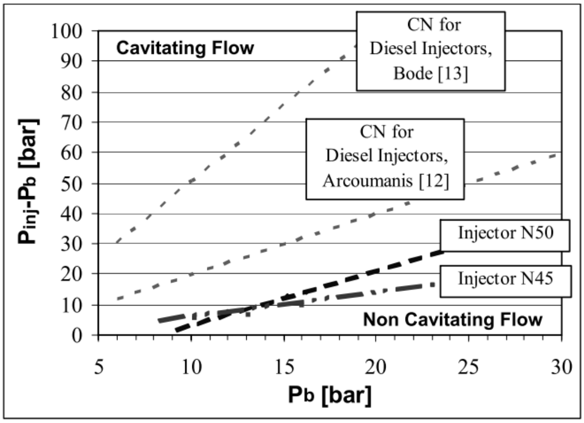

Figure 2.13: Injection pressure and discharge conditions relationship with cavitating and non-cavitating flow for Diesel injectors and two GDi multi-hole injectors with drill angles of 45° (N45) and 50° (N50). From GILLES-BIRTH *et al. [74].*

Due to the internal flow characteristics in GDi multi-hole nozzles and the low ambient pressure conditions that they can encounter in the cylinder, the flash boiling of the flow can occur in real engine conditions and therefore is commonly researched topic in gasoline direct injection systems [75]. In DI engines, pressurized liquid fuel is injected through the nozzle in the combustion chamber, which results in a drop of the local pressure (expansion) of the fuel. In a conventional (non-flashing) injection, the discharge conditions are such that the fuel is still in the liquid phase and then undergoes primary and secondary breakup upon exiting the nozzle. The conventional expansion and the flashing case are represented in Fig 2.14. Flash boiling occurs when a liquid is rapidly depressurized below the corresponding vapor pressure, resulting in a superheated liquid. In the diagram, the initially sub-cooled liquid fuel (1), expands adiabatically going through the metastable region (2) and (3), where the liquid can be superheated without evaporation. Beyond this point (4), the liquid phase becomes unstable and the transition to vapor happens rapidly [76]. Flash boiling is, therefore, a phenomenon that is generally characterized as a fast phase change process, which can be beneficial for rapid vaporization of the spray and mixture preparation inside a cylinder.

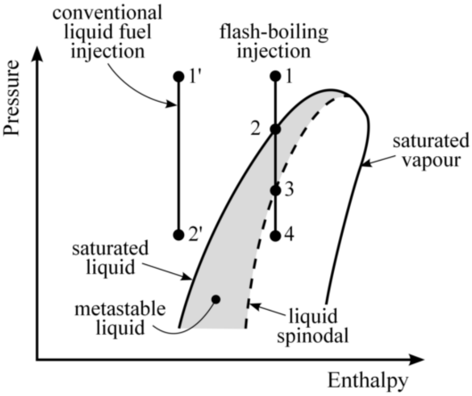

Figure 2.14: Representation of an injection under flashing conditions compared to the conventional case in a pressure-enthalpy diagram. From POURSADEGH *[76].*

Flashing conditions have not been experimented in this work. However, given its importance and relationship with other phenomena investigated here, it is briefly discussed and mentioned in several sections of the document. There is a significant amount of research in flashing conditions for DI gasoline injectors for either internal and external flow [55, 77–84]. MOULAI et al. [82] observed how the interactions between counterbore wall and liquid flow were significantly higher at flashing conditions by imagining the near-nozzle flow with a long-distance microscopic lens. It was observed that at flashing conditions the plumes expand significantly more, increasing their angle, and the interaction with the walls, nozzle tip, and the adjacent plumes. BALDWIN et al. [78] and SAHA et al. [83] studied the internal flow using LES with the focus on vapor generation due to cavitation and flash boiling and also found that the angles of the plumes and the velocity of the droplets increase under flashing conditions. GUO et al. [81] visualized the external spray using a Mie Scattering approach and observed that plumes get wider in flashing conditions. The increased plume interaction can also result in the collapse of the spray towards the axis, a phenomenon that was also observed by MONTANARO and ALLOCCA [80]. The collapse can also happen at high ambient-density conditions, although the onset and development mechanisms are different [81], as was observed by Manin et al. [67]. The study of the collapse of the spray under high density and temperature conditions is examined in detail in Chapter 5.

The internal flow of the ECN GDi nozzle featured in this work has been studied in numerous publications [40, 41, 63, 65, 69, 70, 78, 82, 83, 85–90]. Payri et al. [65] studied the internal geometry of a Spray G nozzle using silicone molds and measured the rate of injection and rate of momentum to calculate the main hydraulic parameters determining the flow of the injector. Payri et al. [40] expanded the rate of injection and rate of momentum measurements and compared the results with internal flow simulations done in Converge. Strek et al. [69] and Duke et al. [87], applied x-ray spray radiography, a methodology previously used in Diesel injectors, to calculate the projected mass of one Spray G nozzle of all sprays (lateral view) and isolating each of the sprays by means of x-ray tomographic radiography, later Matusik et al. [70] measured the near nozzle flow of eight Spray G nozzles by means of x-ray tomographic radiography and studied the influence of small geometrical variations in key dimensions with the differences captured in the near-nozzle flow data. Duke et al. [88] combined the needle lift measurements with the rate of injection, rate of momentum and x-ray spray measurements to study the influence of the needle lift and needle wobble in mass flow perturbations.

On the computational side, most studies use Large Eddy Simulations (LES), on account of the higher level of detail and accuracy typically obtained in the results. Moulai et al. [82] studied the internal flow at three conditions to study how well the model can predict the internal flow in flashing conditions, the model was able to capture cavitation formation and the expansion of the plumes in the counterbore that occurs in flash boiling and validated the findings by imaging the near-nozzle flow with a microscopic objective and high speed camera. Befrui et al. [63] performed VOF-LES simulations for the internal flow of the Spray G nozzle with the focus in evaluating if the methodology was able to capture the increased interaction with the counterbore walls owed to their smaller diameter. Droplet size and velocity probability distributions are extracted for several initial configurations of model parameters and then validated by using the results for a Lagrangian model that was compared with spray penetration experiments. Saha et al. [83, 89] performed numerical simulations of the internal flow using LES and combining the

VOF with a homogeneous relaxation model (HRM), with the focus to capture cavitation and flash boiling. Saha et al. [83] also studied the internal flow introducing the needle transients which resulted in significant differences in the flow pattern and hence in local vapor distributions for flashing and non-flashing conditions. Baldwin et al. [78] incorporated the needle motion measured experimentally using x-rays at Argonne National Laboratory to LES with HRM to capture the vapor generation. It was shown that low needle lift caused generation of vapor at the seat and that the internal flow in the Spray G injector was highly complex, containing many transients and interacting vortexes that result in perturbations in spray angle and mass flux. Later, Saha et al. [90] used a coupled Eulerian-Lagrangian spray simulation to transfer the results from the internal nozzle flow to the external spray using a one-way approach, where the initialization of the Lagrangian simulation is done with the results of a previous Eulerian calculation.

After the methodology and experimental techniques (Chapter 3), the results of the internal flow experiments realized in this work for several Spray-G nozzles are introduced and discussed in detail. Most of the research above and other work is referenced and discussed in combination with the results. In addition, due to the wide variety of different experimental techniques of the results, each section is provided with its own introduction, where relevant research is reviewed.

As the internal flow, the external spray of the Spray G nozzle has also been researched in several works [41, 67, 78, 80, 82, 90–96]. Itani et al. [91] obtained fuel concentration maps using laser induced fluorescence (LIF) for the nominal condition and two other conditions at higher pressure and higher temperature. The results were combined with liquid and vapor penetration measurements to study the mixing process. The effect of temperature (within the range tested) was found to not have a significant effect on the mixing process, whereas the density variation was identified to have the biggest effect owed to the spray collapse developed under high-density conditions. Payri et al. [41] studied in detail the spray collapse under a wide range of ambient temperature and density conditions and concluded that while the density is important to develop the spray collapse, the temperature also has a significant effect on the onset and development. It was observed that the collapse completely changes the shape of the injected cone, thus changing the macroscopic characteristics in terms of vapor and liquid penetration, spray angle and width. These changes affect the mixing process [91] and the velocity of the droplets and surrounding air, as it was shown in particle velocimetry imaging (PIV) performed by Sphicas et al. [92]. In the study, Lagrangian and LES models initialized with different cone angles and plume directions (see definition in Chapter 3) were compared against the experimental results to evaluate how well the simulations were able to capture the phenomena that develop under severe collapsing conditions. The comparison yielded some agreement and potential for the LES simulations to capture the phenomena but concluded that further research should be done in order to develop more predictive models that can capture the collapsing physics. Baldwin et al. [78] and Saha et al. [90] studied the external spray in combination with the internal flow to assess the impact of the development of the flow inside the nozzle with the behavior of the plumes outside, both observing significant influence from cavitation and flash boiling. These studies (and some additional) are reviewed further in Chapter 5 in combination with the introduction of the results obtained in this work of the external spray of the Spray G nozzle.

References

[1] PAYRI, FRANCISCO and DESANTES, JOSE MARIA. *Motores de combustion interna alternativos.* Editorial Reverte, 2011.

[2] FERGUSON, COLIN R and KIRKPATRICK, ALLAN T. *Internal combustion engines: applied thermosciences.* John Wiley & Sons, 2015.

[3] VENEGAS, OSCAR. "Estudio del fenómeno de la cavitación en la inyección diesel mediante la visualización del flujo interno en orificios transparentes." PhD thesis. Universidad Poltécnica de València-Departamento de Máquinas y Motores Térmicos, 2014.

[4] GIMENO, JAIME. "Desarrollo y aplicación de la medida del flujo de cantidad de movimiento de un chorro Diesel." PhD thesis. Universidad Politecnica de Valencia, 2008.

[5] BARDI, MICHELE. "Partial needle lift and injection rate shape effect on the formation and combustion of the Diesel spray". PhD thesis. Valencia (Spain): Universitat Politècnica de València, 2014. DOI: `10.4995/Thesis/10251/37374`.

[6] PAYRI, RAUL, VIERA, JUAN PABLO, GOPALAKRISHNAN, VENKATESH, and SZYMOWITZ, PATRICK. "The effect of nozzle geometry over ignition delay and flame lift-off of reacting direct-injection sprays for three different fuels". *Fuel* (2017).

[7] JIA, TAO MING, LI, GUO XIU, YU, YU SONG, and XU, YANG JIE. "Effects of ultra-high injection pressure on penetration characteristics of diesel spray and a two-mode leading edge shock wave". *Experimental Thermal and Fluid Science*, vol. 79 (2016), pp. 126–133. DOI: `10.1016/j.expthermflusci.2016.07.006`.

[8] REIF, KONRAD. *Gasoline Engine Management.* 2014, p. 354. DOI: `10.1007/978-3-658-03964-6`.

[9] SPHICAS, PANAGIOTIS. "High pressure and high temperature measurements on diesel sprays". PhD thesis. 2013.

[10] ZHAO, FUQUAN, LAI, M-C, and HARRINGTON, DAVID L. "Automotive spark-ignited direct-injection gasoline engines". *Progress in energy and combustion science*, vol. 25.5 (1999), pp. 437–562. DOI: `10.1016/S0360-1285(99)00004-0`.

[11] INGRAHAM, JOSEPH C. *Automobiles races.* 1957.

[12] FORBES, AIRD. *Bosh fuel injection systems. HP Trade.* 2001, p. 29.

[13] BAHATTIN, MUSTAFA and OZDALY, BULENT. "Gasoline Direct Injection". *Fuel Injection.* Ed. by DANIELA SIANO. Chapter 1. Sciyo, 2010, pp. 1–19. DOI: `10.5772/9693`.

[14] PHAM, P.X., VO, D.Q., and JAZAR, R.N. "Development of fuel metering techniques for spark ignition engines". *Fuel*, vol. 206 (2017), pp. 701–715. DOI: `10.1016/j.fuel.2017.06.043`.

[15] BAKER, PAUL and WATSON, HARRY. "MPI Air / Fuel Mixing for Gaseous and Liquid LPG Reprinted From : SI Combustion and Direct Injection SI Engine Technology". *SAE Technical paper 2005-01-0246*, 724 (2005).

[16] CHEN, YU, WANG, YUESEN, and RAINE, ROBERT. "Correlation between cycle-by-cycle variation, burning rate, and knock: A statistical study from PFI and DISI engines". *Fuel*, vol. 206 (2017), pp. 210–218. DOI: `10.1016/j.fuel.2017.06.016`.

[17] SALIBA, GEORGES, SALEH, RAWAD, ZHAO, YUNLIANG, PRESTO, ALBERT A., LAMBE, ANDREW T., FRODIN, BRUCE, SARDAR, SATYA, MALDONADO, HECTOR, MADDOX, CHRISTINE, MAY, ANDREW A., DROZD, GREG T., GOLDSTEIN, ALLEN H., RUSSELL, LYNN M., HAGEN, FABIAN, and ROBINSON, ALLEN L. "Comparison of Gasoline Direct-Injection (GDI) and Port Fuel Injection (PFI) Vehicle Emissions: Emission Certification Standards, Cold-Start, Secondary Organic Aerosol Formation Potential, and Potential Climate Impacts". *Environmental Science & Technology* (2017), acs.est.6b06509. DOI: `10.1021/acs.est.6b06509`.

[18] ZHU, RENCHENG, HU, JINGNAN, BAO, XIAOFENG, HE, LIQIANG, LAI, YITU, ZU, LEI, LI, YUFEI, and SU, SHENG. "Tailpipe emissions from gasoline direct injection (GDI) and port fuel injection (PFI) vehicles at both low and high ambient temperatures". *Environmental Pollution*, vol. 216 (2016), pp. 223–234. DOI: `10.1016/j.envpol.2016.05.066`.

[19] Zhao, Hua. *Advanced direct injection combustion engine technologies and development.* Ed. by Hua Zhao. Cambridge: Woodhead Publishing Limited, 2010.

[20] Johnson, Timothy and Joshi, Ameya. “Review of Vehicle Engine Efficiency and Emissions”. *SAE Technical Paper 2017-01-0907* (2017). doi: `10.4271/2017-01-0907`.

[21] Johnson, Timothy V. “CE-2016-306 Directions in vehicle efficiency and emissions”. *Combustion Engines*, vol. 166.3 (2017), pp. 3–8. doi: `10.19206/CE-2016-306`.

[22] Isenstadt, Aaron, German, John, Dorobantu, Mihai, Boggs, David, and Watson, Tom. “Downsized , boosted gasoline engines”. *The ICCT Internaltional Council of Clean Transportation*, 21 (2016), p. 23.

[23] Sellnau, Mark, Foster, Matthew, Hoyer, Kevin, Moore, Wayne, Sinnamon, James, and Husted, Harry. “Development of a Gasoline Direct Injection Compression Ignition (GDCI) Engine”. *SAE Int. J. Engines*, vol. 7.2 (2014), pp. 835–851. doi: `10.4271/2014-01-1300`.

[24] Iwamoto, Y., Noma, K., Nakayama, O., Yamauchi, T., and Ando, H. “Development of Gasoline Direct Injection Engine”. *SAE Technical Paper 970541*, 412 (1997). doi: `10.4271/970541`.

[25] Harada, Jun, Tomita, Tsutomu, Mizuno, Hiroyuki, Mashiki, Zenichiro, and Ito, Yasushi. “Development of direct injection gasoline engine”. *SAE Technical Paper 970540*, 412 (1997).

[26] Fansler, Todd D, Reuss, David L, Sick, Volker, and Dahms, Rainer N. “Invited Review: Combustion instability in spray-guided stratified-charge engines: A review”. *International Journal of Engine Research*, vol. 16.3 (2015), pp. 260–305. doi: `10.1177/1468087414565675`.

[27] Ikoma, Takuya, Abe, Shizuo, Sonoda, Yukihiro, and Suzuki, Hisao. “Development of V-6 3 . 5-liter Engine Adopting New Direct Injection System”. *SAE Technical Paper 2006-01-1259*, 724 (2006).

[28] Zeng, Wei and Sjöberg, Magnus. "Utilizing boost and double injections for enhanced stratified-charge direct-injection spark-ignition engine operation with gasoline and E30 fuels". *International Journal of Engine Research*, vol. 18.1-2 (2017), pp. 131–142. doi: `10.1177/1468087416685512`.

[29] Schwarz, Christian, Missy, Stephan, Steyer, Helmut, Durst, Bodo, Schünemann, Erik, and Kern, Wolfgang. "The New BMW Four and Six-cylinder Spark-Ignition Engines with Stratified Combustion". *MTZ worldwide*, vol. 68.05 (2007), pp. 2–5. doi: `10.1007/BF03226823`.

[30] Pauer, Thomas, Yilmaz, Hakan, Zumbrägel, Joachim, and Schünemann, Erik. *New Generation Bosch Gasoline Direct-injection Systems*. Tech. rep. 7-8. 2017, pp. 16–23. doi: `10.1007/s38313-017-0053-6`.

[31] Johansson, Anders N, Hemdal, Stina, and Dahlander, Petter. "Reduction of Soot Formation in an Optical Single-Cylinder Gasoline Direct-Injected Engine Operated in Stratified Mode Using 350 Bar Fuel Injection Pressure, Dual-Coil and High-Frequency Ignition Systems". *SAE Int. J. Engines*, vol. 10 (2017). doi: `10.4271/2017-01-9278`.

[32] Costa, M., Sorge, U., Merola, S., Irimescu, A., La Villetta, M., and Rocco, V. "Split injection in a homogeneous stratified gasoline direct injection engine for high combustion efficiency and low pollutants emission". *Energy*, vol. 117 (2016), pp. 405–415. doi: `10.1016/j.energy.2016.03.065`.

[33] Stefan, S. "Optical Diagnostics on FSI Transparent Engine". *FISITA World Automotive Congress, Barcelona*. 2004, pp. 23–27.

[34] Zeng, Wei, Sjöberg, Magnus, Reuss, David L., and Hu, Zongjie. "The role of spray-enhanced swirl flow for combustion stabilization in a stratified-charge DISI engine". *Combustion and Flame*, vol. 168.x (2016), pp. 166–185. doi: `10.1016/j.combustflame.2016.03.015`.

[35] PATEL, R, LADOMMATOS, N, STANSFIELD, P A, WIGLEY, G, GARNER, C P, PITCHER, G, TURNER, J W G, NUGLISCH, H, and HELIE, J. "Un-throttling a direct injection gasoline homogeneous mixture engine with variable valve actuation". *International Journal of Engine Research*, vol. 11.6 (2010), pp. 391–411. DOI: `10.1243/14680874JER604`.

[36] CAIRNS, ALASDAIR, BLAXILL, HUGH, and IRLAM, GRAHAM. "Exhaust Gas Recirculation for Improved Part and Full Load Fuel Economy in a Turbocharged Gasoline Engine". *SAE Technical Paper 2006-01-0047*, 724 (2006). DOI: `10.4271/2006-01-0047`.

[37] SELLNAU, MARK, MOORE, WAYNE, SINNAMON, JAMES, HOYER, KEVIN, FOSTER, MATTHEW, and HUSTED, HARRY. "GDCI Multi-Cylinder Engine for High Fuel Efficiency and Low Emissions". *SAE International Journal of Engines*, vol. 8.2 (2015), pp. 775–790. DOI: `10.4271/2015-01-0834`.

[38] KALGHATGI, GAUTAM and JOHANSSON, BENGT. "Gasoline compression ignition approach to efficient, clean and affordable future engines". *Proceedings of the Institution of Mechanical Engineers, Part D: Journal of Automobile Engineering* (2017), p. 095440701769427. DOI: `10.1177/0954407017694275`.

[39] HOFFMANN, GUY, BEFRUI, BIZHAN, BERNDORFER, AXEL, PIOCK, WALTER F., and VARBLE, DANIEL L. "Fuel System Pressure Increase for Enhanced Performance of GDi Multi-Hole Injection Systems". *SAE Technical Paper 2014-01-1209* (2014). DOI: `10.4271/2014-01-1209`.

[40] PAYRI, RAUL, GIMENO, JAIME, MARTÍ-ALDARAVÍ, PEDRO, and VAQUERIZO, DANIEL. "Internal flow characterization on an ECN GDi injector". *Atomization and Sprays*, vol. 26.9 (2015), pp. 889–919. DOI: `10.1615/AtomizSpr.2015013930`.

[41] PAYRI, RAUL, SALVADOR, FRANCISCO JAVIER, MARTÍ-ALDARAVÍ, PEDRO, and VAQUERIZO, DANIEL. "ECN Spray G external spray visualization and spray collapse description through penetration and morphology analysis". *Applied Thermal Engineering*, vol. 112 (2017), pp. 304–316. DOI: `10.1016/j.applthermaleng.2016.10.023`.

[42] Husted, Harry, Spegar, Timothy D., and Spakowski, Joseph. "The Effects of GDi Fuel Pressure on Fuel Economy". *SAE Technical Paper 2014-01-1438* (2014). doi: `10.4271/2014-01-1438`.

[43] Magneti Marelli. *Gasoline Direct Injection Technology (GDI).* 2017.

[44] Kanda, Mutsumi, Toyokazy, Baika, Senji, Kato, Minoru, Iwamuro, Makoto, Koike, and Akinori, Saito. "Application of a New Combustion Concept to Direct Injection Gasoline Engine". *SAE Technical Paper 2000-01-0531*, vol. 2000.724 (2000). doi: `10.4271/2000-01-0531`.

[45] Motjabi, Mehdi. "Optical Analysis of Multi-Stream GDI Sprays under Various Engine Operating Conditions by". PhD thesis. Loughborough University, 2011.

[46] Dahlander, Petter, Iemmolo, Daniele, and Tong, Yifei. "Measurements of Time-Resolved Mass Injection Rates for a Multi-Hole and an Outward Opening Piezo GDI Injector". *SAE Technical Paper 2015-01-0929* (2015). doi: `10.4271/2015-01-0929.Copyright`.

[47] Vent, Guido and Enderle, Christian. "The new 2.0 l turbo engine from the Mercedes-Benz 4-cylinder engine family". *2nd Aachen Colloquium China*. Stuttgart, 2012, pp. 137–160.

[48] Zigan, L., Schmitz, I., Flügel, a., Wensing, M., and Leipertz, a. "Structure of evaporating single- and multicomponent fuel sprays for 2nd generation gasoline direct injection". *Fuel*, vol. 90.1 (2011), pp. 348–363. doi: `10.1016/j.fuel.2010.08.001`.

[49] Smith, James, Jr, Gerald Szekely, Solomon, Arun, and Parrish, Scott. "A Comparison of Spray-Guided Stratified-Charge Combustion Performance with Outwardly-Opening Piezo and Multi-Hole Solenoid Injectors". *SAE Int. J. Engines*, vol. 4 (2011), pp. 1481–1497. doi: `10.4271/2011-01-1217`.

[50] Rivera, Edwin A., Mastro, Noreen, Zizelman, James, Kirwan, John, and Ooyama, Robert. “Development of Injector for the Direct Injection Homogeneous Market using Design for Six Sigma”. *SAE Technical Papers* (2010). doi: `10.4271/2010-01-0594`.

[51] Yi, Jianwen et al. “Development and Optimization of the Ford 3.5L V6 EcoBoost Combustion System”. *SAE Int. J. Engines*, vol. 2.1 (2009), pp. 1388–1407. doi: `10.4271/2009-01-1494`.

[52] Engine Combustion Network. *ECN Spray G*. 2016.

[53] Befrui, Bizhan, Hoffmann, Guy, Kirwan, John, Piock, Walter, and Schilling, Sebastian. “Analytical Optimization of Delphi GDi Fuel Injection Systems”. *15th Conference "The Working Process of the Internal Combustion Engine"*. September 2015. 2015.

[54] Befrui, Bizhan, Corbinelli, Giovanni, D’Onofrio, Mario, and Varble, Daniel. “GDI Multi-Hole Injector Internal Flow and Spray Analysis”. *SAE Tecnnical Paper 2011-01-1211* (2011). doi: `10.4271/2011-01-1211`.

[55] Postrioti, Lucio, Bosi, Maurizio, Cavicchi, Andrea, Gioia, Rita Di, Bonandrini, Giovanni, Marelli, Magneti, and Spa, Powertrain. “Momentum Flux Measurement on Single-Hole GDI Injector under Flash-Boiling Condition”. *SAE Technical Paper 2015-06-2480* (2015). doi: `10.4271/2015-24-2480`.

[56] Cavicchi, Andrea, Postrioti, Lucio, Giovannoni, Nicola, Fontanesi, Stefano, Bonandrini, Giovanni, and Di Gioia, Rita. “Numerical and experimental analysis of the spray momentum flux measuring on a GDI injector”. *Fuel*, vol. 206 (2017), pp. 614–627. doi: `10.1016/j.fuel.2017.06.054`.

[57] Moon, Seoksu, Komada, Keisuke, Sato, Kiyotaka, Yokohata, Hideaki, Wada, Yoshitaka, and Yasuda, Nobuhiro. “Ultrafast X-ray study of multi-hole GDI injector sprays: Effects of nozzle hole length and number on initial spray formation”. *Experimental Thermal and Fluid Science*, vol. 68 (2015), pp. 68–81. doi: `10.1016/j.expthermflusci.2015.03.027`.

[58] Tu, Po-wen, Cao, Li, Xu, Hongming, Eall, Adam, Venus, Jens Krueger, Srivastava, Dhananjay Kumar, Dean, Karl, and Jing, Daliang. “Numerical Investigation of GDI Injector Nozzle Geometry on Spray Characteristics”. *SAE Technical Paper 2015-01-1906*, 201509061 (2015). doi: `10.4271/2015-01-1906`.

[59] Befrui, Bizhan, Corbinelli, Giovanni, Spiekermann, Peter, Shost, Mark, and Lai, Ming-Chia. “Large Eddy Simulation of GDI Single-Hole Flow and Near-Field Spray”. *SAE International Journal of Fuels and Lubricants*, vol. 5.2 (2012), pp. 620–636. doi: `10.4271/2012-01-0392`.

[60] Befrui, B, Corbinelli, G, Hoffmann, G, Technical, Delphi, and Gillingham, Centre. “Cavitation and Hydraulic Flip in the Outward-Opening GDi Injector Valve-Group”. *SAE International*, vol. 2009-01-14 (2009). doi: `10.4271/2009-01-1483`.

[61] Shost, Mark. “Evaluation Of Nozzle Geometry On High Pressure Gasoline Direct Injection Spray Atomization”. PhD thesis. Wayne State University Dissertations, 2014.

[62] Shost, Mark a., Lai, Ming-Chia, Befrui, Bizhan, Spiekermann, Peter, and Varble, Daniel L. “GDi Nozzle Parameter Studies Using LES and Spray Imaging Methods”. *SAE Technical Paper 2014-01-1434*, vol. 1 (2014). doi: `10.4271/2014-01-1434`.

[63] Befrui, B, Aye, A, Bossi, A, Markle, L E, and Varble, D L. “ECN GDi Spray G : Coupled LES Jet Primary Breakup - Lagrangian Spray Simulation”. *ILASS Americas 28th Annual Conference on Liquid Atomization and Spray Systems*, May (2016).

[64] Payri, Francisco, Payri, Raul, Salvador, Francisco Javier, and Martínez-López, Jorge. “A contribution to the understanding of cavitation effects in Diesel injector nozzles through a combined experimental and computational investigation”. *Computers & Fluids*, vol. 58 (2012), pp. 88–101. doi: `10.1016/j.compfluid.2012.01.005`.

[65] Payri, Raul, Gimeno, Jaime, Marti-Aldaravi, Pedro, and Vaquerizo, Daniel. “Momentum Flux Measurements on an ECN GDi Injector”. *SAE Technical Paper 2015-01-1893* (2015). doi: `10.4271/2015-01-1893`.

[66] Macian, V., Bermudez, V., Payri, R., and Gimeno, J. “New Technique for Determination of Internal Geometry of a Diesel Nozzle With the Use of Silicone Methodology”. *Experimental Techniques*, vol. 27.2 (2003), pp. 39–43. doi: `10.1111/j.1747-1567.2003.tb00107.x`.

[67] Manin, Julien, Jung, Yongjin, Skeen, Scott A, Pickett, Lyle M, Parrish, Scott E, and Markle, Lee E. “Experimental Characterization of DI Gasoline Injection Processes”. *SAE Technical Paper 2015-01-1894* (2015). doi: `10.4271/2015-01-1894`.

[68] Matusik, K.E., Duke, D.J., Swantek, A.B., Powell, C.F., and Kastengren, A.L. “High Resolution X-Ray Tomography of Injection Nozzles”. *ILASS Americas 28th Annual Conference on Liquid Atomization and Spray Systems, Dearborn, MI, May 2016*. May. 2016.

[69] Strek, Piotr, Duke, Daniel, Swantek, Andrew, Kastengren, Alan, Powell, Christopher F., and Schmidt, David P. “X-Ray Radiography and CFD Studies of the Spray G Injector”. *SAE Technical Paper 2016-01-0858*. 2016. doi: `10.4271/2016-01-0858`.

[70] Matusik, K E, Duke, D J, Sovis, N, Swantek, A B, Powell, C F, Payri, R, and Vaquerizo, D. “A study on the relationship between internal nozzle geometry and injected mass distribution of eight ECN Spray G nozzles”. *ILASS – Europe 2017, 28th Annual Conference on Liquid Atomization and Spray Systems*, September (2017). doi: `http://dx.doi.org/10.4995/ILASS2017.2017.4766`.

[71] Bergwerk, W. “Flow pattern in Diesel nozzle spray holes”. *Proc. Inst. Mech. Engrs*, vol. 173, n. 25 (1959).

[72] Bode, J, Chaves, H, Hentschel, W, Kubitzek, A, Obermeier, F, Schindler, K, and Schneider, T. “Fuel spray in Diesel engines. Part I: Spray formation”. *ATA 92A065* (1992).

[73] Arcoumanis, Constantine, Flora, H, Gavaises, Manolis, and Badami, M. “Cavitation in Real-Size Multi-Hole Diesel Injector Nozzles”. *SAE Technical Paper 2000-01-1249*. 2000. doi: `10.4271/2000-01-1249`.

[74] Gilles-Birth, Isabell, Bernhardt, Sören, Spicher, Ulrich, and Rechs, Manfred. "A Study of the In-Nozzle Flow Characteristic of Valve Covered Orifice Nozzles for Gasoline Direct Injection". *SAE Technical Paper 2005-01-3684*, 724 (2005). doi: `10.4271/2005-01-3684`.

[75] Wood, Andrew, Wigley, Graham, and Helie, Jerome. "Flash Boiling Sprays produced by a 6-hole GDI Injector". *17th International Symposium on Applications of Laser Techniques to Fluid Mechanics*, July (2014), pp. 7–10. doi: `10.13140/2.1.5105.3445`.

[76] Poursadegh, Farzad. "An experimental and theoretical investigation of direct fuel injection". PhD thesis. University of Melbourne, 2017, p. 172. doi: `10.1205/fbp.04184`.

[77] Serras-Pereira, J., Van Romunde, Z., Aleiferis, P. G., Richardson, D., Wallace, S., and Cracknell, R. F. "Cavitation, primary break-up and flash boiling of gasoline, iso-octane and n-pentane with a real-size optical direct-injection nozzle". *Fuel*, vol. 89.9 (2010), pp. 2592–2607. doi: `10.1016/j.fuel.2010.03.030`.

[78] Baldwin, E.T., Grover, R.O., Parrish, Scott E, Duke, Daniel J., Matusik, Katarzyna E, Powell, Christopher F, Kastengren, Alan L., and Schmidt, David P. "String flash-boiling in gasoline direct injection simulations with transient needle motion". *International Journal of Multiphase Flow*, vol. 87 (2016), pp. 90–101. doi: `10.1016/j.ijmultiphaseflow.2016.09.004`.

[79] Chan, Qing N., Bao, Yongming, and Kook, Sanghoon. "Effects of injection pressure on the structural transformation of flash-boiling sprays of gasoline and ethanol in a spark-ignition direct-injection (SIDI) engine". *Fuel*, vol. 130 (2014), pp. 228–240. doi: `10.1016/j.fuel.2014.04.015`.

[80] Montanaro, A and Allocca, L. "Flash Boiling Evidences of a Multi-Hole GDI Spray under Engine Conditions by Mie-Scattering Measurements". *SAE Technical Paper 2015-01-1945* (2015).

[81] Guo, Hengjie, Ding, Haichun, Li, Yanfei, Ma, Xiao, Wang, Zhi, Xu, Hongming, and Wang, Jianxin. “Comparison of spray collapses at elevated ambient pressure and flash boiling conditions using multi-hole gasoline direct injector”. *Fuel*, vol. 199 (2017), pp. 125–134. doi: `10.1016/j.fuel.2017.02.071`.

[82] Moulai, Maryam, Grover, Ronald, Parrish, Scott, and Schmidt, David. “Internal and Near-Nozzle Flow in a Multi-Hole Gasoline Injector Under Flashing and Non-Flashing Conditions”. *SAE Technical Paper 2015-01-0944*, 2015-01-0944 (2015). doi: `10.4271/2015-01-0944`.

[83] Saha, Kaushik, Som, Sibendu, Battistoni, Michele, Li, Yanheng, Pomraning, Eric, and Senecal, Peter Kelly. “Numerical Investigation of Two-Phase Flow Evolution of In- and Near-Nozzle Regions of a Gasoline Direct Injection Engine During Needle Transients”. *SAE International Journal of Engines*, vol. 9.2 (2016), pp. 2016–01–0870. doi: `10.4271/2016-01-0870`.

[84] Khan, Muhammad Mahabat, Hélie, Jerome, Gorokhovski, Mikhael, and Sheikh, Nadeem Ahmed. “Experimental and numerical study of flash boiling in gasoline direct injection sprays”. *Applied Thermal Engineering*, vol. 123 (2017), pp. 377–389. doi: `10.1016/j.applthermaleng.2017.05.102`.

[85] Poursadegh, Farzad, Lacey, Joshua S., Brear, Michael J., and Gordon, Robert L. “On the Fuel Spray Transition to Dense Fluid Mixing at Reciprocating Engine Conditions”. *Energy and Fuels*, vol. 31.6 (2017), pp. 6445–6454. doi: `10.1021/acs.energyfuels.7b00050`.

[86] Saha, Kaushik, Som, Sibendu, Battistoni, Michele, Li, Yanheng, Quan, Shaoping, and Kelly Senecal, Peter. “Modeling of Internal and Near-Nozzle Flow for a Gasoline Direct Injection Fuel Injector”. *Journal of Energy Resources Technology*, vol. 138.5 (2016), p. 052208. doi: `10.1115/1.4032979`.

[87] Duke, Daniel J, Swantek, Andrew B, Sovis, Nicolas M, Tilocco, F Zak, Powell, Christopher F, Kastengren, Alan L, Gürsoy, Doğa, and Biçer, Tekin. “Time-resolved X-ray Tomography of Gasoline Direct Injection Sprays”. *SAE Int. J. Engines*, vol. 9 (2015), pp. 143–153. doi: `10.4271/2015-01-1873`.

[88] Duke, Daniel J et al. “Internal and near nozzle measurements of Engine Combustion Network “Spray G” gasoline direct injectors”. *Experimental Thermal and Fluid Science*, vol. 88 (2017), pp. 608–621. doi: `10.1016/j.expthermflusci.2017.07.015`.

[89] Saha, Kaushik, Som, Sibendu, Battistoni, Michele, Li, Yanheng, Quan, Shaoping, and Senecal, Peter Kelly. “Numerical simulation of internal and near-nozzle flow of a gasoline direct injection fuel injector”. *Journal of Physics: Conference Series*, vol. 656.January 2016 (2015), p. 012100. doi: `10.1088/1742-6596/656/1/012100`.

[90] Saha, Kaushik, Quan, Shaoping, Battistoni, Michele, Som, Sibendu, Senecal, P K, and Pomraning, Eric. “Coupled Eulerian Internal Nozzle Flow and Lagrangian Spray Simulations for GDI Systems”. *SAE technical paper 2017-01-0834*. 2017. doi: `10.4271/2017-01-0834`.

[91] Itani, Lama M, Bruneaux, Gilles, Hermant, Laurent, and Schulz, Christof. “Investigation of the Mixing Process and the Fuel Mass Concentration Fields for a Gasoline Direct-Injection Spray at ECN Spray G Conditions and Variants”. *SAE Technical Paper 2015-01-1902* (2015), pp. 1–10. doi: `10.4271/2015-01-1902`.

[92] Sphicas, Panos, Pickett, Lyle M, Skeen, Scott, Frank, Jonathan, Lucchini, Tommaso, Sinoir, David, D’Errico, Gianluca, Saha, Kaushik, and Som, Sibendu. “A Comparison of Experimental and Modeled Velocity in Gasoline Direct-Injection Sprays with Plume Interaction and Collapse”. *SAE Int. J. Fuels Lubr.* Vol. 10 (2017), pp. 184–201. doi: `10.4271/2017-01-0837`.

[93] Montanaro, A., Allocca, L., Lazzaro, M., and Meccariello, G. “Impinging Jets of Fuel on a Heated Surface: Effects of Wall Temperature and Injection Conditions”. *SAE Technical Paper 2016-01-0863*, vol. 2016-April (2016). doi: `10.4271/2016-01-0863`.

[94] LACEY, J., POURSADEGH, F., BREAR, M. J., GORDON, R., PETERSEN, P., LAKEY, C., BUTCHER, B., and RYAN, S. "Generalizing the behavior of flash-boiling, plume interaction and spray collapse for multi-hole, direct injection". *Fuel*, vol. 200 (2017), pp. 345–356. DOI: `10.1016/j.fuel.2017.03.057`.

[95] QUAREMBA, GIUSEPPE, ALLOCCA, LUIGI, AMORESANO, AMEDEO, NIOLA, VINCENZO, MONTANARO, ALESSANDRO, and LANGELLA, GIUSEPPE. "Fuzzy Logic Approach to GDI Spray Characterization". *SAE Technical Paper 2016-01-0874*. 2016. DOI: `10.4271/2016-01-0874`.

[96] LACEY, JOSHUA STUART, POURZAKADEH, FARZAD, BREAR, MICHAEL, PETERSEN, PHRED, LAKEY, CHARLES, RYAN, STEVE, and BUTCHER, BRENDAN. "Optical Characterization of Propane at Representative Spark Ignition , Gasoline Direct Injection Conditions". *SAE International Journal of Engines*, 2016-01-0842 (2016), pp. 21–23. DOI: `10.4271/2016-01-0842.Copyright`.

Chapter 3

Experimental and analytical methodologies

3.1 Introduction

This chapter introduces the experimental equipment used, and the methodology followed to perform the measurements and data analysis presented in the results chapters. The first section is dedicated to describing the injection system, while each of the remaining sections introduces an experimental facility. The experimental configurations used in each of the installations and the steps taken to process the raw data are described here. Most of the results presented in this document have been measured in the laboratories of CMT-Motores Térmicos, except for the x-ray measurements. The x-ray experiments were performed during the research visit at Argonne National Laboratory (ANL) that was part of this doctoral thesis project. The measurements were done utilizing the synchrotron located at the Advanced Photon Source (APS), with the beamlines and equipment located in sector 7-BM and sector 32-ID of the APS.

3.2 Injection system

3.2.1 GDi Injector

The injection system used in this work was one of the paired injectors and drivers manufactured and donated by Delphi to the ECN, serial AV67-026. However, measurements from other injectors with different serials from the same batch are also collected in this work. A total of twelve injectors were donated by Delphi, together with six paired drivers. The six injectors that provided the most similar injected quantities and patternation profiles were selected as "main" from the twelve to ensure maximum possible homogeneity of the hardware [1]. All of the main and back-up injectors, along with the paired drivers and their current locations are shown in Table 3.1 An image of the Spray G injector used can be seen in Fig 3.1.

Table 3.1: List of the main and back-up Spray G injectors, the paired drivers, and the institutions in which they are located.

Primary Injector #	**Driver #**	**Current Location***	**Back-up Inj #**
AV67-016	94	U-Michigan	AV67-011
AV67-017	207	I.Motori	AV67-019
AV67-018	208	U-D-E	AV67-020
AV67-022	246	TU/e	AV67-025
AV67-026	247	CMT	none
AV67-028	248	SNL-E	AV67-029

* As of 06/2017

The injector shown is a multi-hole, spray-guided injector suited for direct injection spark ignition (DISI) operation and was specifically tailored to comply with the specifications set by the ECN group. Table 3.2 shows the design parameters of the injector.

The main characteristics of the internal geometry of the injector can be seen in Fig 3.2, which shows a cut-plane of the nominal dimensions of the nozzle of the injector. The sketch shows the tip of the needle with a spherical shape at full lift (45 µm), the needle seat, and the geometry of two holes. The orifices are "stepped," which is typical in modern GDi injectors. The orifice diameter hereon is always referred to the inner section of the hole, whereas the outer section will be referred to as counterbore.

Figure 3.1: Picture of the Delphi Spray G injector AV67-026 with inlet fuel feed (cast rail) mounted.

3.2.2 Standard conditions

The first condition defined by the ECN group for the GDi injector is known as “Spray G” and is detailed in Table 3.3. The Spray G name is now used to refer to the standard condition as well as the injectors themselves.

Parametric variations beyond Spray G were included by the group to study different phenomena unique to GDi operation, like flash boiling (Spray G2) or early injection (Spray G3). Other conditions were added later that were interesting for causing specific phenomena like spray collapse or because they were gaining attention within the industry or research groups. The following list enumerates the current standard conditions for the ECN GDi injector, along with a brief explanation of the focus for each of the conditions. The parameters shown in each of the items are only those that are different from the standard Spray G condition.

Table 3.2: Injector specifications

Parameter	Design value
Number of holes	8[-]
Inner diameter	165 µm
Outer diameter	388 µm
Spray shape	circular
Spray angle	80°
Drill angle	37°
Bend angle	0°
L/D ratio	2
Hole shape	straight
Manufacturing	EDM
Flow Rate	15 cm^3/s @ 10 MPa

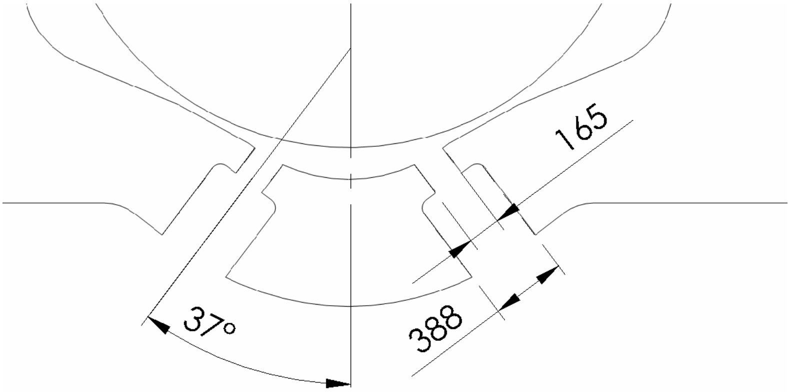

Figure 3.2: Sketch showing the main characteristics of the ECN GDi injector. The sketch represents a cut-plane of the nozzle showing the cross-section of two orifices, needle, needle seat and sac. All dimensions in µm.

- **G2:** [333.15 K 50 kPa]. Flash boiling condition.
- **G3:** [333.15 K 100 kPa]. Early injection condition.
- **G4:** [7 kg/m^3]. Double density condition (Double Spray G).
- **G6:** [3.5 kg/m^3 800 K]. High gas temperature.
- **G7:** [9 kg/m^3 800 K]. Strong collapse case.

Table 3.3: Spray G conditions.

Parameter	Value
Fuel	Iso-Octane
Fuel Pressure	20 MPa
Fuel Temperature	90 °C
Injector Temperature	90 °C
Ambient Pressure	0.6 MPa
Ambient Temperature	300 °C
Energizing Time	680 µs
Injected Quantity	10 mg

- **GM-1:** [680 µs main 1 ms dwell 186 µs post]. Multiple injection 1.

Two injector positions were considered for visualization purposes: a primary orientation recommended in SAE J2715 [2], and a secondary orientation defined with a 22.5° angle from the primary. The primary and secondary orientations are shown in Fig 3.3. In the primary orientation, three separate zones of the sprays are visible and grouped as per Fig 3.3. In this position, the electrical connector and a small mark in the tip of nozzle known as “dimple” are pointing towards the camera. The secondary position is at a 22.5° clockwise angle with respect to the primary and leaves four distinct zones in the spray with two plumes each.

3.2.3 Engine Control Unit

The driver of the injector was also provided by Delphi and is specific to each of the injectors. The driver consists on a simplified Engine Control Unit (ECU) equipped with the necessary electronics to provide the intensity signal to the solenoid of the injector upon receiving a trigger to mark the beginning and duration of the signal. The driver can provide three signals with different intensity levels depending on the injection pressure. Nonetheless, the ECN accorded to only use the “High Pressure” outlet as a means to standardize the driving signals and avoid unnecessary uncertainty. Fig 3.4 shows a picture of the ECU on the left side and three examples of the driving signal used to control the injection on the right side.

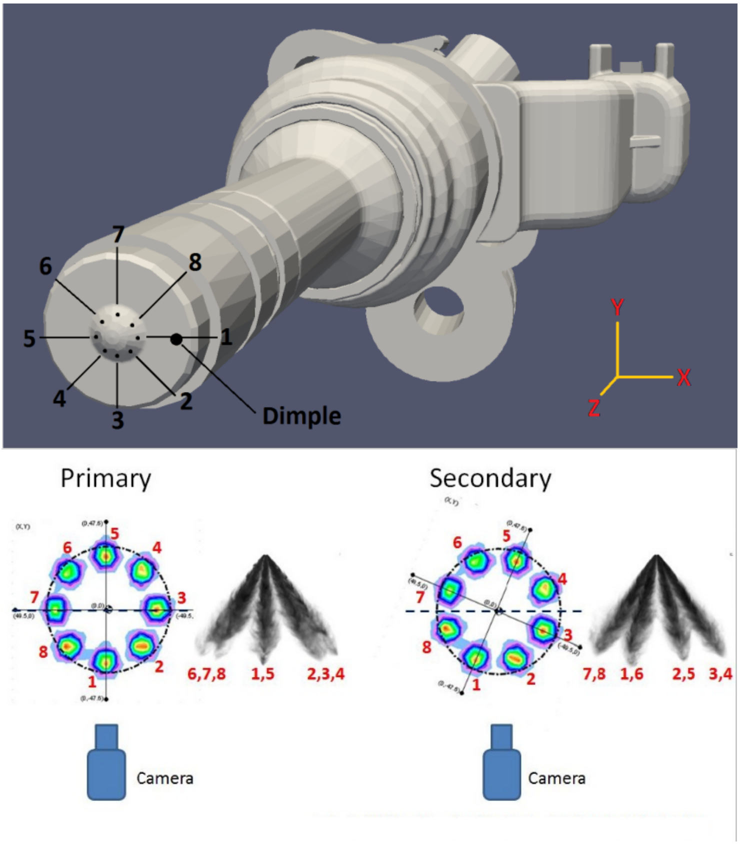

Figure 3.3: Definition of primary and secondary orientation defined for visualization for the ECN GDi injector.

3.2.4 High-pressure fuel delivery system

The system to provide the injector with pressurized fuel used is very similar to the ones used to deliver fuel to a Diesel injector, described previously in several publications [3–5]. The system consists of a high-pressure pump that carries the fuel from the fuel tank to a first common rail used to regulate the pressure of the system. The first rail feeds a second rail where the injector is mounted. This second rail is also equipped with a kistler pressure sensor to log the injection pressure accurately. Given that the pump can pressurize the fuel up to 220 MPa, a security valve is mounted on the second rail to ensure the integrity of the GDi injector, which is only able to safely withstand a pressure of the order of 20 MPa. A sketch of the fuel delivery system is presented in 3.5.

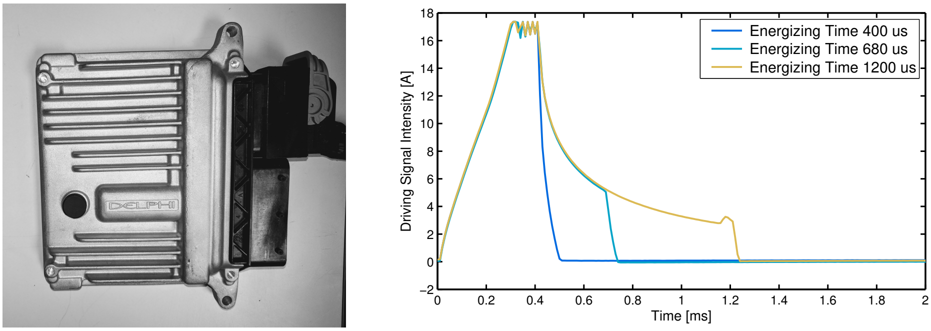

(a) Spray G Engine Control Unit

(b) Examples of driving signals for three energizing times

Figure 3.4: Engine Control Unit and driving signals produced for three different energizing times.

3.3 Rate of Injection

3.3.1 Background

Rate of injection (ROI) is a fundamental characteristic of the fuel injection system, as it determines the quantity and rate at which the fuel is being delivered. It significantly affects performance, noise, and pollutant emissions of modern Diesel engines [6]. Rate of injection was not as relevant in the older PFI gasoline engines, but it becomes critical in modern direct injection gasoline engines [7].

The methodology followed to complete mass flow rate measurements for the ECN GDi used in this work was described in detail in several publications [8, 9], and is based on the set-up typically used for Diesel injectors that has been many times depicted in previous work [3, 4, 6, 10, 11]. The instrument used to determine the rate of injection is the Injection Rate Discharge Curve Indicator (IRDCI), based on the long tube method or Bosch method [12]. The Bosch method is widely used for this purpose due to good dynamic response, high accuracy, and simplicity [3]. A diagram of the instrument can be seen in Fig 3.6.

The internal volume of the rate meter is filled with fuel to have a well-defined boundary condition of the wave propagation process, as it is a function of the pressure and the velocity of sound in the medium. The pressure inside can be adjusted by controlling the pressure of a nitrogen

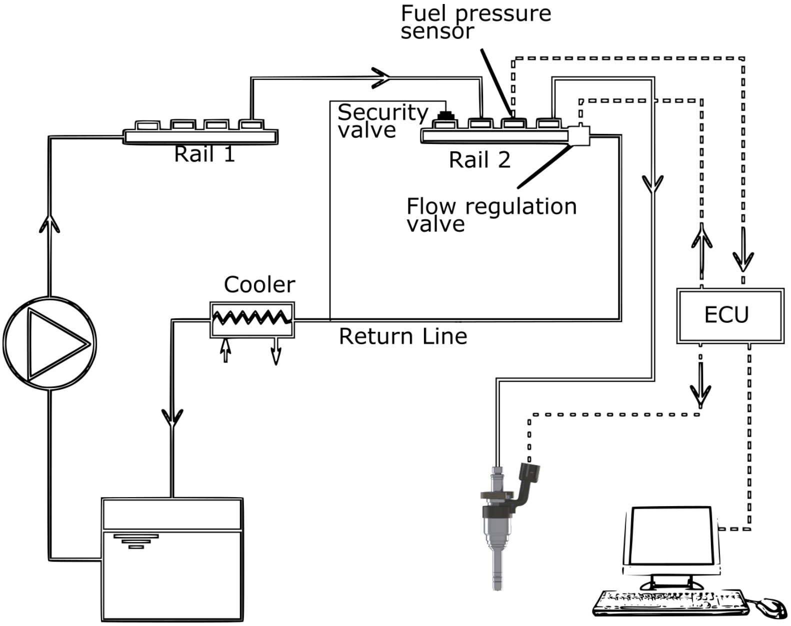

Figure 3.5: Diagram of the circuit used to pressurize and deliver the fuel to the GDi injector.

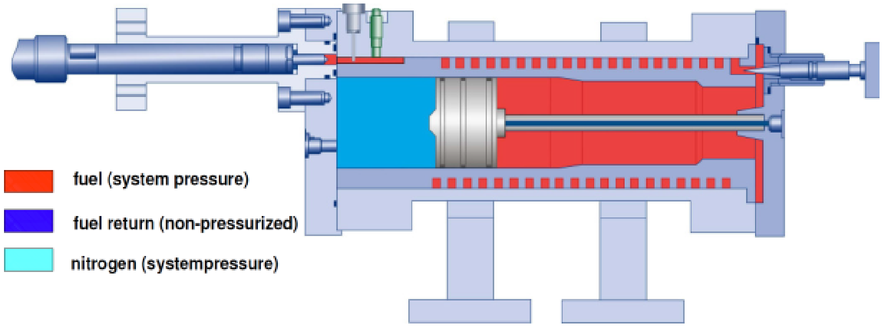

Figure 3.6: Diagram illustrating the parts of the instrument used to determine the mass flow rate.

volume adjacent to the test volume. The injection process generates a pressure wave that travels at a velocity c corresponding to the speed of sound in the medium. The pressure wave produces a pressure variation described by the Allievi equation (3.1).

$$\Delta p = c\rho_f u \tag{3.1}$$

with Δp the pressure increment due to the injection, ρ_f the fuel density, c the speed of sound of the fuel, and u the velocity of the fuel at the orifice outlet. The variation in pressure is measured by a piezoelectric sensor closely positioned to the injector tip. The proximity between the sensor and the outlet of the injector is necessary to avoid delay between the injection and the registered signal, and to minimize the attenuation of the pressure due to friction losses.

The pressure wave due to the injection event travels downstream until it reaches the fuel deposit or release area, whose purpose is to limit the global pressure increase due to the added mass of fuel. Upon reaching the higher cross-sectional area of the deposit, a reflected wave is generated which travels upstream back to the piezoelectric sensor and injector. In order to avoid interference between the two opposing pressure waves, the length of the tube needs to be sufficiently long. The signal from the piezoelectric pressure sensor can be then translated to a time-resolved mass signal through (3.2) knowing the cross-sectional area of the tube.

$$\dot{m}(t) = \frac{A_p \Delta p}{c}, \tag{3.2}$$

where A_p is the cross-sectional area of the tube and $\dot{m}$ is the injection rate.

3.3.2 Set-up and methodology

The injector is mounted on an injector holder specifically designed to adapt to its geometry. Fig 3.7 shows a representation of the injector inside the injector holder. The holder has a cooling circuit, whose the purpose it is maintaining the body of the injector at a controlled temperature.

A picture of the injector holder and injector mounted on the rate meter can be seen in Fig 3.8.

The IRDCI used is a commercially available IAV equipment fitted with a thermocouple to monitor the temperature of the deposit, as it has an influence on the density and speed of sound of the fuel. The equipment is also equipped with an additional pressure sensor (besides the piezoelectric sensor) used to monitor the ambient pressure inside the deposit, which can be modified by controlling the nitrogen pressure in

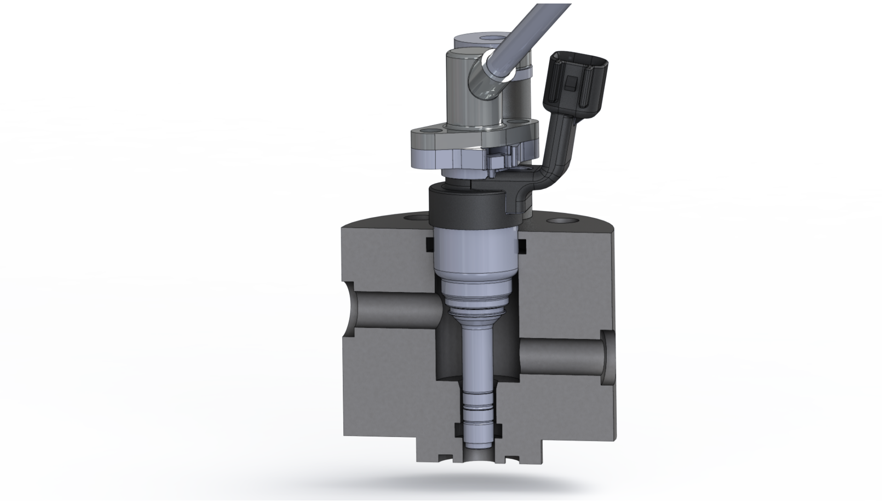

Figure 3.7: Representation of a cut-section of the injector holder used for mass flow rate measurements.

Figure 3.8: Injector, injector holder and IAV rate meter used in the experimental set-up.

an adjacent volume. As mentioned previously, the injector holder has a cooling circuit, whose purpose is to control the temperature of the body of the injector. The cooling circuit is connected through PVC hoses to a proportional-integral-derivative (PID) temperature regulator. The regulator uses a mix of glycol and water to control the temperature because of their good thermal properties.

Given the uncertainties in the determination or available data of the speed of sound of the fuel, and as a standard methodology that has been carried out in many previous publications [3, 4, 9, 13], a gravimetric scale downstream of the rate meter has been used as per Fig 3.9.

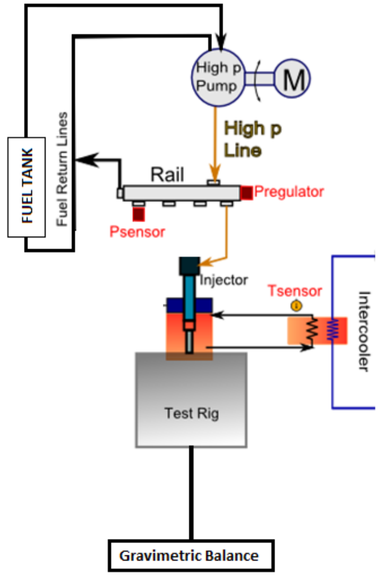

Figure 3.9: Sketch featuring the experimental set-up used for rate of injection measurements.

The value obtained with the gravimetric balance is used to correct the integral (sum) of the rate of injection signal measured with the rate meter. This is done due to the uncertainty of the exact values of the speed of sound of the fuel being used (iso-octane). The speed of sound of the fuel depends on the precise fuel composition and is very sensible to the temperature of the system. Moreover, as the speed of sound data for iso-octane (2,2,4 - Trimethylpentane) were not available, the data for octane published in the NIST webbook [14] were used. The measurement is performed by injecting at a frequency of 10 Hz. When the injected quantity measured by the gravimetric balance has reached stabilization, 50 injections are done and collected with a digital oscilloscope. The rate of injection signal, along with the pressure and driving signal from the ECU are recorded and stored. Then, the value obtained in the gravimetric balance is used to scale the rate of injection signal to make its integral equal to the value measured in the balance (3.3).

$$k_{\text{adjust}} M_{\text{integration}} = M_{\text{balance}}, \tag{3.3}$$

with $M_{\text{integration}}$ and M_{balance} referring to the integral of the average of the 50 repetitions of the ROI signal and the mass measured in the balance per injection upon reaching stabilization. k_{adjust}, is, therefore, the scaling factor between the two and is monitored to typically have it between 0.95 and 1.05.

Because the quantity of fuel in the fuel deposit inside the IRDCI grows as the measurement is being performed, the raw rate of injection signal features a constant increment that is an artifact produced by the accumulation of fuel. The phenomena were studied in detail by Payri et al. [6], and the solution found in the published work was also implemented here to avoid the accumulation effect.

To avoid evaporation of the fuel downstream of the test rig that could produce a negative mass flow from the balance, a long refrigerated tube was used at the outlet of the IRDCI. However, no differences were found when comparing refrigerated and non-refrigerated outlet.

3.4 Rate of Momentum

3.4.1 Background

As stated by Payri et al. [15], the rate of momentum (ROM) of a fluid can be defined by the rate of injection multiplied by the velocity of the fluid. Having an instantaneous mass flow of $\dot{m}$, with density ρ, moving at a velocity of u through a cross-section area of A_0, the rate of injection and rate of momentum can be therefore defined by (3.4) and (3.5) respectively.

$$\dot{m} = \int_{A_0} u\rho \, dA, \tag{3.4}$$

$$\dot{M} = \int_{A_0} u^2\rho \, dA. \tag{3.5}$$

Using ROM data in combination with ROI data allows describing the flow at the outlet of the injector with more detail. In order to describe the flow in a simplified manner, the effective area coefficient (A_{ef}) (3.6) and the effective velocity coefficient (u_{ef}) (3.7) are defined. The meaning of these parameters can be seen graphically in Fig 3.10.

$$A_{\text{ef}} = \frac{\dot{m}_f^2}{\rho_f M_f} \tag{3.6}$$

$$u_{\text{ef}} = \frac{\dot{M}_f}{\dot{m}_f} \tag{3.7}$$

where $\dot{M}_f$ and $\dot{m}_f$ are the rate of injection and rate of momentum of the injected fuel, and ρ_f is the fuel density.

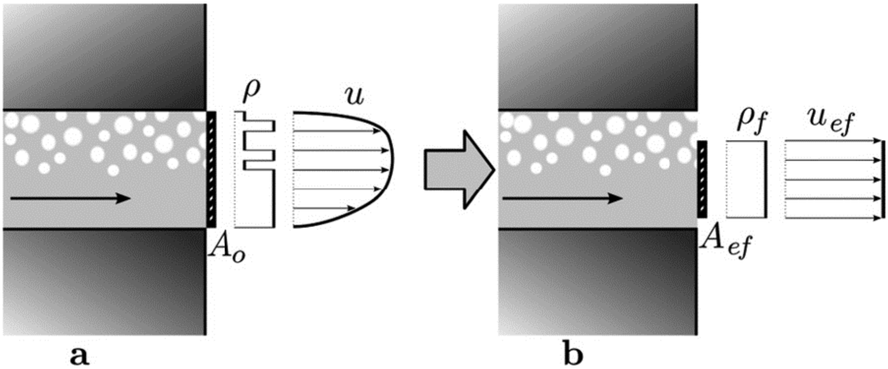

Figure 3.10: Representation of realistic flow at the exit of a nozzle and the simplified description of the fluid through the effective area and effective velocity coefficients.

Fig 3.10 shows the velocity profile of a cavitating flow on the left-hand side and how, by defining the two coefficients, the description can be simplified by conserving mass and momentum flux. Using Bernoulli's equation to the right-hand side flow, a theoretical outlet velocity can be calculated through equation (3.8)

$$u_{\text{th}} = \sqrt{\frac{2\Delta P}{\rho_f}}, \tag{3.8}$$

where ΔP is the pressure difference between inlet and outlet of the nozzle. The discharge coefficient can be now expressed as the mass flow rate divided by the theoretical mass flow rate (3.9).

$$C_d = \frac{\dot{m}}{A_0 \rho_f u_{\text{th}}}. \tag{3.9}$$

The momentum coefficient (3.10) was defined by Payri et al. [16] as the measured momentum at the exit of the injection nozzles divided by the momentum calculated using the theoretical velocity (3.8), or "theoretical momentum." Two additional coefficients were also introduced in their work in order to discriminate the losses: the area coefficient (3.11), which contains the reduction in the effective area, and the velocity coefficient (3.12), containing the reduction of the effective velocity. The discharge coefficient of a nozzle can be then explained combining the two coefficients through (3.13).

$$C_M = \frac{\dot{M}_f}{A_0 \rho_f u_{\text{th}}^2} = \frac{\dot{M}_f}{2 A_0 \Delta P}, \tag{3.10}$$

$$C_a = \frac{A_{\text{eff}}}{A_0} = \frac{D_{\text{eff}}^2}{D_0^2} \tag{3.11}$$

$$C_v = \frac{u_{\text{eff}}}{u_{\text{th}}} \tag{3.12}$$

$$C_d = C_a \, C_v \tag{3.13}$$

3.4.2 Set-up and measurement methodology

The test rig used to perform the rate of momentum measurements was designed and thoroughly described by Gimeno [17]. The vessel features a constant volume chamber and a small optical access, and can be pressurized up to 10 MPa to simulate in-engine pressure conditions. The test rig was originally designed to test Diesel injectors, so several modifications and coupling parts were designed to adapt the geometry of the test rig to the requirements of the GDi injector. A render of the test rig can be seen in Fig 3.11. The image shows the rig and the sensor in yellow through the optical access. The vessel was designed to measure the spray momentum by measuring the force of impact of the full spray with a calibrated piezoelectric sensor.

Figure 3.11: Render of the rate of momentum test rig showing the piezoelectric sensor through the optical access.

The principle of measurement of spray momentum consists of measuring the instantaneous force of impact of the spray against a sensor. Fig 3.12 graphically illustrates this point. As it was proven by Gimeno [17] and Desantes et al. [18], the different hypothesis made when measuring a typical spray coming out of a Diesel injector was equivalent to the force being measured by the sensor. Neglecting gravity effects, and assuming uniform pressure inside the test volume, the main hypothesis is that the direction of air entrainment and the direction of the fuel after impacting the sensor are perpendicular. This implies that the momentum flux by the interaction of the spray with the surrounding atmosphere and the viscous stress in the axial direction are both zero.

Gimeno [17] established that, under the assumption of these hypotheses and stationary state, the force measured by the sensor is equal to the spray momentum. It was also established that those hypotheses were met in the tests carried out with typical Diesel injectors. When experimenting a single-hole Diesel injector, a "frontal configuration" would

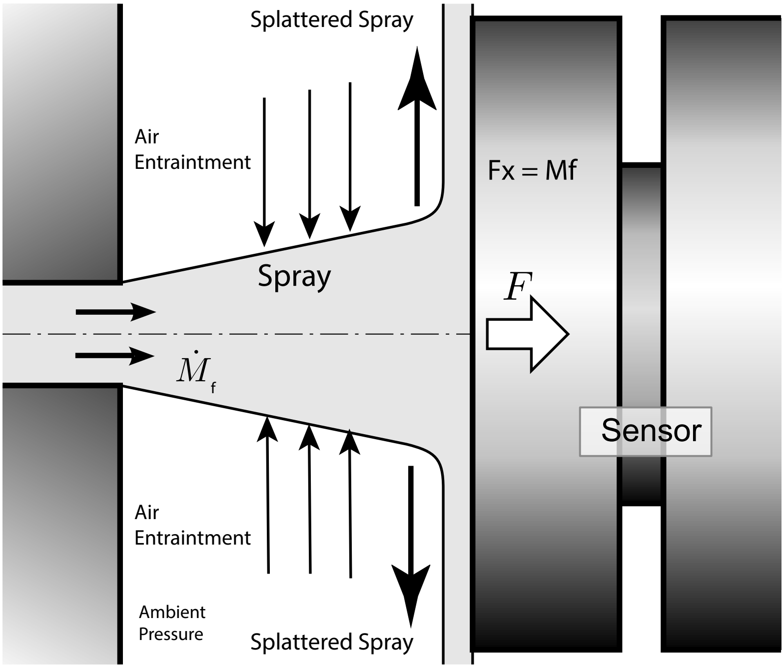

Figure 3.12: Schematic of a spray impacting the sensor for the rate of momentum measurements. Adapted from [17].

be used with the sensor aligned with the injector axis and vessel axis. If a multi-hole Diesel injector was examined, a “lateral configuration” would be mounted instead, with the sensor positioned at one side of the vessel and the injector at an angle with respect to the axis of the vessel, so that the axes of the holes of the injector were aligned with the sensor. Given the different geometry of the GDi injector used in this work and the very different spray pattern that it produces in normal operation, the measurement of rate of momentum for the gasoline injector is more complex and presents more uncertainties than in the Diesel case. The difficulties and uncertainties presented in the measurement were discussed by PAYRI et al. [9]. As stated in the introductory section of the chapter 3.1, the GDi injector spray presents an included angle of approximately 80°, which produces a much narrower spray than a conventional Diesel injector to promote plume interaction and flame propagation [19, 20]. It is precisely for this reason why the lateral configuration used for multi-hole Diesel injectors is not ideal here, due to the plume interaction occurring, the sensor needs to be farther away from the injector, so as not to capture the force of two plumes at the same time. To show the details of the lateral configuration assembly used, Fig 3.13 is shown.

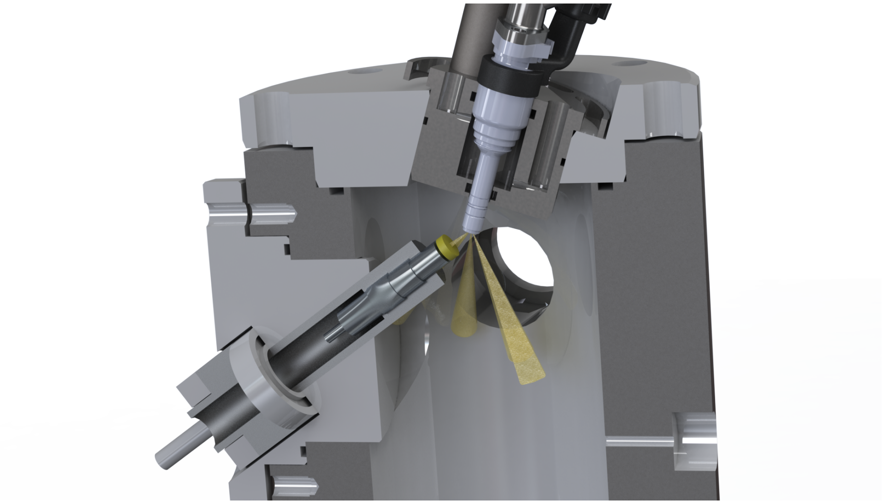

Figure 3.13: Render of the rate of momentum rig with the sensor, GDi injector, and injector holder in the lateral configuration

Because of the necessity of having to put the sensor far away from the nozzle tip, there is no security that the spray is completely collected in the sensor. Also, when the distance is sufficiently high, the aerodynamic effects may take a role in slowing the spray and therefore artificially diminishing the momentum measurement. Given these considerations, the frontal configuration typically used for single-hole nozzles was also tested in the current work. The frontal configuration was mounted to capture the eight sprays produced by the injector at the same time, with the advantage that the sensor can be located close to the tip of the nozzle and all droplets of the spray are sure to impact the sensor. A similar image as the one shown for the lateral configuration can be seen for the frontal configuration in Fig 3.14. While solving some problems, the frontal configuration creates other uncertainties because the sprays no longer impact the sensor at a 90° angle. Moreover, the air entrainment for the combined plumes in the GDi injector is much more complex than the simplified air entrainment depicted in Fig 3.12, and it is likely causing an effect on the measurement.

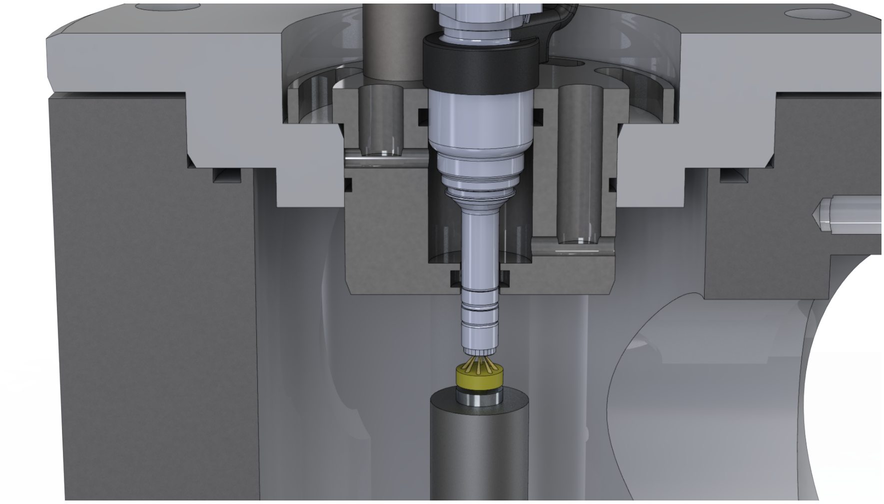

Figure 3.14: Render of the rate of momentum rig with the sensor, GDi injector, and injector holder in the frontal configuration.

In order to correct the measurement of the frontal configuration, the angle of impact of the spray against the sensor had to be known. For this reason, and to check that all sprays were impacting the sensor at the selected distances, a high-speed camera (Photron SA-X2) with a microscopic long-distance objective was mounted in front of the optical access of the rig. Fig 3.15 shows six frames captured by the high-speed camera of the injection event for one of the conditions tested. It can be appreciated how all the sprays are impacting the sensor. For this visualization, the injector was positioned so that the axis of the right-most spray was perpendicular to the camera. Then, the angle of impact could be graphically determined. Given the small difference between the measured angle and the nominal drill angle of the holes (40° versus 37°), and the fact that such methodology is not robust enough, the drill angle of the injector was used to scale the force measured by the sensor (axial component) to the momentum of the spray.

Similarly to the rate of injection methodology, 50 injections are done and recorded for each condition tested. The pressure signal from the rail and the driving signal from the ECU are also recorded by a digital oscilloscope. The results presented for both ROI and ROM measurements are always averages of 50 repetitions.

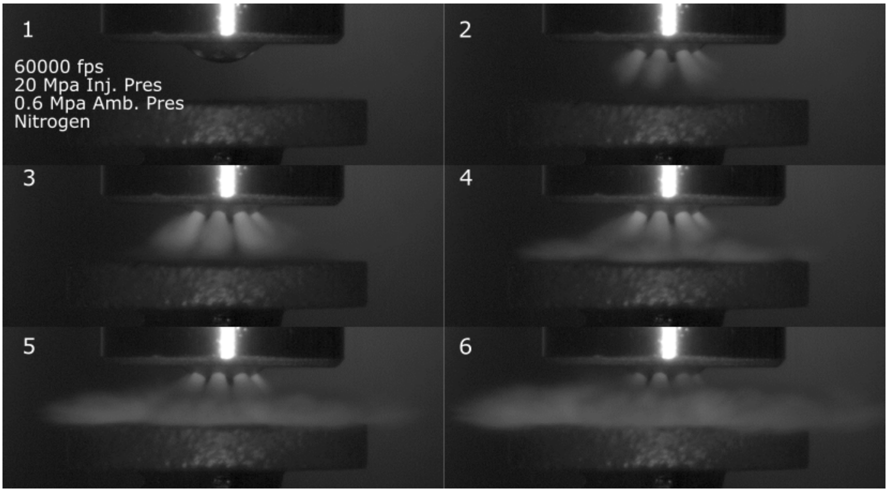

Figure 3.15: Six frames from the moment of injection recorded with a high speed camera through the optical access of the rate of momentum test rig.

3.5 X-ray measurements

3.5.1 Background

The internal flow of an injector is a critical factor that affects all parameters of the injection process from rate of injection and rate of momentum to external spray development, atomization, and mixing. Because of this, the internal geometry, needle lift, cavitation, and near-nozzle flow-field are of critical importance [4, 19, 21–25]. On the other hand, x-rays have been proven to be one of the best tools to determine these critical measurements because of their ability to reflect very small changes accurately [26–28]. X-rays can penetrate through metal which allows visualizing the inside of a nozzle. Moreover, by using monochromatic x-rays beams and calibrating the absorption coefficients of fuel and air, it is possible to determine the mass of fuel in certain regions of interest.

Several measurements using x-rays are included in this thesis. All the x-rays measurements presented here were made during a research visit to Argonne National Laboratory (ANL) wherein the primary purpose was to investigate several aspects of the internal geometry and near-nozzle flow of the Delphi GDi injector featured in this thesis. Also, given that several sets of injectors were made available by the different institutions comprising the ECN, many of the experimental techniques in this section are applied to several injectors, which allowed for the study the differences between each other and how those differences can affect the near-nozzle flow-field.

In particular, the measurements were carried out in the Advanced Photon Source (APS) at ANL, see Fig 3.16. The APS is a synchrotron-radiation light source funded by the Department of Energy of the United States of America and managed by UChicago Argonne LLC. The APS works by generating electrons that are accelerated to relativistic speeds (99.999+% of speed of light) and 450 MeV of energy in a linear accelerator and then to 7 GeV by electromagnets. Upon reaching this high-energy state, the electrons are injected into the storage ring, a 1104-meter circumference ring with more than 1000 electromagnets [29]. The Experiment Hall of the APS surrounds the storage rings and encloses 35 sectors, each with access to x-ray beamlines. The x-ray measurements detailed in the following subsections were executed at sectors 7-BM (Bending Magnet) and 32-ID (Insertion Device) of APS.

Figure 3.16: Aerial photograph of the Advanced Photon Source, from [29].

3.5.2 X-ray imaging. Needle displacement

The x-ray measurements of needle displacement were performed at the 32-ID beamline of the APS at Argonne National Laboratory [30] following a similar procedure as the one detailed by Viera et al. [31]. In this case, the GDi injectors were fed by a fuel delivery system formed by a pressurized cylindrical deposit. The pressure of the cylinder was controlled by controlling the pressure of an adjacent Nitrogen chamber that could transfer the force with a piston. The injection pressure was measured and controlled at the common rail in a similar way as the one explained in section 3.2.1. The fuel was injected into a vessel pressurized with N_2 and equipped with Kapton windows (which have very low absorption of x-rays). The experiments were carried out at room temperature as the experimental set-up was not designed to control for temperature. However, as it is discussed in the results section and was discussed in a previous publication [5], rate of injection for the GDi injector is very insensitive to the temperature of the discharge fluid. Given the direct relation between needle movement and rate of injection, it is unlikely that this affected the results in a significant manner.

The experimental set-up is represented in Fig 3.17. The undulator present at sector 32-ID creates a wave-like path for the electron to travel, which produces broadband, high-energy x-rays. The x-rays used in this experiment are the full spectrum radiation (white-beam mode), as they need to penetrate through a fair amount of metal with good temporal resolution. This entails the use of mechanical slits and a shutter to reduce the heat load on the injector and windows. The nozzle used in these experiments was the ECN Spray G AV67-029.

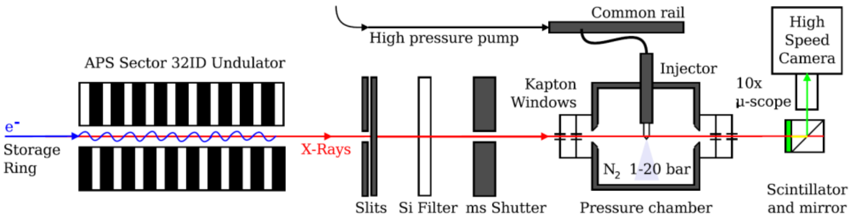

Figure 3.17: Diagram of the set-up used for needle lift measurements, from [31].

Upon reaching the nozzle, a certain amount of energy is absorbed in the metal. Once they pass, the x-rays possess an energy level that is proportional to the amount of metal they went through. Downstream from the nozzle, a scintillator converts the x-ray radiation to visible light. The scintillator reflects the light using a mirror at a 45° angle to a high-speed camera (Photron SA-Z). The camera was suited with a 10x long distance microscopic objective. The signal-to-noise ratio of the images is not high at this point because of the high-speed requirement of the measurement. To increase the signal-to-noise ratio, more than 90 injections were made and averaged for each of the conditions tested. Camera speed was 87500 fps and exposure time was approximately 10 µs.

Given that the ECU can supply three different energizing signals, apart from the main study of needle lift with the standard signal, the three signals were used to drive the injector and see if any differences in the needle lift were caused by different voltages. Fig 3.18 shows two images from the Spray G needle lift experiments. The top image shows the needle before the injection, resting on the needle seat. The image at the bottom (b) shows the needle fully opened.

The horizontal displacement of the needle was also investigated in this campaign, as it can be important to explain variability seen in the rate of injection and rate of momentum results [5]. In order to have the displacement in the two axes, the phase contrast measurements were performed at two different angles using a rotatory stage.

As it was stated before, 90 repetitions were made for each of the conditions. The images from all the repetitions were then averaged to increase the signal-to-noise ratio, and a specifically developed MATLAB routine was run to process the images and extract the needle movement. The routine prompts the user to select a region of interest. Once selected, the routine looks for this template in the following images (each representing a different time) using two-dimensional normalized cross-correlation [32, 33]. The cross-correlation routine executes a matrix multiplication of each of the pixels of the template by the original image in all possible positions of the (smaller) template. Because the algorithm is normalized, the multiplication returns the maximum result when all pixels are equal to each other. This procedure is repeated with three different regions of interest to minimize random errors and to have a quantifiable deviation. As a double-check to the methodology, the routine substitutes

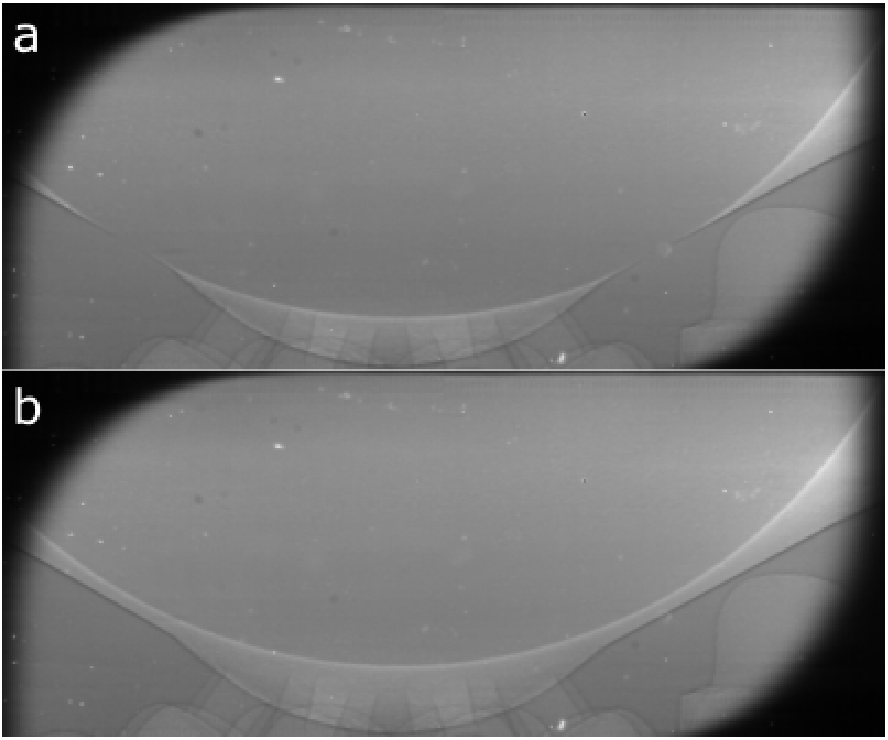

Figure 3.18: Two images from the Spray G needle lift experiments, a) with needle complete closed and b) with needle fully opened.

the selected template from the first image in the position where the best match was found in each of the following images so that it is visually easy to notice if there is displacement or the routine does not work properly. Fig 3.19 shows the template selected in the first image and where that template was found at a later time (when needle is fully opened). Given that the substitution is not apparent, the methodology found the proper zone of the image; otherwise, the two parts would not match.

Pixel resolution was approximately 3.9 µm\pixel and was measured with a gold Xradia resolution pattern [34].

3.5.3 Internal nozzle geometry. X-ray tomography

The experimental methodology to determine the internal geometry of the GDi injectors was similar to the needle lift methodology. In this

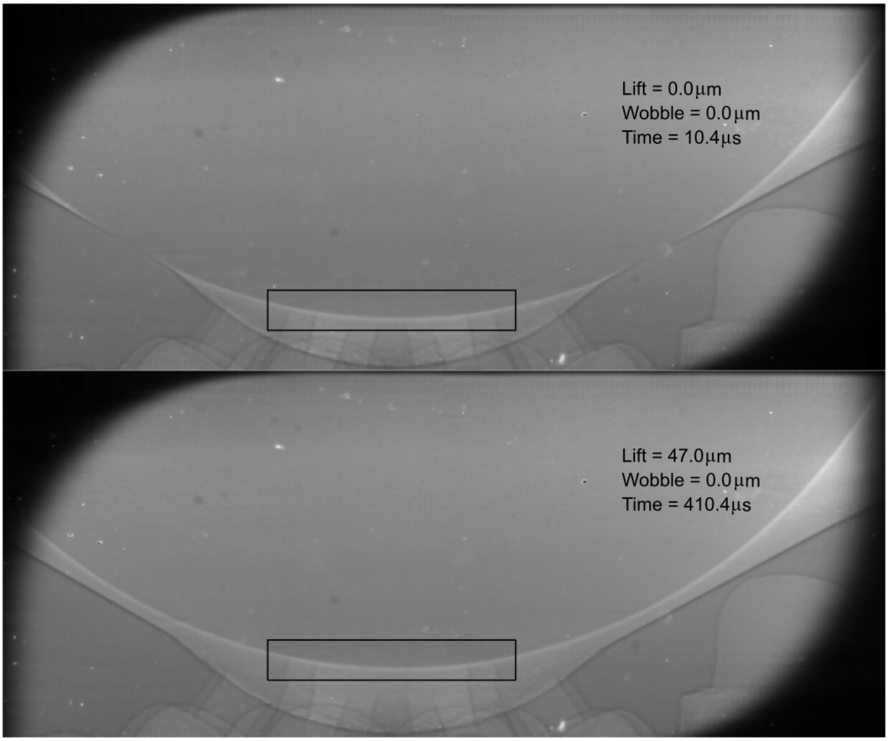

Figure 3.19: Cross-correlation algorithm demonstration. The section inside the black rectangle (template) in the top image is searched for in the following images. The bottom part shows an image captured at later time where the black rectangle zone is pasted from the first image.

case, temporal resolution was not required, and the experiments were executed using the white-beam mode at sector 7-BM [35]. Fig 3.20 shows the experimental set-up used. The polychromatic (white) beam goes through some previous filtering to remove unwanted radiation and then encounters a rotating gate that acts as a beam shutter to limit the heat load on the nozzles. In the same manner as in the needle lift experiments, when the x-rays penetrate the nozzles, the amount of energy they have is proportional to the amount of metal they went through. The x-rays are then converted to visible light by a scintillator and reflected to a CMOS camera (global shutter) fitted with a 5x microscopic objective.

Eight ECN Spray G nozzles were imaged with a pixel resolution of 1.17 μm per pixel, taking five images per rotational angle of the nozzle

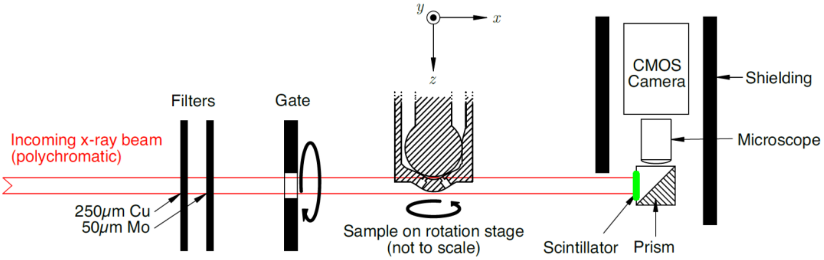

Figure 3.20: Diagram representing the experimental set-up used to measure the internal geometries of Spray G nozzles, from [36].

with a total of 1800 angles (every 0.1° from 0° to 180°). The five images per angle are taken to eliminate high-intensity pixels or "zingers", caused by the ionizing radiation in the CCD sensor, which occur in random locations. The zingers are removed by substituting the saturated pixels with the same (non-saturated) pixels of the other images. Once the zingers are removed, the 5 images are averaged, increasing the signal-to-noise ratio. Fig 3.21 shows one of the captured images after averaging.

Figure 3.21: One of the 1800 images taken for tomographic reconstruction for one of the Spray G injectors (AV67-018).

Once the images are recorded, the complete set is prepared and reconstructed using an open-source python module developed at ANL known as Tomopy [37]. Fig 3.22 shows a slice at the longitudinal plane through two of the holes of the reconstructed geometry on the left-hand side, and a slice of the transverse plane on the right-hand side. The slices have been treated by increasing the contrast and removing some background noise, and are presented to give an example of the state of the data after tomographic reconstruction.

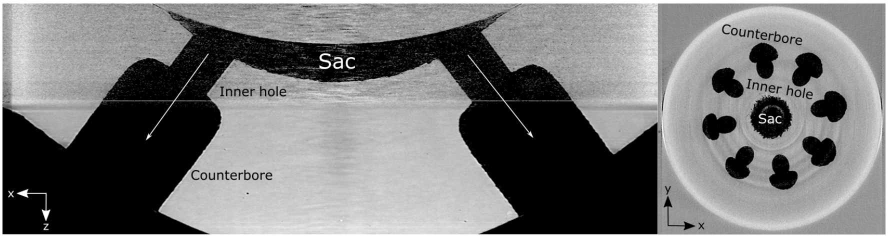

Figure 3.22: Slice at the longitudinal plane (left) and transverse plane (right) of the reconstructed geometry.

Once the geometry is reconstructed, each of the holes is treated separately. The images are cropped eight times, with each time leaving only the part where one of the holes is. Once cropped, the stack is rotated using the nominal drill angles of the holes. Fig 3.23 shows two slices of one of the holes after cropping and rotation. The left-hand side shows the cut in the longitudinal plane of the hole whereas the right-hand side shows a transverse cut.

Using the slices, an algorithm is run to select a threshold based on the intensity levels and binarize the image. Once binarized, elliptical profiles are fitted to the hole to extract the diameter and center. The information of the centers is used to make correction to the rotation made using the drill angle, and the two diameters from the ellipse fitting are averaged. After this procedure, the profile of every hole in the injector is known for any of the locations. Fig 3.24 shows the extracted profile of all orifices of injector Spray G 12# as an example of the procedure.

The key dimensions extracted from the geometry analysis are:

1. Hole inlet diameter
2. Hole outlet diameter

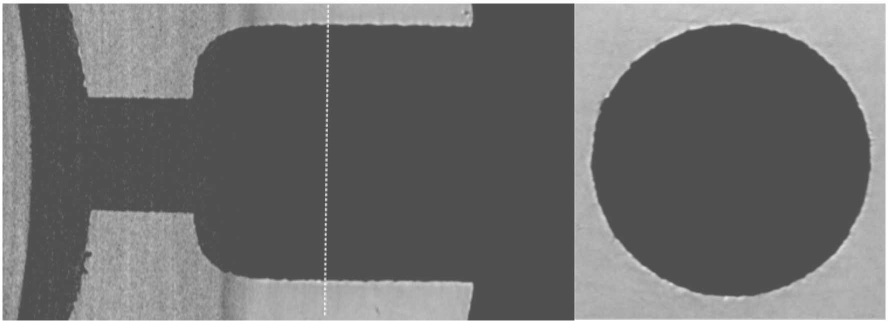

Figure 3.23: Slice of hole in its longitudinal plane (left) and on its transverse plane (right). Dashed white line represents the position of the transverse slice.

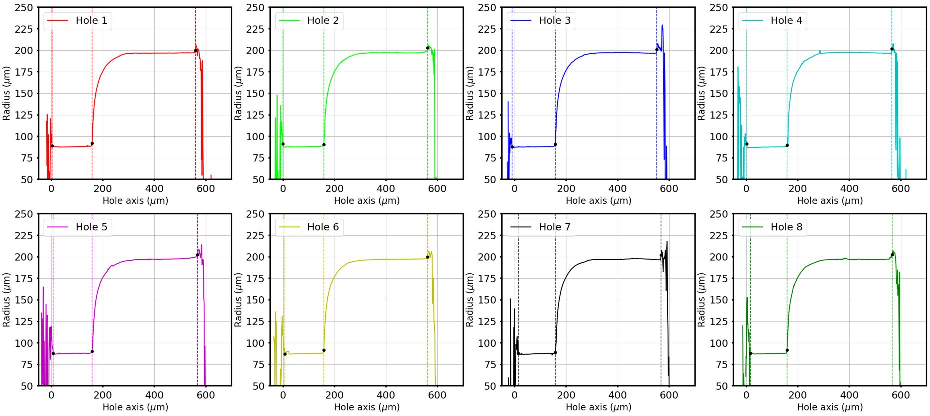

Figure 3.24: Extracted profiles of all the orifices for one of the injectors tested.

3. Hole inlet radius
4. Hole outlet radius
5. Hole length
6. Drill angle
7. Counterbore inlet diameter
8. Counterbore outlet diameter
9. Counterbore fillet
10. Counterbore exit radius

11. Counterbore depth

Fig 3.25 graphically shows the dimensions listed above.

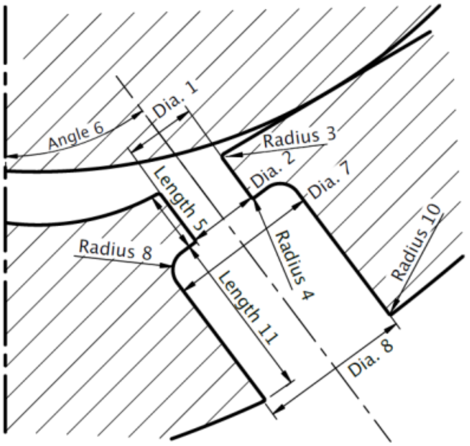

Figure 3.25: Key dimensions investigated for the Spray G nozzles geometry.

3.5.4 Near-field x-ray radiography

To measure the density distribution of the near nozzle zone of the spray (0.1 mm - 10 mm), time-resolved x-ray radiography was employed on two of the ECN Spray G injectors (AV67-012 and AV67-028). These measurements were performed at sector 7-BM of the APS [35]. The principles of the measurements are discussed in several publications [38–40] and are also briefly explained in [36]. For these measurements, a monochromatic x-ray beam of average energy of 8 keV is focused to a 5 µm by 6 µm point using several highly accurate focusing mirrors. Fig 3.26 presents a simplified diagram of the experimental set-up. After focusing, the beam goes through filtering and passes through the spray where some of its energy is absorbed. A fast diode downstream of the injector receives the transmission of the beam. The line-of-sight, time-resolved mass of the spray can thus be calculated by knowing the transmission of the beam without spray and the attenuation coefficient of the fuel using the Lambert-Beer law (3.14).

$$M_l(x, y, \theta, t) = -\frac{1}{\mu_f} \log \left[\frac{I(x, y, \theta, t)}{I_0(x, y, \theta, t)} \right] = \int \rho_{\mathrm{fuel}\,dz}, \tag{3.14}$$

where M_l is the mass in the line of sight of the beam, μ is the fuel attenuation coefficient, I_0 and I are the transmission signal of the beam before and after passing the test zone respectively.

For each of the injector positions and each injection event, a transmission signal resolved in time with the information of the evolution of mass in the particular spot is recorded. Several injections are recorded and averaged for each of the positions, and a complete "map" is measured by moving the injector in small steps along the y-z plane. The grid spanned from 0.1 mm to 10 mm in the axial direction (z) and was varied in the perpendicular direction (y) depending on the thickness of the spray at that z position. There were several hundred radial positions for each axial position and there were around 300 shots per grid point, which resulted in several million time-resolved measurements per mapping.

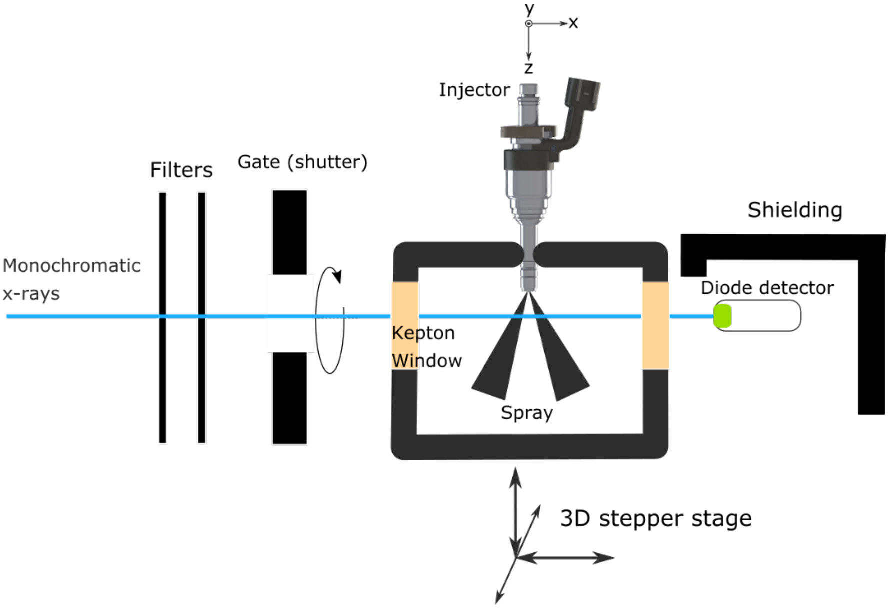

Figure 3.26: Diagram of the experimental set-up used in 7-BM beamline for the x-ray radiography measurements.

The maps were measured at the primary orientation of the injector (see 3.2.1), with the electrical connector pointing to the detector. Fig

3.27 presents two instants of the processed density map for one the Spray G injectors (AV67-012).

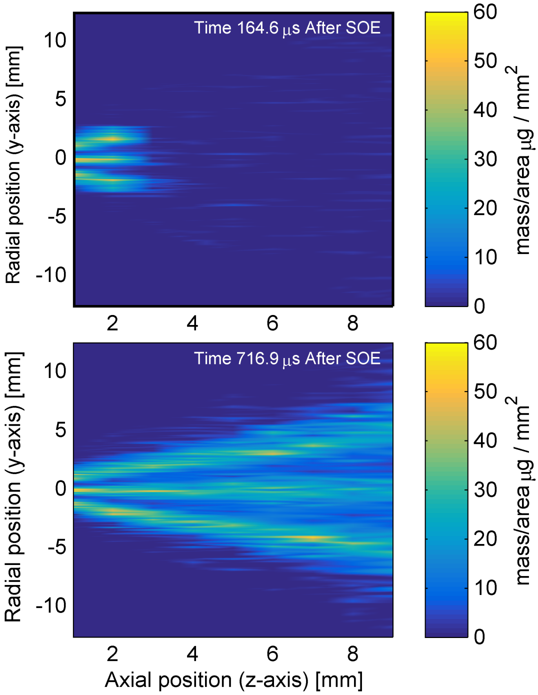

Figure 3.27: X-ray radiography maps at two time instants showing the mass per unit area for the AV67-012 ECN injector.

Given the particular characteristics of the x-ray measurements, the boundary conditions of the measurements were not the standard Spray G conditions discussed in section 3.3. The safety standards inside the beamlines are extremely high due to the radiation from x-rays, and because a security issue of one hutch could affect the entire storage ring. Therefore, the use of a controllable temperature chamber was not possible at the moment. Moreover, the fuel needs to have a high x-rays absorption coefficient to be able to measure differences with air. For this reason, the fuel used was a gasoline surrogate with a contrast agent, with a much higher absorption coefficient than iso-octane. Table 3.4 details the differences between the boundary conditions for the x-rays experiments at Argonne and the nominal Spray G condition.

Table 3.4: Differences between the boundary conditions for x-rays measurements and nominal Spray G.

Variable	Spray G nominal	Argonne condition
Fuel	iso-octane	gasoline calibration fluid with contrast agent
-Temperature [K]	363	298
-Injector Body Temp [K]	363	298
-Injection Pres [Mpa]	20	19
-Density [kg/m^3]	659	838
-Viscosity [cSt]	0.3	1.15
-Vapor Pressure [kPa]	75	0.6
Ambient Gas	N_2	N_2
-Temperature [K]	573	298
-Pressure [bar]	5.97	3.15
-Density [kg/m^3]	3.5	3.6

3.5.5 Near-nozzle x-ray tomographic radiography

The plume-to-plume variation was also studied by measuring the fuel mass distribution in a plane perpendicular to the injector axis. The "slice" of the spray was at 2 mm from the nozzle tip. The close distance was chosen to preserve as much information from the internal flow as possible and try to link the differences observed between injectors to differences in the nozzle geometries. Thus, the experiments were realized for the same set of injectors as the nozzle tomography experiments. The measurements were also executed at 7BM beamline of APS at Argonne, and the particular experimental set-up was very similar to the one used for the radiography experiments, as can be seen in the simplified diagram of the set-up in Fig 3.28. In this case, a radial swipe is done at 2 mm axial distance from the tip. Once a swipe is finished, the injector is rotated using a rotatory stage and a swipe at different radial positions is performed again. The injector is rotated a total of 180° angle in steps of 1° for the completion of one "slice". As the measurements were done for eight different Spray G injectors, only one axial distance (2 mm from nozzle tip) was measured.

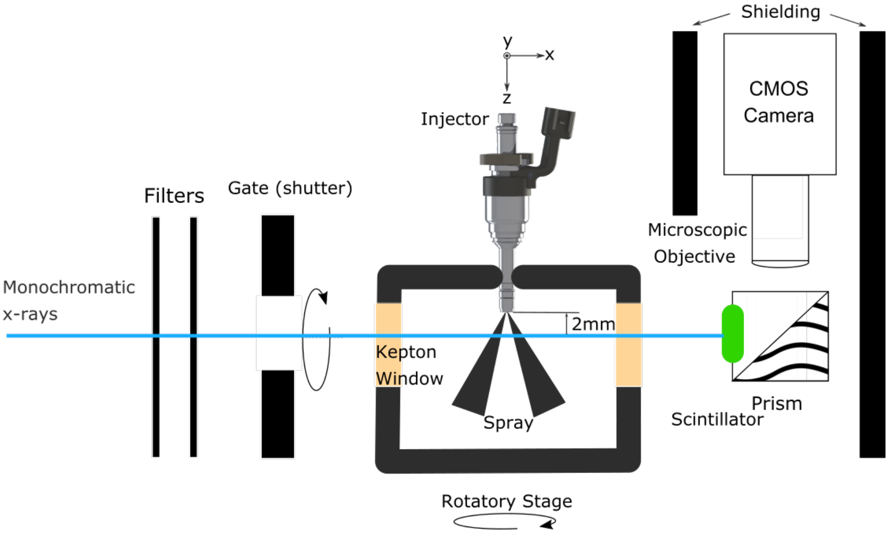

Figure 3.28: Simplified representation of the experimental set-up for the spray tomography measurements.

Following the same procedure that was detailed by DUKE et al. [38] and DUKE et al. [36], the time-resolved tomographic reconstruction of the data was performed applying a penalized maximum likelihood (PML) algorithm [37].

3.6 External Spray Visualization

3.6.1 Introduction

The hardware used in these measurements was the Spray G injector serial #26. Only the primary orientation of the injector was visualized (with electrical connector looking to the side). The experimental campaigns were done in a High-Pressure and High-Temperature test rig. The vessel consists of a Constant Pressure Flow Rig (CPFR) described in numerous works [41–43]. The temperature is monitored with two 0.5 mm thermocouples inside the vessel positioned close to the injector (but not so close that the fuel could impact on them). The temperature is controlled by a PID that regulates the power output to two resistors inside the vessel. Measurements are performed only when the temperature reaches stabilization. In the optical configuration, two high-speed cameras were used at the same time; one recording the images corresponding to Schlieren (or Shadowgraph), and the other recording the images coming from the DBI technique.

As stated above, the optical techniques used were DBI and Single-Pass Schlieren Shadowgraph. The set-up involved using two Photron SA5 high-speed cameras. The field of view of both DBI and Schlieren is a lateral view of the injector (primary orientation). The complete set-up from a top view is presented in Fig 3.29. The image contains all of the optical equipment represented realistically and a horizontal cut-off of the High-Pressure and High-Temperature vessel to provide a direct view of the injector, the sprays, and the windows.

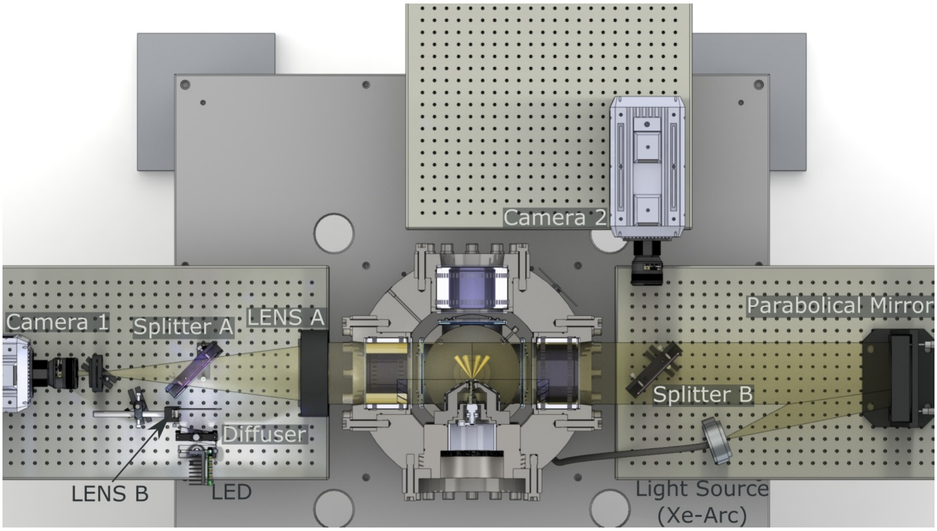

Figure 3.29: Schematic representation of the optical arrangement.

The frame rate and viewing window size (resolution) for the two cameras were not kept constant throughout the experiments in order to optimize the acquisition speed to the size needed for the different conditions. This practice allowed for record the high ambient density and temperature conditions, where the required field of view is reduced, at a higher speed. Table 3.5 contains a summary of the different settings used in the experimental campaign. It is important to remark that the frame rate of the two cameras was always the same for a given condition in order to record the images for the two techniques at the same instants.

Table 3.5: Summary of settings for the two cameras.

Technique	Camera	Frame Rate [kfps]	Resolution [pix/mm]	Illumination
Schlieren	Photron SA5	31 - 37.5	5.78	Xe-arc
DBI			7.05	White LED

The particular details for each subsystem are explained in the following subsections.

3.6.2 Single-Pass Schlieren technique

Single-Pass Schlieren is a widely used technique to characterize vapor penetration of single-hole injectors as it provides a lateral view of the vapor penetration [44]. Given the characteristics of a GDi injector, the included spray angle is very small (≈ 80°) compared to the Diesel case (≈ 150°), resulting in the spray moving forward (axially) more than sideways. For this reason, it makes sense to use the lateral view rather than the frontal view to characterize the morphology of the spray [45–47].

The optical path starts with the punctual light source at the bottom right of Fig 3.29, which was produced by a continuous Xe-Arc lamp connected to an optical fiber. The fiber was fitted to a holder with a 0.6 mm diameter hole. The light expands until it reaches the parabolic mirror, whose purpose it is to collimate the light and redirect it to the test zone. The collimated (parallel) beams of light are subject to be deviated from their original path by density gradients in the path traveled. The beams of light that encounter fuel from the sprays, either in liquid or vapor phase, will be deviated from their original path. Downstream of the vessel, the light passes through a 400 mm focal length lens (Lens A) that will focus the light back to a point. In the position where the point is formed (focal length of Lens A), the shadowgraph cutting device is mounted. In this case, a circular-pattern cutting device has been selected as it cuts the deviated light in a symmetrical manner. The cutting device, or diaphragm, is a critical part of the experiment, as it provides a direct control of the sensitivity of the technique. Right after the diaphragm, the high-speed camera records the image formed in the set-up. The image will be composed of black zones that represent the light that has been deviated by the spray and discarded in the cut-off device, and clearer zones representing the background of the images where the light has not been deviated (or sufficiently deviated) and collected in the camera.

3.6.3 Diffused Back Illumination

DBI has been used several times with satisfactory results [48, 49], and has also become the standard for Liquid Length measurements in the ECN [49].

In the arrangement, the pulse of light (60 ns) is emitted by a purposely designed ultra-fast white LED (bottom left of Fig 3.29). The light then passes through a plane diffuser and a lens (Lens B) to obtain a diffused light wide enough to cover the complete test area. The pulse then impacts a 50\50 (transparency\reflectivity) beam splitter (Splitter A), which redirects the light towards the injected fuel. When the pulses of light reach the spray, one out of three possibilities will occur: first, the light will encounter sprayed fuel in liquid phase in its path and therefore will be blocked; two, the light will encounter the vapor phase of sprays and be slightly deviated and attenuated; or third, the light will go through a zone where only the ambient gas is present, and it will be thus undisturbed. After the test zone and the window, the pulses of light are reflected by Splitter B to a high-speed camera (camera 2), where the images formed in the experiment are recorded. Those images will be a composition of black zones (blocked light from liquid phase of the sprays), white zones (undisturbed light), and gray zones (zones with vapor phase). Given that in the case of DBI, the pulses of light going through the test area are not parallel (light is diffused), no focusing is done to the light, and no cut-off device is mounted in front of the camera; the gray and white areas do not possess sufficient contrast to be distinguished by the processing algorithms. The images captured by the camera are then essentially images where the liquid phase of the spray appears dark and the background and vapor phase appear white or light gray.

3.6.4 Spray data processing methodology

Image Processing

The processing of the images is one of the most important parts of any visualization data analysis [50]. The processing of all the images has been done using an internally developed algorithm in which the general processing of the images is independent of the type of technique used to capture them. Nonetheless, given the difference in the experiments and therefore in the images obtained, a preprocessing algorithm is used before the general processing algorithm to adapt the different kind of images. The strategy used in the preprocessing of the images is as follows:

1. Background subtraction. The preprocessing code prepares the background of the image and subtracts it to generate images where the minimum luminosity of the scene is normalized to zero. In the DBI technique, where the changes in density of the ambient are not reflected in the captured images, the background is considered static. For the static case, a simple average of the first few images (before the injection event) is sufficient to prepare the background to subtract (8 images were used). In the case of Schlieren, where the density gradients are made visible, the movement of the ambient gas in the background of the image is noticeable, which creates the necessity of calculating a new (dynamic) background for every image. In the dynamic case, the background is calculated in two steps: first, everything from the previous image that was not detected as spray is taken and put in the same place in the current image; and second, the part of the previous image where the sprays were detected is taken and filled with the corresponding positions of the background generated with the average of the first eight images (the static background).
2. Threshold calculation. In order to detect the contour of the spray in the processing algorithm, it is necessary to create a binary (black and white) image, where the white part is the detected spray and the black part is the rest. A threshold has to be determined in order to create the binary image. The threshold is therefore a luminosity intensity value that represents the barrier of spray and background. There are many ways to calculate the threshold in order to perform binarization. Two methods have been used in this work depending

on the type of technique. For DBI, an approach using an optical thickness threshold has been used, as it is the standard within the ECN group. It consists on calculating the extinction of the images with respect to the background (log I/I_0) and considering the extinction bellow a certain value as liquid and the rest as background. For the Schlieren experiments, a fixed approach was selected [41, 51]. In the fixed approach, the intensity threshold is calculated as a constant percentage (3.5%) of the dynamic range of the image.

Once the preprocessing code finishes with the images, these are passed to the processing code for binarization and cleaning. The binarization is made simply by applying the threshold calculated in the previous step. Given that the original images are not perfectly homogeneous and some zones in the background can appear more illuminated, the resulting binary images and sectors do not perfectly represent the sprays and some cleaning is necessary. A binary image erosion is applied to the images in order to disconnect the white pixels areas that are connected by less than 2 pixels (connectivity). Once the erosion is performed, a minimum area filter is applied that eliminates any area that contains less than a set number of pixels. Finally, a binary image dilation is performed to restore the surface of the remaining white zones to their original size.

Fig 3.30 graphically shows the steps described previously. Top left presents the original image to be processed, top center shows the image with the background subtracted, top right is the result of the binarization with the calculated threshold. Once the binarization has been made, bottom left presents the image with the erosion filter applied whereas bottom center shows the image with the minimum area and dilation filters. Lastly, bottom right shows the original image with the detected contour overlapped.

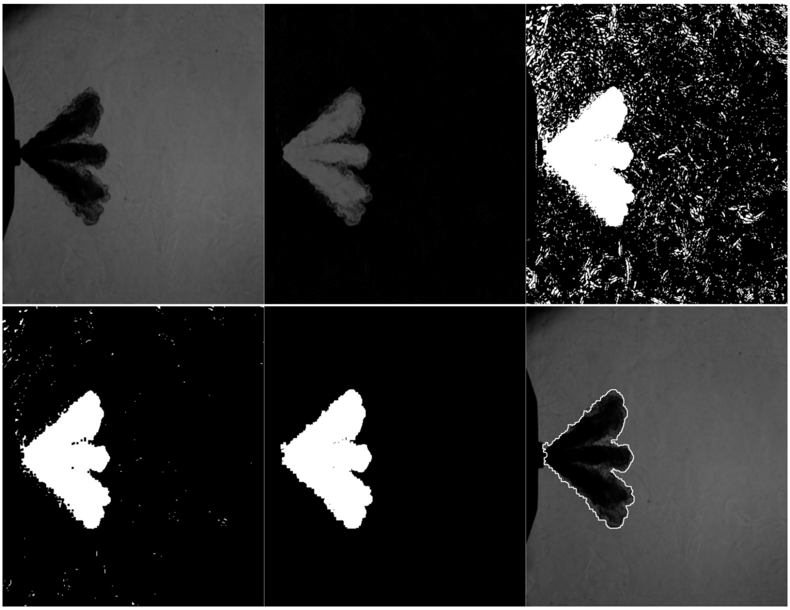

Figure 3.30: Example of the image processing for an Schlieren image. Top left, original image. Top center, original with subtracted background. Top right, raw binarization. Bottom left, erosion filter applied. Bottom center, minimum area and dilation filters applied. Bottom right, original image with detected contour overlapped.

Contour Processing

After the image processing algorithms detect the contour of the sprays, these contours pass to the post-processing codes to extract the results. The two main results that can be generally extracted from the performed experiments are penetration and spray angle.

The penetration is extracted by selecting the farthest point of the spray contour, taking only the axial distance to the nozzle.

The angle is a difficult measurement to determine given the complexity of extracting representative results due to the high dependence on the definition used. In the case of the liquid phase contours, the main source of uncertainty is that there are certain conditions where the shape of the spray is not completely conical (or triangular if it is observed from one side), and the lines composing the outer contour can be rounded. Fig 3.31 shows two different images from DBI experiments with the detected contour overlapped. The calculated angle is plotted with dashed lines and the injection conditions are given in the pictures. The angle has been calculated performing a least square fit with the lower and upper parts of contour. It can be noted the significant difference between the shape of the contours from the two images. On the left-hand side image, where temperature and density are lower, the outer shape of the contour can be approximated with a triangle. However, on the right-hand side case, the outer part of the contour is more rounded and irregular. This creates the necessity to set the final limit of the contour used for the fit not very far away, whereas the initial limit has to be put very close to the nozzle (in order to avoid parallel lines if the first part of the spray is disregarded). The limits that were used after consideration were from 1% to 50% of the axial spray penetration.

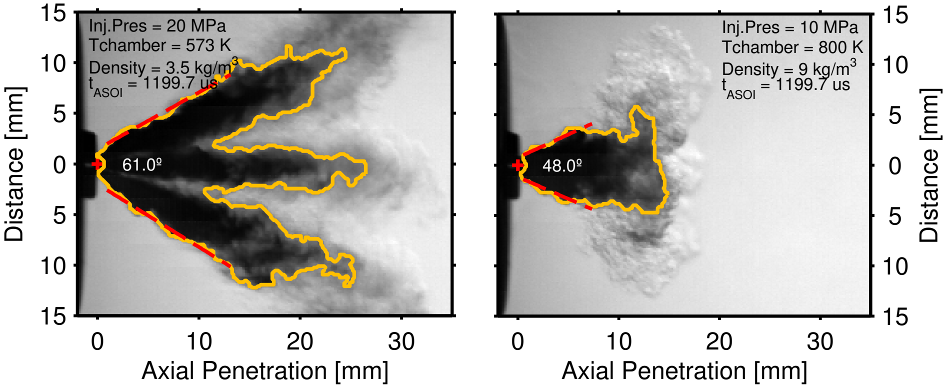

Figure 3.31: DBI Images at different temperature and density conditions with the detected contours overlapped to show the angle determination methodology.

Right-hand side image in Fig 3.31 shows the difficulty and uncertainty that may be encountered when calculating the angles using liquid phase captured via the DBI technique. For the vapor case, Fig 3.32 presents the same information extracted from Schlieren images. In this case, the low density condition at the left side of the figure shows how the same method applied in Fig 3.31 can also work for the Schlieren visualization. However, the right-hand side case with a higher value of density (but not as high as the right-hand side image of Fig 3.31) shows a different enough contour up to the point of not being able to apply an angle definition that can properly describe the phenomenon. This image presents a thin spray cone in the beginning close to the nozzle but then rapidly expands to an oval shaped contour, effectively rendering the calculated angle meaningless. Given that the angle does not describe the first zone or second zone, the computed value does not describe the shape of the contour and therefore it does not hold any relation with the phenomena taking place. This phenomenon that occurs at moderate densities and can also occur at lower densities (3.5 kg/m^3) at later times After Start of Injection (ASOI), has made incompatible all the definitions tried with the vapor phase of the spray and consequently caused that no vapor phase spray angles are shown in the current work. This is an example of how important more studies of GDi sprays are to properly and accurately describe the development of the fuel during and after the injection event.

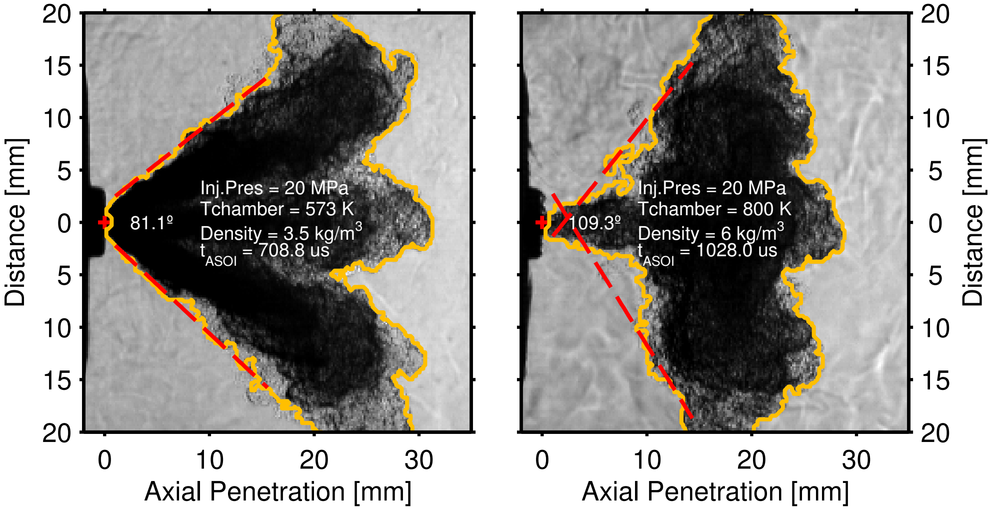

Figure 3.32: Schlieren Images at different temperature and density conditions with the detected contours overlapped to show the angle determination methodology for vapor phase.

Ten repetitions have been obtained for each of the conditions. The repetitions are processed individually by the image processing algorithms and the results obtained by the contour processing are averaged using a moving average strategy. The procedure can be summarized as follows:

1. The data within the interval $t_i \pm \Delta t/2$ is considered, where t_i is the instantaneous time, and Δt is the time window selected (9 μs for all experiments).
2. Using the data selected in the interval, a linear fit is performed and the averaged value $\hat{y}$ is evaluated by computing $f(t_i)$, where $f(t)$ is the equation obtained for the fit.
3. The algorithm is repeated by moving t_i with a certain step selected through the complete time of each dataset.

References

[1] Engine Combustion Network. *ECN Spray G.* 2016.

[2] Hung, David L.S., Harrington, David L., Gandhi, Anand H., Markle, Lee E., Parrish, Scott E., Shakal, Joseph S., Sayar, Hamid, Cummings, Steven D., and Kramer, Jason L. "Gasoline Fuel Injector Spray Measurement and Characterization - A New SAE J2715 Recommended Practice". *SAE Int. J. Fuels Lubr.* Vol. 1.1 (2009), pp. 534–548. doi: `10.4271/2008-01-1068`.

[3] Bardi, Michele. "Partial needle lift and injection rate shape effect on the formation and combustion of the Diesel spray". PhD thesis. Valencia (Spain): Universitat Politècnica de València, 2014. doi: `10.4995/Thesis/10251/37374`.

[4] Venegas, Oscar. "Estudio del fenómeno de la cavitación en la inyección diesel mediante la visualización del flujo interno en orificios transparentes." PhD thesis. Universidad Poltécnica de València-Departamento de Máquinas y Motores Térmicos, 2014.

[5] Payri, Raul, Gimeno, Jaime, Bracho, Gabriela, and Vaquerizo, Daniel. "Study of liquid and vapor phase behavior on Diesel sprays for heavy duty engine nozzles". *Applied Thermal Engineering*, vol. 107 (2016), pp. 365–378. doi: `10.1016/j.applthermaleng.2016.06.159`.

[6] Payri, Raul, Salvador, F.J. Francisco Javier, Gimeno, Jaime, and Bracho, Gabriela. "A new methodology for correcting the signal cumulative phenomenon on injection rate measurements". *Experimental Techniques*, vol. 32.February (2008), pp. 46–49. doi: `10.1111/j.1747-1567.2007.00188.x`.

[7] Zhao, Hua. *Advanced direct injection combustion engine technologies and development.* Ed. by Hua Zhao. Cambridge: Woodhead Publishing Limited, 2010.

[8] Payri, Raul, Gimeno, Jaime, Martí-Aldaraví, Pedro, and Vaquerizo, Daniel. "Internal flow characterization on an ECN GDi injector". *Atomization and Sprays*, vol. 26.9 (2015), pp. 889–919. doi: `10.1615/AtomizSpr.2015013930`.

[9] Payri, Raul, Gimeno, Jaime, Marti-Aldaravi, Pedro, and Vaquerizo, Daniel. "Momentum Flux Measurements on an ECN GDi Injector". *SAE Technical Paper 2015-01-1893* (2015). doi: `10.4271/2015-01-1893`.

[10] Payri, Raul, Gimeno, Jaime, Novella, Ricardo, and Bracho, Gabriela. "On the rate of injection modeling applied to direct injection compression ignition engines". *International Journal of Engine Research* (2016). doi: `10.1177/1468087416636281`.

[11] Plazas, Alejandro Hernan. "Modelado unidimensional de inyectores common-rail Diesel". PhD thesis. Valencia: E.T.S. Ingenieros Industriales. Universidad Politécnica de Valencia, 2005.

[12] Bosch, Wilhelm. "The Fuel Rate Indicator: a New Measuring Instrument for Display of the Characteristics of Individual Injection". *SAE Paper 660749* (1966).

[13] Payri, R, Gimeno, J, Viera, J P, and Plazas, A H. "Effect of Partial Needle Lift on the Hydraulic and Evaporative Performance Characteristics of a Common rail Diesel Fuel Injector". *THIESEL 2012 Conference on Thermo- and Fluid Dynamic Processes in Diesel Engines*. 2012, pp. 1–19.

[14] Linstrom, P. J., Mallard, W. G, and Eds., Gaithersburg. *Thermophysical Properties of Fluid Systems in NIST Chemistry WebBook*. 2011.

[15] Payri, Raul, Gimeno, Jaime, Venegas, Oscar, and Plazas, Alejandro Hernan. "Experimental and computational study of the influence of partial needle lift on nozzle flow in diesel fuel injectors". *Atomization and Sprays*, vol. 22 (2012), pp. 687–714. doi: `10.1615/AtomizSpr.2012005810`.

[16] Payri, R, García, J M, Salvador, F J, and Gimeno, J. "Using spray momentum flux measurements to understand the influence of diesel nozzle geometry on spray characteristics". *Fuel*, vol. 84.5 (2005), pp. 551–561.

[17] Gimeno, Jaime. "Desarrollo y aplicación de la medida del flujo de cantidad de movimiento de un chorro Diesel." PhD thesis. Universidad Politecnica de Valencia, 2008.

[18] DESANTES, JOSE MARIA, PAYRI, RAUL, SALVADOR, FRANCISCO JAVIER, and GIL, ANTONIO. "Development and validation of a theoretical model for diesel spray penetration". *Fuel*, vol. 85.7-8 (2006), pp. 910–917.

[19] MOON, SEOKSU, KOMADA, KEISUKE, SATO, KIYOTAKA, YOKOHATA, HIDEAKI, WADA, YOSHITAKA, and YASUDA, NOBUHIRO. "Ultrafast X-ray study of multi-hole GDI injector sprays: Effects of nozzle hole length and number on initial spray formation". *Experimental Thermal and Fluid Science*, vol. 68 (2015), pp. 68–81. DOI: `10.1016/j.expthermflusci.2015.03.027`.

[20] PAYRI, RAUL, SALVADOR, FRANCISCO JAVIER, MARTÍ-ALDARAVÍ, PEDRO, and VAQUERIZO, DANIEL. "ECN Spray G external spray visualization and spray collapse description through penetration and morphology analysis". *Applied Thermal Engineering*, vol. 112 (2017), pp. 304–316. DOI: `10.1016/j.applthermaleng.2016.10.023`.

[21] PAYRI, RAUL, VIERA, JUAN PABLO, GOPALAKRISHNAN, VENKATESH, and SZYMKOWICZ, PATRICK G. "The effect of nozzle geometry over internal flow and spray formation for three different fuels". *Fuel*, vol. 183 (2016), pp. 20–33. DOI: `10.1016/j.fuel.2016.06.041`.

[22] PAYRI, RAUL, VIERA, JUAN PABLO, GOPALAKRISHNAN, VENKATESH, and SZYMOWITZ, PATRICK. "The effect of nozzle geometry over ignition delay and flame lift-off of reacting direct-injection sprays for three different fuels". *Fuel* (2017).

[23] SHOST, MARK. "Evaluation Of Nozzle Geometry On High Pressure Gasoline Direct Injection Spray Atomization". PhD thesis. Wayne State University Dissertations, 2014.

[24] SAHA, KAUSHIK, SOM, SIBENDU, BATTISTONI, MICHELE, LI, YANHENG, POMRANING, ERIC, and SENECAL, PETER KELLY. "Numerical Investigation of Two-Phase Flow Evolution of In- and Near-Nozzle Regions of a Gasoline Direct Injection Engine During Needle Transients". *SAE International Journal of Engines*, vol. 9.2 (2016), pp. 2016–01–0870. DOI: `10.4271/2016-01-0870`.

[25] Strek, Piotr, Duke, Daniel, Swantek, Andrew, Kastengren, Alan, Powell, Christopher F., and Schmidt, David P. "X-Ray Radiography and CFD Studies of the Spray G Injector". *SAE Technical Paper 2016-01-0858*. 2016. doi: `10.4271/2016-01-0858`.

[26] Kostas, J., Honnery, D., Soria, J., Kastengren, A., Liu, Z., Powell, C. F., and Wang, J. "Effect of nozzle transients and compressibility on the penetration of fuel sprays". *Applied Physics Letters*, vol. 95.2 (2009). doi: `10.1063/1.3182821`.

[27] Swantek, Andrew, Kastengren, Alan, Duke, Daniel, Tilocco, Zak, Sovis, Nicolas, and Powell, Christopher F. "Quantification of Shot-to-Shot Variation in Single Hole Diesel Injectors". *SAE International Journal of Fuels and Lubricants*, vol. 8.1 (2015), pp. 2015–01–0936. doi: `10.4271/2015-01-0936`.

[28] Duke, Daniel, Swantek, Andrew, Kastengren, Alan, Fezzaa, Kamel, and Powell, Christopher. "Recent Developments in X-ray Diagnostics for Cavitation". *SAE Int. J. Fuels Lubr.* Vol. 8.1 (2015), pp. 135–146. doi: `10.4271/2015-01-0918`.

[29] ANL. *Advanced Photon Source Overview.*

[30] Shen, Qun, Lee, Wah-Keat, Fezzaa, Kamel, Chu, Yong S., De Carlo, Francesco, Jemian, Peter, Ilavsky, Jan, Erdmann, Mark, and Long, Gabrielle G. "Dedicated full-field X-ray imaging beamline at Advanced Photon Source". *Nuclear Instruments and Methods in Physics Research Section A: Accelerators, Spectrometers, Detectors and Associated Equipment*, vol. 582.1 (2007), pp. 77–79. doi: `10.1016/j.nima.2007.08.169`.

[31] Viera, Juan Pablo, Payri, Raul, Swantek, Andrew B, Duke, Daniel J., Sovis, Nicolas, Kastengren, Alan L., and Powell, Christopher F. "Linking instantaneous rate of injection to X-ray needle lift measurements for a direct-acting piezoelectric injector". *Energy Conversion and Management*, vol. 112 (2016), pp. 350–358. doi: `10.1016/j.enconman.2016.01.038`.

[32] Haralick, Robert M and Linda, G. Shapiro. *Computer and Robot Vision.* Vol. 2. 1992, pp. 316–317.

[33] LEWIS, J P. “Fast normalized cross-correlation”. *Vision interface.* Vol. 10. 1. 1995, pp. 120–123.

[34] ANL. *APS Xradia Resolution Pattern.*

[35] KASTENGREN, ALAN, POWELL, CHRISTOPHER F, ARMS, DOHN, DUFRESNE, ERIC M, GIBSON, HAROLD, and WANG, JIN. “The 7BM beamline at the APS: a facility for time-resolved fluid dynamics measurements”. *Journal of Synchrotron Radiation*, vol. 19.4 (2012), pp. 654–657. DOI: `10.1107/S0909049512016883`.

[36] DUKE, DANIEL J et al. “Internal and near nozzle measurements of Engine Combustion Network “Spray G” gasoline direct injectors”. *Experimental Thermal and Fluid Science*, vol. 88 (2017), pp. 608–621. DOI: `10.1016/j.expthermflusci.2017.07.015`.

[37] GÜRSOY, DOGA, DE CARLO, FRANCESCO, XIAO, XIANGHUI, and JACOBSEN, CHRIS. “TomoPy: a framework for the analysis of synchrotron tomographic data”. *Journal of synchrotron radiation*, vol. 21.5 (2014), pp. 1188–1193.

[38] DUKE, DANIEL J, SWANTEK, ANDREW B, SOVIS, NICOLAS M, TILOCCO, F ZAK, POWELL, CHRISTOPHER F, KASTENGREN, ALAN L, GÜRSOY, DOĞA, and BIÇER, TEKIN. “Time-resolved X-ray Tomography of Gasoline Direct Injection Sprays”. *SAE Int. J. Engines*, vol. 9 (2015), pp. 143–153. DOI: `10.4271/2015-01-1873`.

[39] KASTENGREN, ALAN L, TILOCCO, F ZAK, DUKE, DANIEL J, POWELL, CHRISTOPHER F, ZHANG, XUSHENG, and MOON, SEOKSU. “Time-resolved X-ray radiography of sprays from engine combustion network spray a diesel injectors”. *Atomization and Sprays*, vol. 24.3 (2014).

[40] KASTENGREN, ALAN and POWELL, CHRISTOPHER F. “Synchrotron X-ray techniques for fluid dynamics”. *Experiments in Fluids*, vol. 55.3 (2014). DOI: `10.1007/s00348-014-1686-8`.

[41] PAYRI, RAUL, GIMENO, JAIME, VIERA, JUAN PABLO, and PLAZAS, ALEJANDRO HERNAN. “Needle lift profile influence on the vapor phase penetration for a prototype diesel direct acting piezoelectric injector”. *Fuel*, vol. 113 (2013), pp. 257–265. DOI: `10.1016/j.fuel.2013.05.057`.

[42] Bardi, Michele, Payri, Raul, Malbec, Louis-Marie, Bruneaux, Gilles, Pickett, Lyle M, Manin, Julien, Bazyn, Tim, and Genzale, Caroline L. “Engine Combustion Network: Comparison of Spray Development, Vaporization, and Combustion in Different Combustion Vessels”. *Atomization and Sprays*, vol. 22.10 (2012), pp. 807–842. doi: `10.1615/AtomizSpr.2013005837`.

[43] Payri, Raul, Viera, Juan Pablo, Pei, Yuanjiang, and Som, Sibendu. “Experimental and numerical study of lift-off length and ignition delay of a two-component diesel surrogate”. *Fuel*, vol. 158 (2015), pp. 957–967. doi: `10.1016/j.fuel.2014.11.072`.

[44] Benajes, Jesus, Payri, Raul, Bardi, Michele, and Martí-aldaraví, Pedro. “Experimental characterization of diesel ignition and lift-off length using a single-hole ECN injector”. *Applied Thermal Engineering*, vol. 58.1-2 (2013), pp. 554–563. doi: `10.1016/j.applthermaleng.2013.04.044`.

[45] Manin, Julien, Jung, Yongjin, Skeen, Scott A, Pickett, Lyle M, Parrish, Scott E, and Markle, Lee E. “Experimental Characterization of DI Gasoline Injection Processes”. *SAE Technical Paper 2015-01-1894* (2015). doi: `10.4271/2015-01-1894`.

[46] Blessinger, M, Manin, Julien, Skeen, Scott A, Meijer, M, Parrish, Scott E, and Pickett, Lyle M. “Quantitative mixing measurements and stochastic variability of a vaporizing gasoline direct-injection spray”. *International Journal of Engine Research*, vol. 16.2 (2015), pp. 238–252. doi: `Doi10.1177/1468087414531971`.

[47] Montanaro, A and Allocca, L. “Flash Boiling Evidences of a Multi-Hole GDI Spray under Engine Conditions by Mie-Scattering Measurements”. *SAE Technical Paper 2015-01-1945* (2015).

[48] Manin, Julien, Bardi, Michele, and Pickett, Lyle M. “Evaluation of the liquid length via diffused back-illumination imaging in vaporizing diesel sprays”. *Comodia*. Fukuoka, 2012.

[49] MEIJER, M, MALBEC, LOUIS-MARIE M, BRUNEAUX, GILLES, and SOMERS, L.M.T. M T. “Engine Combustion Network:‘Spray A’Basic Measurements and Advanced Diagnostics”. *ICLASS 2012, 12th Triennial International Conference on Liquid Atomization and Spray Systems.* 2012, pp. 2–6.

[50] MACIAN, VICENTE, PAYRI, RAUL, GARCIA, ANTONIO, and BARDI, MICHELE. “Experimental evaluation of the best approach for diesel spray images segmentation”. *Experimental Techniques*, vol. 36.6 (2012), pp. 26–34. DOI: `10.1111/j.1747-1567.2011.00730.x`.

[51] PAYRI, RAUL, GIMENO, JAIME, BARDI, MICHELE, and PLAZAS, ALEJANDRO. “Effect of Injection Rate Shaping Over Diesel Spray Development in Non Reacting Evaporative Conditions”. *ASME 2012 Internal Combustion Engine Division Spring Technical Conference.* Torino, Italy: ASME, 2012, p. 347. DOI: `10.1115/ICES2012-81206`.

Chapter 4

Internal and near-nozzle flow. Results and discussion

4.1 Introduction

This chapter presents the results of the geometry, internal, and near-nozzle flow of GDi injectors tested in the work. The results comprise the geometries of several Spray G nozzles, the hydraulic characterization of the injector through rate of injection, rate of momentum, needle lift, as well as, the near-nozzle flow obtained through spray radiography and tomography x-ray measurements. The chapter follows a lineal approach in the presentation of the measurements from the inner part (geometry) to the near-field external spray (spray radiography and tomography).

Most of the measurements done in the current work have been done extensively in Diesel research field, like ROI and ROM [1–7]. Even measurements of internal geometry and newer techniques such as near-field spray measurements have been done first to Diesel hardware mainly because the properties of Diesel sprays are critical for engine operation, and have been critical since the introduction of direct injection Diesel systems [8, 9]. Because of this, and because characteristics of Diesel sprays are often better understood than GDi sprays [4, 10, 11], many comparisons are made throughout the results sections between the GDi hardware featured in the current work and common Diesel injectors.

4.2 Spray G Nozzle Geometry

This section presents the internal geometry of several Spray G nozzles that were measured at Argonne National Lab following the methodology described in 3.5.3. Fig 4.1 shows the extracted quantities of all sets of injectors.

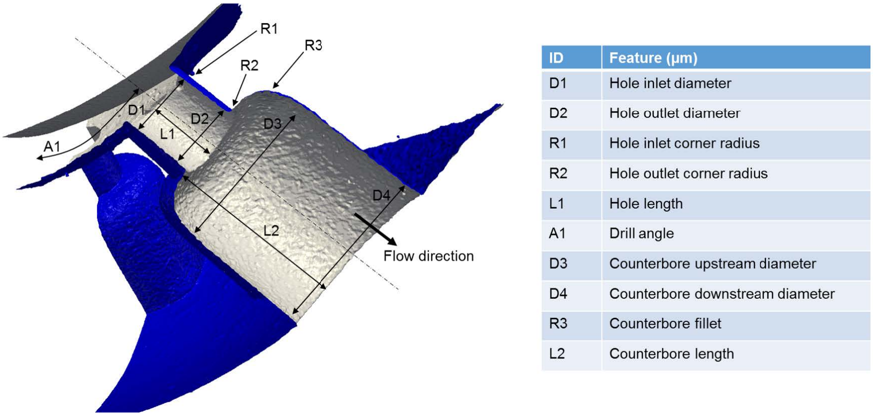

ID	Feature (μm)
D1	Hole inlet diameter
D2	Hole outlet diameter
R1	Hole inlet corner radius
R2	Hole outlet corner radius
L1	Hole length
A1	Drill angle
D3	Counterbore upstream diameter
D4	Counterbore downstream diameter
R3	Counterbore fillet
L2	Counterbore length

Figure 4.1: Measured dimensions of Spray G from x-ray nozzle tomography

As previously explained in 3.5.3, once the tomography is reconstructed, the axis of each hole is aligned with the x-axis. Then, a canny edge detector with a built-in Gaussian filter of specified standard deviation of $\sigma = 3$ was used to locate the hole cross-section at each slice along the z-plane. A least-squares ellipse fitting algorithm [12] was used to measure the hole diameter and eccentricity. In general, because the eccentricity of the holes was typically less than the spatial resolution, an average of the diameters along the major and minor axes is used as the hole diameter. Any pixel location where the root-mean-square (RMS) error of the elliptic fitting exceeded 20 was removed from the analysis. The total uncertainty in the hole diameter measurements includes the cross-section as a perfect circle of zero eccentricity. This error was typically dominated by the spatial resolution of 1.8 μm. In order to locate the hole inlet, a data point near the center of the hole was chosen as a starting point for a running average of the diameter, moving in the direction of the hole inlet. At each pixel location, the running average was updated, and the location of the hole inlet was defined as the point at which the diameter exceeded 3% of the running mean. A similar procedure was used to locate the hole and counterbore outlets. This technique proved successful in capturing the hole inlet and outlet locations because of the relatively cylindrical diameter profiles of both the holes and the counterbores. The 3% threshold was chosen due to its ability to qualitatively capture the actual inlet and outlet locations. The hole outlet radius of curvature as well as the counterbore fillets were determined by fitting a 5th order polynomial to the hole corner profile and fillet, respectively. The radius of curvature (ROC) was calculated using (4.1),

$$\mathrm{ROC} = \frac{(1 - \dot{y}^2)^{2/3}}{\ddot{y}}, \tag{4.1}$$

where $\dot{y}$ and $\ddot{y}$ are the first and second derivatives of the fitted polynomial, respectively [13]. A 9th order polynomial was used to fit the hole inlet corner profile. The summary with the dimensions extracted from the analaysis is presented in Table 4.1. The relative standard error (RSD) is defined as the value of the measurement deviation σ divided mean μ as in (4.2). This parameter shows the variability in relation to the mean, allowing for comparison among dimensions that vary in magnitude.

$$\mathrm{RSD} = \sigma/\mu, \tag{4.2}$$

Even though nominal dimensions are quoted in the table, it should be made clear that this work does not attempt to compare measured to ideal dimensions, on account of the fact that the thresholds used to obtain the latter and the particular definitions used are unknown. For this reason, comparison between measured and nominal dimensions remains a subject for future work. The important point to note is that the same thresholds and methods of calculating nozzle dimensions are applied to all eight nozzles in order to maintain any errors associated with the data analysis as systematic errors.

D1 and D2 are the inner hole diameters measured at the two different sections, one near the nozzle seat and near close the hole outlet where the counterbore starts. The close values of these diameters and the fact that the standard deviation and root relative standard deviation are also similar indicate that the hole is cylindrical. The same can also be said of the counterbore, where the diameter measured at two diameters

Table 4.1: Hole dimensions measured by x-ray nozzle tomography and norminal dimensions from the manufacturer.

Feature ID	Mean [µm]	St Deviation [µm]	RSD	Nominal [µm]
D1	174.7	1.43	0.0082	165
D2	175.6	1.45	0.0083	165
R1	3.5	0.77	0.22	0
R2	2.4	0.81	0.34	0
L1	150	8.9	0.06	170
A1	38[°]	0.62[°]	0.016	37[°]
D3	393.3	1.45	0.0037	388
D4	393.8	1.26	0.0032	388
R3	40.3	2.05	0.051	40
L2	406.6	24.11	0.028	470

yields the same mean and standard deviation. The biggest values of the relative standard error are for the inlet and outlet radius of curvature. The high values come from the difficulty of properly capturing such a small and sharp feature, where tiny variation in the contour can cause the polynomial fit to be different. Nonetheless, much of the variability it is actually in the geometry as it can be seen when analyzing the inlet and outlet radii versus the azimuthal position (rotation along the axes of the holes). Fig 4.2 shows the variation of the inlet radius of one hole of a Spray G injector as the azimuthal angle θ is incremented. It can be noted how the inlet radius diminishes until is almost a straight angle in the last images.

Although only one hole of one injector is shown, this characteristic is repetitive through holes and injectors. Fig 4.3 shows the behavior of the fitted internal radius versus θ for all holes of Spray G injector. As stated before, the high frequency variability of the results is attributed to both small changes in the geometry and the difficulty of performing the fit to calculate the radius of curvature. Apart from the variability, a decreasing slope can be observed as θ is increased.

From Table 4.1, it can also be noted that the hole length divided by its diameter (L/D) is lower than 1. This relation between the length of the orifice and the diameter determines how developed the flow is before exiting the inner hole and entering the counterbore. In diesel injectors,

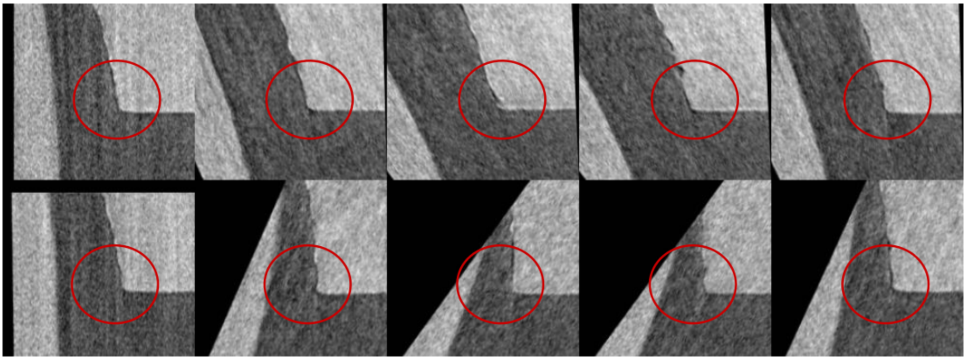

Figure 4.2: Detail of inlet corner radius in ten rotation positions (rotating along the hole axis) for a hole of one of the Spray G injector. The red circle underlays the feature of interest and how the radius varies (decreases) as θ increases, from a higher radius to almost a straight angle.

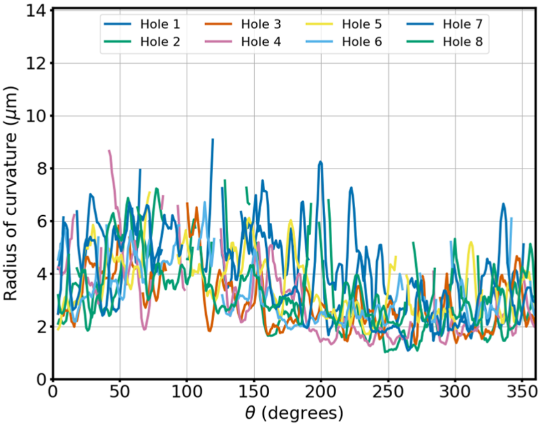

Figure 4.3: Inlet radius for all holes of one of the injectors versus hole rotation (θ).

this magnitude is usually between 4-10, and even then the flow cannot be considered fully developed at the exit of the nozzle, as the length of the orifices is still smaller than the entrance length for turbulent flows [14, 15]. With a much smaller L/D ratio, the influence of the geometric characteristics at the orifice inlet (like the sudden change of diameter and sharp radius of curvature), will remain in the flow when it exits the nozzle. Moreover, the chocking of the flow by the low needle lift (see section 4.3) will also contribute to the influence.

The discharge coefficient, calculated in section 4.4 is also related to the L/D value. Lichtarowicz et al. [16] gathered the results from multiple researchers using nozzles with different L/D, showing the influence on the discharge coefficient (at high Reynolds numbers). The plot shows that the discharge coefficient dramatically decreases for L/D values lower than 2, which is explained by flow separation phenomena making the effective cross-section area much smaller than the geometrical area.

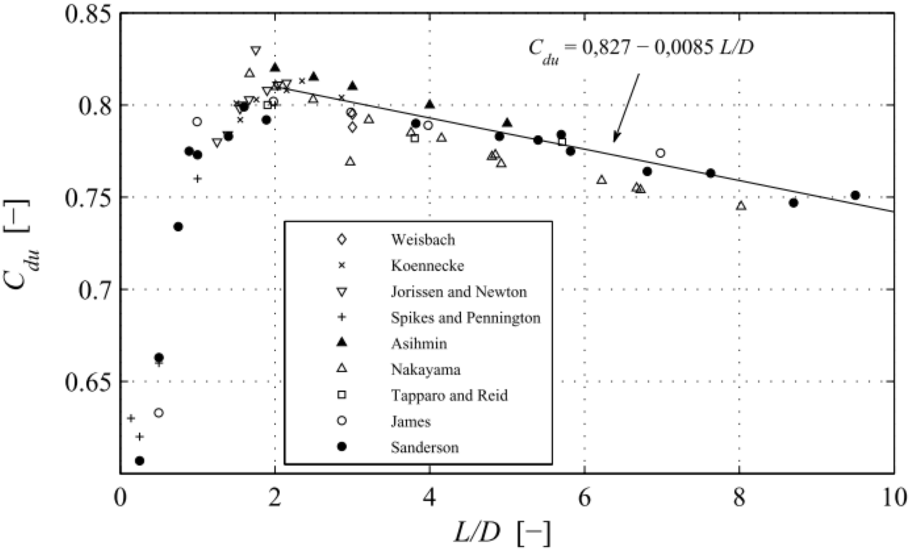

Figure 4.4: Discharge coefficients (for elevated Reynolds numbers for nozzles with different L/D for non-cavitating conditions, from [14].)

Moon et al. [17] studied the influence of several L/D values for GDi nozzles and reported that decreasing L/D ratios were desirable as they resulted in a decrease of the break-up length and an increase in the exit velocity. Similar results were obtained by the numerical investigation using VOF-LES [18, 19]. They argued that the L/D ratio variation of the inner hole has a significant influence on the flow, and reducing this magnitude can increase the velocity, spray angle and reduce the break-up length. In fact, it is the flow separation at the nozzle entrance that creates the instabilities and promote the short-distance primary break-up [20]. Low L/D ratios are desirable but for a given hole diameter, this value limits the amount of metal that can be used in the nozzle. In order to reach the necessary structural strength to withstand the pressurized flow, an increased wall thickness is necessary in the GDi nozzle designs. The counterbore allows to reach the desired L/D ratio without making the actual orifices longer by adding extra thickness to the tip of the nozzle [21]. The counterbore also serves as a shield for the high temperatures reached in the combustion chamber and prevents or limits the buildup of deposits at the nozzle exit, which is critical given the direct impact they can have on combustion performance.

The geometry presented in this section allows to set a base to explain and understand the different phenomena that is presented in the internal flow results sections. Also, the geometry of the 8 Spray G injectors measured is studied in conjunction with the spray tomography and spray radiography measurements to develop a model that represents the geometrical parameters that are more likely to cause differences in near-nozzle flow in section 4.6.

4.3 Needle displacement

Moon et al. [17, 22] argued that modern GDi injectors are designed with low needle lift to generate turbulence and better atomize the spray. The lifts are normally a few tens of micrometers [17, 23] which is smaller than the orifice diameters (around 160 µm). The low needle lift in GDi nozzles throttles the flow prior to reaching the orifice, which increases turbulence and contributes to the spray atomization. This section presents the needle lift measurements performed at Argonne National Laboratory following the procedure described in section 3.5.2. These measurements provide unique vision and data on the movement of the needle in the Spray G injector that can help understand the development of the flow downstream. All the measurements presented in this section were done to the Spray G AV67-029.

Fig 4.5 shows a montage of the images captured for one of the conditions tested in the phase contrast experiments. The number appearing at the mid-bottom of the images represent the image number and goes from 25 to 105 (approximately 274 µs to 1180 µs). The number of images recorded per shot was 200, with the first image synchronized with the ECU commanding signal and the mechanical gates (xrays shutter). The circular shape at the top-left and bottom-right are the shadows of the mechanical gates used as a shutter in order to diminish the heat-load of the nozzle. A total of 96 shots were made per test, each with 200 images per shot as mentioned previously. The individual shots were averaged together to create a movie with higher contrast which makes feature-tracking easier by the processing algorithm.

Fig 4.6 shows the processed needle lift for the modified Spray G conditions at the bottom and the standard driving signal from the ECU at the top. The modified conditions are detailed in 3.5.2 and were used given the particularities of the experimental facilities at Argonne. The intensity signal is sent from the ECU and received in the coil of the injector, after what is known as the hydraylic delay (around 300 µs) the needle starts lifting. The needle rises from the resting position to the top position very quickly in approximately 80 µs where slightly overshoots. It then stabilized rapidly to around 50 µm until the end of injection where the needle closes.

The small variation in needle lift that starts around 800 µs ASOE is likely due to the change of shape of the driving current. This shape is common in GDi ECUs, they first supply a high current or “boost” to lift the needle as fast as possible, then the current output is accommodated to a smaller value in order to decrease the charge in the coils and help the needle to close as fast as possible. This small fickle in the lift does not cause an effect in the ROI as shown in section 4.4.

The needle wobble is plotted in blue lines in the bottom graph of Fig 4.6. The wobble appears to be random and small in absolute value. The x and y axes of the wobble were calculated by combining the needle lift data measured at two rotation angles of the nozzle. The color shades around the lines represent the measurement deviation. As was explained in section 3.5.2, the movement of the needle was captured us-

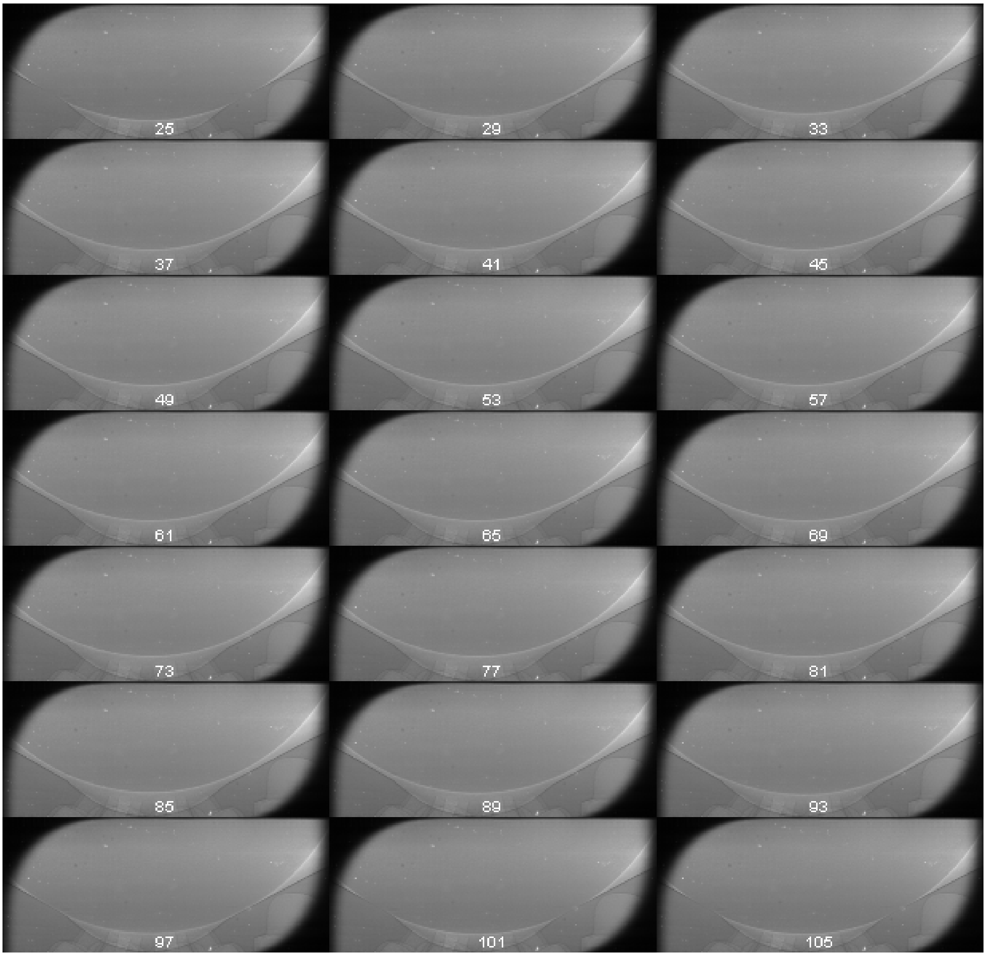

Figure 4.5: Montage of needle lift visualization images for one of the conditions of the phase contrast experiments. The sequence goes from the image 25 (274 μs) to the image 105 (1088 μs).

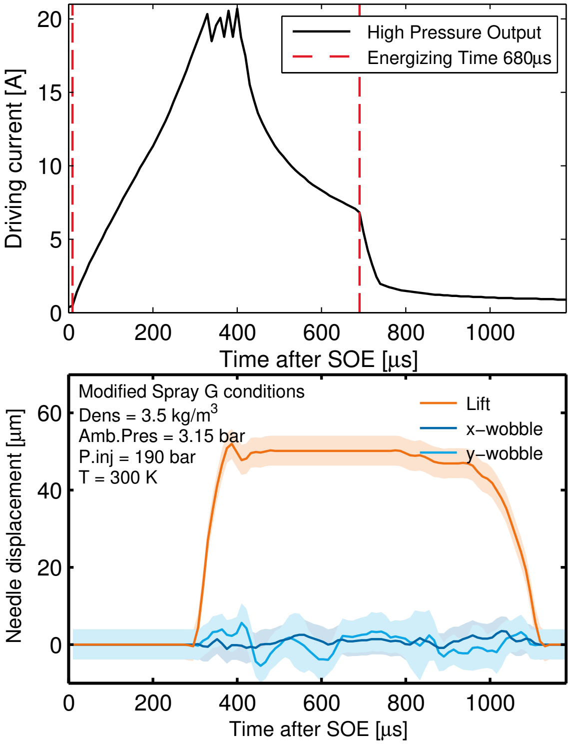

Figure 4.6: Driving current from the ECU on the top. Needle lift and horizontal "wobble" motion for the modified Spray G conditions on the bottom.

ing 2D normalized cross-correlation. The algorithm was run three times with different templates, which allowed to have smoother lines and an estimation of the deviation of the procedure. However, given that the pixel resolution was 3.9 µm per pixel, the deviation considered was the minimum between the one from the three runs and the one corresponding to a shift of one pixel (3.9 µm). It can be appreciated that the absolute value of the deviation is mostly lower than the deviation itself. This amount of horizontal needle movement does not likely affect rate of injection as it was stated by [24], and does likely not affect the spray development downstream given the small values obtained.

Fig 4.7 shows the three possible current outputs of the ECU at the top, and the needle lift produced by those signals at the bottom. It can be appreciated that the needle behaves in the same way at the beginning, even with the “boost” currents being different. This fact implies that the needle lift in this type of injector does not depend on the current as long as it is sufficiently high. However, as can be noted at the end of energizing, the different signals produce different durations. The total time from opening to closing is specified in the legend of the bottom graph of Fig 4.6. The pulse with the highest current (the standard Spray G signal) produces a longer duration than the rest, this is likely due to the coil of the injector taking more time to “de-energize”. Apart from a slight change in the duration, no other changes are observed in the needle movement with respect to the driving signal received.

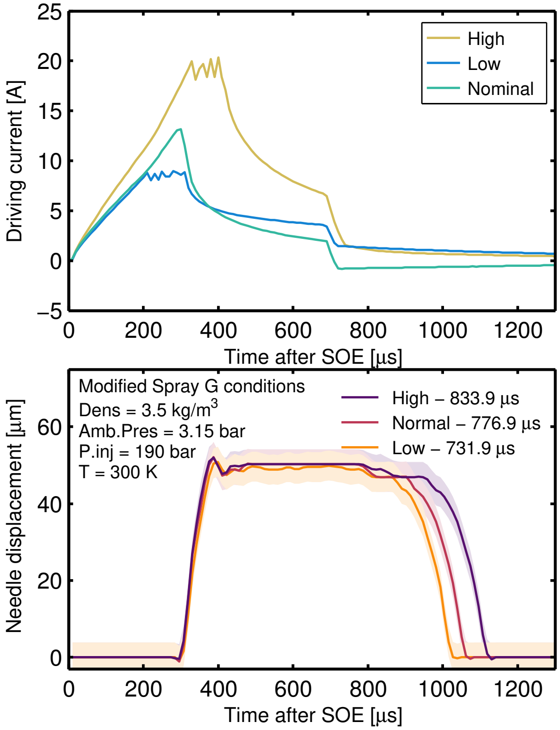

Figure 4.7: The three different intensity outputs available in the ECU (top) and the needle lift produced by each (bottom). High is the standard output.

In order to understand the behavior of the needle with low energizing times that would be relevant for certain operating conditions in an engine like idle or multiple injection strategies, a swipe using low energizing times was performed on the AV67-029 Spray G injector. Fig 4.8 shows the resulting needle lift for the different energizing times tested. The first value that provided a measurable lift was 180 µs, with the lower value of 160 µs not being able to move the needle. The low energizing times provide a driving signal that is over well before the needle has started to move, which produces a longer hydraulic delay in the shorter durations. The first value tested that reached the full lift was 260 µs. It is important to underlie that the values of energizing times lower than this will provide an even lower lift than design and therefore throttle the flow more. This fact can effectively change the development of the flow downstream. It can be observed in Fig 4.8 that the injection duration and lift are not linearly proportional to the energizing time. This is specially obvious between the 240 µs and the 260 µs lines, where the small difference of 20 µs produces a high increase of total opened time and around 15 µm more of needle lift .

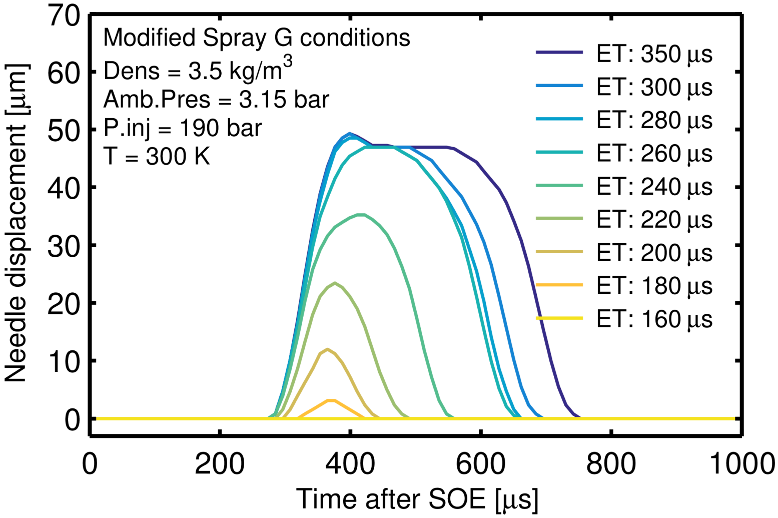

Figure 4.8: Needle lift for a command duration swipe. The durations tested varied from 160 µs to 350 µs.

Multiple or split injection operation has been shown to have the potential of benefiting the combustion process and reduce pollutants output under moderate load operation [25]. It was also shown that the possibility of delivering multiple injection in conjunction with precise small quantities can lead to improve fuel economy, reduce pollutant emissions [26], and can also be a strategy to control engine knocking [27]. Moreover, the promising Gasoline Compression Ignition (GCI) and Gasoline Direct Compression Ignition (GDCI) systems, actively rely on the delivery of a multiple late injection strategy to create a high concentration of fuel locally to serve as the ignition point at the end of the compression strokes [28, 29]. Because of the increasing importance of multiple injection strategies, the ECN created a condition denominated Spray G-M1 consisting on a main injection of 680 µs, 1 ms of dwell time, and 186 µs post-injection with the rest of parameters equal to the standard Spray G condition. The needle lift produced by the multiple command signal is represented in Fig 4.9. It can be appreciated that the lift produced by the 186 µs post injection is much higher than the one that is produced by the 180 µs featured in Fig 4.8, and is even higher than the line corresponding to 200 µs and 220 µs ET. This behavior can be due to the needle moving differently in dynamic than in static response due to the close time between main event and post-injection. It is also likely related to the pressure wave of the fuel right after the main injection event. The pressure can oscillate substantially after the injection event and can be considerably lower at the time the post-injection is realized which can change the lift produced by the command. In order to study how this effect can change the delivery of the fuel, this behavior is also studied in the Rate of Injection section 4.4.

4.4 Rate of injection

Part of the results presented in this section are based on previously published papers that are a component of this work [4, 30]. The focus of the study of the rate of injection for the ECN GDi injector was first to evaluate how the common variables subject to change in normal engine operation affect the ROI for the type of hardware in use here. With this purpose, the effects of injection pressure, ambient pressure, energizing time, fuel temperature, and even injection frequency were individually tested, resulting in a large conditions matrix and long experimental campaign. The methodology followed to complete the rate of injection work was described in section 3.3.

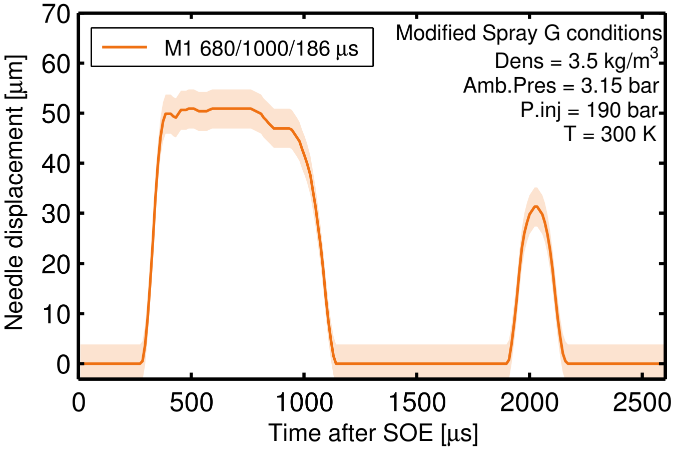

Figure 4.9: Needle lift for the Spray G multiple injection condition (Spray G-M1). The needle lift reached in the post-injection is not what it would correspond for a single injection of that duration.

The rate of injection measurements were done in several experimental campaigns. The first campaign had over 60 different conditions, with several swipes of injection pressure, back pressure, temperature and even injection frequency. The first experimental campaign was carried out with the original seals of the GDi injector. Those type of seals are common, and can be found in other GDi injectors from different manufacturers. The original seals in these injectors are not designed for constant assembly and disassembly of the part, which is generally the case in experimental work. The wearing caused in the original seals, possibly created the disparity of the opening transient of the ROI with respect of measurements from other institutions. This finding motivated the repetition of some measurements from the first experimental campaign with a new design of the injector holder that allowed using o-rings for sealing. Fig 4.10 shows the rate of injection for Spray G AV67-026 at nominal Spray G condition and an additional line with the same conditions but with an injection pressure of 100 bar. It can be seen in the figure that the main differences between the measurements with the original seals and with o-rings are in the opening and closing transients, especially at the higher injection pressure. The opening transient of the line corresponding to the original seals measurements presents and overshot similar to the one observed in the continuous line but right after the overshot, the rate of injection bounces down. This behavior has not been observed with other measurements from other institutions and it would be explained by a small displacement of the nozzle as a reaction of the pressure wave generated.

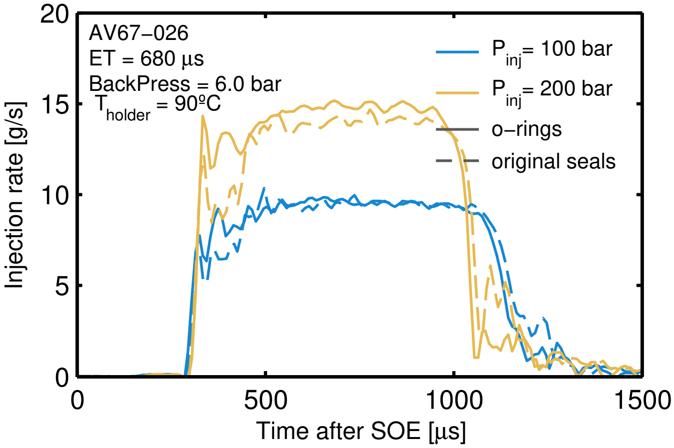

Figure 4.10: Rate of injection versus time for standard Spray G conditions and an additional condition with 100 bar of injection pressure. Solid lines represent the measurements done in the second experimental campaign with the improved design of the injector holder. Dashed lines represent the measurements from the first experimental campaign.

Fig 4.11 compares the second set of experiments with the o-rings seals with ROI data from General Motors (GM). General Motors is an institution involved with the ECN, specially with the GDi topics. They carried out ROI measurements with a similar methodology than the one described here to two Spray G injectors: AV67-016 and AV67-028. It can be appreciated in the Figure that nozzles 026 (the one experimented in CMT) and 028 provide very similar steady state ROI, whereas 016 provides a slightly higher mass flow. Apart from this difference, the opening transient of the second experimental campaign is very close to the one observed with in the GM data. The transient presents an overshot at the end of the ramp-up, a rebound and finally stabilization and closing. The rebound seems more amortiguated in the CMT data which may be due to differences in the pressure sensors within the rate meters or variations in the experimental set-up. The overshot at the end of the ramp-up is consistent for the three lines and is likely related to the overshot in the needle lift observed in 4.3.

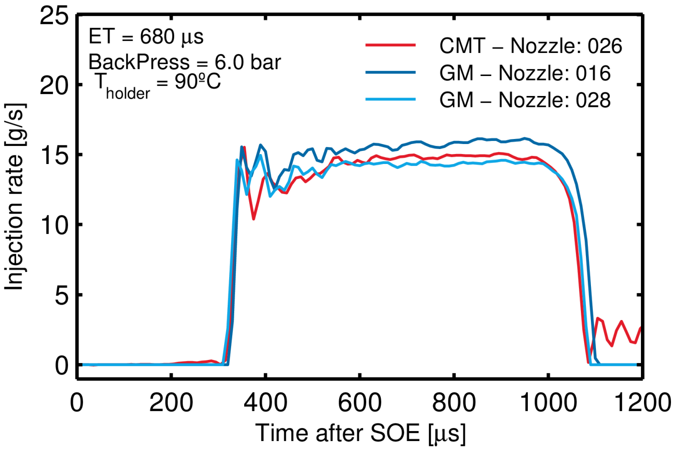

Figure 4.11: Rate of injection measured in the second experimental campaign for Spray G AV67-026 compared with ROI measured by GM of injectors AV67-016 and AV67-028.

The following subsections present the individual effects that the variables studied have on the rate of injection of injector AV67-26.

4.4.1 Effect of injection pressure and ambient pressure

The effect of injection pressure on rate of injection is well known for Diesel injectors [14]. A higher injection pressure will produce a higher rate of injection rate mainly due to the rise in the flow velocity. The relationship of proportionality between injection pressure and ROI is given in (4.3).

$$\dot{m} \propto \sqrt{P_{\text{inj}} - P_{\text{back}}} = \sqrt{\Delta P}, \tag{4.3}$$

with P_{inj} and P_{back} the injection pressure and the ambient pressure respectively. Fig 4.12 shows the injection rate for a swipe of rail pressure for the standard Spray G ambient pressure (6 bar). As expected, the increasing injetion pressure provides a higher rate of injection. It can also be noted how the start of injection (SOI) is not modified by the rail pressure as is generally the case in Diesel hardware [14]. This is probably because the force applied to the needle by the coil is considerably higher than the one opposing force caused by the pressurized fuel. On the other hand, it can be appreciated that the delay of end of injection is considerably affected by the pressure. In this case, when the current signal from the ECU finishes, the pressure in the inlet line of the injector forces the needle to close, “helping” the spring that the injector uses to this end.

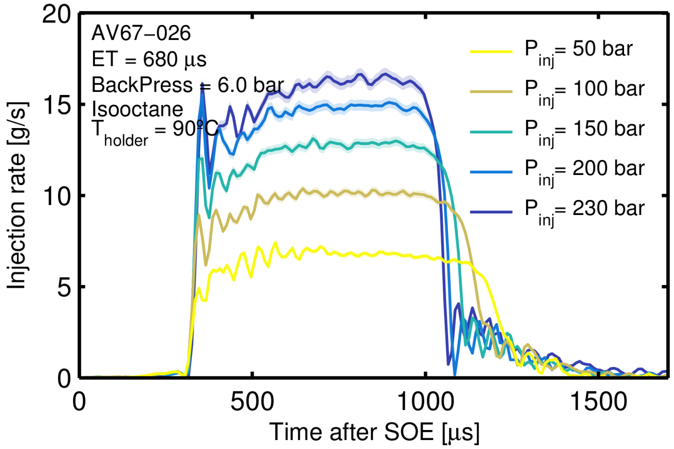

Figure 4.12: Measured mass flow for an injection pressure swipe maintaining the rest of parameters at standard Spray G conditions.

Additionally, the effect of the ambient or discharge pressure is represented in Fig 4.13. In this case the maximum change in pressure drop (ΔP) is only of 21 bar, so the effect on injection rate is not as noticeable here as it was in Fig 4.12 where the magnitude of the pressure drop change was much higher between lines. Even if the mass flow lines are close, the ambient pressure comparison allows to see the change in the behavior of the opening and closing transients. The increase in the discharge pressure amortiguates the overshot produced at the end of the opening and closing ramps. Given that different discharge pressures were not tested in the needle motion experiments, it is not possible to know whether the difference in the opening and closing transients are due to change in the needle motion or just the pressure wave generated by the injection.

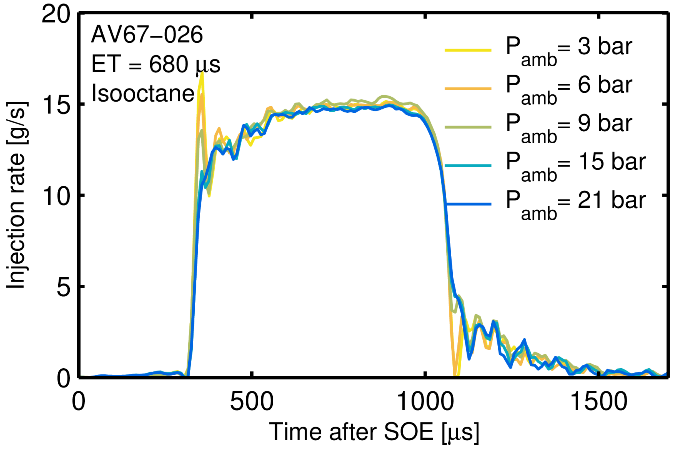

Figure 4.13: Measured mass flow for a discharge pressure swipe maintaining the rest of parameters at standard Spray G conditions.

In order to visualize how accurately the proportionality factor in equation (4.3) explains the change in mass flow by the change in injection pressure, Fig 4.14 is shown next. The graph shows the same lines that were plotted in Fig 4.12, with each signal divided by the square root of the pressure drop (i.e the proportionality factor in (4.3)). The lines appear now close to each other but are still ordered by the value of injection pressure which implies that there is still a factor not accounted for in the normalization. This factor is the change in the discharge coefficient (defined in section 3.4) and will be studied in the next section.

4.4.2 Effect of Temperature

The effect of temperature on a piezoelectric Diesel injector was evaluated in a previous study [31]. Even though there are many differences between Diesel and GDi behavior, the physical qualitative effects that temperature produces on the viscosity and density on liquid fuels are still the same. Salvador et al. [31] established that there is a competition between the effect of temperature on density and in viscosity and the resulting effects found on steady state injection rate were small. On the contrary, the primary effects of temperature on rate of injection were for a ballistic diesel injector in the opening and closing transients. Those

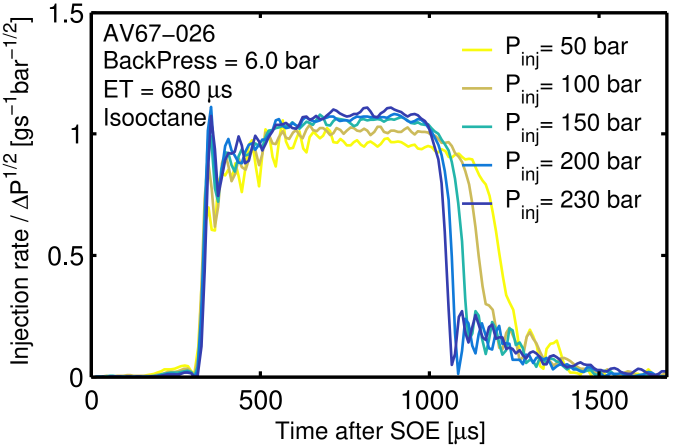

Figure 4.14: Mass flow rate divided by the square root of the pressure drop. All lines should merge into one if this factor completely explained the effect of injection pressure and ambient pressure on injection rate.

effects were increasingly evident as the temperature dropped to the minimum of the range tested in their study at 253 K. The range studied in the current work was much smaller, from around 45 °C to 85 °C. In this range, for the ECN GDi injector, no influence of temperature was found either on steady state ROI or the ROI signals measured. Fig 4.4.2 shows the effect of temperature on the measured rate of injection. As was discussed in section 3.3, the temperature of the fuel and the body of the injector is controlled by a water jacket in the injector holder. By varying the fuel temperature, the temperature of the fuel in the rate meter volume also changes. Fig 4.15(a) shows the steady state rate of injection versus the fuel temperature and versus the temperature inside the rate meter (system temperature). It can be appreciated that there is no correlation of ROI with neither. Moreover, Fig 4.15(b) shows the ROI signal for some conditions in the top graph. It is clear that for the range of temperatures experimented, there are no appreciable differences in the signals caused by the temperature variation.

4.4.3 Injection duration study

Given the ET variation studied in the needle lift section 4.3, a similar study using the same energizing times was also done for the rate of in-

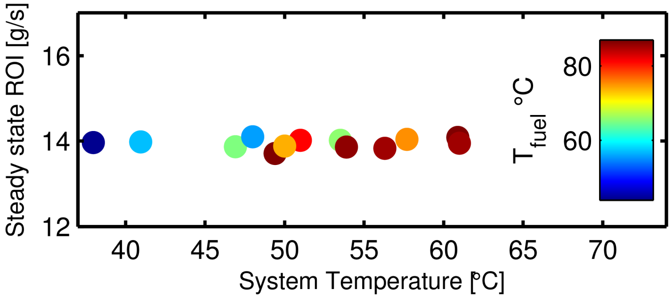

(a) Steady state ROI versus fuel temperature and system temperature

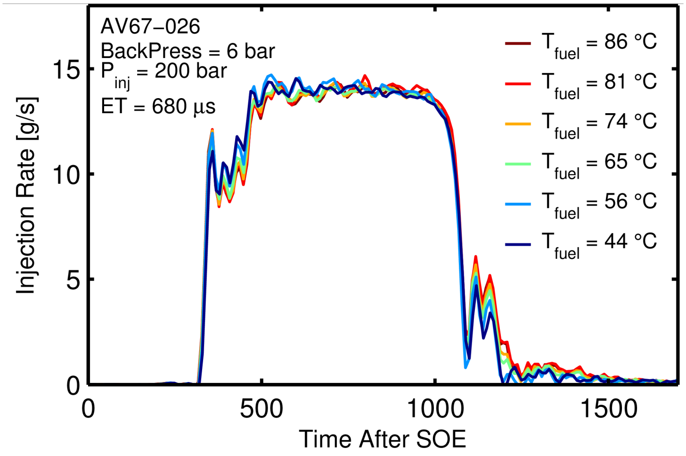

(b) Injection Rate for different fuel temperatures

Figure 4.15: Effect of temperature on steady state ROI (a) and on the rate of injection signal (b)

jection measurements. The energizing time effect on the rate of injection is plotted on Fig 4.4.3. The bottom graph with the needle lift lines is repeated here from section 4.3 for clarity. The minimum value of ET tested in the rate of injection campaign was 180 µs as that is the first value that produced a measurable ROI. As can be seen in the top graph, the value of 160 µs was not enough to lift the needle. Even though the first values of 180 and 200 µs lift the needle enough to allow the nozzle to deliver fuel, the operation with this short injections is not stable and the injected quantity is very unreliable. The first value that allowed stable operation was with 220 µs and as can be seen in the graph, this value is almost reaching the peak value of the rest of the longer ETs, while the lift produced is about 70 % of the maximum lift. The injected quantity for 220 µs is around 0.2 mg which is close to the minimum quantity that can be reliable injected at 200 bar injection pressure.

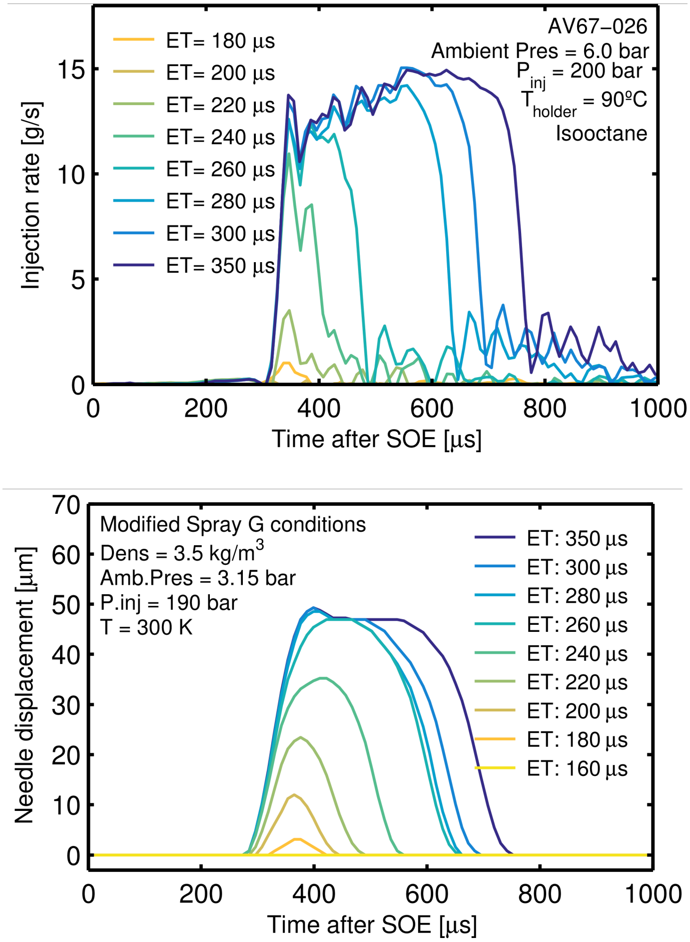

Figure 4.16: Rate of injection (top) and needle lift (bottom) for a range of short ET pulses.

The needle lift campaign was only done with an injection pressure of 20 MPa, but the energizing time study of rate of injection was also done for 10 MPa of rail pressure. In order to show the different behavior of the injector at different pressures, Fig 4.17 is presented. In the plot, the lowest 5 values of energizing time are chosen for the comparison. The first characteristic that can be noted is that for low ETs, the maximum value of ROI is higher for the lower rail pressures which may seem counterintuitive. This is related to the dependence of the needle movement with the inlet fluid pressure. Typical GDi injectors are directly actuated by the solenoid, meaning that instead of actuating on a control volume to raise the needle by creating a difference of pressures like in Diesel injectors, the electromagnetic force of the solenoid is directly used here to lift the needle. This means that a higher inlet pressure will create a higher force to push against and therefore the energy needed for the needle to lift increases with the rail pressure. One of the effects of this design is that with low ETs, the injection rate is higher for the lower injection pressures as can be clearly seen in the 220 µs lines. On the other hand, for the same reason, inlet pressures "helps" to close the needle. This results in the injection being longer for the lower injection pressure when the ETs are short.

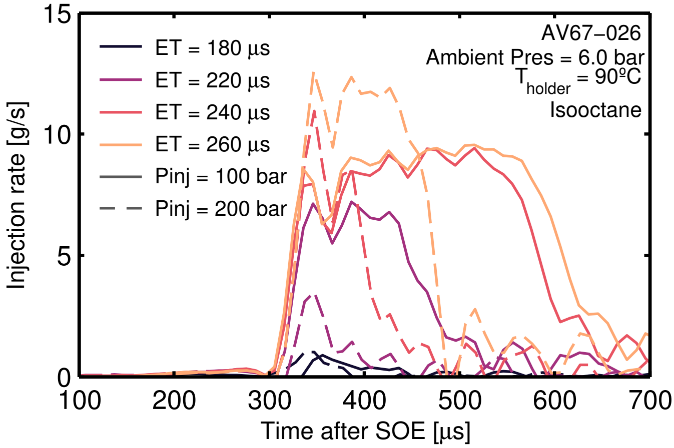

Figure 4.17: Injection rate comparison at two rail pressures for 5 different energizing times.

4.4.4 Multiple injections

Multiple injection strategies are outside the scope of the thesis. Nonetheless, as previously stated in the needle displacement section 4.4, given the increasing interest in multiple injections for GDi engines, several tests were made in the rate of injection campaign that are presented in this section. Because of the increasing interest, the Engine Combustion Network (ECN) added a multiple injection condition (Spray G-M1) with a main pulse of 680 µs followed by a dwell time (DT) of 1000 µs and a post pulse of 185 µs, with the rest of variables the same as those from the standard Spray G.

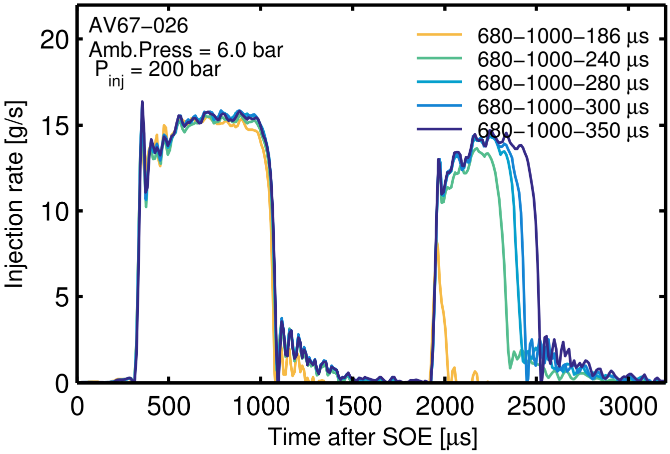

Figure 4.18: Mass flow rate for multiple injection commands signals. The legend represents the main injection - the dwell time - and the post injection.

Fig 4.18 shows the injection rate for the ECN condition along with a swipe of post injections. While in Diesel injectors the effect of the pressure wave is noticeable in closely spaced injections, in this case the difference of the magnitude of injection rate between single and double injections is remarkable. When comparing the injection rate signal from Fig 4.17 with the same ET in the post-injection in Fig 4.18, it can be clearly seeing that in post-injections the mass flow is much higher. For instance, the line of 186 µs is barely visible in the single injection, whereas in the double injection the peak is almost 10 g/s. This difference is almost one order of magnitude and while it might be related to the pressure wave dynamics affecting the second injection, the difference is far too big for that to be the only cause. This behavior could be related to the solenoid of the injector retaining charge after the first injection, which would make the energization in the second command considerable faster and therefore the needle takes less time to open.

The needle lift for the split condition (Spray G-M1) was presented in section 4.3. Nonetheless, is interesting to compare here the needle lift for the second injection of the split condition with the one with a single injection as represented in Fig 4.19. It must be noted that the ET of the second injection in the split case is not exactly the same as the ET for the single injection case. However, this small difference of 6 µs is not important enough to change any conclusion in the comparison. It can be seen in the graph that whereas the needle almost goes fully opened in the second injection for the split case, it barely opens in the single case. This confirms that the effect seen previously in Figs 4.17 and 4.18 is not due to wave dynamics but rather to the difference in the needle opening. The behavior reported here can be very important as it can dramatically change the expected quantity of fuel delivered and it can also prove to be difficult to model.

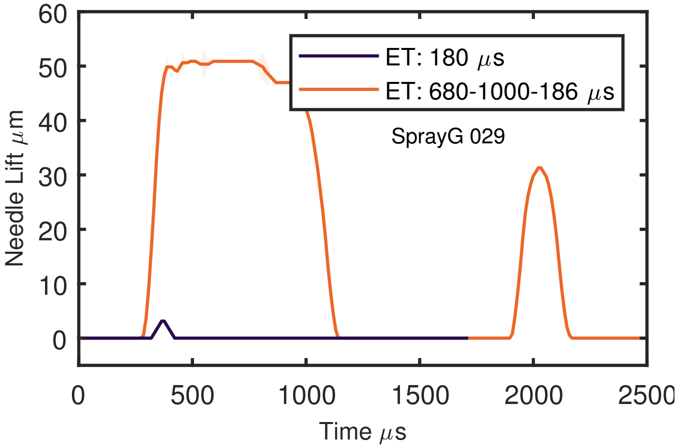

Figure 4.19: Needle lift comparison for the split injection with an electrical command signal of 680-1000-186 µs and a single injection with an ET of 180 µs.

The experimental campaign for multiple injection cases also included a swipe of dwell time. This parameter is important as it can phase the second injection with the optimum moment to provide the fuel, for instance at the end of the compression stroke in a stratified strategy. The minimum dwell time that provides two separate injection was 300 µs for an injection pressure of 20 MPa and the maximum observed was 400 µs for an injection pressure of 7.5 MPa. Fig 4.20 shows the injection rate with the dwell time variation for a main injection of 680 µs and a post-injection of 186 µs. As expected, the main injection remains equal and only the variability due to experimental uncertainties can be appreciated. However, the post-injection is *(very)* dependant on the dwell time and the behavior seems oscillating, first decreasing until 600 µs of dwell and then increasing again later for longer dwell times. There are only three variables that can be affecting the second injection: the rail pressure, the energizing signal, and the needle movement.

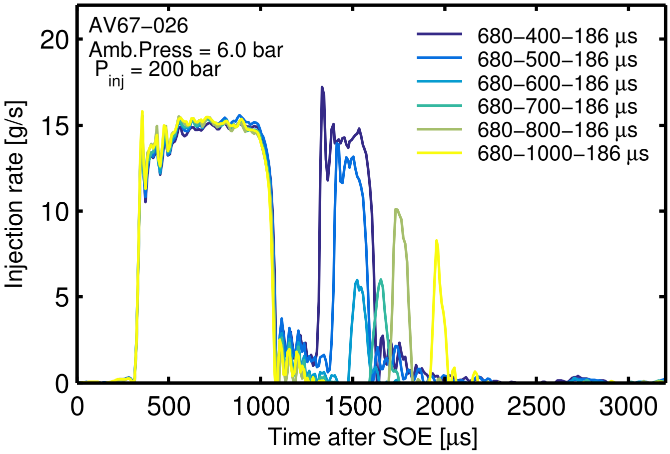

Figure 4.20: Injection rate for split injection strategies with a variation of the duration of the dwell time from 400 µs to 1000 µs.

The experimental setup included a piezo-electric kistler pressure sensor mounted in the common rail as stated in Chapter 3. This sensor recorded the pressure wave generated by the injection and was used here to produce Fig 4.21. The colors for the different dwell times are maintained in this plot. It should be noted that there is a time shift between the injection rate and the pressure signal and is because of the distance between the rail and the injector which was about 30 mm, which translates to about 400 µs shift. The first decay of pressure marks the first injection, then the pressure builds up until it decays slightly again at different times depending on the dwell time of the second injection. The blue line with the shortest dwell time (blue) has the most noticeable second decay, the others are increasingly difficult to discern due to the noise of the signal. The difference of about 4 bar in the initial rail pressure for the two lines at the bottom of the graph were produced by the PID controller which has a certain tolerance error from the set-point. When comparing 4.20 and 4.21, it is clear that there is no correlation between the pressure in the rail and the mass flow rate behavior. First, the lines of 700 and 800 µs of dwell time have almost identical pressure signals with less than 1 bar of maximum differences and yet the injection rate for the two of them look very different, one reaching 5 g/s and the other more than 10 g/s. Moreover, the difference between any given pressure signal at any given time is not more than 5-6 bar, but the dispersity between some post-injections can be up to the order of three. It is interesting how the 500 µs and 600 µs dwell-time lines produce such different second injections being so closely spaced in time. Nonetheless, the pressure fluctuations presented are measured in the common rail, the inside of the nozzle could present higher pressure fluctuations that are not measured by the sensor, as the system can act as a filter and attenuate them. However, in this case, the high frequency pressure fluctuations would create more variability in the second injection rather than different but consistent injection rates.

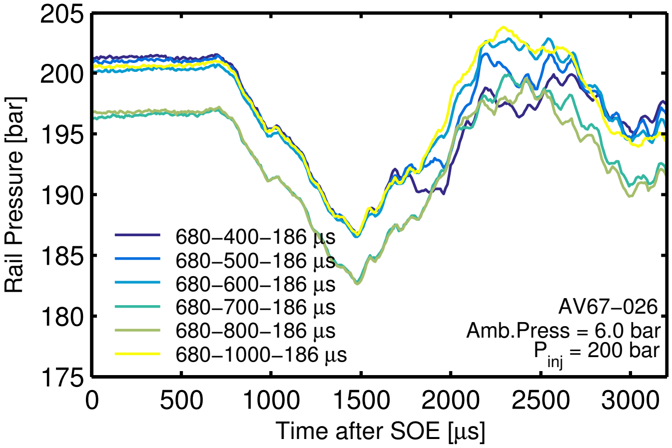

Figure 4.21: Pressure signals measured at the rail for the conditions presented in 4.20.

The second variable to examine is the energizing signal. This signal was measured with a clamp ammeter to the positive electric cable that connects to the injector. Fig 4.22 shows the intensity pulse sent from the driver to the injector for the conditions presented in Fig 4.20. Sometimes these instruments are not able to set the zero value properly, giving an offset from the actual signal. This occurred with the 680-1000-186 µs line and therefore it is not represented in the plot. It can be seen in the plot that after the first signal which is identical as expected, the other signals start in sequence depending on the dwell time, which was modified in increments of 100 µs. It can be observed how the intensity does not go down all the way to zero after the first command. On the contrary, it slowly decreases from around 1 A until the second signal is sent. It may look that this slope is the one causing the different current peaks, but the differences of the consecutive peaks is much higher than this slope. As stated previously, the coil of the injector may retain some charge which might be causing the difference in the maximum peaks and also the slow decay of the current after energization. However, it is clear that the different signals measured are not correlated with the dependance of the mass flow rate and the dwell time. While the current pulse sent is nicely ordered in a decreasing manner, the behavior reported in Fig 4.20 is oscillating and the differences are much bigger in magnitude.

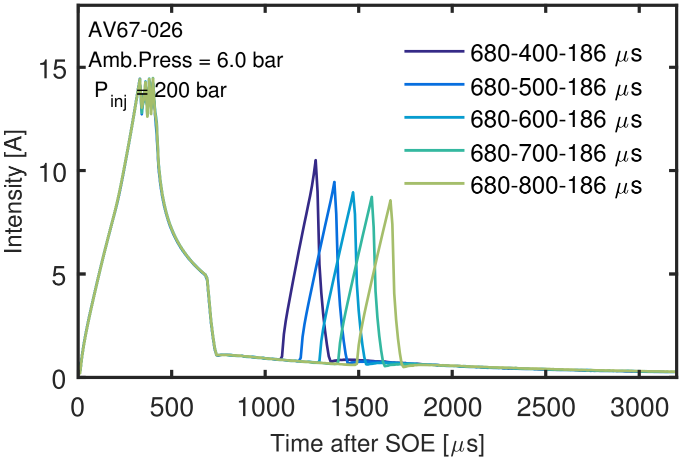

Figure 4.22: Energizing signal in Amperes sent to the injector from the driver (ECU) for the conditions presented in 4.20, except the 680-1000-186 µs condition, where the measurement was not properly recorded.

One possible explanation of the phenomena taking place is the needle dynamics after closing. The algorithm used to process the needle movement did not capture movement after closure. However, upon visual inspection with the magnified images, it can be noted that the needle in fact rebounds when it hits the seat, moving slowly up and down at a certain frecuency. The developed processing tool was not able to capture this movement because it is slow and even smaller than one pixel per image. Moreover, the tool process the images three times, each with one template selected by the user. If the movement is captured only in one of the runs and not in the other it would be averaged down. Because of this limitation, the closing of the needle was manually processed with magnified images (up to 600%). The process involved putting a point in a feature of the edge of the needle and tracking that feature as consistently as possible in the following images. An image of the needle feature and the points tracked is shown in Fig 4.23.

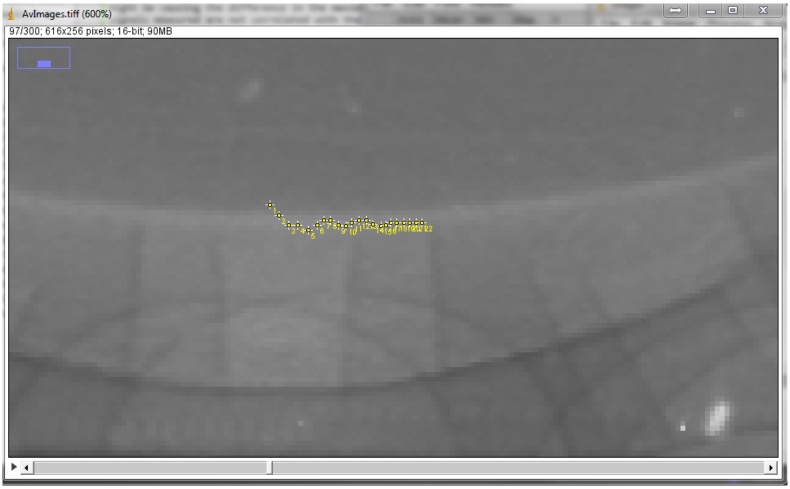

Figure 4.23: Screen capture of the needle feature and the points that were put to track it in the following images. The points are not in the same vertical line because this didn't allow to put them close enough.

Once the information of the indiviual points is gathered and stored, it can be compared with the mass flow rate of the split strategies shown earlier. Fig 4.24 shows the rate of injection of the first three lines (dwell times of 400, 500 and 600 µs) appearing in Fig 4.20. No legend or text is displayed in this case for clarity, the reader can check the information in Fig 4.20. The needle lift obtained with the procedure described above is plotted in red in the right y-axis on Fig 4.24. It can be noted how the small movement of the needle could be related with the high-frecuency mass flow rate variation at the end of injection. Unfortunately the resolution of the x-ray experiments in the needle lift movies did not allow to continue tracking the needle after a certain time where the movement was too small. However, this graph shows that this small oscillating movement could be affecting the second injection, depending greatly on the timing of the latter. If the second injection is phased with the upward movement, the force to move the needle could decrease enough to make a difference in the time it takes to open and in the injected mass for small ETs. The opposite can also apply, if the timing of the second injection is phased with the downward movement of the needle, then the effect would be inverted and the injection rate would decrease. This oscillating behavior of the needle after EOI can help explain the oscillating behavior of the split injections presented in Fig 4.21 that could not be explained by pressure waves or differences in the command signals. However, more rate of injection experiments and specially, more needle lift experiments with these type of split signals would be necessary to confirm this theory. Moreover, the needle lift experiments would benefit from an increased spatial resolution. Also, a physical model of the injector would also be necessary to establish that the difference in forces needed to move the needle caused by the rebounding would be enough to make a difference in its dynamics after another energizing signal is sent. This theory could explain the difference in movement observed in close-coupled injections, but it is quickly dampened down and therefore it still does not explain the different behavior of the rate of injection and needle motion represented in Fig 4.19, where the dwell time is 1000 µs. In this case, and as was stated previously, the order of magnitude difference between the second injection in the split injection strategy and a single injection of the same ET, could be related to parasitic currents in the solenoid that are not reflected when measuring the command signal with the ammeter clamp. At the moment at which this work was written, these phenomena occurring with the split injection cases in the GDi injectors used are not well understood. However, previous work focusing on spray velocity using a post-injection with different dwell times [32], identified a higher velocity for the needle lift in some post-injections caused by the bouncing of the needle. In order to confirm the results obtained here, it is recommended as future work to continue the research in this area with physical models as well as further phase-contrast experimentation in order to completely understand how the injector behaves in multiple injections.

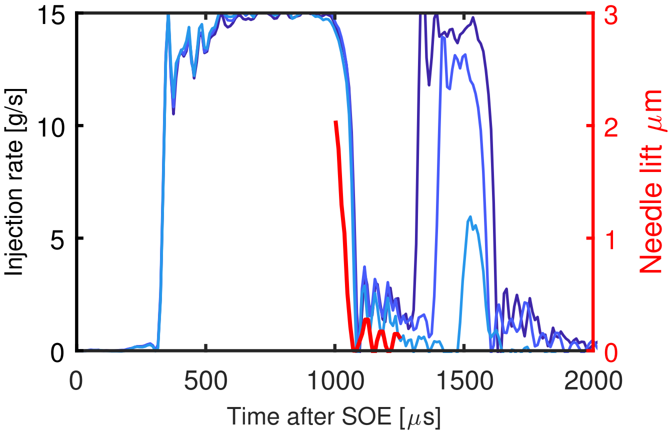

Figure 4.24: Rate of injection for three of the conditions in Fig 4.20 on the left axis, needle lift extracted with the manual procedure on the right axis in red.

4.5 Rate of momentum

Momentum flux was measured using two different methodologies that were described in section 3.4 in Chapter 3. Momentum flux was measured for a wide variety of injections pressure and ambient pressure conditions to study the influence of those variables. The conditions studied in the lateral configurations were reduced, as the measurements had to be repeated for several holes. The following sections present the results of the momentum flux experimental campaigns.

4.5.1 Evaluation of the frontal and lateral methodologies

Given that in the frontal configuration the air entrainment and momentum dissipation to the ambient can be playing a role, the effect of the distance between the injector and the sensor was investigated by moving the sensor to three different positions from 1.8 to 2.8 mm from the nozzle tip. Fig 4.25 shows the momentum flux measured at three different distances between the sensor and the injector. If the air entrainment affects the results, then varying the distance of the sensor would vary the results. It can be noted that the variation from 1.8 to 2.8 mm (maximum distance at which the spray is completely collected) does not significantly change the momentum rate measured, meaning that there is negligible effect of the gas entrainment when using Helium.

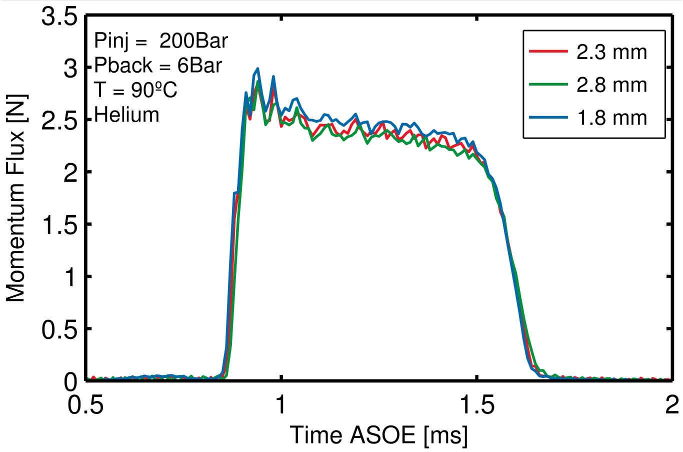

Figure 4.25: Momentum flux versus time using the frontal configuration for three distances between the sensor and the nozzle tip.

A similar comparison is done using the data measured with the lateral configuration methodology as shown in Fig 4.26. In this case, the comparison is done with the stabilized rate of momentum, calculated by averaging the steady state zone of the signal. The different symbols in the graph represent the measurement for different orifices, good agreement is seen between the holes, with the differences attributed to a combination of different flow (the inside of the nozzle is not axisymmetric) and experimental uncertainty. As seen in the graph, in the lateral configuration, the steady state momentum flux depends on the distance between the injector and the sensor, which must be much higher than in the frontal configuration case in order to not capture more than one spray at a time. The distance dependence increases with increasing ambient pressure which can be due to two possibilities. The first is that at a certain ambient pressure and distance, the "cone angle" of the plume is big enough to make the spray wider than the sensor, so not all the spray momentum would be measured. The other is that even though the spray is perpendicular to the sensor, air entrainment could be playing a role here as well. Plume interaction is needed in GDi injectors to promote flame propagation inside the cylinder. This plume interaction can substantially modify the expected macroscopic trends of the spray, as it is shown later on in Chapter 5, and can also cause that air is not entering the fuel in the same way in zones where there is an adjacent plume. It is likely that the combination of these two possibilities increases the uncertainty of the measurement and makes it variable with the distance and therefore less reliable.

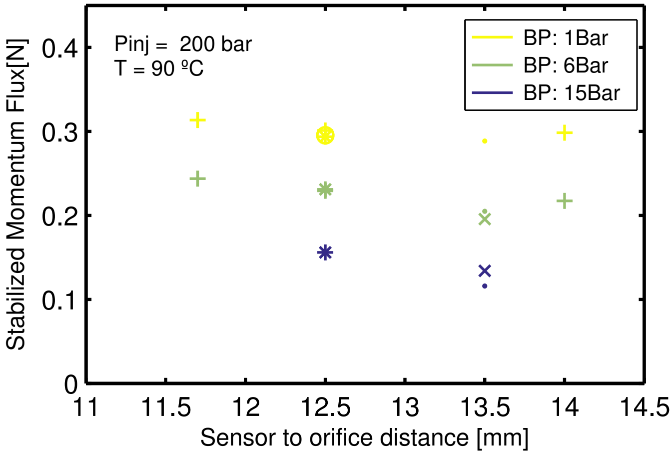

Figure 4.26: Stabilized rate of momentum at different ambient pressures versus the distance from the nozzle tip to the sensor. Different symbols represent different orifices.

The momentum flux of a spray is directly proportional to the pressure drop between inlet and outlet of the injector nozzles as it was established in the methodology chapter (Chapter 3). Fig 4.27 represents the steady state momentum flux calculated in the same manner as in the previous figure with colors representing different ambient pressures and symbols representing the configurations. The repeated points for the lateral configuration data represent data from different orifices. The data for the frontal configuration approximately follow a straight line from zero to the maximum value of momentum flux obtained for the highest injection pressure and lowest ambient pressure, in accordance with the theory. However, in the lateral configuration, the points are not aligned in the same manner. In this case, the lines have different slopes depending on the ambient pressure, which is contrary to the expected behavior and theory [14]. Also, the zero momentum intercepts of those lines are different than zero which would not be possible. Moreover, even when the ambient pressure is low (1 bar), the momentum measured with the lateral configuration is considerably lower than the one measured with the frontal configuration (divided by the number of orifices). These two facts are a consequence of the added uncertainty of the effects described above, both going in the direction of decreasing the measured momentum. Given these results, it is obvious that the lateral configuration methodology does not provide reliable data and therefore only the frontal configuration data will be used in the rest of the sections of the document. Nonetheless, granted a careful set-up of the experiment with the lateral configuration, the data can still be useful to provide hole-to-hole flow variability which can be interesting given the non-axisymmetrical geometry of the nozzle.

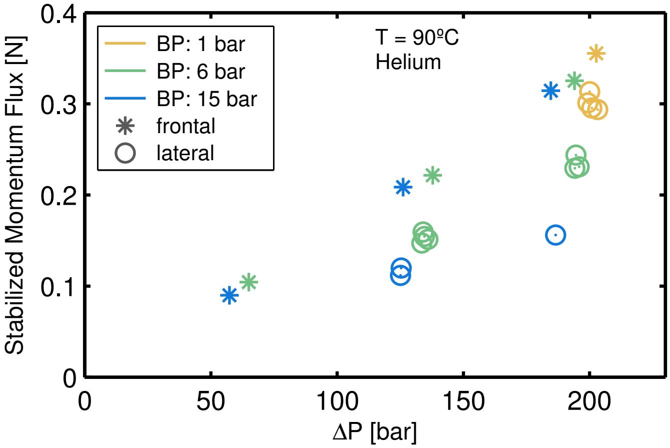

Figure 4.27: Stabilized momentum flux comparison between the lateral and frontal configurations for three different back pressure (BP) levels.

4.5.2 Hydraulic coefficients

As previously discussed in the methodology chapter (Chapter 3), the discharge coefficient can be separated into two coefficients that represent how much of the theoretical velocity (C_v) and how much of the geometrical area (C_a) is available in the spray. To calculate these coefficients, the frontal configuration data were used.

Fig 4.28 and Fig 4.29 show the velocity coefficient and effective velocity respectively. Gimeno [14] showed that a non-cavitating diesel injector provides a velocity coefficient that has an asymptotic correlation with the square root of the pressure drop, with the effective velocity depending linearly with that same magnitude. In this GDi injector, the observed behaviour is different. The C_v grows at first with the $\sqrt{\Delta P}$ and then slightly drops. Moreover, the relationship does not seem to follow an asymptotic curve, although more data points would be necessary to assess this properly. On the other hand, the effective velocity behaves linearly up until the highest values of pressure drop, where the behavior starts to look asymptotic. This changes in the trend make the coefficient of velocity at the higher values of ΔP also change the growing tendency.

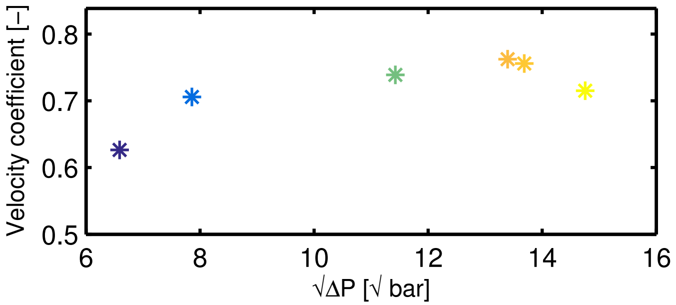

Figure 4.28: relationship of the velocity coefficient with the square root of the pressure drop

Continuing with the study of the hydraulic coefficients, Fig 4.30 shows the effective diameter, which is calculated through the area coefficient. It represents how much of the actual orifice is being "used" by the flow. The nominal diameter of the Spray G injectors is 165 µm, although the internal geometry showed that the value is closer to 175 µm. The graph shows values considerably lower than that and not a clear tendency with

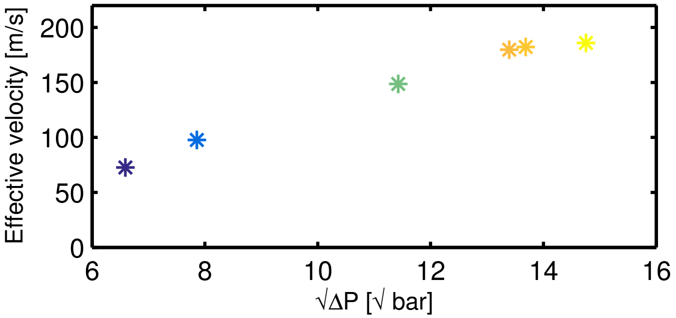

Figure 4.29: Effective velocity of the flow coming out of the orifices versus the square root of the pressure drop.

the pressure drop. The coefficient of area (and therefore the effective diameter) is higher as the flow is more turbulent as shown by [14] which can explain the increase of the point at highest value of ΔP. However, it would not explain the value of the first point appearing in the figure.

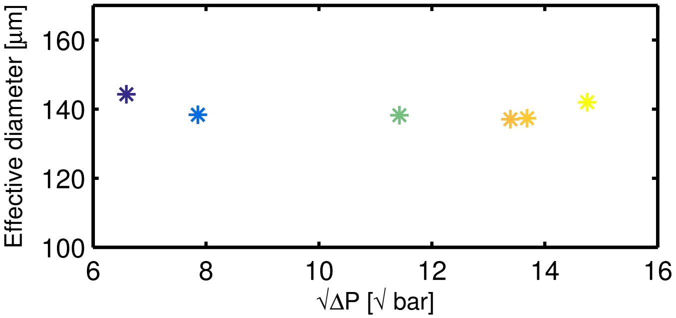

Figure 4.30: Evolution of the effective diameter of the nozzle with the square root of the pressure drop.

Finally, the discharge coefficient is shown in Fig 4.31. It can be seen that there is a slight rising tendency with the pressure drop but the discharge coefficient remains fairly constant throughout the range of injection pressure studied (which covers more than the nominal operational range of the injector.)

The low values for the coefficient of velocity, the effective diameter and the discharge coefficient and the unclear tendencies they have

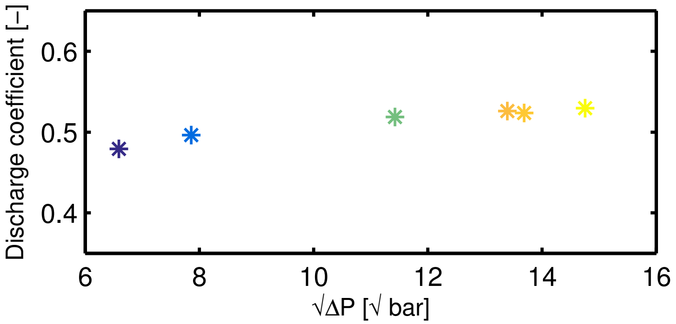

Figure 4.31: Discharge coefficient (Cd) of the Spray G nozzle evolution with the square root of the pressure drop.

with the square root of the pressure drop (or Reynold's) is completely different compared to typical diesel injectors, where the tendencies are clear and the values are significantly higher, even with cavitating nozzles [14, 33]. This substantial differences come from the fundamental difference in design of modern GDi injectors, and as seen throughout the section, dramatically affects the internal flow characteristics of the injectors. Modern GDi injectors are designed with bigger holes, stepped geometries and operate at a much lower pressure. Moreover, the needle lift for the Spray G injector is only 45 µm which is more than three times smaller than the orifices internal diameters. These differences in design are mostly aimed at increasing turbulence and mixing, decreasing spray break-up length, and to promote plume-to-plume interaction for correct flame propagation. The low values of the hydraulic coefficients studied in the section are a result of the flow being choked in the needle due to low needle lift, the sharp corners between the needle seat and the holes, and the low value of L/D in the nozzle orifices, which have been shown to cause separation of flow and recirculation zones [17–21, 34]. The resulting behavior for the internal and external flow of these type of GDi injectors, is therefore much more complex than in the Diesel case given the choking of the flow in the needle, the presence of the counterbore, the plume interaction, etc. The number of variables included and the complexity of analyzing each of them separately is a massive endeavor that must be undertaken if the goal of creating completely predictive injection and combustion models is pursued.

4.6 Near-nozzle x-ray radiography and spray tomography

4.6.1 X-ray radiography. Projected mass

Apart from the internal nozzle geometry measurements, near-field spray radiography experiments were performed at Sector 7-BM in the APS of Argonne National Laboratory. Part of these measurements were presented in several publications [24, 35]. This section comprises the results from two types of experiments. The first was the spray radiography, which yielded the projected mass in the "primary orientation" lateral plane. The principles were detailed in the methodology chapter in section 3.5.4. In brief, a monochromatic x-ray beam is focused to a 5 x 6 μm^2 (full width at half maximum) spot using a pair of x-ray focusing mirrors. The beam passes through a line of sight in the spray and the transmission of the x-rays is recorded on a fast PiN diode. By translating the spray through the fixed beam, a time-resolved, ensemble-average distribution map of the spray is obtained through equation (3.14). Fig 4.32 shows a time sequence of the ensemble-averaged data. Each of the individual images contain all of the measured positions at a given time. Each position was measured 300 times and is resolved in time with around 1200 grid points in the complete swipe. The blue triangle represents the limits of the grid.

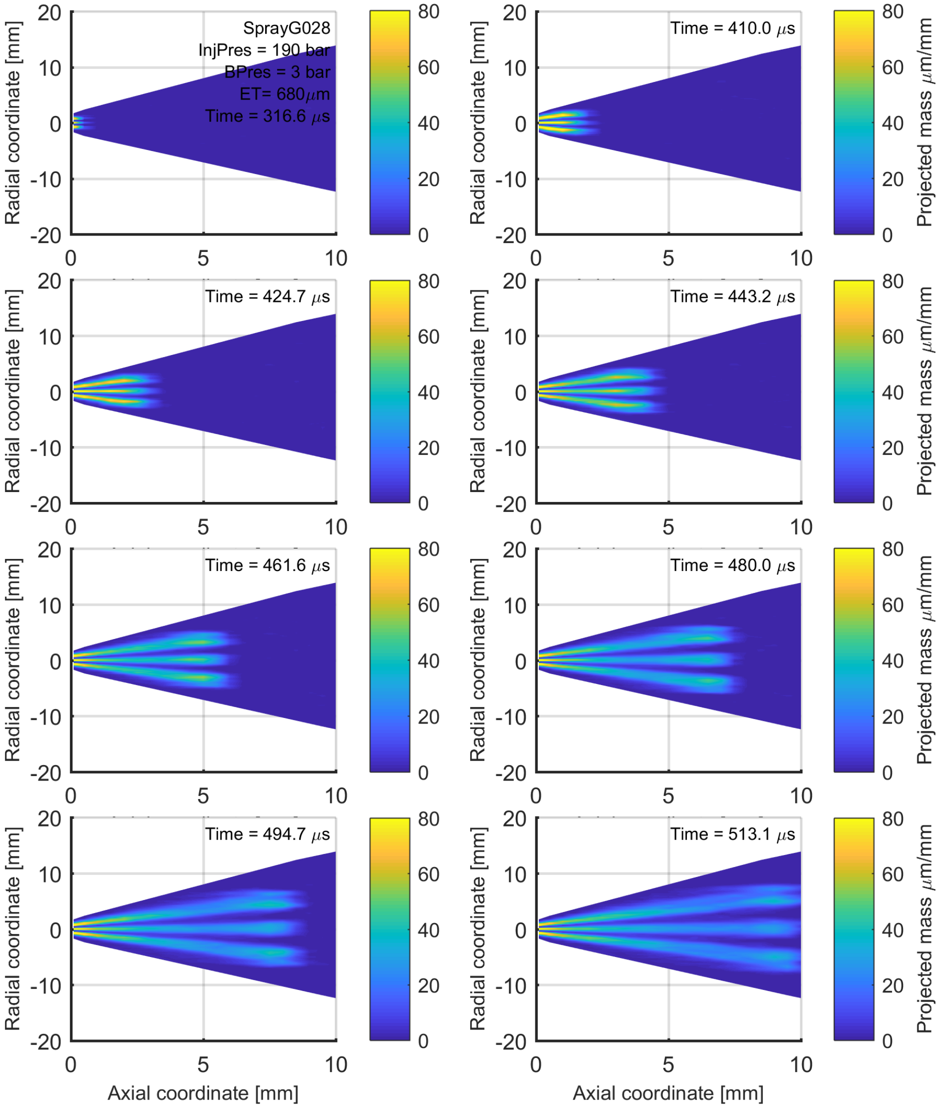

Figure 4.32: Montage of injection process for one of the tests of spray radiography. The images are created by plotting together all of the measured positions (one per shot) and interpolating the grid. Therefore, one image contains a large number of injections.

Similar x-ray radiography data have been used before to calculate spray penetration during the first millimeters of the nozzle showing good agreement with visualization data [24], which is done similarly to the methodology explained for visualization data (see section 3.6). However, the interest of this analysis is limited because it only provides the penetration for the first 9 mm of the spray and because the information represents thousands of injections, which makes the contour at the spray tip not well-defined. One possible way of validating the x-ray radiography experiments, is comparing them to the injection rate presented in 4.4. The x-ray radiography data provides the "area density" of the spray, therefore integrating along the radial and axial coordinates can provide the total mass in the domain. After the SOI, the total mass in the region would start to rise and then stabilize after a given time that is dependent on the size of the region. The steady state injection rate is then calculated fitting a line to the rising slope of the mass from the SOI until before the total mass in the region stabilizes. Fig 4.33 graphically represents this process. The slope of the fit would be the steady state rate of injection calculated using this methodology. The value is compared to the steady state ROI (presented in Fig 4.11, section 4.4) in Table 4.2 showing good agreement.

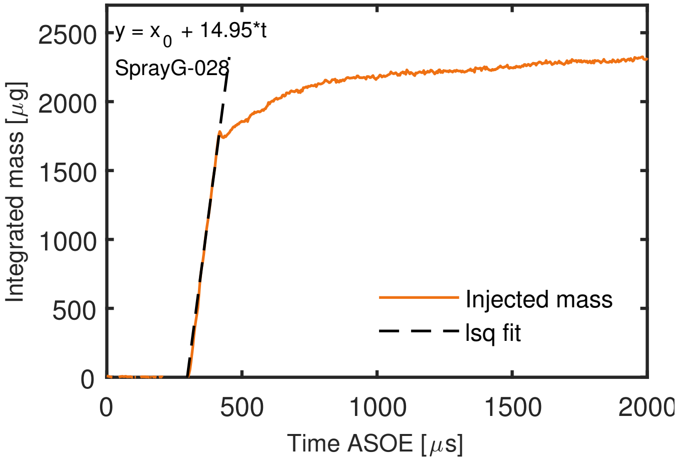

Figure 4.33: Double integration of x-ray radiography data in the domain versus time. The slope of the fit represents the stabilized rate of injection

As stated before, the radiography data was taken at discrete coordinates by making swipes in the radial positions for several axial distances. The axial distances for the SprayG-028 injector are shown in Table 4.3.

Table 4.2: comparison of the steady state roi for the SprayG-026 and the integrated mass of the SprayG-028

ROI [g/s] SprayG-028 Radiography	ROI [g/s] SprayG-028 Rate meter
14.95	14.71

Table 4.3: Axial positions for the x-ray radiography experiments for SprayG-028

Axial position [mm]	*0.1, 0.5, 1, 1.5, 2, 2.5, 3, 3.5, 4, 4.5, 5, 5.5, 6, 6.5, 7, 7.5, 8, 8.5, 9, 9.5, 10*

For each one of the axial distances, the Transverse Integrated Mass (TIM) can be calculated by integrating all the radial grid points measured. This provides the planar density of the spray at the selected locations, and was calculated through equation (4.4).

$$\mathrm{TIM}(z,t)\,[\mu g/mm] = \int_{x_i} M(y,z,t)\,dy \tag{4.4}$$

Fig 4.34 represents the TIM for all of the axial positions measured. Even though the positions are discrete, the legend was chosen to be represented as a colobar for clarity. It can be appreciated how the TIM increases as the axial distance from the nozzle tip is increased, which signifies a deceleration of the flow in space and in time.

During steady state, there is no accumulation of mass in the domain, so changes in the time-average steady-state TIM can be directly related to relative change in mass-averaged axial velocity with axial position [36]. Therefore, the deceleration can be calculated by comparing the TIM at a particular axial distance with the TIM at the nozzle exit through equation (4.5).

$$\frac{V_{\mathrm{ma}}(z,t)}{V_e} = \frac{\mathrm{TIM}(0,t)}{\mathrm{TIM}(z,t)}, \tag{4.5}$$

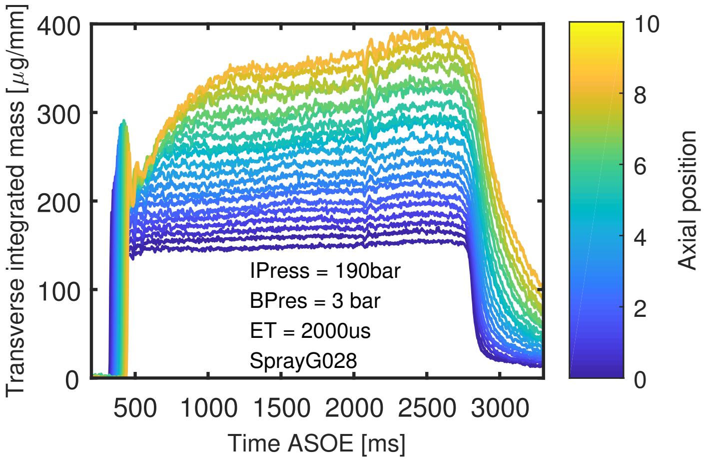

Figure 4.34: Transeve Integrated Mass (TIM) for all the axial positions experimented in the x-ray radiography of the SprayG-028. At steady state, an increase in the TIM is related to a deceleration of the flow.

where $V_{\text{ma}}(z, t)$ represents the mass-averaged velocity at axial position z and time t, and V_e represents the velocity at the nozzle exit.

As it was discussed in the geometry section 4.2, these nozzles are designed with a very low L/D ratio, which combined with the low needle lift produce flow separation, low discharge coefficient, short break-up distances, etc. A key characteristic of this kind of nozzles produced by their design is the fast deceleration of the flow compared with typical Diesel injectors as can be seen represented in Fig 4.35. The graph represents the normalized velocity decay profiles for SprayG-028 compared to several Diesel Spray A injectors, using the normalized V_{ma} in the y-axis and a normalized axial distance in the x-axis. The non-dimesional length scale is used on the horizontal axis to account for variations in the ambient to liquid density ratio (ρ_a/ρ_l) and the effective diameter of the jet d_{eff}:

$$Z^* = \frac{z}{d_{\text{eff}}}\sqrt{\frac{\rho_a}{\rho_l}} \tag{4.6}$$

The non-dimensional scale was used before to describe the evolution of turbulent gas jets [36]. The effective diameter was determined previously in section 4.4. As expected, the Spray G injector presents a much bigger decay of the velocity in the axial direction, especially at the exit of the nozzle where the decreasing slope is maximum. Upon close inspection, it can be noted how the diesel sprays remain mostly undisturbed, even with a slight increase in the velocity for the first three points (circles). In this near-nozzle region, the flow from Diesel injectors is unperturbed until what is known as the intact core [9, 37]. This intact core is not manifested for the Spray G nozzle (in the primary orientation in red or the secondary orientation in black), because of the high turbulence in the flow and because the extra-thickness of the counterbore does not allow the measurement to be performed at the inner hole exit, where this phenomenon could be occurring. The fast decay of velocity evidences a rapid momentum exchange with the ambient and a rapid expansion of the sprays, which are key design features in GDi injectors to promote flame propagation and limit wall impingement [17, 18, 20, 38].

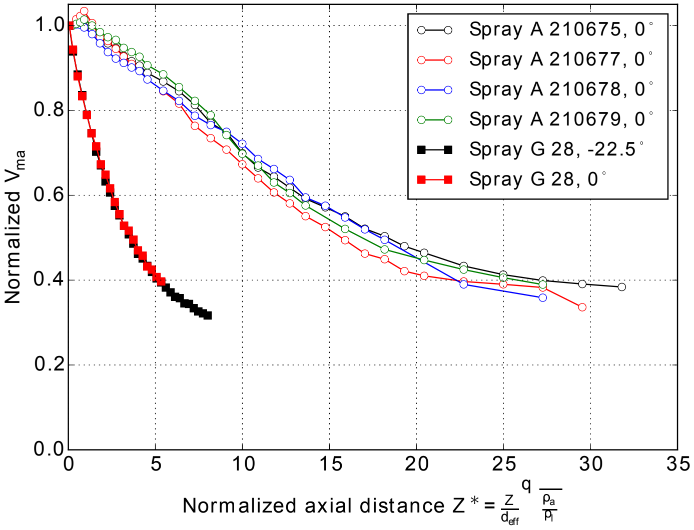

Figure 4.35: Normalized velocity decay profiles for Spray G compared to ECN Spray A diesel injectors at P_{inj} = 1500 bar, P_b = 20 bar. Reproduced from [24].

4.6.2 X-ray tomographic radiography. Plume Isolation

Due to the close spacing of the 8 holes, only 3 or 4 plumes are visible from any line of sight. In order to isolate individual plumes, x-ray tomographic radiography was employed [39]. In this study, the same nozzles that were tested in the phase-contrast tomographies for the geometry reconstructions were used here as well. The methodology was detailed in section 3.5.5. Basically, the nozzles were scanned horizontally at the plane $z = 2$ mm and rotated 180°. A penalized maximum likelihood algorithm [40] was used to reconstruct the quantitative time-resolved, ensemble-average density fields. Fig 4.36 shows a montage of the reconstructed density maps at two millimeters from the nozzle tip for all the SprayG nozzles measured. The density was time-averaged through the steady-state part of the injection. As can be seen, this technique allows to isolate each of the plumes coming out of the injectors and quantitatively evaluate plume-to-plume and nozzle-to-nozzle differences. In order to compare the mass of each plume, a mask had to be created to separate the image in eight different zones, one per spray. The masking process was done by creating an algorithm able to identify the center of the nozzle by joining lines between two opposing plumes. Once the center was calculated, the algorithm would divide the image joining the center with the mid distance of two adjacent plume centers. After the image was separted into eight segments, the segments were shrunken to avoid contact between them. This practice proved important in order to prevent assigning mass from one plume to the adjacent in the post-processing, which would make the time-resolved TIM fluctuate excessively. Several masking procedures were used until the results showed independence from the masks. Furthermore, given that the masks do not occupy the complete grid of measurements, some mass is not attributed to none of the holes and missed in the integrations. The amount of mass missed can be up to 10% of the total injected mass. It is clear that there are many differences between the nozzles and plumes that can be observed in Fig 4.36. However, this visualization is not ideal to identify specific phenomena and differences, but rather to give a general perspective of the data that was measured in the campaign. In order to show the differences between the measured nozzles, Fig 4.37 is presented next.

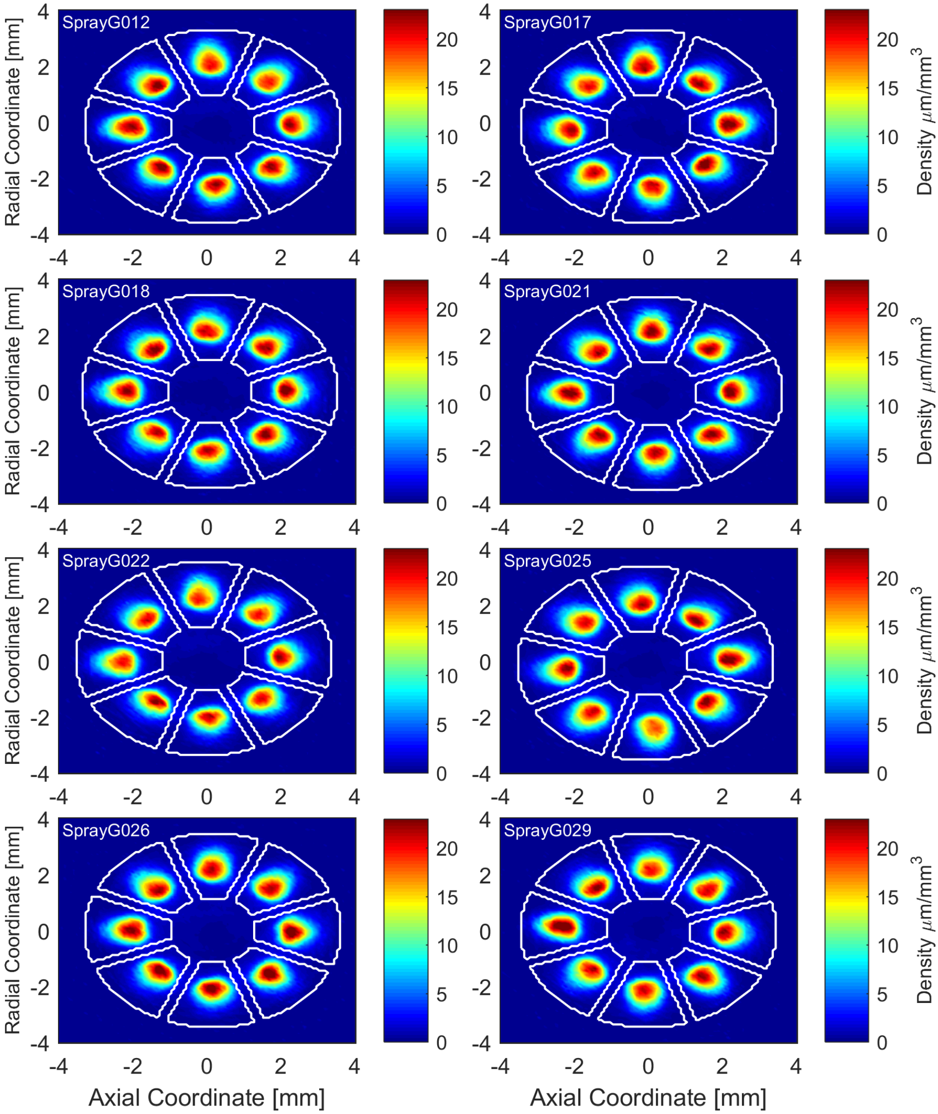

Figure 4.36: Montage of the reconstructed x-rays radiography slices at 2 mm from the nozzle tip for all the Spray G nozzles measured. The eight plumes are going outside the page towards the reader. The images show the time-averaged results for the steady-state part of the injection.

The transverse integrated mass (TIM) was calculated through equation (4.4) as it was done previously for the radiography results. Fig 4.37 compares the planar mass passing through the 2 mm axial position for all the nozzles. It can be observed that all the injectors show similar behavior, except SprayG-022 that shows a decreased mass flow than the rest. The main differences between all nozzles are the start and end of injection times. This disparity can be related to differences in the injectors, but it can also be related to the fact that the same driver was used for all the nozzles, instead of using each nozzle with the original paired driver. Another difference is the magnitude of the peak at the end of the rising slope, which mainly varies between two levels for all the different curves. This peak has also being observed before in the ROI, needle lift and ROM measurements. Given that the overshot of the needle was identified in the phase-contrast experiments, it is natural to assume that this is the reason to observe it here as well. Nonetheless, as it was also the case for the ROM results, an accumulation phenomena can also be contributing to the effect. As the needle opens, the first droplets come out with very low velocities, whereas the flow coming out later is not as throttled and can have a faster velocity, effectively catching up to the fuel injected first. Therefore, the observed peak is attributed to the needle overshot and the accumulation phenomena, and the differences between the peaks are therefore attributed to changes in the needle overshot or the outlet velocity in the first instants of the injection. Unfortunately, the needle lift experiments were only performed for one of the injectors, so discerning between the two contributing effects is not possible.

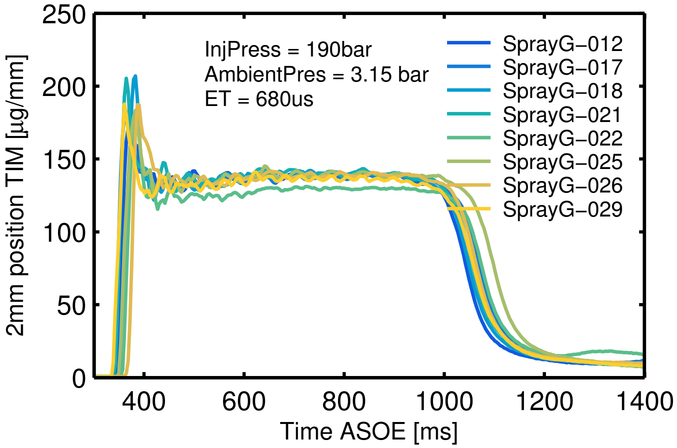

Figure 4.37: Transverse integraged mass at 2 mm from the nozzle tip for all the Spray G injectors tested.

Fig 4.38 shows the TIM of each of the holes separately for 4 of the nozzles experimented with the tomographic radiography technique. An interesting characteristic that can be observed in the individual plots is the different frecuencies of the signals that remain equal in one nozzle but change nozzle to nozzle. This is especially obvious between SprayG-17 and SprayG-18, where the TIM oscillates at a higher frequency. This was attributed to the masking procedure at first but the analysis was repeated using a range of masks and the results always maintained these characteristics frequencies. It is likely that this characteristic alone does not affect the spray development in a significant way. Nonetheless, it would be interesting to know if it is this differences comes from the injectors or from the measurement system and it is left as a topic for future research. It can be noted that the mass of all the holes is similar between injectors, also conserving a similar amount of variability. Some nozzles present a higher flowing hole, like SprayG-18 and SprayG-029, which is likely related to changes in specific geometrical characteristics of the holes. The dribble is known as the amount of mass injected after the EOI, and it is of great importance as it can cause locally rich mixture that create soot HC emissions and fuel deposits [41, 42]. The dribble attributed to the rebound of the needle after closure and the volume of the fuel that is left in the sac of the needle seat and can change depending on the ambient pressure and temperature conditions [42]. All the injectors tested produced some amount of dribble, with the most noticeable being hole 7# of SprayG-17. It is important to remark that the data presented in Fig 4.38 is the average of many shots. Therefore, for a particular phenomenon to be noticeable in the results, it must happen in a statistically significant manner.

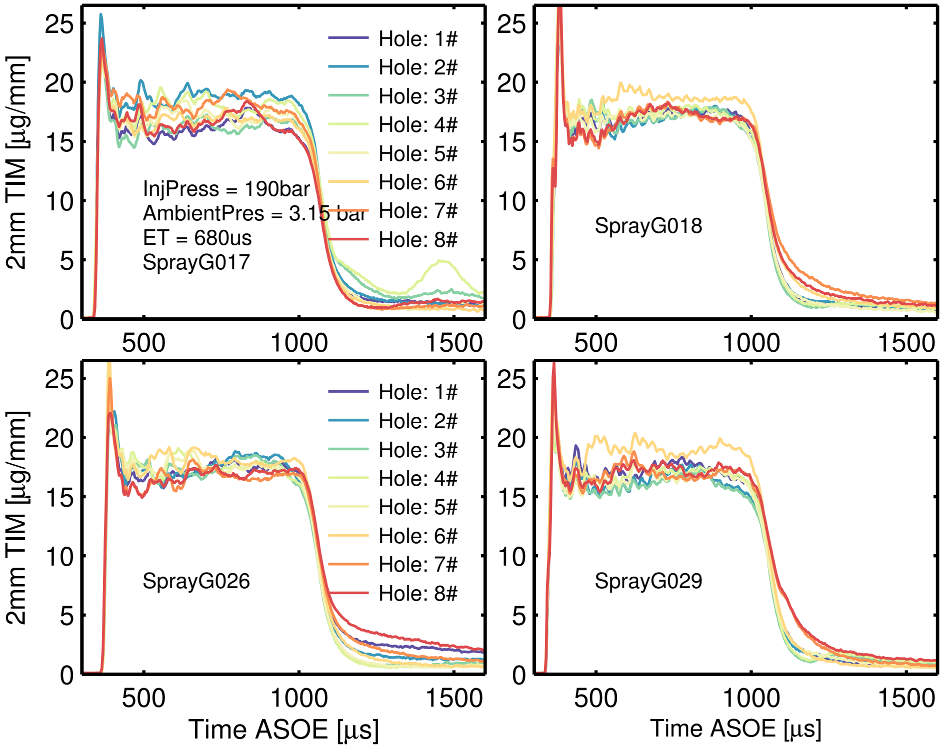

Figure 4.38: Transverse integrated mass at the 2mm axial position from the nozzle tip for 4 out of the 8 nozzles measured.

Internal geometry and near-nozzle study

This subsection combines the internal geometry presented in 4.2 and the isolated near-nozzle flow data to evaluate what geometrical variability from the nominal geometry are linked to the small changes observed in the near-nozzle mass distribution.

A multiple linear regression analysis was performed in order to combine the near-nozzle flow data from all isolated holes from the eight experimented nozzles with their internal geometry. It is important to underlie that the study here is to assess how the differences observed in the geometry of the holes affected the near-nozzle mass. Because the injectors have the exact same nominal geometry, if a certain geometrical dimension does not change from hole to hole in the nozzles, it will not affect the flow and its effect might be hidden. It is important to distinguish the following study from a study that can predict differences in flow in any nozzle, as the key dimensions here barely change. Fig 4.39 shows the variability of the geometrical parameters used for the model as well as the variability of the predictor variable. It can be noted the low variation of diameters. Moreover, even though the RSD of the inlet and outlet radii is high, this change translates to around one micron in absolute terms.

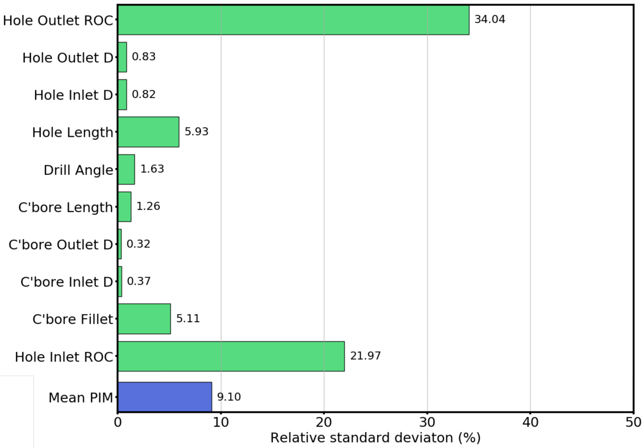

Figure 4.39: Relative standard deviation σ for the geometrical dimensions measured.

In the analysis, each orifice was treated as a sample point, allowing statistics to be carried out of $n = 64$ (8 injectors with 8 orifices) observations. The TIM or PIM (Planar integrated mass) was averaged during the steady portion of the injection [35]. The general model for the multiple linear regression given n observations is described in equation (4.7).

$$y_i = \beta_0 + \beta_1 x_{i,1} + \beta_2 x_{i,2} + \ldots \beta_m x_i + \epsilon \quad \text{for } i = 1, 2, 3, \ldots n, \tag{4.7}$$

where y_i is the predictor variable (the average TIM), $x_1, \ldots x_m$ are the explanatory variables (the dimensions listed in Table 4.1), $\beta_0 \ldots \beta_m$ are the coefficients, and ϵ is a normally distributed random variable to account for noise in the data. The coefficients were obtained using a least-squares approach, where the linear regression model attempts to minimize the sum of squared residuals between the observed and predicted values. The value of the coefficient of determination, R^2, is used to assess the goodness of fit as well as to indicate if the addition of a geometric feature improves the overall predictability of the model. Table 4.4 provides a summary of the statistics for each measured dimension, calculated by treating each nozzle hole as an independent observation.

Table 4.4: Coefficients and standard errors for the multiple regression model

Predictor	Coefficient	RSD [%]	p-value
const	-0.4258	.	0.0001
Hole inlet radius	0.5799	21.97	**0.0001**
Cbore inlet D	-0.3542	0.37	**0.001**
Hole Length	0.0212	5.93	**0.050**
Hole inlet D	0.4091	0.82	0.094
Cbore Outlet D	0.116	0.32	0.259
Hole Outlet radius	0.111	34.04	0.302

It can be seen that the p-value is lower than 0.05 only for the first three predictors (apart from the constant), meaning that the rest of variables not significant in the model (given the range of variations in the dimensions). To get these results, all the variables are fed into an algorithm that performs the fit several times trying different input variables until the highest R^2 is obtained. The value of R^2 was 48%, which means that only 48% of the changes in the data are explained by the model. A plot showing the response versus each one of the significant predictors is shown in Fig 4.40

Given the low values of the R^2 coefficient and the high magnitude of the p-values, it is clear that the response variable (TIM at 2mm) is not well correlated with the geometric dimensions measured in the injectors. This fact, by no means, can be used to conclude that the flow is not related to the internal geometry. It only demonstrates that the small differences found in the flow in all orifices using the tomographic radiography are probably not due to the small variability of the key dimensions in the internal geometry of the holes. Also, because the differences in the

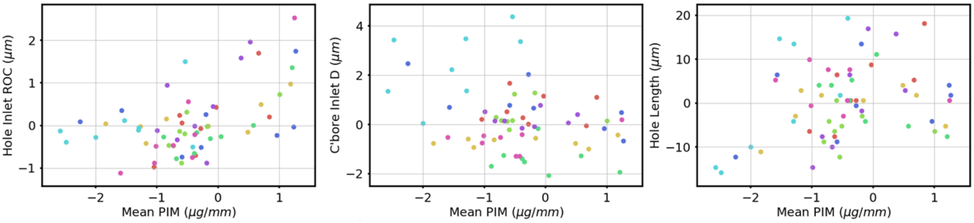

Figure 4.40: Scatter plots of response versus the most significant predictors (lowest p-value)

response and in the predictor variables are very small between holes and injectors, random variability of the boundary conditions of the experiments and other random errors can be sufficient to prevent the establishment of a good correlation. On the other hand, given the low needle lift and its effect on the flow, small changes in the needle displacement could be more significant than the measured differences in the geometry. It is therefore recommended for future work to measure the needle movement and injection rate of the eight Spray G injectors whose geometry was determined to provide a good understanding regarding the significance of injector-to-injector variability in the near-nozzle flow.

4.7 Conclusions

This section summarizes the chapter and presents the main conclusion extracted from the internal flow experimental results.

1. Internal Geometry. The section presents the key geometrical dimension extracted using X-ray tomographic reconstruction of eight Spray G nozzles. The deviations in these critical dimensions are low between all the nozzles, with the biggest differences obtained in the inner hole and counterbore radii. The short L/D ratio in the nozzles can explain many phenomena observed in the hydraulic characterization presented in the chapter.
2. Needle Lift. The lift of the needle and the random movement (wobble) obtained in X-ray phase contrast experiments was shown. The magnitude of the wobble is small and does not seem correlated with the mass flow variability in steady state. However, the overshoot

of the needle on its way up is shown in the rate of injection measurements. One of the most important conclusions is that the lift is highly linked to the dwell time in multiple injections. It was shown that the behavior of the needle changes completely for short ETs in single injections compared to the split injection case.

3. Rate of Injection. The methodology used many times for Diesel injectors has been adapted and utilized for the Spray G hardware tested in this thesis. The effect of pressure and temperature was studied, showing the expected trends in case of the pressure and no effect from the temperature within the range studied. The rate of injection overshot was linked to the needle lift. The perturbations in the steady state were not related to the wobble, but rather to the turbulence caused by the short L/D and low needle lift.

   Several ETs were studied and it was shown that the rate of injection can be higher for lower injection pressure if the duration of the command signal is sufficiently low. This behavior was attributed to the design of GDi injectors, where the needle is lifted directly by the solenoid working against the inlet pressure of the injector. For short ETs, the force exerted by the coil is canceled out by the inlet pressure, which produces the counterintuitive trend with the injection pressure.

   In addition, the mass flow of multiple injections was also studied showing surprising results. It was seen that the rate of injection was greatly dependent on dwell time, with oscillating behavior as the dwell increased. This behavior is still not completely understood but it is likely linked to the movement of the needle after closing, which was shown by tracking the small movement from the needle lift images.

4. Rate of Momentum. As it was done with the rate of injection, the rate of momentum methodology was adapted from Diesel injectors to experiment a GDi nozzle. Given the particular characteristics of GDi sprays, two configurations were used, a lateral configuration to measure the momentum flux of individual plumes and a frontal methodology, where all the plumes were measured at the same time. Due mainly to the spacing of the plumes, it was seen that the lateral methodology did not provide coherent results, which resulted in the use of the results with the frontal configuration. By combining

the rate of injection and rate of momentum measurements, several hydraulic coefficients could be calculated and used to describe the flow. It was seen that the low discharge coefficient was caused by a small effective velocity and effective area, which is ultimately caused by the internal geometry (Low L/D, counterbore and low needle lift).

5. Near-nozzle X-ray radiography and spray tomography. Two different near-nozzle experiments were done using monochromatic X-rays in sector 7-BM at APS in Argonne National Lab. The first methodology provided the projected mass from the primary injector orientation (from the side) and was used to calculate the instantaneous mass distribution in the domain. The total mass injected was validated with the rate of injection showing good agreement. It was shown that the methodology could be used to calculate the transverse integrated mass (TIM), which was shown to increase rapidly with the axial position. It was shown that the increase in TIM is linked to the rapid deceleration of the spray, which was compared to previously studied Diesel injectors. The rapid spray deceleration is linked again to the internal geometry of the injectors, short L/D ratio and low needle lift, which causes short primary spray break-up and the marked deceleration observed.

   In the spray radiography, the resulting mass of the spray is seen from the side (primary orientation), where the plumes are grouped together. In order to isolate the different plumes, spray tomographic radiography was performed, measuring in a plane two millimeters from the nozzle tip of eight Spray G nozzles. The time-averaged reconstructed results were shown in two-dimensional plots. Also, the time-resolved mass coming out of the different holes was presented. The close agreement regarding mass flow for the holes within the same injectors and for different injectors was examined. The most different one was injector #22, that produced slightly lower steady state mass flow than the rest. The perturbations in the integrated mass had a different frequency injector to injector but the same for different orifices within the same injector, which was attributed to experimental issues.

   The spray tomography of the eight nozzles was combined with the internal geometry measurements and a model was obtained linking the differences in mass with the differences in geometry. The model identified the counterbore radius as the parameter that affected the flow the most. However, the coefficient of the determination of the model resulted very low, meaning that only a small percentage of the variability of the flow could be linked to the differences in geometry. However, the low coefficient of determination does not imply that the geometry does not affect the flow but rather that the small flow variability between nozzles is not well correlated with the low differences found in the key geometrical dimensions. Given the low differences between injectors, and the high complexity and turbulence in these nozzles due to their particular design, this result is not surprising.

References

[1] Benajes, Jesus, Pastor, Jose Vicente, Payri, Raul, and Plazas, Alejandro Hernan. “Analysis of the influence of Diesel nozzle geometry in the Injection Rate characteristic”. *Journal of Fluids Engineering (ASME).* Vol. 126 (2004), pp. 63–71.

[2] Payri, Raul, Tormos, Bernardo, Salvador, Francisco Javier, and Plazas, Alejandro Hernan. “Using one-dimensional modelling codes to analyse the influence of diesel nozzle geometry on injection rate characteristics”. *International Journal of Vehicle Design*, vol. 38.1 (2005), pp. 58–78.

[3] Winklhofer, Ernst, Wiesler, B, Ahmadi-Befrui, B, and Cresnoverh, G. “The influence of injection rate shaping on Diesel fuel sprays - an experimental study”. *Proceedings of the Institution of Mechanical Engineers, Part D: Journal of Atomobile Engineering*, vol. 206 (1992), pp. 173–183.

[4] Payri, Raul, Gimeno, Jaime, Bracho, Gabriela, and Vaquerizo, Daniel. “Study of liquid and vapor phase behavior on Diesel sprays for heavy duty engine nozzles”. *Applied Thermal Engineering*, vol. 107 (2016), pp. 365–378. doi: `10.1016/j.applthermaleng.2016.06.159`.

[5] Luo, Fuqiang, Cui, Huifeng, and Dong, Shaofeng. “Transient measuring method for injection rate of each nozzle hole based on spray momentum flux”. *Fuel*, vol. 125 (2014), pp. 20–29. doi: `10.1016/j.fuel.2014.02.011`.

[6] Payri, Raul, García, Antonio, Domenech, Vicent, Durrett, Russell P, Plazas, Alejandro Hernan, Garcia, Antonio, Domenech, Vicent, Durrett, Russell P, and Plazas, Alejandro Hernan. “An experimental study of gasoline effects on injection rate, momentum flux and spray characteristics using a common rail diesel injection system”. *Fuel*, vol. 97 (2012), pp. 390–399. doi: `10.1016/j.fuel.2011.11.065`.

[7] Postrioti, Lucio, Bosi, Maurizio, Cavicchi, Andrea, Gioia, Rita Di, Bonandrini, Giovanni, Marelli, Magneti, and Spa, Powertrain. "Momentum Flux Measurement on Single-Hole GDI Injector under Flash-Boiling Condition". *SAE Technical Paper 2015-06-2480* (2015). doi: `10.4271/2015-24-2480`.

[8] Kostas, J., Honnery, D., Soria, J., Kastengren, A., Liu, Z., Powell, C. F., and Wang, J. "Effect of nozzle transients and compressibility on the penetration of fuel sprays". *Applied Physics Letters*, vol. 95.2 (2009). doi: `10.1063/1.3182821`.

[9] Fansler, Todd D and Parrish, Scott E. "Spray measurement technology: a review". *Measurement Science and Technology*, vol. 26.1 (2015), p. 012002. doi: `10.1088/0957-0233/26/1/012002`.

[10] Payri, Raul, Salvador, Francisco Javier, Martí-Aldaraví, Pedro, and Vaquerizo, Daniel. "ECN Spray G external spray visualization and spray collapse description through penetration and morphology analysis". *Applied Thermal Engineering*, vol. 112 (2017), pp. 304–316. doi: `10.1016/j.applthermaleng.2016.10.023`.

[11] Costa, M., Marchitto, L., Merola, S.S., and Sorge, U. "Study of mixture formation and early flame development in a research GDI (gasoline direct injection) engine through numerical simulation and UV-digital imaging". *Energy*, vol. 77 (2014), pp. 88–96. doi: `10.1016/j.energy.2014.04.114`.

[12] Nicky van Foreest. *Fitting an Ellipse to a Set of Data Points.*

[13] Kastengren, Alan, Powell, Christopher F, Arms, Dohn, Dufresne, Eric M, Gibson, Harold, and Wang, Jin. "The 7BM beamline at the APS: a facility for time-resolved fluid dynamics measurements". *Journal of Synchrotron Radiation*, vol. 19.4 (2012), pp. 654–657. doi: `10.1107/S0909049512016883`.

[14] Gimeno, Jaime. "Desarrollo y aplicación de la medida del flujo de cantidad de movimiento de un chorro Diesel." PhD thesis. Universidad Politecnica de Valencia, 2008.

[15] White, Frank. *Fluid Mechanics.* 2010, p. 862. doi: `10.1111/j.1549-8719.2009.00016.x.Mechanobiology`.

[16] LICHTAROWICZ, A, DUGGINS, R K, and MARKLAND, E. “Discharge coefficients for incompressible non-cavitating flow through long orifices”. *Journal of Mechanical Engineering Science*, vol. 7.2 (1965), pp. 210–219. DOI: `10.1243/JMES_JOUR_1965_007_029_02`.

[17] MOON, SEOKSU, KOMADA, KEISUKE, SATO, KIYOTAKA, YOKOHATA, HIDEAKI, WADA, YOSHITAKA, and YASUDA, NOBUHIRO. “Ultrafast X-ray study of multi-hole GDI injector sprays: Effects of nozzle hole length and number on initial spray formation”. *Experimental Thermal and Fluid Science*, vol. 68 (2015), pp. 68–81. DOI: `10.1016/j.expthermflusci.2015.03.027`.

[18] TU, PO-WEN, CAO, LI, XU, HONGMING, EALL, ADAM, VENUS, JENS KRUEGER, SRIVASTAVA, DHANANJAY KUMAR, DEAN, KARL, and JING, DALIANG. “Numerical Investigation of GDI Injector Nozzle Geometry on Spray Characteristics”. *SAE Technical Paper 2015-01-1906*, 201509061 (2015). DOI: `10.4271/2015-01-1906`.

[19] SHOST, MARK A., LAI, MING-CHIA, BEFRUI, BIZHAN, SPIEKERMANN, PETER, and VARBLE, DANIEL L. “GDi Nozzle Parameter Studies Using LES and Spray Imaging Methods”. *SAE Technical Paper 2014-01-1434*, vol. 1 (2014). DOI: `10.4271/2014-01-1434`.

[20] BEFRUI, BIZHAN, CORBINELLI, GIOVANNI, SPIEKERMANN, PETER, SHOST, MARK, and LAI, MING-CHIA. “Large Eddy Simulation of GDI Single-Hole Flow and Near-Field Spray”. *SAE International Journal of Fuels and Lubricants*, vol. 5.2 (2012), pp. 620–636. DOI: `10.4271/2012-01-0392`.

[21] SHOST, MARK. “Evaluation Of Nozzle Geometry On High Pressure Gasoline Direct Injection Spray Atomization”. PhD thesis. Wayne State University Dissertations, 2014.

[22] MOON, SEOKSU, LI, TIANYUN, SATO, KIYOTAKA, and YOKOHATA, HIDEAKI. “Governing parameters and dynamics of turbulent spray atomization from modern GDI injectors”. *Energy*, vol. 127 (2017), pp. 89–100. DOI: `10.1016/j.energy.2017.03.099`.

[23] Mitroglou, N, Nouri, J M, Yan, Y, Gavaises, M, and Arcoumanis, C. “Spray Structure Generated by Multi-Hole Injectors for Gasoline Direct-Injection Engines Reprinted From : Diesel Injection SI Engine Technology”. *SAE Technical Paper 2007-01-1417* (2007). doi: `10.4271/2007-01-1417`.

[24] Duke, Daniel J et al. “Internal and near nozzle measurements of Engine Combustion Network “Spray G” gasoline direct injectors”. *Experimental Thermal and Fluid Science*, vol. 88 (2017), pp. 608–621. doi: `10.1016/j.expthermflusci.2017.07.015`.

[25] Costa, Michela, Allocca, Luigi, Montanaro, Alessandro, Sorge, Ugo, Iorio, B, Cnr, Istituto Motori, and Marconi, Viale. “Multiple Injection in a Mixed Mode GDI Boosted Engine”. *SAE Technical Paper* (2010), p. 15.

[26] Hoffmann, Guy, Befrui, Bizhan, Berndorfer, Axel, Piock, Walter F., and Varble, Daniel L. “Fuel System Pressure Increase for Enhanced Performance of GDi Multi-Hole Injection Systems”. *SAE Technical Paper 2014-01-1209* (2014). doi: `10.4271/2014-01-1209`.

[27] Marseglia, G., Costa, M., Catapano, F., Sementa, P., and Vaglieco, B.M. “Study about the link between injection strategy and knock onset in an optically accessible multi-cylinder GDI engine”. *Energy Conversion and Management*, vol. 134 (2017), pp. 1–19. doi: `10.1016/j.enconman.2016.12.012`.

[28] Sellnau, Mark, Foster, Matthew, Hoyer, Kevin, Moore, Wayne, Sinnamon, James, and Husted, Harry. “Development of a Gasoline Direct Injection Compression Ignition (GDCI) Engine”. *SAE Int. J. Engines*, vol. 7.2 (2014), pp. 835–851. doi: `10.4271/2014-01-1300`.

[29] Sellnau, Mark, Moore, Wayne, Sinnamon, James, Hoyer, Kevin, Foster, Matthew, and Husted, Harry. “GDCI Multi-Cylinder Engine for High Fuel Efficiency and Low Emissions”. *SAE International Journal of Engines*, vol. 8.2 (2015), pp. 775–790. doi: `10.4271/2015-01-0834`.

[30] PAYRI, RAUL, GIMENO, JAIME, MARTI-ALDARAVI, PEDRO, and VAQUERIZO, DANIEL. "Momentum Flux Measurements on an ECN GDi Injector". *SAE Technical Paper 2015-01-1893* (2015). DOI: `10.4271/2015-01-1893`.

[31] SALVADOR, FRANCISCO JAVIER, GIMENO, JAIME, CARRERES, MARCOS, and CRIALESI-ESPOSITO, MARCO. "Fuel temperature influence on the performance of a last generation common-rail diesel ballistic injector. Part I: Experimental mass flow rate measurements and discussion". *Energy Conversion and Management*, vol. 114 (2016), pp. 364–375. DOI: `10.1016/j.enconman.2016.02.042`.

[32] WIGLEY, GRAHAM, WOOD, ANDREW, and HELIE, JEROME. "Experimental Investigation on the Stream to Stream Interactions for a Multi-hole GDI Injector with Multiple Injection Strategies". *10th International Congress, Engine Combustion Processes, Current Problems and Modern Technologies, March 24th-25th, 2011, München, Germany.* 2011, pp. 1–12.

[33] DESANTES, JOSE MARIA, PAYRI, RAUL, SALVADOR, FRANCISCO JAVIER, and GIMENO, JAIME. "Measurements of spray momentum for the study of cavitation in diesel injection nozzles". *SAE Technical Paper 2003-01-0703* (2003). DOI: `10.4271/2003-01-0703`.

[34] SAHA, KAUSHIK, SOM, SIBENDU, BATTISTONI, MICHELE, LI, YANHENG, POMRANING, ERIC, and SENECAL, PETER KELLY. "Numerical Investigation of Two-Phase Flow Evolution of In- and Near-Nozzle Regions of a Gasoline Direct Injection Engine During Needle Transients". *SAE International Journal of Engines*, vol. 9.2 (2016), pp. 2016–01–0870. DOI: `10.4271/2016-01-0870`.

[35] MATUSIK, K E, DUKE, D J, SOVIS, N, SWANTEK, A B, POWELL, C F, PAYRI, R, and VAQUERIZO, D. "A study on the relationship between internal nozzle geometry and injected mass distribution of eight ECN Spray G nozzles". *ILASS – Europe 2017, 28th Annual Conference on Liquid Atomization and Spray Systems*, September (2017). DOI: `http://dx.doi.org/10.4995/ILASS2017.2017.4766`.

[36] Kastengren, Alan L., Powell, Christopher F, Wang, Yujie, Im, Kyoung-Su, and Wang, Jin. “X-Ray Radiography Measurements of Diesel Spray Structure At Engine-Like Ambient Density”. *Atomization and Sprays*, vol. 19.11 (2009), pp. 1031–1044. doi: `10.1615/AtomizSpr.v19.i11.30`.

[37] Bardi, Michele. “Partial needle lift and injection rate shape effect on the formation and combustion of the Diesel spray”. PhD thesis. Valencia (Spain): Universitat Politècnica de València, 2014. doi: `10.4995/Thesis/10251/37374`.

[38] Tor, Università, Roma, Vergata, Demaio, A, and Numidia, S. “Reduction of Spray Momentum for GDI High- Pressure Injectors – A Necessary Step to Accomplish Series Production Super-Charged DI-Engines”. *SAE Technical Paper 2005-01-0104*, 724 (2005).

[39] Duke, Daniel J, Swantek, Andrew B, Sovis, Nicolas M, Tilocco, F Zak, Powell, Christopher F, Kastengren, Alan L, Gürsoy, Doğa, and Biçer, Tekin. “Time-resolved X-ray Tomography of Gasoline Direct Injection Sprays”. *SAE Int. J. Engines*, vol. 9 (2015), pp. 143–153. doi: `10.4271/2015-01-1873`.

[40] Gürsoy, Doga, De Carlo, Francesco, Xiao, Xianghui, and Jacobsen, Chris. “TomoPy: a framework for the analysis of synchrotron tomographic data”. *Journal of synchrotron radiation*, vol. 21.5 (2014), pp. 1188–1193.

[41] Musculus, Mark P B, Miles, Paul C., and Pickett, Lyle M. “Conceptual models for partially premixed low-temperature diesel combustion”. *Progress in Energy and Combustion Science*, vol. 39.2-3 (2013), pp. 246–283. doi: `10.1016/j.pecs.2012.09.001`.

[42] Battistoni, Michele, Xue, Qingluan, and Som, Sibendu. “Large-Eddy Simulation (LES) of Spray Transients: Start and End of Injection Phenomena”. *Oil & Gas Science and Technology – Revue d’IFP Energies nouvelles*, vol. 71.1 (2016), p. 4. doi: `10.2516/ogst/2015024`.

Chapter 5

External Spray Visualization. Results and analysis

5.1 Introduction

GDi engines rely more on the quality and conditions of the delivered spray than the older PFI systems, where simpler injectors could suffice to provide with the needed fuel. Given the current trend toward the utilization of GDi engines,; research is also shifting focus toward the newer systems [1–3]. GDi injectors can present phenomena such as flash boiling, cavitation and spray collapse that is more complex than the PFI counterparts and different than in the well-documented behavior of Diesel sprays [4].

The macroscopic characteristics of the injected spray are of great importance on GDi engines, as it affects evaporation, mixing and undesirable phenomena like wall impingement. Spray-guided GDi injectors must provide a finely-atomized spray, the plumes have to be close together to avoid local zones with low fuel concentration that can prevent the flame propagation and cause misfire, and they have to be delivered quickly and precisely. Chapter 4 focused on the understanding and the description of the internal flow of the spray G nozzles. This chapter presents the results of the visualization experiments carried out in order to describe the behavior of the injected plumes of the Spray G type injectors.

Given the involvement of this work with the Spray G topic of the Engine Combustion Network, some results presented here were obtained by other institutions. Contributions from other institutions were put together and analyzed in conjunction with the data measured in this work to deliver a presentation on the topic for the 5th workshop of the ECN that took place in April 2017 in Wayne State University in Detroit [5]. The contributed data consisted either on raw visualization movies that were processed following the methodology described in section 3.6 or in CFD data that was used to evaluate the state of the art of the computational methods used for predicting GDi sprays behavior. Any result that was measured or obtained by other institution is clearly labeled to credit their work.

It has been shown throughout the internal flow chapter how the design characteristics of the GDi nozzles like short L/D, low needle lift, counter-bore, etc; produce many differences in the flow compared to the well-documented and better understood Diesel counterparts. Because of this, it is also expected that the external flow be different and therefore evaluation of the uncertainties derived from the visualization experiments was deemed necessary. The chapter has been separated into two parts. The first part presents the results at a few of the standard Spray G conditions, combining the results from different institutions and discussing the uncertainties that GDi nozzles may have caused by the particular characteristics of their design. Even if the simulation of the flow in the Spray G injector is out of the scope of the thesis, some CFD results from two institutions are also used in this first part to discuss the status and the limitations that they currently present. The second part is dedicated to the study of the macroscopic behavior of the spray and its dependence with the ambient temperature and pressure conditions. Given the great change in the expected morphology of the spray under certain conditions, this second part is focused on describing what is known as the collapse of the spray and the effects it has on the macroscopic spray characteristics.

5.2 ECN Spray G visualization experiments.

This section presents the results gathered in multiple institutions collaborating with the ECN of the external behavior of the spray. The contributed data was analyzed and presented in the 5th workshop of the ECN that took place in Wayne State University in Detroit on April 2017 [5].

5.2.1 Vapor phase visualization.

The vapor experiments performed at CMT were done following the methodology described in 3.6. Experiments from Sandia National Laboratory (SNL), Instituto Motori, and University of Melbourne were also used here. Instituto Motori and University of Melbourne used a technique known as Quasi-Simultaneous Mie Scattering (QSMS) where a frame straddling technique is used to record one frame from a Mie Scattering set-up and the next from the Schlieren set-up, thus obtaining the visualization of liquid and vapor of the same event at almost the exact same time. Sandia used a setup similar to the one used at CMT, with one high-speed camera for the vapor phase and another for the liquid. Only the raw data was received from Instituto Motori, University of Melbourne and SNL. After adapting the different formats and type of images, the movies were processed in the same manner as the ones obtained in-house, described in section 3.6.4.

As it was shown in section 3.6.4, one of the most important steps in determining what part of the images are spray and what part are background is the thresholding value. The threshold was defined as a fixed percentage of the dynamic range of the image and represents the minimum intensity value in the image that is considered spray. In order to test how sensitive the results are to the threshold used, all the movies were processed using several thresholds. The resulting axial penetration for all the contributing institutions with all the different threshold for the standard Spray G condition is presented in Fig 5.1. The lines are colored by institutions, with the line-style representing the value of the threshold used for the binarization of images. The figure shows good agreement between all the institutions as expected, given the high-contrast images provided by the Schlieren methodology. The results are also robust to the threshold used, it can be noted how most of the different lines are overlapped with each other. The main discrepancies appear after the end of injection, when no more fuel is being injected and the remaining liquid evaporates and mixes with the air. At this point, it is expected to see variability between thresholds and institutions, given that the contrast severely decreases and the sensitivity of the set-up becomes critical.

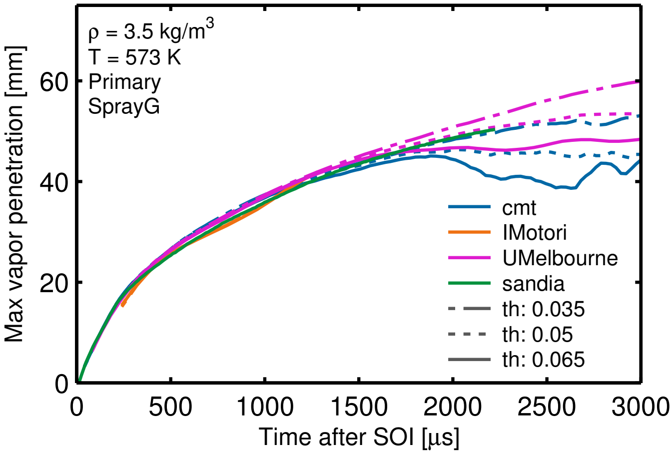

Figure 5.1: Maximum axial vapor penetration calculated using 3 different thresholding values for the vapor visualization data at Spray G conditions.

Even when the penetration results can be close between institutions and robust with different thresholds, the images coming from different set-ups could present many differences. Fig 5.2 shows a comparison of the radial profile versus time at 15 mm from the nozzle tip for the experiments done in University of Melbourne and CMT. It can be noted that while showing good agreement in penetration (in Fig 5.1), the profiles look quite different, which can be of importance if looking at the spray angle, width or area.

Given the behavior of these GDi injectors, calculating the angle of the sprays can be very problematic, and even meaningless as it was stated in section 3.6. For this reason, the profile comparisons such as the one presented in Fig 5.2 and spray widths comparisons are used instead.

The width of the sprays for the conditions appearing in Fig 5.2 calculated using the three different thresholds are plotted in Fig 5.3. It can be noted how the spray width is more dependent on the threshold than the spray penetration for both conditions but specially for the dataset from University of Melbourne. This is because the leading edge of the spray is typically well-defined and has good contrast with the background due to

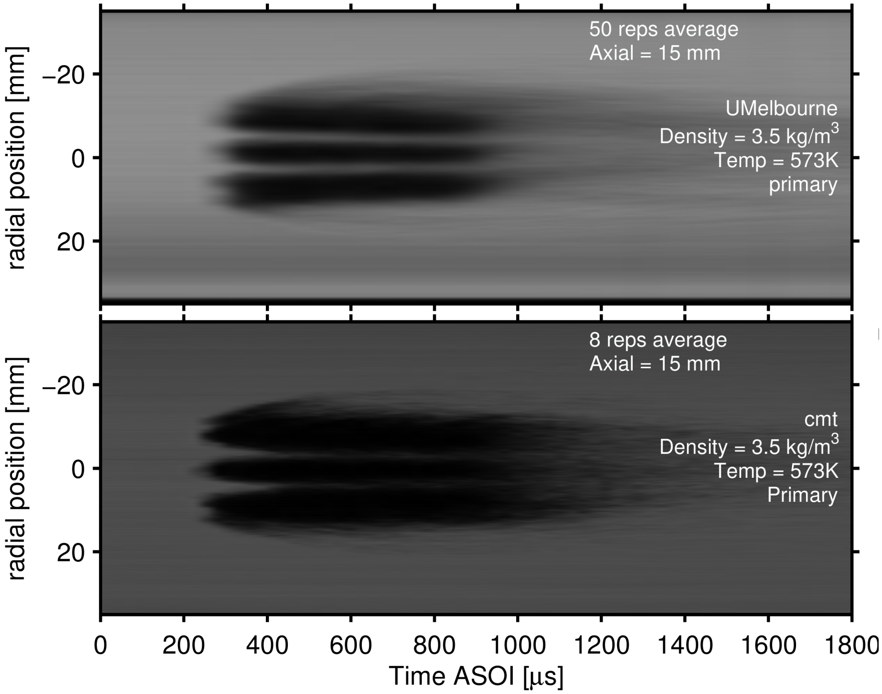

Figure 5.2: Radial profiles at 15 mm axial position from nozzle tip. Movies from University of Melbourne and CMT-Motores Térmicos. Each column of pixels is taken from the 15 mm axial position in the original images and concatenated to generate this kind of visualization.

the quantity of fuel and the fact that it might have some part in liquid phase. The radial edges of the spray at a certain axial position have different degrees of evaporation as time advances and the quantity of fuel remaining there is less. If the set-up does not have a high contrast between spray and background, the methodology is susceptible of missing the spray with a high threshold or picking up more than there really is if the threshold is too low. From Fig 5.2 it can be noted how the radial profile with the CMT images provide well-defined edges, which in turn makes the variation of the width in Fig 5.3 considerably lower.

The results have shown that the Schlieren methodology for determining the vapor contours provides robust results in spray axial penetration but it can provide a fair amount of uncertain results when looking at

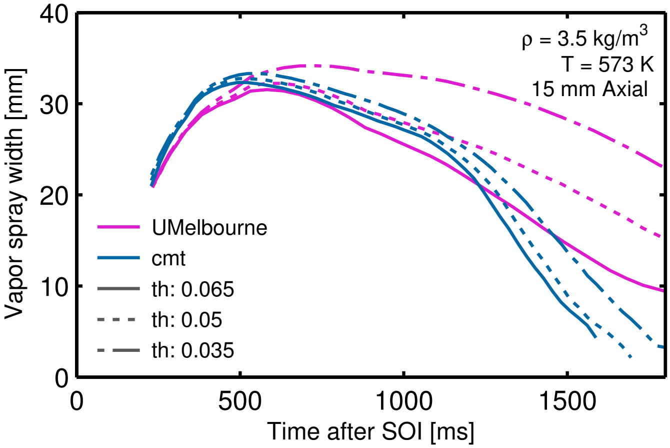

Figure 5.3: Radial width versus time for the Schlieren visualization (vapor) at Spray G standard conditions. Comparison between data gathered at CMT and University of Melbourne using three thresholds for binarization in the processing algorithm.

the radial profiles. Because of this, it is recommended to adjust the level of sensitivity of the optical arrangement given that it can be important in order to decrease the uncertainty generated by the spray detection procedure.

5.2.2 Liquid phase visualization

Liquid phase visualization was also performed in this work and received from multiple institutions as part of the ECN topic. SNL provided the images using the DBI methodology similar to the one detailed in Section 3.6, while University of Melbourne provided the liquid images from the quasi-simultaneous Mie scattering set-up defined in the previous section. The methodology used in CMT for the liquid phase was mainly DBI and was the one described in 3.6. However, a few conditions were also done using a Mie Scatter set-up. The Mie-Scatter set-up used at CMT resulted in light reflections in the windows that were not possible to avoid, which resulted in limited usability of the images gathered with this methodology.

Detecting only the liquid phase of the spray is normally harder to do than detecting the complete spray (vapor and liquid). This is because the results can be more dependent on the methodology and the particularities of the setup [6]. Mie Scattering can provide robust results when the illumination used is sufficiently powerful, and it is useful in combination with a Schlieren set-up to form a QSMS configuration that can provide liquid and vapor contours of the same event using only one high-speed camera. The main issue of this type of light-scatter imaging is that it is highly sensitive to the orientation of the illumination source which can affect the liquid penetration results significantly from different set-ups [6]. Fig 5.4 shows a radial profile at 15 mm from the nozzle tip using the images from the Mie-Scattering methodology gathered in-house and by the University of Melbourne. University of Melbourne illuminated from the front (injector axis) and collected the scattered light from the side, while at CMT the illumination and recording was done in the same side. This resulted in the sprays from CMT being more illuminated than the ones at University of Melbourne. However, the increased illumination and contrast came with the cost of light reflections on the windows that could not be avoided, which severely limited the usability of the images. Given the variability of results with respect to the set-up used, and the fact that the DBI technique is the recommended practice for liquid determination of the ECN, the present work will focus on the data gathered with the DBI technique for the liquid phase determination.

DBI is an extinction imaging technique widely used to detect liquid penetration and liquid length in Diesel sprays [7, 8]. The attenuation of light passing through a medium with particles or dropplets is related to the optical thickness (KL) through the Beer-Lamber law. The main advantage over Mie Scatter is that it provides a quantitative measurement of the optical thickness which is normalized to the specifics of the set-up used. Given that DBI is also the standard methodology in the ECN group for liquid length and liquid penetration measurements, it was chosen here as the primary technique for determining the liquid contours of the Spray G injector. Nonetheless, results using the DBI technique can also have many uncertainties that can make the optical thickness very dependent on the specific set-up used. The main cause of uncertainty in this methodology that can significantly affect the results are the gradients of the refractive index along the optical path, known as beam steering. Moreover, in the case of the Spray G injectors used in this work, the fact that there are different number of plumes depending on the zone of the spray makes the optical thickness more difficult to define. In the primary

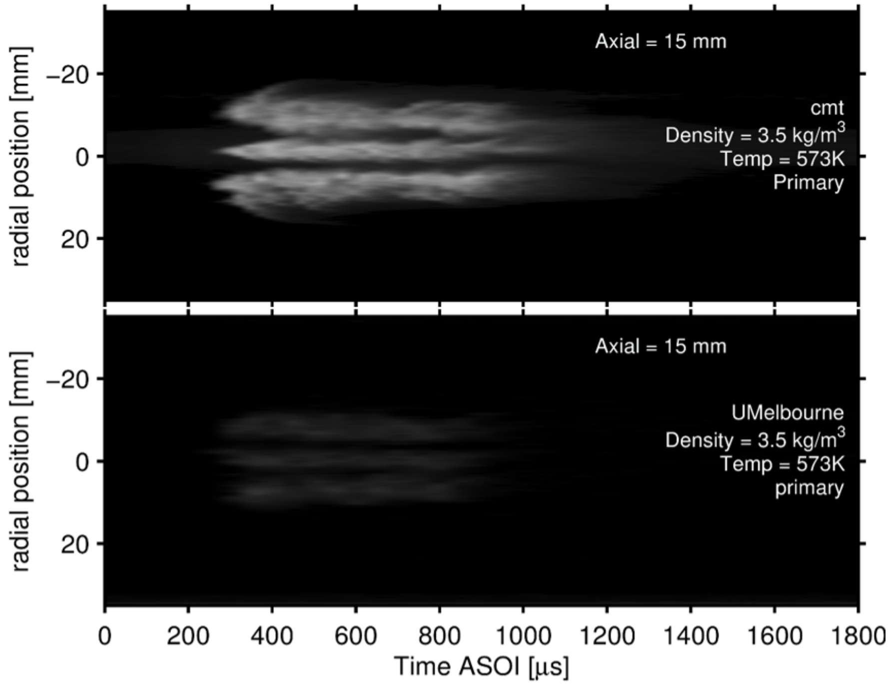

Figure 5.4: Radial profile comparison of the Mie Scattering visualization between CMT and University of Melbourne.

orientation, the camera sees three groups of plumes, with three plumes at the top, two in the middle and three at the bottom. There also might be zones where only the fuel from one of the plumes is visible (integrated) along a particular line of sight. This variability in the number of plumes in the region of interest, combined with beam-steering effects, imposes that the critical optical thickness (threshold) used to discern the liquid from the background is low enough that could capture the attenuation caused by just one plume and high enough that the attenuation caused beam-steering is discarded.

Fig 5.5 shows a sequence of four images obtained with the DBI technique at CMT (left) and Sandia (right). The images are colored with the optical thickness calculated in each pixel and the condition shown is the high-temperature and high-density condition (Spray G9). This condition was selected because the beam-steering artifacts would be higher here than in the standard condition given the higher density gradients inside the chamber. It can be noted how both set-ups are sensitive to beam-steering, with the effect being more obvious in the left-hand side images. Because of this, a threshold sensitivity study was carried out for the liquid phase, similar to the one presented in the previous section.

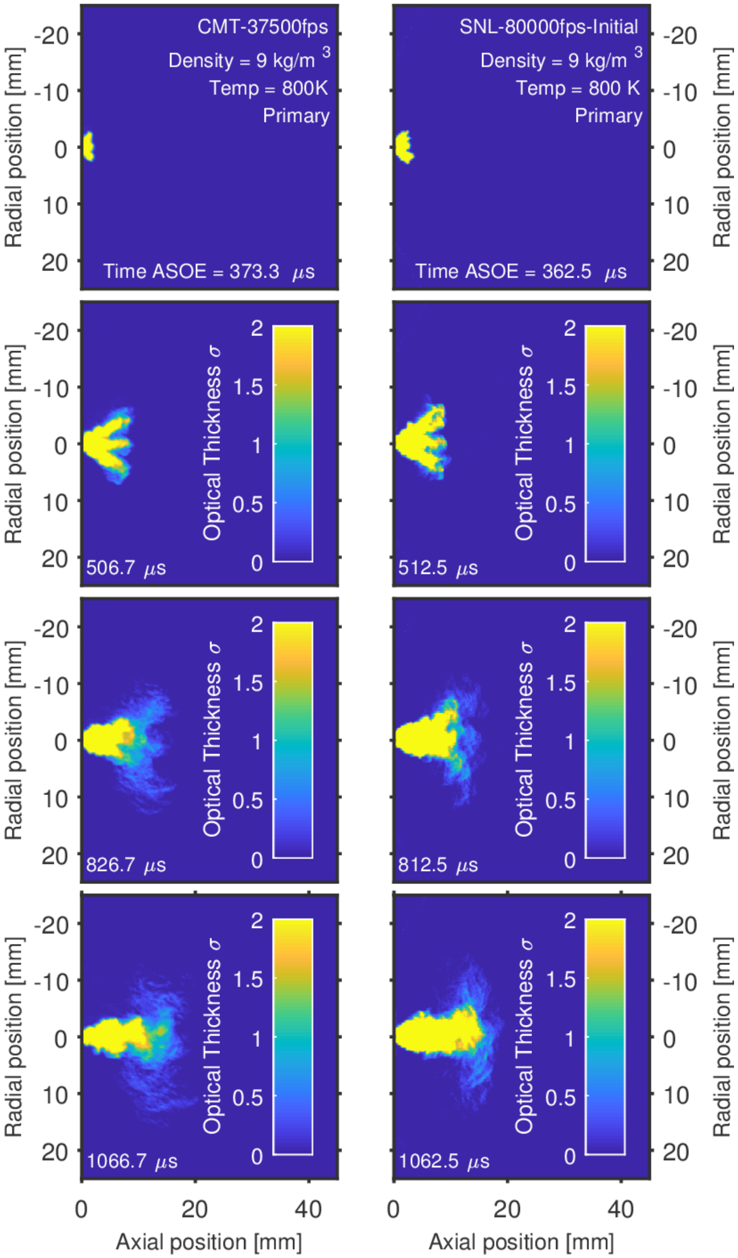

Figure 5.5: Comparison of the optical thickness values in 4 images obtained using a DBI technique from Sandia (left) and CMT (right). The set of images are recorded by different high speed cameras at different speed and therefore the times are not exactly the same.

As stated in section 3.6, the threshold for the DBI methodology is defined as the attenuation (optical thickness) that is required for a certain pixel to be considered spray. The images from SNL and CMT were processed using the same methodology with four different thresholds in order to evaluate the sensitivity of the results to the binarization procedure. The figure shows good agreement between institutions for the standard Spray G conditions and even for the high temperature and high density condition (Spray G9) presented in Fig 5.5. The lines are grouped by color, with close agreement between the institutions when using the same threshold, this means that a certain optical thickness results in a certain penetration. However, the dispersion between the results obtained with different values of thresholds prevents the determination of the “real” axial penetration, and the selection of one of the thresholds is going to imply a level of uncertainty on top of the shot-to-shot variability.

The high temperature and high density condition presents less variability than the Spray G condition, where less beam-stearing effects should be expected. This is caused by the collapse of the spray which will be treated in detail in the next section. In this case, all the plumes collapse together in the axis of the injector and create a high concentration of fuel in the tip of the spray, thus increasing the contrast with respect of the background. This effectively makes the penetration results less sensitive to the threshold, even when the beam-stearing effects are increased due to an increase in the refractive index gradient within the chamber [9].

The radial widths comparisons for the conditions presented in Fig 5.2.2 are plotted in Fig 5.7. The first row shows the data at 5 mm from the nozzle tip, while the bottom row shows the widths at the 15 mm position. It can be noted that the widths for the different thresholds are very close together when the position is close to the nozzle tip. This is due to the spray at this position has not opened yet and there is not much evaporation, resulting in a high fuel concentration that creates high attenuation of light. It can be noted how the width of the spray does not remain constant for the high density condition, but decreases over time. This behavior results from the collapse of the spray that attracts the plumes towards the injector axis. As mentioned previously, spray collapse will be treated in the following section.

The lines at the 15 mm position show more dispersion, because at this

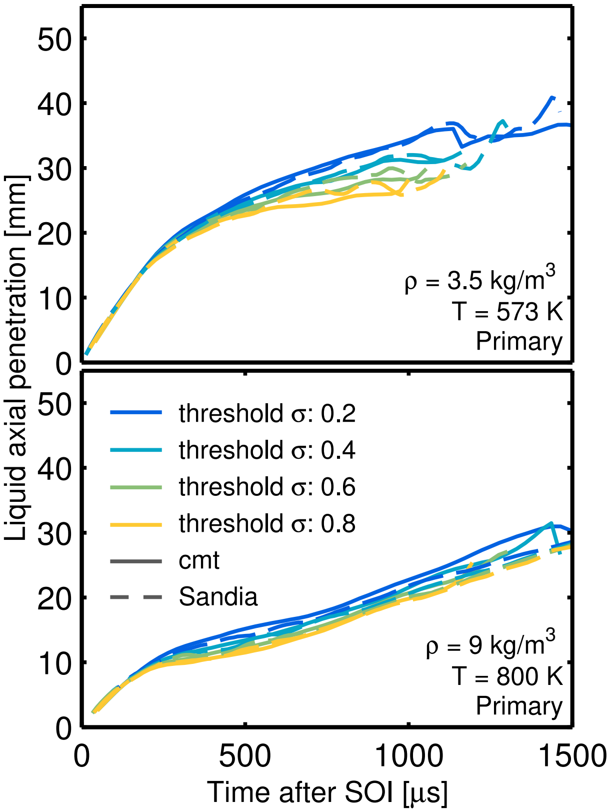

Figure 5.6: Comparison of the liquid penetration using the images from SNL and CMT at Spray G (top) and Spray G9 conditions (bottom) using 4 different thresholds.

point the spray is more spread out (wider) and the concentration of fuel is not as high creating less attenuation. Nonetheless, there is a dramatic difference between the Spray G condition and the high-temperature and density condition (Spray G9). In the latter, the variability between thresholds and setups is quite high, with the biggest difference for the blue line that represents an optical thickness threshold of $\sigma = 0.2$. At this condition, the beam-steering effects that were shown in Fig 5.5 are creating significant uncertainties that prevent to determine the actual width of the spray.

Beam steering has been an issue in many spray visualization experiments. WESTLYE et al. [10] did an important work of characterization and standardization of the DBI methodology that can result in the setup being insensitive to beam steering in high-density and high-temperature conditions relevant to those encountered by Diesel and GDi sprays. The recommendations in their work on DBI optical arrangements should be used in future visualization experiments in order to avoid the uncertainty caused by beam steering and obtain more robust results. Nonetheless, it can be noted that for lower density and temperature and for closer axial positions the spread of the lines is much lower.

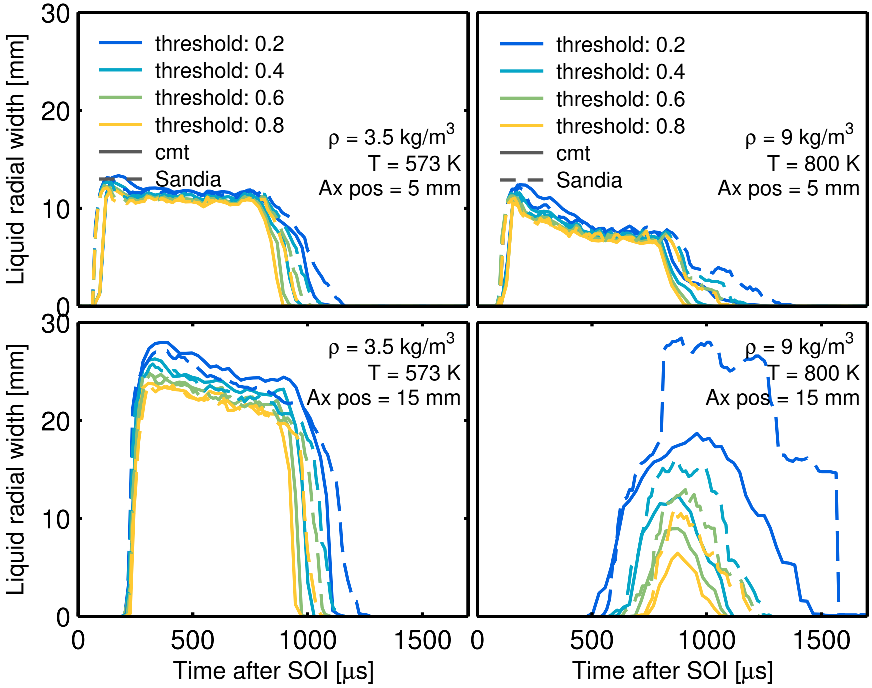

Figure 5.7: Radial width comparison between CMT and SNL liquid contours for Spray G conditios (left column) and Spray G9 conditions (right column) at 5 mm from the nozzle tip (top row) and 15 mm from the nozzle tip (bottom row).

The conclusions that can be extracted from the data and discussion included in this section is that the threshold does not affect the vapor penetration significantly but it does affect the liquid penetration. Even if the threshold affects the liquid penetration, the results between institutions are robust between thresholds, meaning that comparisons are significant as long as the same threshold is used when comparing. Moreover, given that the spread of the lines for liquid penetration is not very high for the 3 higher thresholds used, these data can be used to calculate the average and standard deviation that takes into account the uncertainties created by the beam-steering sensitivity in the set-ups. Regarding the radial width of the sprays, a value that has been chosen over the spray angle because of the added difficulty of properly defining it, it has been shown that is affected by the threshold used both in Schlieren and in DBI. The effects in Schlieren can be minimized by increasing the sensitivity of the set-up and using as much of the dynamic range of the camera as possible, therefore increasing the contrast between spray and background. The uncertainty with respect to the threshold used is more significant for liquid contours, especially when the axial distance from the nozzle is increased and the conditions are at elevated density and temperature where more refractive-index gradients are present inside the chamber. In the worst case presented in Fig 5.7, where the results are totally dependent on threshold and set-up, only comparisons using data gathered within the same experimental campaign should be compared, and only in order to identify trends. The actual width of the spray at elevated density and temperature conditions is not identifiable with a reasonable deviation with either of the set-ups used by CMT and SNL, resulting in the need of an optimized set-up following the guidelines established by Westlye et al. [10] in order to identify this quantity at any axial location (not only close to the injector).

5.2.3 Comparison of liquid and vapor visualization with computational results.

Lagrangian simulations of the external spray were also submitted to the ECN workshop, compared to the visualization experiments and presented at the workshop [5]. The focus was to evaluate how the models predict the macroscopic behavior of the Spray G injectors, which also serve as a representation of how the models can predict the behavior of typical GDi sprays. The contributions were done by Politecnico di Milano and a group formed by University of Wisconsin, KAUST and Aramco and is represented in the plots as (KWA). Some of the details of the models used by the two contributors are presented in Table 5.1. It can be noted that the models are very different, one being a RANS simulation that might take 1 or 2 hours to be completed and the other an LES simulations that takes over 12 hours with 32 processors. The simulation data from LES contains the averaged data from 5 realizations so that the results are significant.

Table 5.1: Set-up parameters of the models used by the CFD data contributors

Parameter	**Politecnico di Milano**	**KAUST-UW-Aramco**
CFD Code	**OpenFOAM–LibICE**	**OpenFOAM 2.3.x**
Turbulence Model	RANS (Standard k-epislon)	LES dynamic structure
Injection Model	Lagrangian/Huh	Lagrangian/Blob
Primary break-up	Huh-Gosman	Kelvin-Helmholtz
Secondary break-up	-	KH/RT
Vaporizaton	Spalding Number	Frössling correlation
Collision	None	None
Plume direction	**20,25,30,34,37**	**35,40**
Plume cone angle	**9,15,20,25**	**25,30,35,40**
Realizations	-	5 Realizations
Mesh refinement	Adaptative	Static
Total Cell count	120-136k	2.1 M

The defintions of plume direction and plume cone angle are represented in Fig 5.8. Plume direction refers to the angle between the plumes and the injector axis and should be close to the drill angle of the holes (37°) but slightly lower due to separation of the flow from the nozzle-hole wall because of the large turning angle as it was found in previous studies [11–13]. Plume cone angle represents the angle of the individual plumes.

In the case of simulations of GDi sprays, the plume direction and the plume cone angle are parameters that allow to adjust the behavior of the spray in order to match to the experiments. For this work, several plume direction and plume cone angles values were simulated in order to determine which produced better results both in liquid and in vapor penetration.

Fig 5.9 presents the vapor axial penetration results from the simulations performed by Politecnico di Milano compared to the experimental data obtained at CMT (in red). The experimental data presented was calculated by averaging the results obtained with the three different thresholds presented in the previous section, with the shade representing

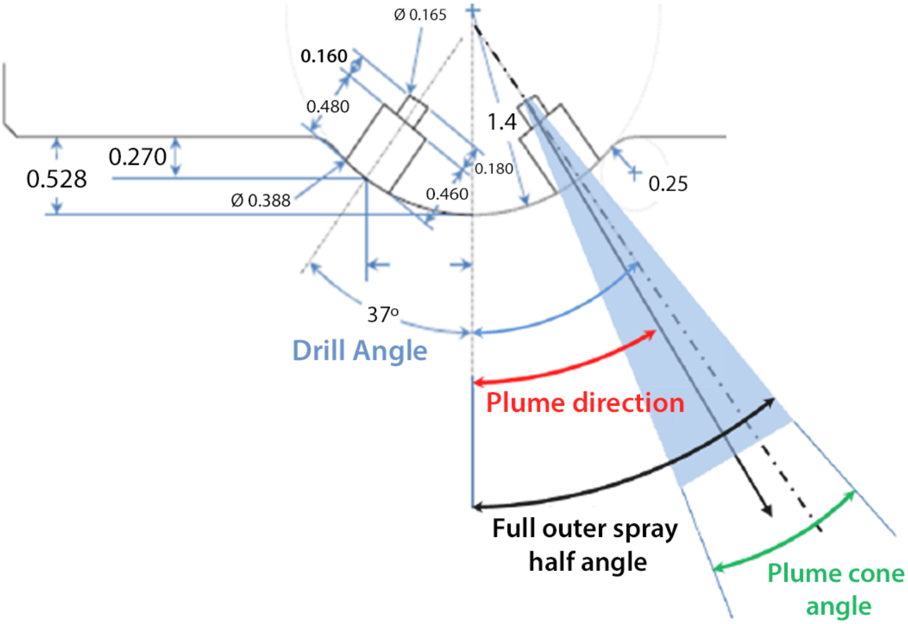

Figure 5.8: Definition of plume direction and plume cone angle, adapted from [14].

the standard deviation of these results. It can be observed that the axial penetration increases as the plume direction decreases, which is expected given that the plumes are directed more towards the injector axis. The plume cone angle has an opposite effect, decreasing penetration as the value increases. This is due to the aerodynamic forces having a bigger effect as the cones get wider, increasing momentum exchange with air and slowing down the spray. It can be seen that for vapor penetration the best match is the 37° plume direction and 9° plume cone angle, which are values close to what can be expected in those dimensions in reality. However, even for the best match, the two lines do not go together from beginning to end.

The comparison using the liquid penetration can be seen in Fig 5.10. As it was done for the vapor penetration, the experimental liquid penetration was calculated by averaging the results from the threshold study using the 3 bigger thresholds (0.4, 0.6, 0.8). The vapor lines have been maintained in order to show how close from the liquid lines they are.

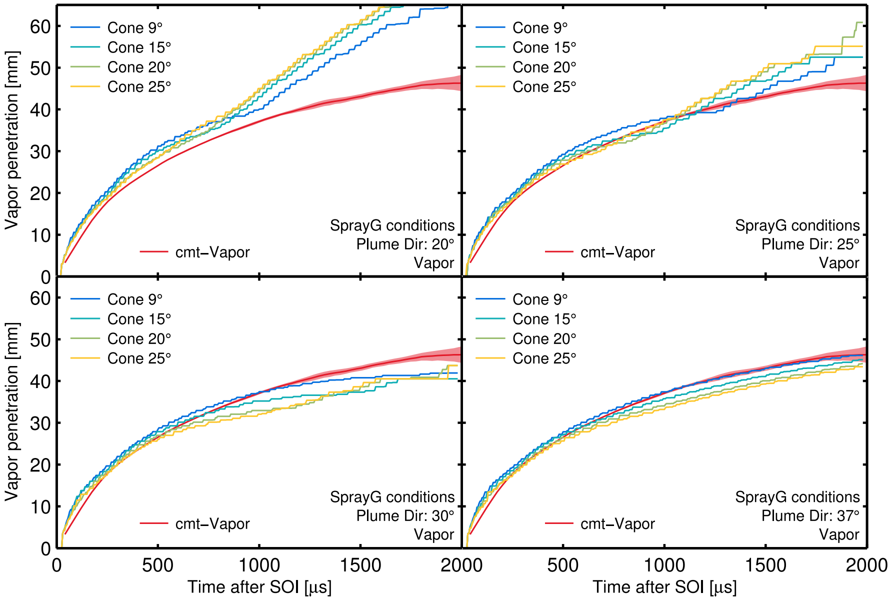

Figure 5.9: Vapor penetration comparison between computational data from Polimi and experimental data from CMT (red). The comparsions show the plume direction (20°, 25°, 30°, 37°) and the plume cone angle variations (9°, 15°, 20°, 25°).

The liquid in the simulation was calculated using an accumulated mass approach with a mass cut-off of 99%. This approach sums all the liquid in the domain and then calculates de penetration as the value where the integrated mass in the spray reaches 99% of the injected mass. It can clearly be seen in the results that the liquid definition and/or the evaporation sub-models are not capturing the trends observed with the experimental data. An additional problem with this definition of the liquid penetration is that when the injection ends, the amount of mass in the domain rapidly decreases, and the algorithm that calculates the liquid penetration clasifies all the remaining fuel, which is scattered in the domain, within the 99% mass cut-off. This leads to the liquid penetration values being meaningless after EOI.

In the case of the vapor, the post-processing algorithms calculate the penetration by checking the furthest point that has a mixture fraction higher than 0.01. This leads to a high sensitivity that in essence detects where all the fuel is, which is qualitatively similar to what is achieved

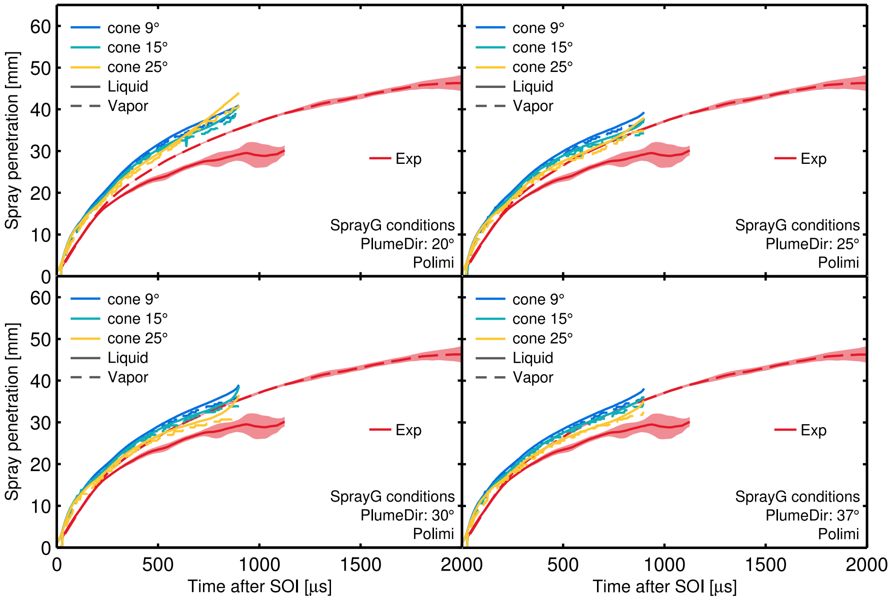

Figure 5.10: Vapor and liquid axial penetration from RANS simulations from Polimi compared to the experimental results (red).

by the Schlieren methodology. When measuring liquid penetration with the DBI methodology, what is actually being measured is the maximum length at which there is still enough liquid fuel in the line-of-sight to create an attenuation that is higher than the optical thickness threshold selected. Because of this, the threshold study performed in the last section for the liquid contours is critical. In the simulations case, there are many ways of calculating the penetration once the computation has finished, and it is important to identify a definition that allows the comparison with the liquid penetration being obtained experimentally. A definition that identifies all (or almost all) of the liquid as liquid penetration is likely going to overestimate the experiments, because isolated scattered droplets are not considered spray in the experimental methodology.

The problematic definition of the liquid penetration in simulations has been identified by many groups. The second contribution done by the group formed by Kaust, University of Wisconsin and Aramco tried to address this issue by submitting data using several definitions, which are shown in Fig 5.11. The methodologies for the determination of liquid penetration presented are:

- **Real cell volume fraction**. Liquid volume fraction with a 0.1% cut-off. This was the standard methodology in the guidelines for the Spray G topic at the moment. The methodology was found to be grid dependent, yielding higher penetration results as the grid size became lower than 1 mm.
- **Artificial cell volume fraction**. Same methodology than the previous but calculated in a generated artificial cell with constant grid size of 1 mm.
- **Cell Mie Scatter**. This method tries to simulate Mie Scattering results by integrating the surface of all the liquid droplets in the domain and projecting into a perpendicular plane. The idea behind it is that the Mie scattering approach results in illumination that is dependent on the surface of the droplets that scatter the light. The intensity collected by the camera is then higher where the there is more droplet area. After the integration, a threshold is applied to obtain the penetration. This threshold has to be calibrated previously.
- **Accumulated mass**. Same methodology than the one used by Polimi. In this case with a cut-off threshold of 97%.

It is clear that the real cell volume fraction method overestimates the liquid penetration from the experiments while the one calculated with the artificial cells is closer. Nonetheless, there is not one unique line that accompanies the experimental results to the end, as the lines stop increasing after a certain time. A similar behavior is observed with the Mie Scatter method, showing good agreement at the beginning of the injection and then falling below the experimental data after a certain time. One of the main issues of this method is that it requires the use of a threshold after the droplet surface has been integrated and that threshold is arbitrary and therefore requires calibration. The methodology that provides the closer agreement with the experiments is the accumulated mass definition, up until the EOI, where the penetration shoots up because the limitation of the method. Even if this method provides the closer results, it is still not recommended because of the arguments mentioned above and because the mass cut-off is arbitrary and therefore useful to model known behavior but not to predict unknown results.

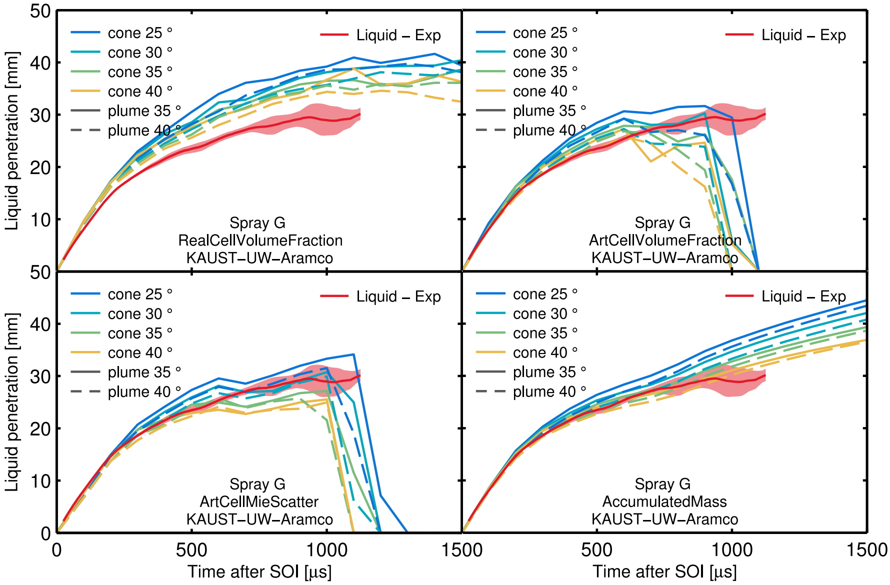

Figure 5.11: LES simulation results for liquid axial penetration calculated using 4 different methodologies versus the experimental results (red).

To finish the penetration comparison, Fig 5.12 is presented. The axial liquid penetration using the accumulated mass method (best match) has been maintained to show that the agreement in the vapor penetration occurs for the same values of plume direction and plume cone angle than in the liquid penetration. This fact is important given that selecting a set of different plume direction and plume cone angle parameters for liquid penetration and vapor penetration would not be coherent.

The simulations from Polimi and KWA have been done with different plume direction and plume cone angles. In particular, the major difference was in the selection of the cone angles, which are very different between the institutions. This comes from the fact that the models and submodels used are very different and those quantities can be used as knobs to adjust the models to the experimental results.

Through this section it has been shown the results obtained by two models in terms of vapor and liquid axial penetration against the results obtained experimentally. The vapor penetration can be well predicted, especially by the LES model, but the liquid penetration has been more problematic. It has been seen that the liquid was following the vapor

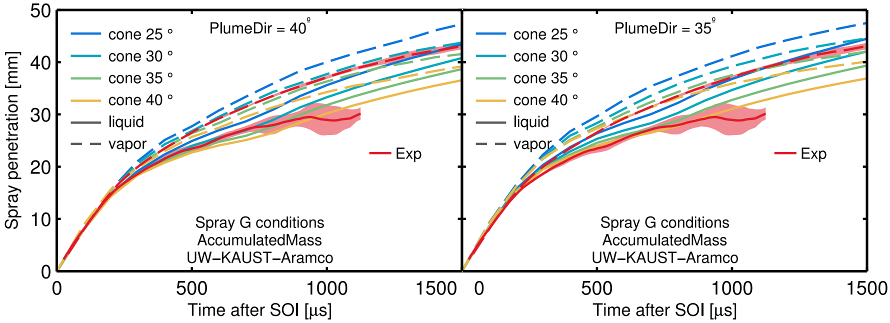

Figure 5.12: Axial penetration comparison with CFD simulations obtained by KWA group. The definition for liquid penetration presented is the one that yielded the best match in the previous comparison (accumulated mass).

very closely in the RANS simulation, which led to the conclusion that the model is not able to capture the evaporation well and that the definition used for the liquid penetration has many limitations. For the LES, while the vapor was well captured, the liquid was calculated using four definitions. The more “physical” definition was the Mie Scatter method, but even there, the application of an arbitrary threshold is necessary to obtain the liquid penetration. The definition that obtained the best match was the same one used by Polimi but with a different threshold and the match for liquid was reached with the same plume direction and cone angle values than the match for vapor.

The computational results presented in this section were only at the standard Spray G condition, which does not present the collapse of the spray within the established energizing time of 680 µs [9]. Sphicas et al. [15] compared the velocity fields of LES and RANS simulations with experimental PIV data for the standard Spray G condition and the highly collapsing case of Spray G9. They showed that the models can not capture well the negative velocity (recirculation) that occurs just before the collapse. They used a strategy in the simulations with several plume direction values and cone angles to find the best match to the experimental results in terms of velocity. Even though some of the LES simulations could follow the recirculation region for the Spray G case, it is clear that much work is still to be done to be able to explain and predict well the behavior of GDi sprays, especially under collapsing conditions. This section has shown that not only working on the models is important but also using a definition for the liquid contours is critical in order to compare to the experimental results coherently. A possibility that is currently under development is using the mass or density variables calculated in the computations and integrating them along the same line of sight used in experiments. This can result in a simulated DBI methodology that is less arbitrary and therefore more robust, with the downside of being much more computationally costly than the current methodologies.

As it could be noted in the introductory chapter, this thesis is not focused on CFD simulations. However, given that one of the ultimate objectives of gathering experimental data is to develop and validate CFD models, the previous analysis served to demonstrate important aspects to consider when comparing CFD models to experimental data.

5.3 Gas density and temperature parametric variations. Spray collapse

5.3.1 Background

CHENG et al. [16] performed experiments using nozzles with different characteristics and number of holes and showed the importance of the plume to plume interaction on the development of spray collapse under flashing conditions in a heated GDi injector. Flash boiling has also been studied in the Spray G injectors by means of simulations [4, 13] and experiments [17–19]. MONTANARO and ALLOCCA [17] showed that for highly flashing conditions, a collapse of the sprays was taking place, transforming the shape of the spray from individual plumes to a cloud of finely atomized fuel. ZENG et al. [20] performed an intensive work of describing GDi multi-hole sprays by relating the macroscopic characteristics to the four forces of relevance: inertia, viscous, drag forces and surface tension by means of the Reynolds number (Re), Weber number (We) and air-to-fuel density ratio (ρ_a/ρ_f). They found significant results and were able to create correlations using the dimensionless numbers and the extensive experimental data. However, The conditions selected for their study did not include flashing or spray collapsing conditions.

Manin et al. [18], performed DBI, Schlieren and Mie scattering visualization experiments in the nominal Spray G conditions, and two additional conditions at higher density and temperature. In their work, they found the collapse of the spray that took place at the higher chamber density and temperature conditions and reported that causes for such phenomenon were probably a combination of enhanced evaporation at higher temperatures and wider sprays at higher ambient densities that created low pressure zones in the middle of the spray cone.

Given the fundamentally different behavior of the sprays under collapsing conditions, and the importance that such change can have on evaporation and mixing (which directly affects combustion), the current section studies the liquid and vapor phases captured with DBI and Schlieren imaging techniques under extensive experimental conditions relevant for GDi injectors with focus on the spray collapsing phenomena. This phenomenon has been described by means of spray penetration and spray angle plots with the support of several raw images and detected contours. The relation among chamber density and temperature is discussed together with the dramatic changes in spray penetration, spray angle and morphology that the collapsing conditions created.

5.3.2 Test Matrix

The experimental conditions selected ranged from 300 K to 800 K of chamber temperature and from 1 kg/m^3 to 9 kg/m^3 of gas density. Low density conditions for low temperature cases were not possible to measure given that the vessel requires a minimum air flow to operate. The test matrix was designed to provide with parametric variations of density, temperature and injection pressure. Table 5.2 shows the specific conditions measured in the experimental test campaign. Not all the possibilities of conditions were measured as that would lead to almost 300 conditions. However, the number of measurements was still quite high, resulting in more than 120 points.

5.3.3 Effects of gas density variations

Several gas-density values may be encountered inside a gasoline engine, and the injector has to be able to supply the proper quantity of fuel at all of these possible conditions. A typical Diesel injector has a very

Table 5.2: Summary of conditions tested in the experimental campaign.

Paremeter	Values
Ambient Gas Density [kg/m^3]	1 - 2.1 - 3 - 3.5 - 4 - 5 - 6 - 7 - 8 - 9
Ambient Gas Temperature [K]	300 - 333 - 400 - 500 - 600 - 700 -800
Injection Pressure [MPa]	10 - 20
Energizing Time [μs]	680 - 1200

clear relation between vapor and liquid penetration with density, and in fact, density is one of the most influential factors on vapor penetration [21–23].

Fig 5.13 shows vapor and liquid penetration results for different densities at 500 K (top) and 700 K (bottom). The density in the top figure ranges from approximately the same values as for the bottom one. It can be appreciated that the trends of liquid and vapor penetration on the top figure are the ones expected and many times reported from Diesel spray research. In the density variation at 700 K, the temperature is sufficient to make possible the stabilization of liquid penetration within the captured time window. The steady values can be seen from around 200 μs ASOI in the lower density conditions. However, the liquid penetration for the higher density conditions (more than 4 kg/m^3) does not stabilize, but rather it keeps increasing and even surpassing the liquid penetration of the lower density conditions.

The phenomena taking place here are quite different to what has been previously reported in Diesel research and it is related to the collapse of the spray plumes, which can also be encountered when experimenting GDi sprays in flash boiling conditions [24, 25]. MANIN et al. [18] performed experiments using different units of the same hardware used in the current work for the Spray G standard condition and two other conditions at higher density and temperature. It was reported that for the cases with high density and temperature, the collapse of the spray plumes inwards (towards the injector axis) became more important. It was also reported, as it was in [26], that the spray collapse was probably taking place due to a combination of factors. It was hypothesized that the enhanced evaporation caused by increased density and temperature, promotes lower pressure inside the spray cone thus increasing the possibility of spray collapse. As it has been stated before, a combination of density

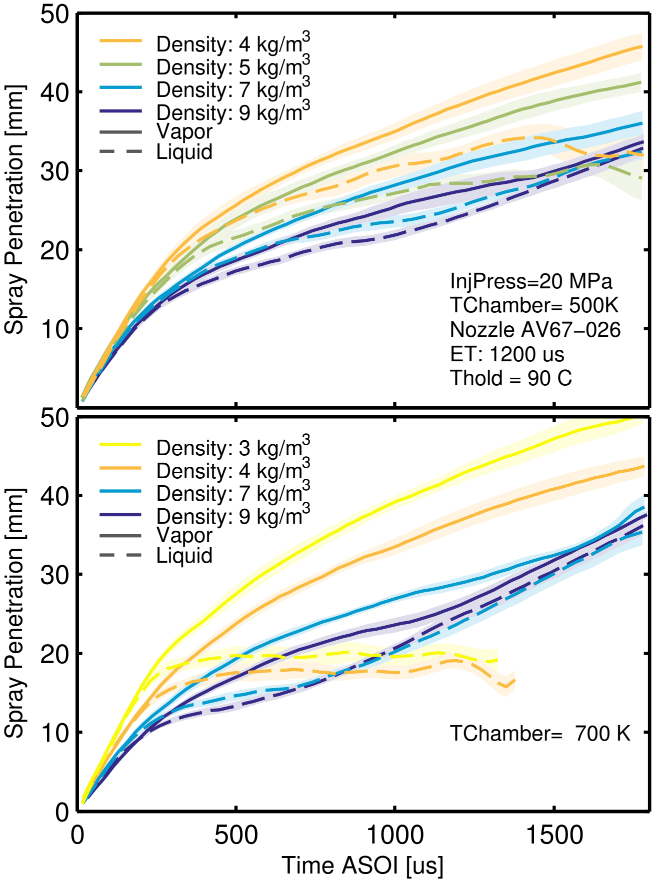

Figure 5.13: Density variations for 500 K (top) and 700 K (bottom) for 20 MPa injection pressure and 1200 μs of energizing time for vapor and liquid penetration.

and temperature conditions promote the development of spray collapse, which can increase penetration [18, 24–26]. The change in penetration and the dramatic change in the spray morphology suggest an important change in the mixing dynamics that could also develop inside an engine cylinder. Even though the test matrix performed in [18] did not allow to make parametric variations of density and temperature, spray collapse phenomenon was linked to a combination of density, temperature and injection conditions. The large test matrix conducted in the work presented here makes possible to perform such parametric variations that can help with the characterization of the complex phenomena taking place in gasoline sprays injection.

Fig 5.14 shows the detected contours (liquid phase) for two of the conditions whose results were shown in Fig 5.13 (bottom). The conditions selected are the most different ones in terms of density in order to evaluate its effect more clearly. It can be seen in the figure that the first (top) images behave as expected, with the lower density case providing a higher penetration and thiner sprays. However, from the second to the third pictures, the spray starts to collapse inwards in the high density case and no individual plumes can be identified. For a given instant after the Start of Injection (SOI), the liquid penetration of the lower density case stabilizes, reaching the so-called Liquid Length value. The collapsing of the sprays in the high density case produces several effects that contribute to increase the axial penetration and change the evaporation rate of the spray:

1. The momentum of the sprays is now only directed axially, away from the nozzle, which can effectively increase the axial distance between the fuel and the nozzle tip.
2. The spray cone angle is greatly diminished and no individual sprays can be identified, reducing the area in contact with surrounding hot air, and consequently diminishing the rate of evaporation.
3. The collapsing of the sprays towards the injector axis and the diminished evaporation rate can create a zone with high fuel concentration. This zone can shield the fuel still being injected from getting in contact with hot air. This effect would significantly reduce momentum exchange between the sprays and the ambient gas and further prevent evaporation.

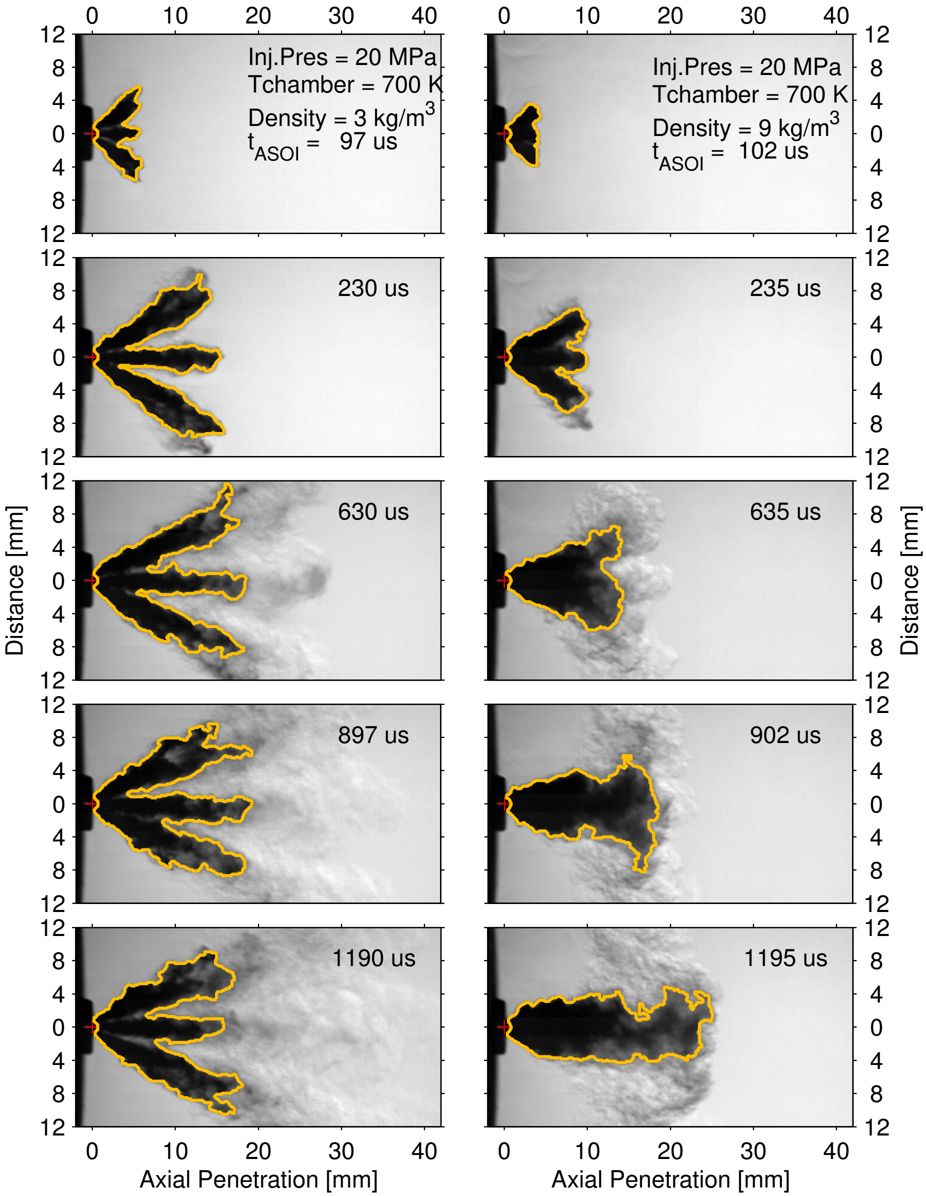

Figure 5.14: Liquid spray comparison between lower density conditions (left) and higher density conditions (right) using raw images and the detected contours.

These effects explain the previously observed behavior in Fig 5.13 (bottom). The liquid penetration, which is greatly affected by the evaporation rate, starts normally at the beginning of the injection, until the spray collapse phenomenon develops. Then, the relation between spray penetration and density inverts and the conditions at higher densities start penetrating more as the phenomena gets more severe.

As it has been stated before, spray collapse is a combination of several factors. This can be appreciated when comparing top and bottom graphs in Fig 5.13. Even though the maximum densities are the same, spray collapse is taking place less intensively and later in the low temperature case (500 K) than in the high temperature case (700 K). It can be noted that no inversion of penetration is taking place in the low temperature case until after the end of the injection (≈ 1500 μs ASOI).

Given the differences seen in Fig 5.14 in the spray morphology between the high and low density cases, another useful parameter to analyze the behavior of the sprays is the spray angle. Fig 5.15 shows the angle of the spray calculated according to section 3.6.4. As it was stated, only the liquid phase angle is presented due to the big uncertainties in the vapor angle determination.

Fig 5.15 presents a low temperature case in the top part (500 K) and a high temperature case in the bottom part (700 K). The conditions presented here are the same than those presented in Fig 5.13. It can be observed that even in the low temperature case, a higher value of density is accompanied by a smaller spray angle, which suggests that there is still spray collapse happening at 500 K (although in a small degree). The lower level of spray collapse happening at 500 K (top graph), compared to the one observed in the 700 K case (bottom graph), is not sufficient to create a big enough effect in spray penetration to be noted when analyzing top graph of Fig 5.13. In order to corroborate that there is still spray collapse happening at 500 K but in a smaller degree than at 700 K, Fig 5.16 is presented. Fig 5.16 provides similar comparison than Fig 5.15 at a lower temperature. It can be appreciated how in this example, the relation between spray angle and density follows the expected trend (opposite to the one appearing in Fig 5.15), where an increase in density produces an increase in the angle of the spray [8, 21].

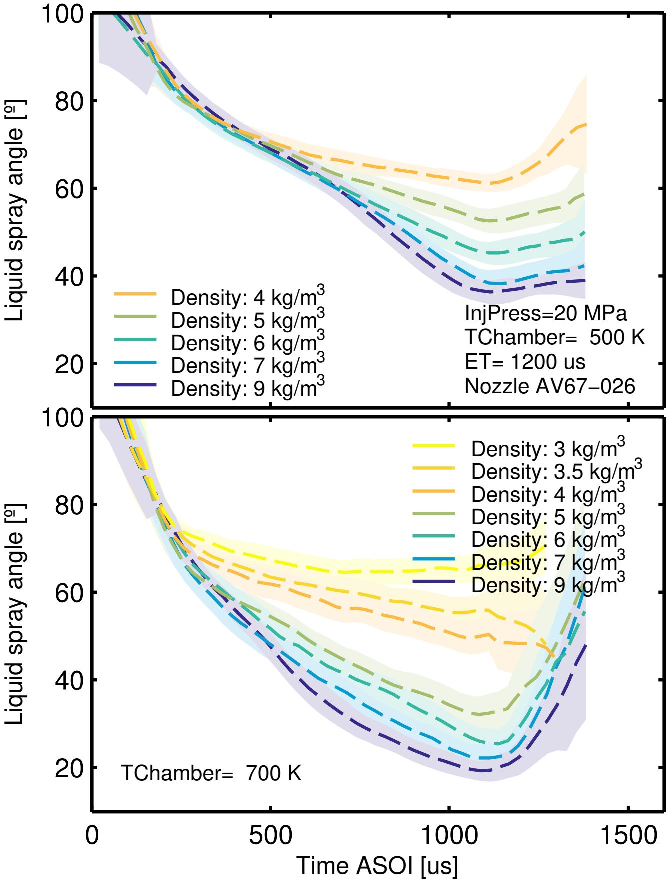

Figure 5.15: Liquid spray angle for different density values for 500 K (top) and 700 K (bottom) for 20 MPa injection pressure and 1200 μs of energizing time.

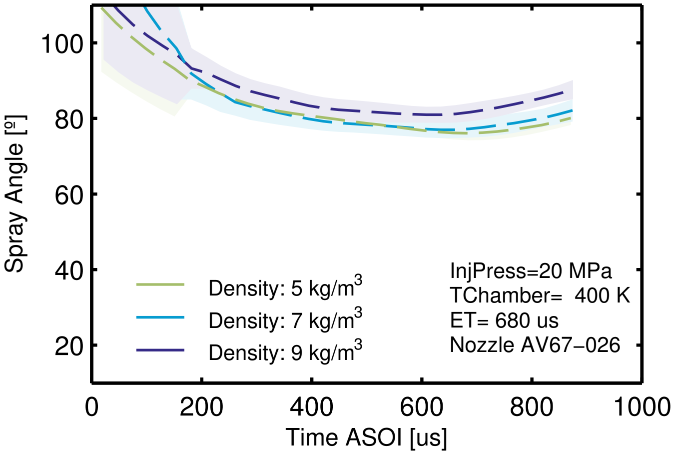

Figure 5.16: Density variations at non-vaporizing conditions (400 K) for liquid spray angle.

For the vapor contours, Fig 5.17 shows the vapor spray width at four different axial distances from the nozzle (5, 10, 20 and 30 mm). It can be seen that the widths are very similar at 5 mm, as the spray has not developed at that point and the shape is mainly dependant on the injection conditions and nozzle geometry. At a higher distance, it can be observed that the spray width is bigger for the higher density conditions but the trend inverses when the width is taken further from the nozzle at 20 or 30 mm. This occurs because the collapse takes time to develop as can be seen in previous penetration or spray angle plots. At the beginning of the injection, the spray develops normally and expands more for higher densities. When the spray collapse develops the spray gets thinner, but the vapor fuel that was already in the chamber remains there. Only the positions that were sufficiently far away to only get fuel after the collapse develops yield lower results for the spray width.

5.3.4 Effect of gas temperature variations

As shown in the test matrix (section 5.3.2), the temperature was varied from 300K to 800K for the measurements. Fig 5.18 shows the effects of changing the gas temperature at density levels of 4 kg/m^3 (top) and 9 kg/m^3 (bottom). On the low density case, the graph shows what could be a typical behavior with temperature, the liquid phase is greatly

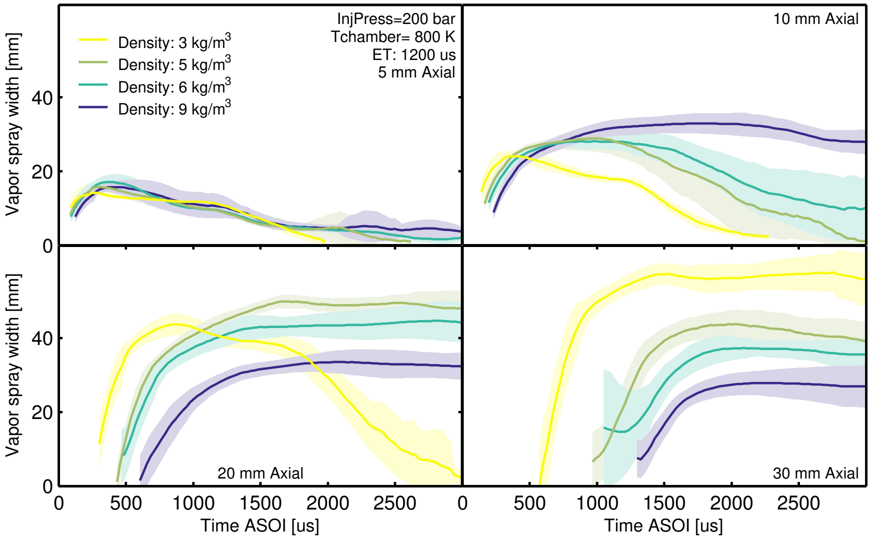

Figure 5.17: Spray width at 4 different axial distances from the nozzle tip.

affected by the variation in temperature, ranging from no evaporation, and therefore almost no difference with the vapor penetration at 330 K, to highly evaporating condition, and therefore a big difference with vapor penetration at 800 K.

The vapor penetration in Diesel sprays is almost independent of the temperature at iso-density, in evaporating conditions [23]. In this case, it can be seen that once the temperature goes beyond 573 K, the differences in vapor penetration are not very high but there is still a small inverse relation with temperature. The differences can be attributed to small changes in the morphology of the sprays at different temperatures, given the close relation between spray penetration, evaporation, and plume to plume interaction showed in the previous section.

The bottom graph in Fig 5.18 shows a different phenomenon than in the low density case. Here, the development of sprays is similar to what was shown in Fig 5.13 for the high temperature case, with the difference that now the inversion of spray penetration has also extended to the vapor phase. The density of the gas is much more important than its temperature for vapor penetration, which is why the comparison presented here can show a clearer picture of the effect of collapse on the

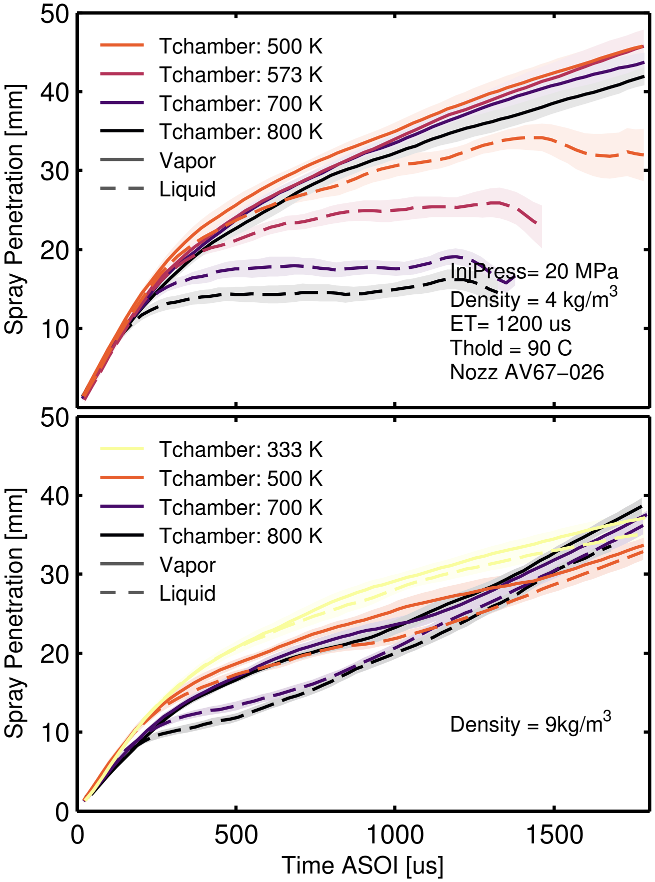

Figure 5.18: Temperature variations for 3 kg/m^3 density (top) and 9 kg/m^3 (bottom) and 20 MPa injection pressure for liquid and vapor penetration.

penetration of the vapor. This is because, in this case, increments in temperature have little effect in vapor penetration while greatly affecting spray collapse (as it has been shown in the previous section). On the other hand, in Fig 5.13 (bottom) the different densities comparison at iso-temperature showed the effects of density in spray collapse together with the effects in vapor penetration, which prevented the apparition of inversion in trends of vapor penetration.

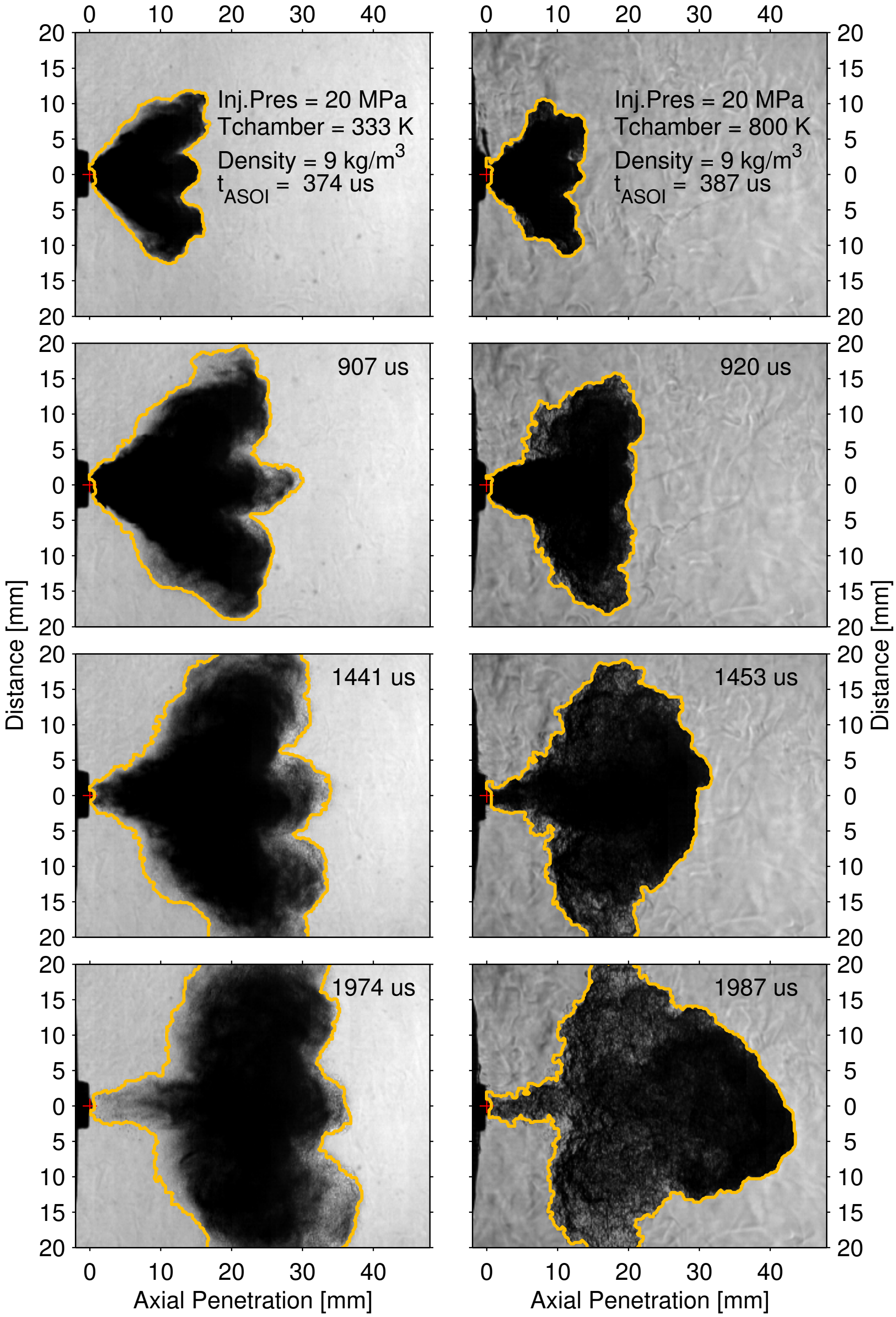

Figure 5.19: Vapor spray comparisons between low temperature case (left) and high temperature case (right) at 9 kg/m^3 of chamber density using raw images and the detected contours overlapped.

Fig 5.19 shows the Schlieren contours for the lowest and highest density conditions in Fig 5.18 (bottom). Given that the conditions represented at the left-hand side of the comparison are non evaporative, the full spray is in liquid phase. As shown in [8], a liquid spray phase has a higher penetration rate than a vaporizing one at the same density. This is related to the ability of the vapor phase of the spray to exchange momentum with the ambient gas at a higher rate than if the sprays were liquid. It is seen in Fig 5.19 that for the first time steps, the expected behavior takes place, and the liquid penetrates more than the vapor. It can be noted in the right-hand side that even in those first time steps, spray collapse is developing and the individual plumes are not identifiable. The spray for the high temperature case penetrates slowly at the beginning of the injection until mass concentrates and shields the incoming spray from the hot surrounding air. This can produce a significant decrease in aerodynamic drag and a decrease in evaporation rate which results in more liquid fuel in the spray tip. These two effects created by the high fuel concentration zone that put collapsing liquid fuel in the spray tip, can explain the increase in spray penetration and therefore explain the inversion in the trends taking place in Fig 5.18.

As it was done in the density variations section 5.3.3, Fig 5.20 is introduced here. The figure compares the effect of gas temperature on liquid spray angle at the same conditions than those in Fig 5.18. Unlike the gas density variations case, the usual effect of chamber gas temperature on spray angle goes in the same direction than the effect of temperature in spray collapse. It is expected that increasing gas temperature will decrease the liquid spray angle, as the evaporation of the liquid fuel is increased with higher temperatures. This effect can be seen in the upper graph of Fig 5.20. However, the lower graph shows that when the density is higher (and consequently the collapsing of the injected spray is greater), the decay of spray angle occurs much more rapidly. This can be quantified by averaging the slope of the Spray Angle in a time range where the decay is approximately constant (in this case 900 - 1000 μs ASOI). The average slope in the low density condition for the four temperatures is -0.025 deg/μs, whereas in the high density conditions is approximately 0.07 deg/μs (not including the lowest temperature for being non-evaporative).

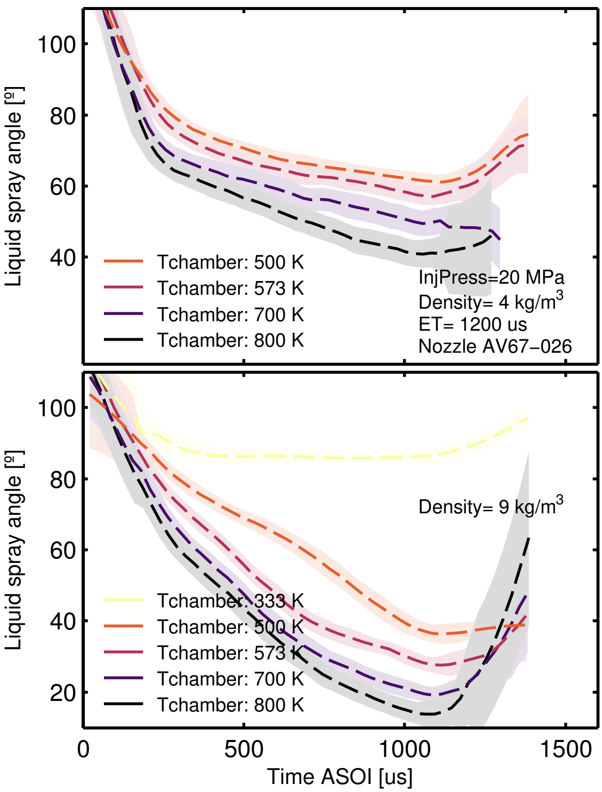

Figure 5.20: Temperature variations for 3 kg/m^3 density (top) and 9 kg/m^3 (bottom) and 20 MPa injection pressure for liquid spray angle.

5.3.5 Effect of injection pressure variation

Another important parameter worth studying is the injection pressure given the variability that the parameter is subject to during the normal operation of an engine. Two injection pressure levels (10 MPa and 20 MPa) were studied for all the gas density and temperature conditions tested. Fig 5.21 shows two graphs at the same level of temperature (700 K) and with a lower density at the top (3 kg/m^3) and a higher density at the bottom (9 kg/m^3) with liquid and vapor penetration lines at the two injection pressures specified.

It can be noted how in the low density case, the injection pressure has the expected effect, greatly affecting vapor penetration but with no effects on the Liquid Length, which is in agreement with Diesel sprays

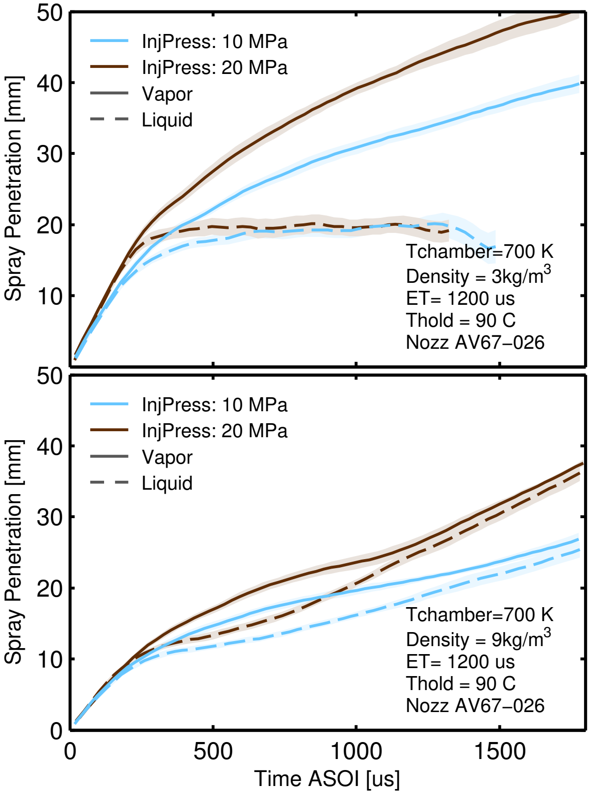

Figure 5.21: Injection pressure variations between a lower (top) and higher (bottom) level of chamber density at 700 K of chamber temperature for liquid and vapor penetration.

literature [8, 21, 27]. However, when the density in the chamber increases to values previously shown in this work to produce spray collapse, stabilized Liquid Length is not reached, and an effect of injection pressure on liquid penetration is observed, being the effect very similar to that on the vapor penetration. It can be hypothesized from the graph, that once the spray has begun to collapse, given the hindered evaporation of the fuel, the liquid phase starts to “follow” or behave like the vapor phase of the spray in terms of axial penetration. This effect is shown by the contour comparisons presented in Fig 5.22 where the contours detected with the image processing algorithms for vapor and liquid phases are plotted without the raw images. This type of visualization allows direct comparison of liquid and vapor penetration over the same graphs. It can be noted in the figure, that in the right-hand side column, where the density condition is significantly higher (9 kg/m^3 versus 3 kg/m^3), the liquid penetration grows following the vapor penetration very closely. Vapor penetration is encountering a higher density and therefore penetrating significantly less than on the left-hand side. This creates the particular shape of vapor contour clearly depicted in the bottom right of Fig 5.22 and also seen in Fig 5.19. The first part of the contour has a conical shape, and then spreads suddenly to an oval shape. Because of this fact, and as it was stated in section 3.6.4, a robust definition that could represent the phenomena occurring at low and high density conditions was not found, therefore, no angle determination has been done on the vapor contours.

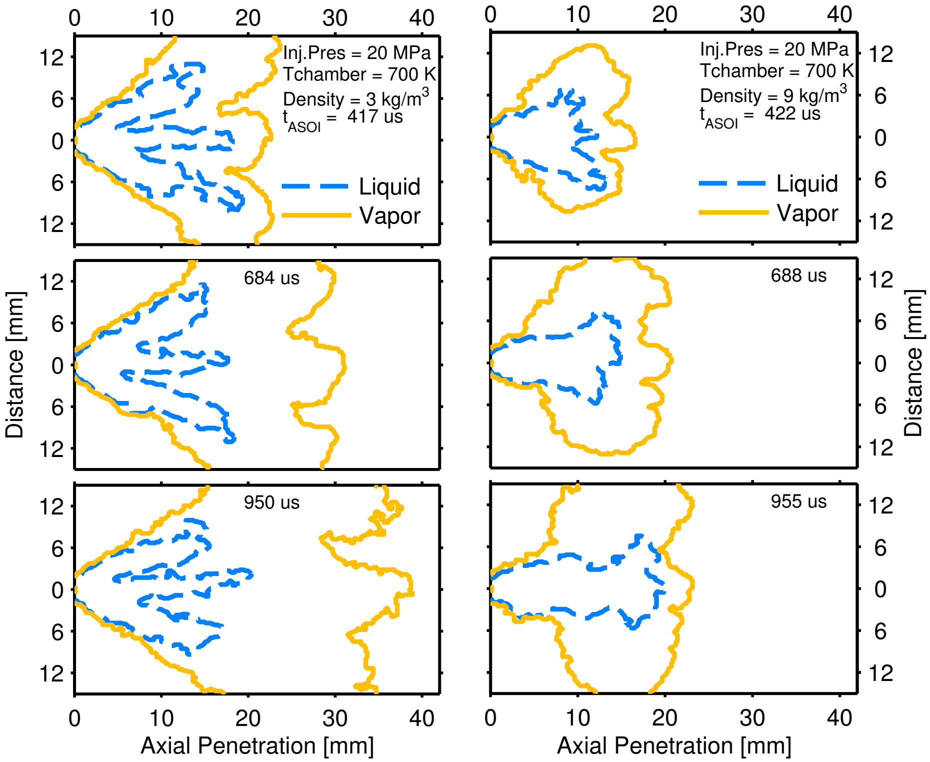

Figure 5.22: Liquid and vapor spray contours comparison between a lower (left) and a higher (right) density level at 700 K of chamber temperature and 20 MPa injection pressure.

5.3.6 Further analysis of density and temperature variations

The current section provides with a general overview of chamber temperature and density effects on spray collapse. Given the relationship shown between density and temperature and the angle decrease (Figs 5.15 and 5.20), one possibility to describe the spray collapse phenomena with a single scalar value is to take the minimum of the spray angle in a certain time window of the injection (900 to 1300 μs ASOI). It should be noted that this analysis is often performed in other studies by averaging a stabilized zone of spray penetration or spray angle [8, 28]. In this case, however, since parameters like spray penetration and spray angle do not reach stabilization except for a few of the conditions tested, the minimum of the spray angle was chosen. Fig 5.23 shows the minimum angle calculated as previously stated for all of the conditions at 20 MPa versus the chamber density (top graph) and versus temperature (bottom graph).

Both graphs provide the same information visualized in a different way. In the top graph, the minimum of the spray angle is decreasing with increasing temperature (color saturation is ordered) which is expected given the higher evaporation rate at higher temperature. For temperatures higher than 500 K, the minimum spray angle decreases with increasing density, whereas for the two lower temperatures, the trend is the opposite (shown in 5.3.3 by Figs 5.15 and 5.16). The aforementioned inverse relation between the minimum spray angle and the density escalate when density is increased. This result makes sense in view of previously presented results which reflected that the spray collapse intensifies the higher the chamber temperature and density become. Bottom graph of Fig 5.23 is very similar to the top graph, it can be clearly seen how the temperature almost has no effect on the spray angle when the density is 3 kg/m^3 or less, but when the density is higher than 4 kg/m^3, the spray angle decreases very rapidly with temperature.

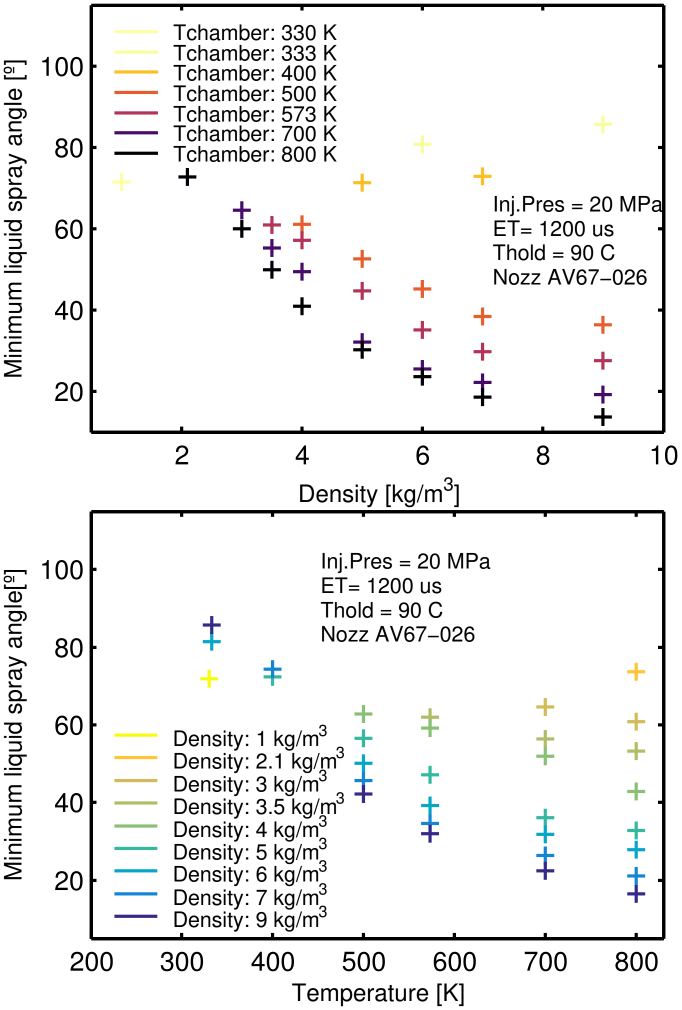

Figure 5.23: Minimum liquid spray angle calculated in the range of 900 to 1300 μs at 20 MPa injection pressure versus density (top) and temperature (bottom). The minimum spray angle has been chosen as a qualitative parameter to represent the degree of spray collapse.

Both graphs appearing in Fig 5.23 show the difficulty in developing empirical correlations for the parameter chosen to represent spray collapse given the change in trends and non-progressive behavior for some conditions. This underlines the importance of research focusing on the understanding of the behavior of GDi sprays, due to the relation between the delivery and development of the fuel with evaporation and mixing (which directly affect the maps of fuel concentration) and the possibility of wall wetting; all with great influence in the combustion process and the generation of pollutants.

5.4 Conclusions

In this chapter, the results of the experiments focused on the external flow of the ECN GDi injector has been presented and discussed. The main conclusions can be summarized as follows:

- ECN Spray G visualization experiments. In this section, visualization experiments performed at several institutions have been presented. In order to evaluate the differences between the setups and not introduce the uncertainty of different post-processing methodologies, the raw movies were processed following the methodology detailed in Chapter 3. In addition, the robustness of the results regarding one of the most important tuning parameters of the post-processing was assessed. The thresholding was done with different values for both the liquid and vapor contours and differences caused by the different thresholds were examined.

  In the vapor phase section, the vapor contours obtained at several institutions at standard Spray G were presented. The vapor penetration between institutions was very similar and the results were very insensitive to the threshold variations which was attributed to the high contrast that can be obtained with the Schlieren methodology. Radial profile comparison at the 15 mm positions were used to compare the evolution of a particular section of the spray between different institutions. It was shown that even though the penetration was very similar, the profiles looked quite different depending on the setup used. The temporal evolution of the width of the spray was used later to evaluate how the different setups might provide different results outside penetration. It was seen that the setup with the lowest contrast was the more sensitive to the change in the thresholding values, and that the setup that used a higher dynamic range between spray and background was very insensitive to the particular thresholding values, showing similar spray widths.

For the liquid phase, two configurations were examined. The first was Mie Scattering, which was compared in terms of penetration and radial profiles. The profiles looked very different, which is consistent with the reported dependency of the results with the particular illumination characteristics. Due to this fact, and because DBI is the standard procedure of the ECN for obtaining the liquid contours, the section focuses on the results obtained with the latter methodology. Good agreement was shown between institutions, although there was a significant dependence of the liquid penetration with the threshold used. In addition, the spray width calculated at several axial positions served to demonstrate the high dependence of the width (and therefore angle) of the cone with both the setup and the threshold used. This unfavorable behavior was attributed to the sensitivity of the setup to capturing beam-steering (density gradients) that create absorption in the same manner as the liquid would, making the particular threshold used a critical value.

In the last part of this section, CFD results performed at several institutions were compared to the experimental results presented earlier. The experimental results were calculated averaging the lines obtained with the thresholds to include the uncertainty from the processing methodology. The simulations were done using RANS and LES approaches and both resulted in better agreement for the vapor phase than the liquid phase. The liquid penetration from the LES results was obtained different methodologies, which served to identify the particular definition for calculating the liquid contours as a current weakness in simulations. It was seen that even with the four different definitions, the liquid penetration was not able to follow the experiments well. Lastly, it was argued that a definition that works similarly to the measurements that are obtained in experiments is necessary in order to have a fair comparison.

- Spray collapse. The extensive experimental campaign allowed studying parametric variations that describe interesting phenomena taking place in this gasoline injector. Density, temperature and injection pressure variations have been shown through vapor and liquid penetration, liquid spray angle, images and detected contours in order to explain the general behavior of the spray, and to focus on the collapse, from which little information is currently available. Spray collapse has been shown to have important consequences in the development of the fuel inside the chamber by causing a change in the expected behavior of liquid and vapor penetration, spray angle and morphology. The changes affect rate of evaporation and as a consequence modify mixing between fuel and air, which is directly related to combustion and engine operation. The relations between spray penetration and spray angle with density and temperature were presented, and it was stated that spray collapse requires both parameters to be moderate or high to develop. It was hypothesized that spray collapse was likely a phenomenon caused by increased evaporation and air entrainment that created low pressure zones in the center of the spray plume pulling the spray inwards. In fact, SPHICAS et al. [15] showed that the increase in the cone angle greatly increases plume interaction. The plumes can get so wide that the interaction between each other occurs very close to the nozzle and a “wall” is formed that prevents the air from entering inside of the cone. The air then pushes against the plumes towards the low pressure zone formed inside the spray which results in the attraction of the plumes. The phenomenon feeds on itself, because the narrower the cone is, the more difficult it is for the air to get inside, as the plume interaction is increased further.

References

[1] Song, Jingeun and Park, Sungwook. “Effect of injection strategy on the spray development process in a single-cylinder optical GDi engine.” *Atomization and Sprays*, vol. 25.9 (2015), pp. 819–836. doi: `10.1615/AtomizSpr.2015012018`.

[2] Zheng, Zhaolei, Liu, Chuntao, Tian, Xuefeng, and Zhang, Xiaoyu. “Numerical study of the effect of piston top contour on GDI engine performance under catalyst heating mode”. *Fuel*, vol. 157 (2015), pp. 64–72. doi: `10.1016/j.fuel.2015.04.054`.

[3] Li, Zhi Hua, He, Bang Quan, and Zhao, Hua. “Application of a hybrid breakup model for the spray simulation of a multi-hole injector used for a DISI gasoline engine”. *Applied Thermal Engineering*, vol. 65.1-2 (2014), pp. 282–292. doi: `10.1016/j.applthermaleng.2013.12.063`.

[4] Strek, Piotr, Duke, Daniel, Swantek, Andrew, Kastengren, Alan, Powell, Christopher F., and Schmidt, David P. “X-Ray Radiography and CFD Studies of the Spray G Injector”. *SAE Technical Paper 2016-01-0858*. 2016. doi: `10.4271/2016-01-0858`.

[5] “Engine Combustion Network 5th Workshop.” *Wayne State University. Detroit.* 2017, https://ecn.sandia.gov/ecn–workshop/.

[6] Pickett, Lyle M, Genzale, Caroline L, and Manin, Julien. “Uncertainty quantification for liquid penetration of evaporating sprays at diesel-like conditions”. *Atomization and Sprays*, vol. 25.5 (2015).

[7] Payri, Raul, Viera, Juan Pablo, Gopalakrishnan, Venkatesh, and Szymkowicz, Patrick G. “The effect of nozzle geometry over internal flow and spray formation for three different fuels”. *Fuel*, vol. 183 (2016), pp. 20–33. doi: `10.1016/j.fuel.2016.06.041`.

[8] Payri, Raul, Gimeno, Jaime, Bracho, Gabriela, and Vaquerizo, Daniel. “Study of liquid and vapor phase behavior on Diesel sprays for heavy duty engine nozzles”. *Applied Thermal Engineering*, vol. 107 (2016), pp. 365–378. doi: `10.1016/j.applthermaleng.2016.06.159`.

[9] Payri, Raul, Salvador, Francisco Javier, Martí-Aldaraví, Pedro, and Vaquerizo, Daniel. “ECN Spray G external spray visualization and spray collapse description through penetration and morphology analysis”. *Applied Thermal Engineering*, vol. 112 (2017), pp. 304–316. doi: `10.1016/j.applthermaleng.2016.10.023`.

[10] Westlye, Fredrik R., Penney, Keith, Ivarsson, Anders, Pickett, Lyle M., Manin, Julien, and Skeen, Scott A. “Diffuse back-illumination setup for high temporally resolved extinction imaging”. *Applied Optics*, vol. 56.17 (2017), p. 5028. doi: `10.1364/AO.56.005028`.

[11] Duke, Daniel J et al. “Internal and near nozzle measurements of Engine Combustion Network “Spray G” gasoline direct injectors”. *Experimental Thermal and Fluid Science*, vol. 88 (2017), pp. 608–621. doi: `10.1016/j.expthermflusci.2017.07.015`.

[12] Saha, Kaushik, Som, Sibendu, Battistoni, Michele, Li, Yanheng, Quan, Shaoping, and Senecal, Peter Kelly. “Numerical simulation of internal and near-nozzle flow of a gasoline direct injection fuel injector”. *Journal of Physics: Conference Series*, vol. 656.January 2016 (2015), p. 012100. doi: `10.1088/1742-6596/656/1/012100`.

[13] Saha, Kaushik, Som, Sibendu, Battistoni, Michele, Li, Yanheng, Pomraning, Eric, and Senecal, Peter Kelly. “Numerical Investigation of Two-Phase Flow Evolution of In- and Near-Nozzle Regions of a Gasoline Direct Injection Engine During Needle Transients”. *SAE International Journal of Engines*, vol. 9.2 (2016), pp. 2016–01–0870. doi: `10.4271/2016-01-0870`.

[14] Engine Combustion Network. *ECN Spray G*. 2016.

[15] Sphicas, Panos, Pickett, Lyle M, Skeen, Scott, Frank, Jonathan, Lucchini, Tommaso, Sinoir, David, D’Errico, Gianluca, Saha, Kaushik, and Som, Sibendu. “A Comparison of Experimental and Modeled Velocity in Gasoline Direct-Injection Sprays with Plume Interaction and Collapse”. *SAE Int. J. Fuels Lubr.* Vol. 10 (2017), pp. 184–201. doi: `10.4271/2017-01-0837`.

[16] Cheng, Qiang, Xu, Min, Zhang, Zhendong, and Xie, Nailiu. “Investigation on the spray characteristics of standard gasoline, n-pentane, iso-octane and ethnaol with a novel heated tip SIDI injector”. *Applied Thermal Engineering*, vol. 110 (2017), pp. 539–552. doi: `10.1016/j.applthermaleng.2016.07.201`.

[17] Montanaro, A and Allocca, L. “Flash Boiling Evidences of a Multi-Hole GDI Spray under Engine Conditions by Mie-Scattering Measurements”. *SAE Technical Paper 2015-01-1945* (2015).

[18] Manin, Julien, Jung, Yongjin, Skeen, Scott A, Pickett, Lyle M, Parrish, Scott E, and Markle, Lee E. “Experimental Characterization of DI Gasoline Injection Processes”. *SAE Technical Paper 2015-01-1894* (2015). doi: `10.4271/2015-01-1894`.

[19] Lacey, Joshua Stuart, Pourzakadeh, Farzad, Brear, Michael, Petersen, Phred, Lakey, Charles, Ryan, Steve, and Butcher, Brendan. “Optical Characterization of Propane at Representative Spark Ignition , Gasoline Direct Injection Conditions”. *SAE International Journal of Engines*, 2016-01-0842 (2016), pp. 21–23. doi: `10.4271/2016-01-0842.Copyright`.

[20] Zeng, Wei, Xu, Min, Zhang, Ming, Zhang, Yuyin, and Cleary, David J. “Macroscopic characteristics for direct-injection multi-hole sprays using dimensionless analysis”. *Experimental Thermal and Fluid Science*, vol. 40 (2012), pp. 81–92. doi: `10.1016/j.expthermflusci.2012.02.003`.

[21] Siebers, Dennis L. “Scaling liquid-phase fuel penetration in diesel sprays based on mixing-limited vaporization”. *SAE Technical Paper 1999-01-0528* (1999). doi: `10.4271/1999-01-0528`.

[22] Payri, Raul, Gimeno, Jaime, Viera, Juan Pablo, and Plazas, Alejandro Hernan. “Schlieren visualization of transient vapor penetration and spreading angle of a prototype diesel direct-acting piezoelectric injector”. *ICLASS 2012*. 2012, pp. 1–8.

[23] Payri, Raul, Gimeno, Jaime, Viera, Juan Pablo, and Plazas, Alejandro Hernan. “Needle lift profile influence on the vapor phase penetration for a prototype diesel direct acting piezoelectric injector”. *Fuel*, vol. 113 (2013), pp. 257–265. doi: `10.1016/j.fuel.2013.05.057`.

[24] Zeng, Wei, Xu, Min, Zhang, Gaoming, Zhang, Yuyin, and Cleary, David J. “Atomization and vaporization for flash-boiling multi-hole sprays with alcohol fuels”. *Fuel*, vol. 95 (2012), pp. 287–297. doi: `10.1016/j.fuel.2011.08.048`.

[25] Parrish, Scott E. and Zink, R. J. “Development and Application of Imaging System To Evaluate Liquid and Vapor Envelopes of Multi-Hole Gasoline Fuel Injector Sprays Under Engine-Like Conditions”. *Atomization and Sprays*, vol. 22.8 (2012), pp. 647–661. doi: `10.1615/AtomizSpr.2012006215`.

[26] Blessinger, M., Meijer, M., Pickett, L.M., Manin, J., and Skeen, S. “Liquid-Vapor penetration and plume-plume interaction of vaporizing iso-octane and ethanol SIDI sprays”. *ILASS Americas, 25th Annual Conference on Liquid Atomization and Spray Systems*. Pittisburgh PA, 2013.

[27] Naber, Jeffrey D and Siebers, Dennis L. “Effects of Gas Density and Vaporization on Penetration and Dispersion of Diesel Sprays”. *SAE Paper 960034*. Vol. 105. 412. Society of Automotive Engineers, Inc., Warrendale, Pennsylvania, USA, 1996, pp. 82–111. doi: `10.4271/960034`.

[28] Desantes, Jose Maria, Payri, Raul, Salvador, Francisco Javier, and Gil, Antonio. “Development and validation of a theoretical model for diesel spray penetration”. *Fuel*, vol. 85.7-8 (2006), pp. 910–917.

Chapter 6

Summary and future works

This chapter summarizes the document, outlining the main conclusions extracted in the work. In the last section, future paths for the research presented here are proposed and discussed.

6.1 Summary

The presented work studied many aspects of GDi injection systems in what constitutes as the first effort of the department in this field. The study is done first through the review of the relevant work and then through extensive experimentation and analysis of internal and external flow of several “Spray G” nozzles from the Engine Combustion Network.

After the general introduction in Chapter 1, the second chapter briefly reviews the historical development of engines in the automotive sector and defines the two types of generalized engines and the particularities of mixture preparation in each, focusing further on the spark ignition systems. Then, the evolution of the fuel delivery systems is presented up to the multi-hole solenoid-actuated injectors used in DISI engines. These types of injectors are described, first generally and then more particularly focusing on the ECN Spray G injector. Lastly, the typical characteristics of internal flow and external spray are discussed, listing and briefly reviewing the majority of the studies done using the hardware used for this work.

The third chapter presents the internal flow results, starting from the geometry of eight Spray G nozzles distributed around the work, needle lift; and then moving to hydraulic measurements: rate of injection and rate of momentum. Lastly, the near-nozzle X-ray experiments are introduced and discussed. The internal geometry section presented the key geometrical dimensions extracted using X-ray tomographic reconstruction methodology available at Argonne National Laboratory. A similar methodology, also with the X-rays at Argonne, was used to determine the needle lift at standard Spray G conditions. The key geometrical dimensions resulted similar for all the tested nozzles with the biggest difference on the counterbore radius. The short L/D ratio and the small lift helped to explain many phenomena presented later in the hydraulic and near-nozzle flow measurements. These results and analyses were used in a publication at *ILASS – Europe 2017, 28th Annual Conference on Liquid Atomization and Spray Systems* with title *A study on the relationship between internal nozzle geometry and injected mass distribution of eight ECN Spray G nozzles.*

The rate of injection and rate of momentum results were discussed, the combination of the two allowed to calculate the area and velocity coefficients and help explain the low values of the discharge coefficient. The effect of the pressure and temperature was evaluated on the rate of injection and it was found that the effect has the expected trend, whereas the temperature had no effect (within the experimented range) on both the stabilized and time-resolved ROI. Several ETs were used to drive the injector for the ROI campaign and it was shown that the rate of injection can be higher for lower injection pressure if the duration of the command signal is sufficiently low. This behavior was attributed to the design of GDi injectors, where the needle is lifted directly by the solenoid working against the inlet pressure of the injector. For short ETs, the force exerted by the coil is canceled out by the inlet pressure, which produces the counterintuitive trend with the injection pressure. In addition, the mass flow of multiple injections was also studied showing surprising results. It was seen that the rate of injection was greatly dependent on dwell time, with oscillating behavior as the dwell increased. This behavior is still not completely understood but it is likely linked to the movement of the needle after closing, which was shown by tracking the small movement from the needle lift images. Two configurations were used for rate of momentum experiments due to the particular characteristics of GDi sprays. It was seen that the lateral methodology did not provide coherent results, which resulted in the use of the results with the frontal configuration. By combining the rate of injection and rate of momentum measurements, several hydraulic coefficients were calculated and used to describe the flow. It was seen that the low discharge coefficient was caused by a small effective velocity and effective area, which is ultimately caused by the internal geometry. These results were published in *SAE Technical Paper 2015-01-1893* with title *Momentum Flux Measurements on an ECN GDi Injector*, and in *Atomization and Sprays 26, 889–919* with title *Internal flow characterization on an ECN GDi injector*.

For the near-nozzle measurements, two different experiments were performed using monochromatic X-rays in sector 7-BM at the Advanced Photon Souce in ANL. The first methodology provided the projected mass from the primary injector orientation (from the side) and was used to calculate the instantaneous mass distribution in the domain. The total mass injected was validated with the rate of injection showing good agreement. It was shown that the methodology could be used to calculate the transverse integrated mass (TIM), which was shown to increase rapidly with the axial position. It was shown that the increase in TIM is linked to the rapid deceleration of the spray, which was compared to previously studied Diesel injectors. The rapid spray deceleration is linked again to the internal geometry of the injectors, short L/D ratio and low needle lift, which causes short primary spray break-up and the marked deceleration observed. In order to isolate the different plumes, spray tomographic radiography was performed, measuring in a plane two millimeters from the nozzle tip of eight Spray G nozzles. The time-averaged reconstructed results were shown in two-dimensional plots. Also, the time-resolved mass coming out of the different holes was presented. The close agreement regarding mass flow for the holes within the same injectors and for different injectors was examined. The perturbations in the integrated mass had a different frequency injector to injector but the same for different orifices within the same injector, which was attributed to experimental issues. These experiments were combined with rate of injection and rate of momentum experiments in a publication made in the journal *Experimental Thermal and Fluid Science* with the title *Internal and near nozzle measurements of Engine Combustion Network "Spray G" gasoline direct injectors.*

Chapter 5 focuses on the external spray, starting with a comparison and study of the contours obtained in different institutions using the same hardware. In order to evaluate the differences between the setups, the raw movies obtained by different institutions were processed following the methodology described in Chapter 3. In this analysis, the robustness of the results with regard to the thresholding values was studied. In the vapor phase section, the vapor contours obtained at several institutions at standard Spray G were presented. The vapor penetration between institutions was very similar and the results were very insensitive to the threshold variations which was attributed to the high contrast that can be obtained with the Schlieren methodology. Radial profile comparison at the 15 mm positions were used to compare the evolution of a particular section of the spray between different institutions. It was shown that even though the penetration was very similar, the profiles looked quite different depending on the setup used. The temporal evolution of the width of the spray was used later to evaluate how the different setups might provide different results outside penetration. It was seen that the setup with the lowest contrast was the more sensitive to the change in the thresholding values, and that the setup that used a higher dynamic range between spray and background was very insensitive to the particular thresholding values, showing similar spray widths. For the liquid phase, two configurations were examined. The first was Mie Scattering, which was compared in terms of penetration and radial profiles. The profiles looked very different, which is consistent with the reported dependency of the results with the particular illumination characteristics. Due to this fact, and because DBI is the standard procedure of the ECN for obtaining the liquid contours, the section focuses on the results obtained with the latter methodology. Good agreement was shown between institutions, although there was a significant dependence of the liquid penetration with the threshold used. In addition, the spray width calculated at several axial positions served to demonstrate the high dependence of the width (and therefore angle) of the cone with both the setup and the threshold used. This unfavorable behavior was attributed to the sensitivity of the setup to capturing beam-steering (density gradients) that create absorption in the same manner as the liquid would, making the particular threshold used a critical value. This analysis, achieved by combining and analyzing data from different institutions, was presented in the fifth ECN Workshop that was held in Wayne State University (Detroit) in April of 2017.

In the last part of this section, CFD results performed at several institutions were compared to the experimental results presented earlier. The experimental results were calculated averaging the lines obtained with the thresholds to include the uncertainty from the processing methodology. The simulations were done using RANS and LES approaches and both resulted in better agreement for the vapor phase than the liquid phase. The liquid penetration from the LES results was obtained using different methodologies, which served to identify the dependency on the particular definition of liquid as a current weakness in simulations. It was seen that even with the four different definitions, the liquid penetration was not able to follow the experiments well. Lastly, it was argued that a methodology that works similarly to the measurements that are obtained in experiments is necessary in order to have a fair comparison.

One of the important contributions of this work was to identify and describe the collapse of the spray under high ambient density and temperature conditions. In the last section of Chapter 5, the large test matrix of liquid and vapor visualization experiments allowed to identify the main variables that affect the macroscopic behavior of the spray. Density, temperature and injection pressure variations were shown through vapor and liquid penetration, liquid spray angle, spray width comparisons, images, and detected contours in order to explain the general behavior of the spray, and to focus on the collapse, from which little information is currently available. It was shown that spray collapse has important consequences in the development of the fuel inside the chamber by causing a change in the expected behavior of liquid and vapor penetration, spray angle, and morphology. The changes affect rate of evaporation and, as a consequence, modify mixing between fuel and air, which is directly related to combustion and engine operation. The relationships between spray penetration and spray angle with density and temperature were presented, and it was shown that spray collapse requires both parameters to be moderately high to develop. The spray collapse is a phenomenon caused by evaporation causing low pressure zones, and by plume interaction blocking the entry of air in the inside of the spray cone. This means that once the collapse starts, it will develop further until the end of injection. The findings presented in this section were published in *Applied Thermal Engineering 112, 304–316* with the title

ECN Spray G external spray visualization and spray collapse description through penetration and morphology analysis.

6.2 Future works

There are many possible ways to continue the work presented in this thesis. This section proposes some interesting routes to continue developing tools and knowledge on GDi injection systems.

Regarding the internal flow, it was seen that the multiple injections behavior was not well understood. Further needle lift measurements of the Spray G nozzle would help to explain the behavior of the rate of injection in multiple injection conditions. Also, needle lift measurements under different ambient pressures can provide the necessary data to understand the overshot seen in the ROI and how it is related to the actual movement of the needle. In addition, needle lift measurements of the same eight nozzles that were used to measure the spray tomographic radiography and internal geometry would provide further understanding regarding the relationship between geometry, needle lift with near-nozzle flow. Moreover, ROI can also be measured for the same set of injectors and corroborate the differences seen in near-nozzle flow. Phase Doppler Anemometry (PDA) can be applied to complement the near-nozzle measurements. The technique can be used to obtain the velocity and droplet size exiting the injector, which would help greatly to understand the flow and ultimately model it.

Further near-nozzle visualization experiments can be done in order to take full advantage of the X-ray measurements. Frontal Mie Scattering visualization using a planar illumination can be used to compare the qualitative (visualization) measurements to the quantitative X-ray measurements and study the possibility of linking them. Regarding the X-ray measurements, they were took with modified boundary conditions due to the particularities of the methodology. Computational simulations as well as experimental efforts improving the setup can clarify how different the results are when the actual boundary conditions are used.

In terms of the external spray and internal flow, flash boiling is an important phenomenon relevant for GDi injection as it was seen in Chapter 2. However, no new experiments have been presented in this thesis due to the impossibility to reach pressure conditions inside the available vessels lower than the atmospheric pressure. In order to continue with the work in GDi injection systems, a new vessel able to reach flash boiling conditions was designed and manufactured within the project of this thesis, although no results are available yet featuring this new hardware. The new vessel is a cube with four accesses on the sides, one at the top and one at the bottom. It can accept up to four optical accesses, leaving one side for air distribution and another for mounting the injector. The vessel has been designed for flexibility, so the injector or windows can be mounted in all sides, including top and bottom. The only restriction is that the either the bottom or the top side must be used for the air distribution. A render of the vessel can be seen in Fig 6.1

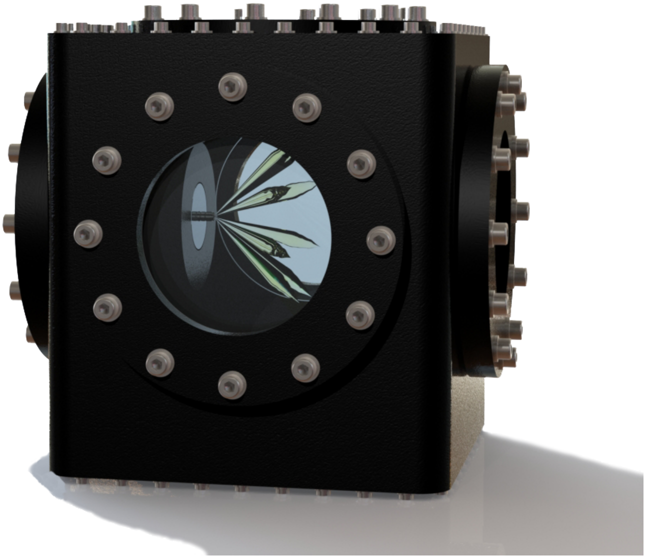

Figure 6.1: Render of the new vessel for GDi sprays visualization experiments

The new test rig is able to reach pressures from 10 kPa to 1.5 MPa, thus allowing to reach both low-pressure conditions for flash boiling and high-pressure conditions to simulate late injection strategies. In addition, it has been designed to be compatible with the PDA system, in order to allow particle size and velocity measurements.

The combination of further needle lift, near-nozzle and hydraulic measurements with visualization experiments of the external spray in flash boiling, as well as, high-pressure conditions, will serve to continue developing experimental procedures and to increase the knowledge of all characteristics of the flow of GDi nozzles. In parallel, all the acquired knowledge and data should be used to create GDi injection models that can accurately predict the exact delivery of fuel, mixing and combustion processes in order to make steps towards the ultimate goal of completely predictive engine models.

Bibliography

ANL. *Advanced Photon Source Overview*, (*cited on: Chap.4-p.78*).

ANL. *APS Xradia Resolution Pattern*, (*cited on: Chap.4-p.81*).

Arcoumanis, Constantine, Flora, H, Gavaises, Manolis, and Badami, M. “Cavitation in Real-Size Multi-Hole Diesel Injector Nozzles”. *SAE Technical Paper 2000-01-1249*. 2000. doi: `10.4271/2000-01-1249`, (*cited on: Chap.3-p.38*).

Bahattin, Mustafa and Ozdaly, Bulent. “Gasoline Direct Injection”. *Fuel Injection.* Ed. by Daniela Siano. Chapter 1. Sciyo, 2010, pp. 1–19. doi: `10.5772/9693`, (*cited on: Chap.3-pp.19,21,24*).

Baker, Paul and Watson, Harry. “MPI Air / Fuel Mixing for Gaseous and Liquid LPG Reprinted From : SI Combustion and Direct Injection SI Engine Technology”. *SAE Technical paper 2005-01-0246*, 724 (2005), (*cited on: Chap.3-p.19*).

Baldwin, E.T., Grover, R.O., Parrish, Scott E, Duke, Daniel J., Matusik, Katarzyna E, Powell, Christopher F, Kastengren, Alan L., and Schmidt, David P. “String flash-boiling in gasoline direct injection simulations with transient needle motion”. *International Journal of Multiphase Flow*, vol. 87 (2016), pp. 90–101. doi: `10.1016/j.ijmultiphaseflow.2016.09.004`, (*cited on: Chap.3-pp.40,41,42,43*).

Bardi, Michele. "Partial needle lift and injection rate shape effect on the formation and combustion of the Diesel spray". PhD thesis. Valencia (Spain): Universitat Politècnica de València, 2014. doi: `10.4995/Thesis/10251/37374`, (*cited on: Chap.3-p.13, Chap.4-pp.64,65,69, Chap.5-p.148*).

Bardi, Michele, Payri, Raul, Malbec, Louis-Marie, Bruneaux, Gilles, Pickett, Lyle M, Manin, Julien, Bazyn, Tim, and Genzale, Caroline L. "Engine Combustion Network: Comparison of Spray Development, Vaporization, and Combustion in Different Combustion Vessels". *Atomization and Sprays*, vol. 22.10 (2012), pp. 807–842. doi: `10.1615/AtomizSpr.2013005837`, (*cited on: Chap.4-p.90*).

Battistoni, Michele, Xue, Qingluan, and Som, Sibendu. "Large-Eddy Simulation (LES) of Spray Transients: Start and End of Injection Phenomena". *Oil & Gas Science and Technology – Revue d'IFP Energies nouvelles*, vol. 71.1 (2016), p. 4. doi: `10.2516/ogst/2015024`, (*cited on: Chap.5-p.152*).

Befrui, B, Aye, A, Bossi, A, Markle, L E, and Varble, D L. "ECN GDi Spray G : Coupled LES Jet Primary Breakup - Lagrangian Spray Simulation". *ILASS Americas 28th Annual Conference on Liquid Atomization and Spray Systems*, May (2016), (*cited on: Chap.3-pp.36,41*).

Befrui, B, Corbinelli, G, Hoffmann, G, Technical, Delphi, and Gillingham, Centre. "Cavitation and Hydraulic Flip in the Outward-Opening GDi Injector Valve-Group". *SAE International*, vol. 2009-01-14 (2009). doi: `10.4271/2009-01-1483`, (*cited on: Chap.3-p.34*).

Befrui, Bizhan, Corbinelli, Giovanni, D'Onofrio, Mario, and Varble, Daniel. "GDI Multi-Hole Injector Internal Flow and Spray Analysis". *SAE Tecnnical Paper 2011-01-1211* (2011). doi: `10.4271/2011-01-1211`, (*cited on: Chap.3-p.33*).

Befrui, Bizhan, Corbinelli, Giovanni, Spiekermann, Peter, Shost, Mark, and Lai, Ming-Chia. "Large Eddy Simulation of GDI Single-Hole Flow and Near-Field Spray". *SAE International Journal of Fuels and Lubricants*, vol. 5.2 (2012), pp. 620–636. doi: `10.4271/2012-01-0392`, (*cited on: Chap.3-pp.34,35,36, Chap.5-pp.113,142,148*).

Befrui, Bizhan, Hoffmann, Guy, Kirwan, John, Piock, Walter, and Schilling, Sebastian. "Analytical Optimization of Delphi GDi Fuel Injection Systems". *15th Conference "The Working Process of the Internal Combustion Engine"*. September 2015. 2015, (*cited on: Chap.3-pp.32,33,36*).

Benajes, Jesus, Pastor, Jose Vicente, Payri, Raul, and Plazas, Alejandro Hernan. "Analysis of the influence of Diesel nozzle geometry in the Injection Rate characteristic". *Journal of Fluids Engineering (ASME).* Vol. 126 (2004), pp. 63–71, (*cited on: Chap.5-p.107*).

Benajes, Jesus, Payri, Raul, Bardi, Michele, and Martí-aldaraví, Pedro. "Experimental characterization of diesel ignition and lift-off length using a single-hole ECN injector". *Applied Thermal Engineering*, vol. 58.1-2 (2013), pp. 554–563. doi: `10.1016/j.applthermaleng.2013.04.044`, (*cited on: Chap.4-p.92*).

Bergwerk, W. "Flow pattern in Diesel nozzle spray holes". *Proc. Inst. Mech. Engrs*, vol. 173, n. 25 (1959), (*cited on: Chap.3-p.37*).

Blessinger, M, Manin, Julien, Skeen, Scott A, Meijer, M, Parrish, Scott E, and Pickett, Lyle M. "Quantitative mixing measurements and stochastic variability of a vaporizing gasoline direct-injection spray". *International Journal of Engine Research*, vol. 16.2 (2015), pp. 238–252. doi: `Doi10.1177/1468087414531971`, (*cited on: Chap.4-p.92*).

Blessinger, M., Meijer, M., Pickett, L.M., Manin, J., and Skeen, S. "Liquid-Vapor penetration and plume-plume interaction of vaporizing iso-octane and ethanol SIDI sprays". *ILASS Americas, 25th Annual Conference on Liquid Atomization and Spray Systems.* Pittisburgh PA, 2013, (*cited on: Chap.6-pp.190,192*).

Bode, J, Chaves, H, Hentschel, W, Kubitzek, A, Obermeier, F, Schindler, K, and Schneider, T. "Fuel spray in Diesel engines. Part I: Spray formation". *ATA 92A065* (1992), (*cited on: Chap.3-p.38*).

Bosch, Wilhelm. "The Fuel Rate Indicator: a New Measuring Instrument for Display of the Characteristics of Individual Injection". *SAE Paper 660749* (1966), (*cited on: Chap.4-p.65*).

CAIRNS, ALASDAIR, BLAXILL, HUGH, and IRLAM, GRAHAM. "Exhaust Gas Recirculation for Improved Part and Full Load Fuel Economy in a Turbocharged Gasoline Engine". *SAE Technical Paper 2006-01-0047*, 724 (2006). DOI: `10.4271/2006-01-0047`, (*cited on: Chap.3-p.27*).

CAVICCHI, ANDREA, POSTRIOTI, LUCIO, GIOVANNONI, NICOLA, FONTANESI, STEFANO, BONANDRINI, GIOVANNI, and DI GIOIA, RITA. "Numerical and experimental analysis of the spray momentum flux measuring on a GDI injector". *Fuel*, vol. 206 (2017), pp. 614–627. DOI: `10.1016/j.fuel.2017.06.054`, (*cited on: Chap.3-p.33*).

CHAN, QING N., BAO, YONGMING, and KOOK, SANGHOON. "Effects of injection pressure on the structural transformation of flash-boiling sprays of gasoline and ethanol in a spark-ignition direct-injection (SIDI) engine". *Fuel*, vol. 130 (2014), pp. 228–240. DOI: `10.1016/j.fuel.2014.04.015`, (*cited on: Chap.3-p.40*).

CHEN, YU, WANG, YUESEN, and RAINE, ROBERT. "Correlation between cycle-by-cycle variation, burning rate, and knock: A statistical study from PFI and DISI engines". *Fuel*, vol. 206 (2017), pp. 210–218. DOI: `10.1016/j.fuel.2017.06.016`, (*cited on: Chap.3-p.20*).

CHENG, QIANG, XU, MIN, ZHANG, ZHENDONG, and XIE, NAILIU. "Investigation on the spray characteristics of standard gasoline, n-pentane, iso-octane and ethnaol with a novel heated tip SIDI injector". *Applied Thermal Engineering*, vol. 110 (2017), pp. 539–552. DOI: `10.1016/j.applthermaleng.2016.07.201`, (*cited on: Chap.6-p.188*).

COSTA, M., MARCHITTO, L., MEROLA, S.S., and SORGE, U. "Study of mixture formation and early flame development in a research GDI (gasoline direct injection) engine through numerical simulation and UV-digital imaging". *Energy*, vol. 77 (2014), pp. 88–96. DOI: `10.1016/j.energy.2014.04.114`, (*cited on: Chap.5-p.107*).

COSTA, M., SORGE, U., MEROLA, S., IRIMESCU, A., LA VILLETTA, M., and ROCCO, V. "Split injection in a homogeneous stratified gasoline direct injection engine for high combustion efficiency and low pollutants emission". *Energy*, vol. 117 (2016), pp. 405–415. DOI: `10.1016/j.energy.2016.03.065`, (*cited on: Chap.3-pp.25,26,31*).

Costa, Michela, Allocca, Luigi, Montanaro, Alessandro, Sorge, Ugo, Iorio, B, Cnr, Istituto Motori, and Marconi, Viale. “Multiple Injection in a Mixed Mode GDI Boosted Engine”. *SAE Technical Paper* (2010), p. 15, (*cited on: Chap.5-p.118*).

Dahlander, Petter, Iemmolo, Daniele, and Tong, Yifei. “Measurements of Time-Resolved Mass Injection Rates for a Multi-Hole and an Outward Opening Piezo GDI Injector”. *SAE Technical Paper 2015-01-0929* (2015). doi: `10.4271/2015-01-0929.Copyright`, (*cited on: Chap.3-p.29*).

Desantes, Jose Maria, Payri, Raul, Salvador, Francisco Javier, and Gil, Antonio. “Development and validation of a theoretical model for diesel spray penetration”. *Fuel*, vol. 85.7-8 (2006), pp. 910–917, (*cited on: Chap.4-p.73, Chap.6-p.204*).

Desantes, Jose Maria, Payri, Raul, Salvador, Francisco Javier, and Gimeno, Jaime. “Measurements of spray momentum for the study of cavitation in diesel injection nozzles”. *SAE Technical Paper 2003-01-0703* (2003). doi: `10.4271/2003-01-0703`, (*cited on: Chap.5-p.142*).

Duke, Daniel J, Swantek, Andrew B, Sovis, Nicolas M, Tilocco, F Zak, Powell, Christopher F, Kastengren, Alan L, Gürsoy, Doğa, and Biçer, Tekin. “Time-resolved X-ray Tomography of Gasoline Direct Injection Sprays”. *SAE Int. J. Engines*, vol. 9 (2015), pp. 143–153. doi: `10.4271/2015-01-1873`, (*cited on: Chap.3-p.41, Chap.4-pp.86,90, Chap.5-p.149*).

Duke, Daniel J et al. “Internal and near nozzle measurements of Engine Combustion Network “Spray G” gasoline direct injectors”. *Experimental Thermal and Fluid Science*, vol. 88 (2017), pp. 608–621. doi: `10.1016/j.expthermflusci.2017.07.015`, (*cited on: Chap.3-p.41, Chap.4-pp.83,86,90, Chap.5-pp.116,143,144,148, Chap.6-p.181*).

Duke, Daniel, Swantek, Andrew, Kastengren, Alan, Fezzaa, Kamel, and Powell, Christopher. “Recent Developments in X-ray Diagnostics for Cavitation”. *SAE Int. J. Fuels Lubr.* Vol. 8.1 (2015), pp. 135–146. doi: `10.4271/2015-01-0918`, (*cited on: Chap.4-p.77*).

ENGINE COMBUSTION NETWORK. *ECN Spray G.* 2016, (*cited on: Chap.3-p.31, Chap.4-p.60, Chap.6-p.182*).

"Engine Combustion Network 5th Workshop." *Wayne State University. Detroit.* 2017, https://ecn.sandia.gov/ecn–workshop/, (*cited on: Chap.6-pp.168,169,180*).

FANSLER, TODD D and PARRISH, SCOTT E. "Spray measurement technology: a review". *Measurement Science and Technology*, vol. 26.1 (2015), p. 012002. DOI: `10.1088/0957-0233/26/1/012002`, (*cited on: Chap.5-pp.107,148*).

FANSLER, TODD D, REUSS, DAVID L, SICK, VOLKER, and DAHMS, RAINER N. "Invited Review: Combustion instability in spray-guided stratified-charge engines: A review". *International Journal of Engine Research*, vol. 16.3 (2015), pp. 260–305. DOI: `10.1177/1468087414565675`, (*cited on: Chap.3-pp.22,23,26,30,31*).

FERGUSON, COLIN R and KIRKPATRICK, ALLAN T. *Internal combustion engines: applied thermosciences.* John Wiley & Sons, 2015, (*cited on: Chap.3-pp.10,19,20,21*).

FORBES, AIRD. *Bosh fuel injection systems. HP Trade.* 2001, p. 29, (*cited on: Chap.3-p.18*).

GILLES-BIRTH, ISABELL, BERNHARDT, SÖREN, SPICHER, ULRICH, and RECHS, MANFRED. "A Study of the In-Nozzle Flow Characteristic of Valve Covered Orifice Nozzles for Gasoline Direct Injection". *SAE Technical Paper 2005-01-3684*, 724 (2005). DOI: `10.4271/2005-01-3684`.

GIMENO, JAIME. "Desarrollo y aplicación de la medida del flujo de cantidad de movimiento de un chorro Diesel." PhD thesis. Universidad Politecnica de Valencia, 2008, (*cited on: Chap.3-p.13, Chap.4-pp.72,73,74, Chap.5-pp.112,122,123,139,140,141,142*).

GUO, HENGJIE, DING, HAICHUN, LI, YANFEI, MA, XIAO, WANG, ZHI, XU, HONGMING, and WANG, JIANXIN. "Comparison of spray collapses at elevated ambient pressure and flash boiling conditions using multi-hole gasoline direct injector". *Fuel*, vol. 199 (2017), pp. 125–134. DOI: `10.1016/j.fuel.2017.02.071`, (*cited on: Chap.3-pp.40,41*).

Gürsoy, Doga, De Carlo, Francesco, Xiao, Xianghui, and Jacobsen, Chris. “TomoPy: a framework for the analysis of synchrotron tomographic data”. *Journal of synchrotron radiation*, vol. 21.5 (2014), pp. 1188–1193, (*cited on: Chap.4-pp.84,90, Chap.5-p.149*).

Harada, Jun, Tomita, Tsutomu, Mizuno, Hiroyuki, Mashiki, Zenichiro, and Ito, Yasushi. “Development of direct injection gasoline engine”. *SAE Technical Paper 970540*, 412 (1997), (*cited on: Chap.3-p.21*).

Haralick, Robert M and Linda, G. Shapiro. *Computer and Robot Vision.* Vol. 2. 1992, pp. 316–317, (*cited on: Chap.4-p.80*).

Hoffmann, Guy, Befrui, Bizhan, Berndorfer, Axel, Piock, Walter F., and Varble, Daniel L. “Fuel System Pressure Increase for Enhanced Performance of GDi Multi-Hole Injection Systems”. *SAE Technical Paper 2014-01-1209* (2014). doi: `10.4271/2014-01-1209`, (*cited on: Chap.3-pp.28,29, Chap.5-p.119*).

Hung, David L.S., Harrington, David L., Gandhi, Anand H., Markle, Lee E., Parrish, Scott E., Shakal, Joseph S., Sayar, Hamid, Cummings, Steven D., and Kramer, Jason L. “Gasoline Fuel Injector Spray Measurement and Characterization - A New SAE J2715 Recommended Practice”. *SAE Int. J. Fuels Lubr.* Vol. 1.1 (2009), pp. 534–548. doi: `10.4271/2008-01-1068`, (*cited on: Chap.4-p.63*).

Husted, Harry, Spegar, Timothy D., and Spakowski, Joseph. “The Effects of GDi Fuel Pressure on Fuel Economy”. *SAE Technical Paper 2014-01-1438* (2014). doi: `10.4271/2014-01-1438`, (*cited on: Chap.3-p.28*).

Ikoma, Takuya, Abe, Shizuo, Sonoda, Yukihiro, and Suzuki, Hisao. “Development of V-6 3 . 5-liter Engine Adopting New Direct Injection System”. *SAE Technical Paper 2006-01-1259*, 724 (2006), (*cited on: Chap.3-p.22*).

Ingraham, Joseph C. *Automobiles races.* 1957, (*cited on: Chap.3-p.18*).

ISENSTADT, AARON, GERMAN, JOHN, DOROBANTU, MIHAI, BOGGS, DAVID, and WATSON, TOM. "Downsized , boosted gasoline engines". *The ICCT Internaltional Council of Clean Transportation*, 21 (2016), p. 23, (*cited on: Chap.3-pp.21,23*).

ITANI, LAMA M, BRUNEAUX, GILLES, HERMANT, LAURENT, and SCHULZ, CHRISTOF. "Investigation of the Mixing Process and the Fuel Mass Concentration Fields for a Gasoline Direct-Injection Spray at ECN Spray G Conditions and Variants". *SAE Technical Paper 2015-01-1902* (2015), pp. 1–10. DOI: `10.4271/2015-01-1902`, (*cited on: Chap.3-pp.42,43*).

IWAMOTO, Y., NOMA, K., NAKAYAMA, O., YAMAUCHI, T., and ANDO, H. "Development of Gasoline Direct Injection Engine". *SAE Technical Paper 970541*, 412 (1997). DOI: `10.4271/970541`, (*cited on: Chap.3-p.21*).

JIA, TAO MING, LI, GUO XIU, YU, YU SONG, and XU, YANG JIE. "Effects of ultra-high injection pressure on penetration characteristics of diesel spray and a two-mode leading edge shock wave". *Experimental Thermal and Fluid Science*, vol. 79 (2016), pp. 126–133. DOI: `10.1016/j.expthermflusci.2016.07.006`, (*cited on: Chap.3-p.14*).

JOHANSSON, ANDERS N, HEMDAL, STINA, and DAHLANDER, PETTER. "Reduction of Soot Formation in an Optical Single-Cylinder Gasoline Direct-Injected Engine Operated in Stratified Mode Using 350 Bar Fuel Injection Pressure, Dual-Coil and High-Frequency Ignition Systems". *SAE Int. J. Engines*, vol. 10 (2017). DOI: `10.4271/2017-01-9278`, (*cited on: Chap.3-pp.23,28,32*).

JOHNSON, TIMOTHY V. "CE-2016-306 Directions in vehicle efficiency and emissions". *Combustion Engines*, vol. 166.3 (2017), pp. 3–8. DOI: `10.19206/CE-2016-306`, (*cited on: Chap.3-pp.21,26*).

JOHNSON, TIMOTHY and JOSHI, AMEYA. "Review of Vehicle Engine Efficiency and Emissions". *SAE Technical Paper 2017-01-0907* (2017). DOI: `10.4271/2017-01-0907`, (*cited on: Chap.3-pp.21,23,26*).

KALGHATGI, GAUTAM and JOHANSSON, BENGT. "Gasoline compression ignition approach to efficient, clean and affordable future engines". *Proceedings of the Institution of Mechanical Engineers, Part D: Journal of Automobile Engineering* (2017), p. 095440701769427. DOI: `10.1177/0954407017694275`, (*cited on: Chap.3-p.27*).

Kanda, Mutsumi, Toyokazy, Baika, Senji, Kato, Minoru, Iwamuro, Makoto, Koike, and Akinori, Saito. "Application of a New Combustion Concept to Direct Injection Gasoline Engine". *SAE Technical Paper 2000-01-0531*, vol. 2000.724 (2000). doi: `10.4271/2000-01-0531`, (*cited on: Chap.3-p.29*).

Kastengren, Alan L., Powell, Christopher F, Wang, Yujie, Im, Kyoung-Su, and Wang, Jin. "X-Ray Radiography Measurements of Diesel Spray Structure At Engine-Like Ambient Density". *Atomization and Sprays*, vol. 19.11 (2009), pp. 1031–1044. doi: `10.1615/AtomizSpr.v19.i11.30`, (*cited on: Chap.5-pp.146,147*).

Kastengren, Alan L, Tilocco, F Zak, Duke, Daniel J, Powell, Christopher F, Zhang, Xusheng, and Moon, Seoksu. "Time-resolved X-ray radiography of sprays from engine combustion network spray a diesel injectors". *Atomization and Sprays*, vol. 24.3 (2014), (*cited on: Chap.4-p.86*).

Kastengren, Alan and Powell, Christopher F. "Synchrotron X-ray techniques for fluid dynamics". *Experiments in Fluids*, vol. 55.3 (2014). doi: `10.1007/s00348-014-1686-8`, (*cited on: Chap.4-p.86*).

Kastengren, Alan, Powell, Christopher F, Arms, Dohn, Dufresne, Eric M, Gibson, Harold, and Wang, Jin. "The 7BM beamline at the APS: a facility for time-resolved fluid dynamics measurements". *Journal of Synchrotron Radiation*, vol. 19.4 (2012), pp. 654–657. doi: `10.1107/S0909049512016883`.

Khan, Muhammad Mahabat, Hélie, Jerome, Gorokhovski, Mikhael, and Sheikh, Nadeem Ahmed. "Experimental and numerical study of flash boiling in gasoline direct injection sprays". *Applied Thermal Engineering*, vol. 123 (2017), pp. 377–389. doi: `10.1016/j.applthermaleng.2017.05.102`, (*cited on: Chap.3-p.40*).

Kostas, J., Honnery, D., Soria, J., Kastengren, A., Liu, Z., Powell, C. F., and Wang, J. "Effect of nozzle transients and compressibility on the penetration of fuel sprays". *Applied Physics Letters*, vol. 95.2 (2009). doi: `10.1063/1.3182821`, (*cited on: Chap.4-p.77, Chap.5-p.107*).

LACEY, J., POURSADEGH, F., BREAR, M. J., GORDON, R., PETERSEN, P., LAKEY, C., BUTCHER, B., and RYAN, S. “Generalizing the behavior of flash-boiling, plume interaction and spray collapse for multi-hole, direct injection”. *Fuel*, vol. 200 (2017), pp. 345–356. DOI: `10.1016/j.fuel.2017.03.057`, (*cited on: Chap.3-p.42*).

LACEY, JOSHUA STUART, POURZAKADEH, FARZAD, BREAR, MICHAEL, PETERSEN, PHRED, LAKEY, CHARLES, RYAN, STEVE, and BUTCHER, BRENDAN. “Optical Characterization of Propane at Representative Spark Ignition , Gasoline Direct Injection Conditions”. *SAE International Journal of Engines*, 2016-01-0842 (2016), pp. 21–23. DOI: `10.4271/2016-01-0842.Copyright`, (*cited on: Chap.3-p.42, Chap.6-p.188*).

LEWIS, J P. “Fast normalized cross-correlation”. *Vision interface*. Vol. 10. 1. 1995, pp. 120–123, (*cited on: Chap.4-p.80*).

LI, ZHI HUA, HE, BANG QUAN, and ZHAO, HUA. “Application of a hybrid breakup model for the spray simulation of a multi-hole injector used for a DISI gasoline engine”. *Applied Thermal Engineering*, vol. 65.1-2 (2014), pp. 282–292. DOI: `10.1016/j.applthermaleng.2013.12.063`, (*cited on: Chap.6-p.167*).

LICHTAROWICZ, A, DUGGINS, R K, and MARKLAND, E. “Discharge coefficients for incompressible non-cavitating flow through long orifices”. *Journal of Mechanical Engineering Science*, vol. 7.2 (1965), pp. 210–219. DOI: `10.1243/JMES_JOUR_1965_007_029_02`, (*cited on: Chap.5-p.112*).

LINSTROM, P. J., MALLARD, W. G, and EDS., GAITHERSBURG. *Thermophysical Properties of Fluid Systems in NIST Chemistry WebBook.* 2011, (*cited on: Chap.4-p.70*).

LUO, FUQIANG, CUI, HUIFENG, and DONG, SHAOFENG. “Transient measuring method for injection rate of each nozzle hole based on spray momentum flux”. *Fuel*, vol. 125 (2014), pp. 20–29. DOI: `10.1016/j.fuel.2014.02.011`, (*cited on: Chap.5-p.107*).

MACIAN, V., BERMUDEZ, V., PAYRI, R., and GIMENO, J. “New Technique for Determination of Internal Geometry of a Diesel Nozzle With the Use of Silicone Methodology”. *Experimental Techniques*, vol. 27.2 (2003), pp. 39–43. DOI: `10.1111/j.1747-1567.2003.tb00107.x`, (*cited on: Chap.3-p.37*).

Macian, Vicente, Payri, Raul, Garcia, Antonio, and Bardi, Michele. “Experimental evaluation of the best approach for diesel spray images segmentation”. *Experimental Techniques*, vol. 36.6 (2012), pp. 26–34. doi: `10.1111/j.1747-1567.2011.00730.x`, (*cited on: Chap.4-p.94*).

Magneti Marelli. *Gasoline Direct Injection Technology (GDI)*. 2017, (*cited on: Chap.3-pp.29,32*).

Manin, Julien, Bardi, Michele, and Pickett, Lyle M. “Evaluation of the liquid length via diffused back-illumination imaging in vaporizing diesel sprays”. *Comodia*. Fukuoka, 2012, (*cited on: Chap.4-p.93*).

Manin, Julien, Jung, Yongjin, Skeen, Scott A, Pickett, Lyle M, Parrish, Scott E, and Markle, Lee E. “Experimental Characterization of DI Gasoline Injection Processes”. *SAE Technical Paper 2015-01-1894* (2015). doi: `10.4271/2015-01-1894`, (*cited on: Chap.3-pp.37,41,42, Chap.4-p.92, Chap.6-pp.188,189,190,192*).

Marseglia, G., Costa, M., Catapano, F., Sementa, P., and Vaglieco, B.M. “Study about the link between injection strategy and knock onset in an optically accessible multi-cylinder GDI engine”. *Energy Conversion and Management*, vol. 134 (2017), pp. 1–19. doi: `10.1016/j.enconman.2016.12.012`, (*cited on: Chap.5-p.119*).

Matusik, K E, Duke, D J, Sovis, N, Swantek, A B, Powell, C F, Payri, R, and Vaquerizo, D. “A study on the relationship between internal nozzle geometry and injected mass distribution of eight ECN Spray G nozzles”. *ILASS – Europe 2017, 28th Annual Conference on Liquid Atomization and Spray Systems*, September (2017). doi: `http://dx.doi.org/10.4995/ILASS2017.2017.4766`, (*cited on: Chap.3-pp.37,41, Chap.5-pp.143,154*).

Matusik, K.E., Duke, D.J., Swantek, A.B., Powell, C.F., and Kastengren, A.L. “High Resolution X-Ray Tomography of Injection Nozzles”. *ILASS Americas 28th Annual Conference on Liquid Atomization and Spray Systems, Dearborn, MI, May 2016*. May. 2016, (*cited on: Chap.3-pp.37,38*).

Meijer, M, Malbec, Louis-Marie M, Bruneaux, Gilles, and Somers, L.M.T. M T. "Engine Combustion Network:'Spray A'Basic Measurements and Advanced Diagnostics". *ICLASS 2012, 12th Triennial International Conference on Liquid Atomization and Spray Systems*. 2012, pp. 2–6, (*cited on: Chap.4-p.93*).

Mitroglou, N, Nouri, J M, Yan, Y, Gavaises, M, and Arcoumanis, C. "Spray Structure Generated by Multi-Hole Injectors for Gasoline Direct-Injection Engines Reprinted From : Diesel Injection SI Engine Technology". *SAE Technical Paper 2007-01-1417* (2007). doi: `10.4271/2007-01-1417`, (*cited on: Chap.5-p.113*).

Montanaro, A and Allocca, L. "Flash Boiling Evidences of a Multi-Hole GDI Spray under Engine Conditions by Mie-Scattering Measurements". *SAE Technical Paper 2015-01-1945* (2015), (*cited on: Chap.3-pp.40,42, Chap.4-p.92, Chap.6-p.188*).

Montanaro, A., Allocca, L., Lazzaro, M., and Meccariello, G. "Impinging Jets of Fuel on a Heated Surface: Effects of Wall Temperature and Injection Conditions". *SAE Technical Paper 2016-01-0863*, vol. 2016-April (2016). doi: `10.4271/2016-01-0863`, (*cited on: Chap.3-p.42*).

Moon, Seoksu, Komada, Keisuke, Sato, Kiyotaka, Yokohata, Hideaki, Wada, Yoshitaka, and Yasuda, Nobuhiro. "Ultrafast X-ray study of multi-hole GDI injector sprays: Effects of nozzle hole length and number on initial spray formation". *Experimental Thermal and Fluid Science*, vol. 68 (2015), pp. 68–81. doi: `10.1016/j.expthermflusci.2015.03.027`, (*cited on: Chap.3-pp.33,35, Chap.4-pp.74,77, Chap.5-pp.112,113,142,148*).

Moon, Seoksu, Li, Tianyun, Sato, Kiyotaka, and Yokohata, Hideaki. "Governing parameters and dynamics of turbulent spray atomization from modern GDI injectors". *Energy*, vol. 127 (2017), pp. 89–100. doi: `10.1016/j.energy.2017.03.099`, (*cited on: Chap.5-p.113*).

Motjabi, Mehdi. "Optical Analysis of Multi-Stream GDI Sprays under Various Engine Operating Conditions by". PhD thesis. Loughborough University, 2011, (*cited on: Chap.3-pp.29,30*).

Moulai, Maryam, Grover, Ronald, Parrish, Scott, and Schmidt, David. “Internal and Near-Nozzle Flow in a Multi-Hole Gasoline Injector Under Flashing and Non-Flashing Conditions”. *SAE Technical Paper 2015-01-0944*, 2015-01-0944 (2015). doi: `10.4271/2015-01-0944`, (*cited on: Chap.3-pp.40,41,42*).

Musculus, Mark P B, Miles, Paul C., and Pickett, Lyle M. “Conceptual models for partially premixed low-temperature diesel combustion”. *Progress in Energy and Combustion Science*, vol. 39.2-3 (2013), pp. 246–283. doi: `10.1016/j.pecs.2012.09.001`, (*cited on: Chap.5-p.152*).

Naber, Jeffrey D and Siebers, Dennis L. “Effects of Gas Density and Vaporization on Penetration and Dispersion of Diesel Sprays”. *SAE Paper 960034*. Vol. 105. 412. Society of Automotive Engineers, Inc., Warrendale, Pennsylvania, USA, 1996, pp. 82–111. doi: `10.4271/960034`, (*cited on: Chap.6-p.202*).

Nicky van Foreest. *Fitting an Ellipse to a Set of Data Points*, (*cited on: Chap.5-p.108*).

Parrish, Scott E. and Zink, R. J. “Development and Application of Imaging System To Evaluate Liquid and Vapor Envelopes of Multi-Hole Gasoline Fuel Injector Sprays Under Engine-Like Conditions”. *Atomization and Sprays*, vol. 22.8 (2012), pp. 647–661. doi: `10.1615/AtomizSpr.2012006215`, (*cited on: Chap.6-pp.190,192*).

Patel, R, Ladommatos, N, Stansfield, P A, Wigley, G, Garner, C P, Pitcher, G, Turner, J W G, Nuglisch, H, and Helie, J. “Un-throttling a direct injection gasoline homogeneous mixture engine with variable valve actuation”. *International Journal of Engine Research*, vol. 11.6 (2010), pp. 391–411. doi: `10.1243/14680874JER604`, (*cited on: Chap.3-p.27*).

Pauer, Thomas, Yilmaz, Hakan, Zumbrägel, Joachim, and Schünemann, Erik. *New Generation Bosch Gasoline Direct-injection Systems*. Tech. rep. 7-8. 2017, pp. 16–23. doi: `10.1007/s38313-017-0053-6`, (*cited on: Chap.3-pp.23,26,29,30,32,36*).

Payri, Francisco and Desantes, Jose Maria. *Motores de combustion interna alternativos*. Editorial Reverte, 2011, (*cited on: Chap.3-pp.9,12,16,17,18*).

PAYRI, FRANCISCO, PAYRI, RAUL, SALVADOR, FRANCISCO JAVIER, and MARTÍNEZ-LÓPEZ, JORGE. "A contribution to the understanding of cavitation effects in Diesel injector nozzles through a combined experimental and computational investigation". *Computers & Fluids*, vol. 58 (2012), pp. 88–101. DOI: `10.1016/j.compfluid.2012.01.005`, (*cited on: Chap.3-p.36*).

PAYRI, R, GARCÍA, J M, SALVADOR, F J, and GIMENO, J. "Using spray momentum flux measurements to understand the influence of diesel nozzle geometry on spray characteristics". *Fuel*, vol. 84.5 (2005), pp. 551–561, (*cited on: Chap.4-p.72*).

PAYRI, R, GIMENO, J, VIERA, J P, and PLAZAS, A H. "Effect of Partial Needle Lift on the Hydraulic and Evaporative Performance Characteristics of a Common rail Diesel Fuel Injector". *THIESEL 2012 Conference on Thermo- and Fluid Dynamic Processes in Diesel Engines.* 2012, pp. 1–19, (*cited on: Chap.4-p.69*).

PAYRI, RAUL, GARCÍA, ANTONIO, DOMENECH, VICENT, DURRETT, RUSSELL P, PLAZAS, ALEJANDRO HERNAN, GARCIA, ANTONIO, DOMENECH, VICENT, DURRETT, RUSSELL P, and PLAZAS, ALEJANDRO HERNAN. "An experimental study of gasoline effects on injection rate, momentum flux and spray characteristics using a common rail diesel injection system". *Fuel*, vol. 97 (2012), pp. 390–399. DOI: `10.1016/j.fuel.2011.11.065`, (*cited on: Chap.5-p.107*).

PAYRI, RAUL, GIMENO, JAIME, BARDI, MICHELE, and PLAZAS, ALEJANDRO. "Effect of Injection Rate Shaping Over Diesel Spray Development in Non Reacting Evaporative Conditions". *ASME 2012 Internal Combustion Engine Division Spring Technical Conference.* Torino, Italy: ASME, 2012, p. 347. DOI: `10.1115/ICES2012-81206`, (*cited on: Chap.4-p.95*).

PAYRI, RAUL, GIMENO, JAIME, BRACHO, GABRIELA, and VAQUERIZO, DANIEL. "Study of liquid and vapor phase behavior on Diesel sprays for heavy duty engine nozzles". *Applied Thermal Engineering*, vol. 107 (2016), pp. 365–378. DOI: `10.1016/j.applthermaleng.2016.06.159`, (*cited on: Chap.4-pp.64,79,80, Chap.5-pp.107,119, Chap.6-pp.173,194,200,202,204*).

Payri, Raul, Gimeno, Jaime, Marti-Aldaravi, Pedro, and Vaquerizo, Daniel. “Momentum Flux Measurements on an ECN GDi Injector”. *SAE Technical Paper 2015-01-1893* (2015). doi: `10.4271/2015-01-1893`, (*cited on: Chap.3-pp.37,41, Chap.4-pp.65,69,74, Chap.5-p.119*).

Payri, Raul, Gimeno, Jaime, Martí-Aldaraví, Pedro, and Vaquerizo, Daniel. “Internal flow characterization on an ECN GDi injector”. *Atomization and Sprays*, vol. 26.9 (2015), pp. 889–919. doi: `10.1615/AtomizSpr.2015013930`, (*cited on: Chap.3-pp.28,32,41, Chap.4-p.65*).

Payri, Raul, Gimeno, Jaime, Novella, Ricardo, and Bracho, Gabriela. “On the rate of injection modeling applied to direct injection compression ignition engines”. *International Journal of Engine Research* (2016). doi: `10.1177/1468087416636281`, (*cited on: Chap.4-p.65*).

Payri, Raul, Gimeno, Jaime, Venegas, Oscar, and Plazas, Alejandro Hernan. “Experimental and computational study of the influence of partial needle lift on nozzle flow in diesel fuel injectors”. *Atomization and Sprays*, vol. 22 (2012), pp. 687–714. doi: `10.1615/AtomizSpr.2012005810`, (*cited on: Chap.4-p.70*).

Payri, Raul, Gimeno, Jaime, Viera, Juan Pablo, and Plazas, Alejandro Hernan. “Schlieren visualization of transient vapor penetration and spreading angle of a prototype diesel direct-acting piezoelectric injector”. *ICLASS 2012*. 2012, pp. 1–8, (*cited on: Chap.6-p.190*).

Payri, Raul, Gimeno, Jaime, Viera, Juan Pablo, and Plazas, Alejandro Hernan. “Needle lift profile influence on the vapor phase penetration for a prototype diesel direct acting piezoelectric injector”. *Fuel*, vol. 113 (2013), pp. 257–265. doi: `10.1016/j.fuel.2013.05.057`, (*cited on: Chap.4-pp.90,95, Chap.6-pp.190,197*).

Payri, Raul, Salvador, F.J. Francisco Javier, Gimeno, Jaime, and Bracho, Gabriela. “A new methodology for correcting the signal cumulative phenomenon on injection rate measurements”. *Experimental Techniques*, vol. 32.February (2008), pp. 46–49. doi: `10.1111/j.1747-1567.2007.00188.x`, (*cited on: Chap.4-pp.65,70*).

PAYRI, RAUL, SALVADOR, FRANCISCO JAVIER, MARTÍ-ALDARAVÍ, PEDRO, and VAQUERIZO, DANIEL. "ECN Spray G external spray visualization and spray collapse description through penetration and morphology analysis". *Applied Thermal Engineering*, vol. 112 (2017), pp. 304–316. DOI: `10.1016/j.applthermaleng.2016.10.023`, (*cited on: Chap.3-pp.28,32,41,42, Chap.4-p.74, Chap.5-p.107, Chap.6-pp.177,187*).

PAYRI, RAUL, TORMOS, BERNARDO, SALVADOR, FRANCISCO JAVIER, and PLAZAS, ALEJANDRO HERNAN. "Using one-dimensional modelling codes to analyse the influence of diesel nozzle geometry on injection rate characteristics". *International Journal of Vehicle Design*, vol. 38.1 (2005), pp. 58–78, (*cited on: Chap.5-p.107*).

PAYRI, RAUL, VIERA, JUAN PABLO, GOPALAKRISHNAN, VENKATESH, and SZYMKOWICZ, PATRICK G. "The effect of nozzle geometry over internal flow and spray formation for three different fuels". *Fuel*, vol. 183 (2016), pp. 20–33. DOI: `10.1016/j.fuel.2016.06.041`, (*cited on: Chap.4-p.77, Chap.6-p.173*).

PAYRI, RAUL, VIERA, JUAN PABLO, GOPALAKRISHNAN, VENKATESH, and SZYMOWITZ, PATRICK. "The effect of nozzle geometry over ignition delay and flame lift-off of reacting direct-injection sprays for three different fuels". *Fuel* (2017), (*cited on: Chap.3-p.14, Chap.4-p.77*).

PAYRI, RAUL, VIERA, JUAN PABLO, PEI, YUANJIANG, and SOM, SIBENDU. "Experimental and numerical study of lift-off length and ignition delay of a two-component diesel surrogate". *Fuel*, vol. 158 (2015), pp. 957–967. DOI: `10.1016/j.fuel.2014.11.072`, (*cited on: Chap.4-p.90*).

PHAM, P.X., VO, D.Q., and JAZAR, R.N. "Development of fuel metering techniques for spark ignition engines". *Fuel*, vol. 206 (2017), pp. 701–715. DOI: `10.1016/j.fuel.2017.06.043`, (*cited on: Chap.3-pp.19,20,23,24,26,27*).

PICKETT, LYLE M, GENZALE, CAROLINE L, and MANIN, JULIEN. "Uncertainty quantification for liquid penetration of evaporating sprays at diesel-like conditions". *Atomization and Sprays*, vol. 25.5 (2015), (*cited on: Chap.6-p.173*).

Plazas, Alejandro Hernan. “Modelado unidimensional de inyectores common-rail Diesel”. PhD thesis. Valencia: E.T.S. Ingenieros Industriales. Universidad Politécnica de Valencia, 2005, (*cited on: Chap.4-p.65*).

Postrioti, Lucio, Bosi, Maurizio, Cavicchi, Andrea, Gioia, Rita Di, Bonandrini, Giovanni, Marelli, Magneti, and Spa, Powertrain. “Momentum Flux Measurement on Single-Hole GDI Injector under Flash-Boiling Condition”. *SAE Technical Paper 2015-06-2480* (2015). doi: `10.4271/2015-24-2480`, (*cited on: Chap.3-pp.33,40, Chap.5-p.107*).

Poursadegh, Farzad. “An experimental and theoretical investigation of direct fuel injection”. PhD thesis. University of Melbourne, 2017, p. 172. doi: `10.1205/fbp.04184`, (*cited on: Chap.3-pp.39,40*).

Poursadegh, Farzad, Lacey, Joshua S., Brear, Michael J., and Gordon, Robert L. “On the Fuel Spray Transition to Dense Fluid Mixing at Reciprocating Engine Conditions”. *Energy and Fuels*, vol. 31.6 (2017), pp. 6445–6454. doi: `10.1021/acs.energyfuels.7b00050`, (*cited on: Chap.3-p.41*).

Quaremba, Giuseppe, Allocca, Luigi, Amoresano, Amedeo, Niola, Vincenzo, Montanaro, Alessandro, and Langella, Giuseppe. “Fuzzy Logic Approach to GDI Spray Characterization”. *SAE Technical Paper 2016-01-0874*. 2016. doi: `10.4271/2016-01-0874`, (*cited on: Chap.3-p.42*).

Reif, Konrad. *Gasoline Engine Management*. 2014, p. 354. doi: `10.1007/978-3-658-03964-6`, (*cited on: Chap.3-pp.15,17,18,20,25,28,32*).

Rivera, Edwin A., Mastro, Noreen, Zizelman, James, Kirwan, John, and Ooyama, Robert. “Development of Injector for the Direct Injection Homogeneous Market using Design for Six Sigma”. *SAE Technical Papers* (2010). doi: `10.4271/2010-01-0594`, (*cited on: Chap.3-pp.31,33*).

Saha, Kaushik, Quan, Shaoping, Battistoni, Michele, Som, Sibendu, Senecal, P K, and Pomraning, Eric. “Coupled Eulerian Internal Nozzle Flow and Lagrangian Spray Simulations for GDI Systems”. *SAE technical paper 2017-01-0834*. 2017. doi: `10.4271/2017-01-0834`, (*cited on: Chap.3-pp.41,42,43*).

Saha, Kaushik, Som, Sibendu, Battistoni, Michele, Li, Yanheng, Pomraning, Eric, and Senecal, Peter Kelly. “Numerical Investigation of Two-Phase Flow Evolution of In- and Near-Nozzle Regions of a Gasoline Direct Injection Engine During Needle Transients”. *SAE International Journal of Engines*, vol. 9.2 (2016), pp. 2016–01–0870. doi: `10.4271/2016-01-0870`, (*cited on: Chap.3-pp.40,41,42, Chap.4-p.77, Chap.5-p.142, Chap.6-pp.181,188*).

Saha, Kaushik, Som, Sibendu, Battistoni, Michele, Li, Yanheng, Quan, Shaoping, and Kelly Senecal, Peter. “Modeling of Internal and Near-Nozzle Flow for a Gasoline Direct Injection Fuel Injector”. *Journal of Energy Resources Technology*, vol. 138.5 (2016), p. 052208. doi: `10.1115/1.4032979`, (*cited on: Chap.3-p.41*).

Saha, Kaushik, Som, Sibendu, Battistoni, Michele, Li, Yanheng, Quan, Shaoping, and Senecal, Peter Kelly. “Numerical simulation of internal and near-nozzle flow of a gasoline direct injection fuel injector”. *Journal of Physics: Conference Series*, vol. 656.January 2016 (2015), p. 012100. doi: `10.1088/1742-6596/656/1/012100`, (*cited on: Chap.3-p.41, Chap.6-p.181*).

Saliba, Georges, Saleh, Rawad, Zhao, Yunliang, Presto, Albert A., Lambe, Andrew T., Frodin, Bruce, Sardar, Satya, Maldonado, Hector, Maddox, Christine, May, Andrew A., Drozd, Greg T., Goldstein, Allen H., Russell, Lynn M., Hagen, Fabian, and Robinson, Allen L. “Comparison of Gasoline Direct-Injection (GDI) and Port Fuel Injection (PFI) Vehicle Emissions: Emission Certification Standards, Cold-Start, Secondary Organic Aerosol Formation Potential, and Potential Climate Impacts”. *Environmental Science & Technology* (2017), acs.est.6b06509. doi: `10.1021/acs.est.6b06509`, (*cited on: Chap.3-p.20*).

Salvador, Francisco Javier, Gimeno, Jaime, Carreres, Marcos, and Crialesi-Esposito, Marco. “Fuel temperature influence on the performance of a last generation common-rail diesel ballistic injector. Part I: Experimental mass flow rate measurements and discussion”. *Energy Conversion and Management*, vol. 114 (2016), pp. 364–375. doi: `10.1016/j.enconman.2016.02.042`, (*cited on: Chap.5-p.124*).

Schwarz, Christian, Missy, Stephan, Steyer, Helmut, Durst, Bodo, Schünemann, Erik, and Kern, Wolfgang. “The New BMW Four and Six-cylinder Spark-Ignition Engines with Stratified Combustion”. *MTZ worldwide*, vol. 68.05 (2007), pp. 2–5. doi: `10.1007/BF03226823`, (*cited on: Chap.3-p.23*).

Sellnau, Mark, Foster, Matthew, Hoyer, Kevin, Moore, Wayne, Sinnamon, James, and Husted, Harry. “Development of a Gasoline Direct Injection Compression Ignition (GDCI) Engine”. *SAE Int. J. Engines*, vol. 7.2 (2014), pp. 835–851. doi: `10.4271/2014-01-1300`, (*cited on: Chap.3-p.21, Chap.5-p.119*).

Sellnau, Mark, Moore, Wayne, Sinnamon, James, Hoyer, Kevin, Foster, Matthew, and Husted, Harry. “GDCI Multi-Cylinder Engine for High Fuel Efficiency and Low Emissions”. *SAE International Journal of Engines*, vol. 8.2 (2015), pp. 775–790. doi: `10.4271/2015-01-0834`, (*cited on: Chap.3-p.27, Chap.5-p.119*).

Serras-Pereira, J., Van Romunde, Z., Aleiferis, P. G., Richardson, D., Wallace, S., and Cracknell, R. F. “Cavitation, primary break-up and flash boiling of gasoline, iso-octane and n-pentane with a real-size optical direct-injection nozzle”. *Fuel*, vol. 89.9 (2010), pp. 2592–2607. doi: `10.1016/j.fuel.2010.03.030`.

Shen, Qun, Lee, Wah-Keat, Fezzaa, Kamel, Chu, Yong S., De Carlo, Francesco, Jemian, Peter, Ilavsky, Jan, Erdmann, Mark, and Long, Gabrielle G. “Dedicated full-field X-ray imaging beamline at Advanced Photon Source”. *Nuclear Instruments and Methods in Physics Research Section A: Accelerators, Spectrometers, Detectors and Associated Equipment*, vol. 582.1 (2007), pp. 77–79. doi: `10.1016/j.nima.2007.08.169`, (*cited on: Chap.4-p.79*).

Shost, Mark. “Evaluation Of Nozzle Geometry On High Pressure Gasoline Direct Injection Spray Atomization”. PhD thesis. Wayne State University Dissertations, 2014, (*cited on: Chap.3-pp.34,36, Chap.4-p.77, Chap.5-pp.113,142*).

Shost, Mark a., Lai, Ming-Chia, Befrui, Bizhan, Spiekermann, Peter, and Varble, Daniel L. “GDi Nozzle Parameter Studies Using LES and Spray Imaging Methods”. *SAE Technical Paper 2014-01-1434*, vol. 1 (2014). doi: `10.4271/2014-01-1434`, (*cited on: Chap.3-p.35, Chap.5-pp.113,142*).

Siebers, Dennis L. “Scaling liquid-phase fuel penetration in diesel sprays based on mixing-limited vaporization”. *SAE Technical Paper 1999-01-0528* (1999). doi: `10.4271/1999-01-0528`, (*cited on: Chap.6-pp.190,194,202*).

Smith, James, Jr, Gerald Szekely, Solomon, Arun, and Parrish, Scott. “A Comparison of Spray-Guided Stratified-Charge Combustion Performance with Outwardly-Opening Piezo and Multi-Hole Solenoid Injectors”. *SAE Int. J. Engines*, vol. 4 (2011), pp. 1481–1497. doi: `10.4271/2011-01-1217`, (*cited on: Chap.3-p.31*).

Song, Jingeun and Park, Sungwook. “Effect of injection strategy on the spray development process in a single-cylinder optical GDi engine.” *Atomization and Sprays*, vol. 25.9 (2015), pp. 819–836. doi: `10.1615/AtomizSpr.2015012018`, (*cited on: Chap.6-p.167*).

Sphicas, Panagiotis. “High pressure and high temperature measurements on diesel sprays”. PhD thesis. 2013, (*cited on: Chap.3-p.15*).

Sphicas, Panos, Pickett, Lyle M, Skeen, Scott, Frank, Jonathan, Lucchini, Tommaso, Sinoir, David, D’Errico, Gianluca, Saha, Kaushik, and Som, Sibendu. “A Comparison of Experimental and Modeled Velocity in Gasoline Direct-Injection Sprays with Plume Interaction and Collapse”. *SAE Int. J. Fuels Lubr.* Vol. 10 (2017), pp. 184–201. doi: `10.4271/2017-01-0837`, (*cited on: Chap.3-pp.42,43, Chap.6-pp.187,208*).

Stefan, S. “Optical Diagnostics on FSI Transparent Engine”. *FISITA World Automotive Congress, Barcelona.* 2004, pp. 23–27, (*cited on: Chap.3-p.25*).

Strek, Piotr, Duke, Daniel, Swantek, Andrew, Kastengren, Alan, Powell, Christopher F., and Schmidt, David P. “X-Ray Radiography and CFD Studies of the Spray G Injector”. *SAE Technical Paper 2016-01-0858.* 2016. doi: `10.4271/2016-01-0858`, (*cited on: Chap.3-pp.37,41, Chap.4-p.77, Chap.6-pp.167,188*).

Swantek, Andrew, Kastengren, Alan, Duke, Daniel, Tilocco, Zak, Sovis, Nicolas, and Powell, Christopher F. “Quantification of Shot-to-Shot Variation in Single Hole Diesel Injectors”. *SAE International Journal of Fuels and Lubricants*, vol. 8.1 (2015), pp. 2015–01–0936. doi: `10.4271/2015-01-0936`, (*cited on: Chap.4-p.77*).

TOR, UNIVERSITÀ, ROMA, VERGATA, DEMAIO, A, and NUMIDIA, S. "Reduction of Spray Momentum for GDI High- Pressure Injectors – A Necessary Step to Accomplish Series Production Super-Charged DI-Engines". *SAE Technical Paper 2005-01-0104*, 724 (2005), (*cited on: Chap.5-p.148*).

TU, PO-WEN, CAO, LI, XU, HONGMING, EALL, ADAM, VENUS, JENS KRUEGER, SRIVASTAVA, DHANANJAY KUMAR, DEAN, KARL, and JING, DALIANG. "Numerical Investigation of GDI Injector Nozzle Geometry on Spray Characteristics". *SAE Technical Paper 2015-01-1906*, 201509061 (2015). DOI: `10.4271/2015-01-1906`, (*cited on: Chap.3-p.34, Chap.5-pp.113,142,148*).

VENEGAS, OSCAR. "Estudio del fenómeno de la cavitación en la inyección diesel mediante la visualización del flujo interno en orificios transparentes." PhD thesis. Universidad Poltécnica de València-Departamento de Máquinas y Motores Térmicos, 2014, (*cited on: Chap.3-pp.13,14,15, Chap.4-pp.64,65,69,77*).

VENT, GUIDO and ENDERLE, CHRISTIAN. "The new 2.0 l turbo engine from the Mercedes-Benz 4-cylinder engine family". *2nd Aachen Colloquium China*. Stuttgart, 2012, pp. 137–160, (*cited on: Chap.3-pp.31,38*).

VIERA, JUAN PABLO, PAYRI, RAUL, SWANTEK, ANDREW B, DUKE, DANIEL J., SOVIS, NICOLAS, KASTENGREN, ALAN L., and POWELL, CHRISTOPHER F. "Linking instantaneous rate of injection to X-ray needle lift measurements for a direct-acting piezoelectric injector". *Energy Conversion and Management*, vol. 112 (2016), pp. 350–358. DOI: `10.1016/j.enconman.2016.01.038`, (*cited on: Chap.4-p.79*).

WESTLYE, FREDRIK R., PENNEY, KEITH, IVARSSON, ANDERS, PICKETT, LYLE M., MANIN, JULIEN, and SKEEN, SCOTT A. "Diffuse back-illumination setup for high temporally resolved extinction imaging". *Applied Optics*, vol. 56.17 (2017), p. 5028. DOI: `10.1364/AO.56.005028`, (*cited on: Chap.6-pp.178,180*).

WHITE, FRANK. *Fluid Mechanics*. 2010, p. 862. DOI: `10.1111/j.1549-8719.2009.00016.x.Mechanobiology`, (*cited on: Chap.5-p.112*).

WIGLEY, GRAHAM, WOOD, ANDREW, and HELIE, JEROME. "Experimental Investigation on the Stream to Stream Interactions for a Multi-hole GDI Injector with Multiple Injection Strategies". *10th International Congress, Engine Combustion Processes, Current Problems and Modern Technologies, March 24th-25th, 2011, München, Germany.* 2011, pp. 1–12, (*cited on: Chap.5-p.135*).

WINKLHOFER, ERNST, WIESLER, B, AHMADI-BEFRUI, B, and CRESNOVERH, G. "The influence of injection rate shaping on Diesel fuel sprays - an experimental study". *Proceedings of the Institution of Mechanical Engineers, Part D: Journal of Atomobile Engineering*, vol. 206 (1992), pp. 173–183, (*cited on: Chap.5-p.107*).

WOOD, ANDREW, WIGLEY, GRAHAM, and HELIE, JEROME. "Flash Boiling Sprays produced by a 6-hole GDI Injector". *17th International Symposium on Applications of Laser Techniques to Fluid Mechanics*, July (2014), pp. 7–10. DOI: `10.13140/2.1.5105.3445`, (*cited on: Chap.3-p.39*).

YI, JIANWEN et al. "Development and Optimization of the Ford 3.5L V6 EcoBoost Combustion System". *SAE Int. J. Engines*, vol. 2.1 (2009), pp. 1388–1407. DOI: `10.4271/2009-01-1494`, (*cited on: Chap.3-pp.31,32,33*).

ZENG, WEI and SJÖBERG, MAGNUS. "Utilizing boost and double injections for enhanced stratified-charge direct-injection spark-ignition engine operation with gasoline and E30 fuels". *International Journal of Engine Research*, vol. 18.1-2 (2017), pp. 131–142. DOI: `10.1177/1468087416685512`, (*cited on: Chap.3-pp.23,26*).

ZENG, WEI, SJÖBERG, MAGNUS, REUSS, DAVID L., and HU, ZONGJIE. "The role of spray-enhanced swirl flow for combustion stabilization in a stratified-charge DISI engine". *Combustion and Flame*, vol. 168.x (2016), pp. 166–185. DOI: `10.1016/j.combustflame.2016.03.015`, (*cited on: Chap.3-p.26*).

ZENG, WEI, XU, MIN, ZHANG, GAOMING, ZHANG, YUYIN, and CLEARY, DAVID J. "Atomization and vaporization for flash-boiling multi-hole sprays with alcohol fuels". *Fuel*, vol. 95 (2012), pp. 287–297. DOI: `10.1016/j.fuel.2011.08.048`, (*cited on: Chap.6-pp.190,192*).

Zeng, Wei, Xu, Min, Zhang, Ming, Zhang, Yuyin, and Cleary, David J. "Macroscopic characteristics for direct-injection multi-hole sprays using dimensionless analysis". *Experimental Thermal and Fluid Science*, vol. 40 (2012), pp. 81–92. doi: `10.1016/j.expthermflusci.2012.02.003`, (*cited on: Chap.6-p.188*).

Zhao, Fuquan, Lai, M-C, and Harrington, David L. "Automotive spark-ignited direct-injection gasoline engines". *Progress in energy and combustion science*, vol. 25.5 (1999), pp. 437–562. doi: `10.1016/S0360-1285(99)00004-0`, (*cited on: Chap.3-pp.16,29*).

Zhao, Hua. *Advanced direct injection combustion engine technologies and development*. Ed. by Hua Zhao. Cambridge: Woodhead Publishing Limited, 2010, (*cited on: Chap.3-pp.20,21,22,23,24,27,29,31, Chap.4-p.65*).

Zheng, Zhaolei, Liu, Chuntao, Tian, Xuefeng, and Zhang, Xiaoyu. "Numerical study of the effect of piston top contour on GDI engine performance under catalyst heating mode". *Fuel*, vol. 157 (2015), pp. 64–72. doi: `10.1016/j.fuel.2015.04.054`, (*cited on: Chap.6-p.167*).

Zhu, Rencheng, Hu, Jingnan, Bao, Xiaofeng, He, Liqiang, Lai, Yitu, Zu, Lei, Li, Yufei, and Su, Sheng. "Tailpipe emissions from gasoline direct injection (GDI) and port fuel injection (PFI) vehicles at both low and high ambient temperatures". *Environmental Pollution*, vol. 216 (2016), pp. 223–234. doi: `10.1016/j.envpol.2016.05.066`, (*cited on: Chap.3-p.20*).

Zigan, L., Schmitz, I., Flügel, a., Wensing, M., and Leipertz, a. "Structure of evaporating single- and multicomponent fuel sprays for 2nd generation gasoline direct injection". *Fuel*, vol. 90.1 (2011), pp. 348–363. doi: `10.1016/j.fuel.2010.08.001`, (*cited on: Chap.3-p.31*).